

2012-01-01

Evaluation of Residual, Post-Service Creep-Rupture Properties of S-816 Turbine Buckets

Jonathan Carlos Contreras

University of Texas at El Paso, joncc211@gmail.com

Follow this and additional works at: https://digitalcommons.utep.edu/open_etd

 Part of the [Materials Science and Engineering Commons](#), [Mechanics of Materials Commons](#), and the [Oil, Gas, and Energy Commons](#)

Recommended Citation

Contreras, Jonathan Carlos, "Evaluation of Residual, Post-Service Creep-Rupture Properties of S-816 Turbine Buckets" (2012). *Open Access Theses & Dissertations*. 2062.
https://digitalcommons.utep.edu/open_etd/2062

This is brought to you for free and open access by DigitalCommons@UTEP. It has been accepted for inclusion in Open Access Theses & Dissertations by an authorized administrator of DigitalCommons@UTEP. For more information, please contact lweber@utep.edu.

EVALUATION OF RESIDUAL, POST-SERVICE CREEP-RUPTURE
PROPERTIES OF S-816 TURBINE BUCKETS

JONATHAN CARLOS CONTRERAS

Department of Metallurgical and Materials Engineering

APPROVED:

Stephen W. Stafford, Ph.D., Chair

Lawrence E. Murr, Ph.D.

James E. Becvar, Ph.D.

Benjamin C. Flores, Ph.D.
Dean of the Graduate School

Copyright ©

By

Jonathan Carlos Contreras

2012

Dedicated to the courageous few that have been, are, and will be persistent in their vision.

EVALUATION OF RESIDUAL, POST-SERVICE CREEP-RUPTURE
PROPERTIES OF S-816 TURBINE BUCKETS

By

JONATHAN CARLOS CONTRERAS, B.S. Metallurgical and Materials Engr.

THESIS

Presented to the Faculty of the Graduate School of

The University of Texas at El Paso

in Partial Fulfillment

of the Requirements

for the Degree of

MASTER OF SCIENCE

Department of Metallurgical and Materials Engineering

THE UNIVERSITY OF TEXAS AT EL PASO

December 2012

Acknowledgements

First and foremost, I would like to thank my committee members, Dr. Stephen W. Stafford, Dr. L. E. Murr, and Dr. James Becvar, for their commitment to this endeavor; it has been an honor and a privilege to have received your guidance and tutelage.

The following individuals were instrumental to the progression and finalization of this project; I thank each and every one of these individuals deeply and sincerely for their efforts and their commitment to my success: Mr. David Brown, Mrs. Faye Ekberg, Ms. Nayeli Camacho, Ms. Flor Gallegos, Ms. Beatriz Tarango, Mrs. Sandra Aguirre-Covarrubias, Mr. Julio Rincon, and Mr. Christopher Bradley (UTEP); Mr. John Chandler and Mr. Gary Vito (Colorado School of Mines); Mr. and Mrs. Dan and Ann Schmidt, Mr. Jason D. Schmidt, and Mr. Joshua Martinez (Colorado Metallurgical Services).

I thank the following three individuals for instilling in me a passion for intellectual and spiritual growth, and the courage to be myself: Mr. Kenneth E. Jones, Mr. Luis A. Juarez, and Ms. Christine J. O'Leary.

I am blessed to have been continuously supported and nurtured by my immediate family throughout my academic career; the envisionment and achievement of the goals that I have set out for myself have and will continue to be fueled by their faith in me. I thank them (especially my brilliant sister, Ms. Tania S. Contreras) wholeheartedly for enabling my aspirations and for teaching me, in their own way, that the fountain of life is belief.

Finally, to the love of my life and most ardent supporter, Ms. Tami Kay Dashley, I thank you. Your sacrifices and patient love have developed me into a better man, the man I want to be for you—love and light, death is the road to awe.

Abstract

An increase in the cost-effectiveness of turbine buckets can be realized by increasing their time before overhaul (TBO) and/or rejuvenating them back into a re-usable state after they have sustained creep damage. This research investigation proposes to answer the following questions: (1) what is the actual condition of the turbine buckets that have reached the end of the manufacturer's service life?; (2) can the manufacturer's service life be extended?; (3) what possibilities exist for re-furbishing the buckets and re-using them? Creep-rupture testing is to be conducted on specimens made from two sets of post-service turbine buckets, in an air atmosphere. As-received and post-rupture specimen characterization of microstructural features, coupled with hardness tests, will be conducted; fractographic examination of rupture surfaces will also be conducted.

Table of Contents

	Page
Acknowledgements.....	v
Abstract.....	vi
Table of Contents.....	vii
List of Tables.....	x
List of Figures.....	xi
Chapter 1: Introduction.....	1
1.1 History and Background.....	1
1.2 Research Incentive.....	2
1.3 Overview of Co-base Superalloy System and S-816.....	3
1.4 The Creep Phenomenon.....	11
1.5 Degradation and Failure Mechanisms of Co-base Superalloys.....	13
1.6 Creep-Rupture Testing.....	20
Chapter 2: Experimental Procedure.....	22
2.1 Creep-Rupture Testing and Apparatus.....	22
2.2 Creep-Rupture Specimen Preparation.....	27
2.3 Testing Parameters.....	30
2.4 Post-Rupture Specimen Characterization.....	32
2.5 Creep-Rupture Data Analysis.....	33
2.6 Metallographic Analysis.....	34
2.7 Energy Dispersive X-ray Spectroscopy.....	35

2.8 Microhardness Testing.....	36
2.9 Fractographic Analysis.....	36
Chapter 3: Results.....	38
3.1 Post-Rupture Specimen Characterization.....	38
3.2 Creep-Rupture Data Analysis.....	55
3.3 Metallographic Analysis.....	64
3.4 Energy Dispersive X-ray Spectroscopy.....	73
3.5 Microhardness Testing.....	102
3.6 Fractographic Analysis.....	104
Chapter 4: Discussion.....	122
4.1 Post-Rupture Specimen Characterization.....	122
4.2 Creep-Rupture Data Analysis.....	122
4.3 Metallographic Analysis.....	125
4.4 Energy Dispersive X-ray Spectroscopy.....	127
4.5 Microhardness Testing.....	128
4.6 Fractographic Analysis.....	129
Chapter 5: Conclusions.....	131
Appendix A.....	134
Appendix B.....	159
Appendix C.....	181
Appendix D.....	202
References.....	217

Curriculum Vita.....	219
----------------------	-----

List of Tables

Table 1. Range of elemental weight percentages in S-816 chemical composition [4].....	4
Table 2. Compilation of reference hardness data of the S-816 alloy in different material forms..	11
Table 3. Creep-rupture testing scheme used in research investigation.....	31
Table 4. Time to rupture and elongation percentage data gathered from creep-rupture testing of seven creep-rupture specimens; test parameters and specimen designations also exhibited.....	55
Table 5. Approximate chemical composition of microconstituents at three different locations in figure 192.....	74
Table 6. Approximate chemical composition of microconstituents at two different locations in figure 196.....	79
Table 7. Approximate chemical composition of microconstituents at four different locations in figure 197.....	83
Table 8. Approximate chemical composition of the microconstituent at a single location in figure 204.....	89
Table 9. Approximate chemical composition of the microstructural matrix at single locations in figures 207 and 208.....	93
Table 10. Approximate chemical composition of microconstituents at different locations in figures 215 and 216.....	98
Table 11. Compilation of average hardness values of twelve, as-received, metallographic specimens used in research investigation.....	102
Table 12. Compilation of average hardness values of metallographic specimens produced from seven creep-rupture specimens used in research investigation.....	103

List of Figures

Figure 1. Change in γ -to- ϵ transformation temperature ($^{\circ}\text{C}$) by 1.0 a/o addition of different alloying elements.....	4
Figure 2. S-816 solution annealed at 2150 $^{\circ}\text{F}$ (1177 $^{\circ}\text{C}$), aged for 16 hrs. at 1400 $^{\circ}\text{F}$ (760 $^{\circ}\text{C}$), and air cooled. The FCC matrix contains blocky, primary MC carbides in the form of CbC (NbC) and grain-boundary precipitates primarily in the form of Cr_{23}C_6 . Etched with a solution of 92 mL HCl, 5 mL H_2SO_4 , and 3 mL HNO_3 . 500 X original magnification [5].....	6
Figure 3. S-816 micrograph from the platform (dovetail) section of a turbine bucket from set 128. Original magnification: 200X.....	7
Figure 4. Effect of solutionization temperature, cooling method, and tempering temperature on tensile properties of S-816 bar [4].....	8
Figure 5. Stress-strain curves at room and elevated temperatures for aged S-816 bar [4].....	9
Figure 6. Effect of test temperature on tensile properties of aged S-816 bar and solutionized S-816 sheet [4].....	9
Figure 7. Creep curves at 1350, 1500, and 1650 $^{\circ}\text{F}$ for aged S-816 bar [4].....	10
Figure 8. Master curves for total strain and creep rupture of aged S-816 alloy [4].....	10
Figure 9. Schematic illustration of creep-curve shapes; ϵ_r and t_r represent the strain and total time at which rupture occurs, respectively [14].....	12
Figure 10. Schematic of the diffusional void growth mechanism [8].....	15
Figure 11. Scanning electron image of grain boundary sliding in a nickel wire [10].....	17
Figure 12. Idealized schematic of the creep process [10].....	18

Figure 13. Characteristic MC carbides in as-cast MM-509 Co-base superalloy; original magnification: 375X [2].....	19
Figure 14. Schematic drawing of creep-rupture testing apparatus [14]; modified from original to depict actual testing assembly used in this research investigation.....	23
Figure 15. Schematic drawing demonstrating cross-sectional view (along longitudinal orientation) of specimen-holding assembly [15].....	24
Figure 16. Plot of data used for empirical determination of extensometer's inch to mV ratio.....	26
Figure 17. Rod-and-tube type extensometer typically used in elevated-temperature creep testing [16].....	27
Figure 18. Turbine bucket from set 128; dashed lines demonstrate where sectioning was conducted.....	29
Figure 19. Core produced from sectioning of turbine bucket.....	29
Figure 20. Schematic drawing of creep-rupture specimen produced for this research investigation; specimen dimensions are in inches.....	30
Figure 21. Photographic image of the twelve specimens used for metallographic analysis of a bucket from set 128; the longitudinally-cut specimen surfaces (light grey in coloration) were mounted face-down in resin and metallographically prepared.....	34
Figure 22. Photographic image of the entirety of specimen S1 in the post-ruptured state.....	38
Figure 23. Macro-photographic image of the fracture surface of the specimen S1 halve demonstrated on the left-hand side in figure 22.....	38
Figure 24. Macro-photographic image of the fracture surface of the specimen S1 halve demonstrated on the left-hand side in figure 22.....	39

Figure 25. Macro-photographic image of the region where rupture occurred in specimen S1.....	39
Figure 26. Photographic image of the entirety of specimen S2 in the post-ruptured state.....	40
Figure 27. Macro-photographic image of the fracture surface of the specimen S2 halve demonstrated on the left-hand side in figure 26.....	40
Figure 28. Macro-photographic image of the fracture surface of the specimen S2 halve demonstrated on the right-hand side in figure 26.....	41
Figure 29. Macro-photographic image of the region where rupture occurred in specimen S2.....	41
Figure 30. Photographic image of the entirety of specimen S4 in the post-ruptured state.....	42
Figure 31. Macro-photographic image of the fracture surface of the specimen S4 halve demonstrated on the left-hand side in figure 30.....	43
Figure 32. Macro-photographic image of the fracture surface of the specimen S4 halve demonstrated on the left-hand side in figure 30.....	43
Figure 33. Macro-photographic image of the region where rupture occurred in specimen S4.....	44
Figure 34. Photographic image of the entirety of specimen S5 (set 128) in the post-ruptured state.....	45
Figure 35. Macro-photographic image of the fracture surface of the specimen S5 (set 128) halve demonstrated on the left-hand side in figure 34.....	45
Figure 36. Macro-photographic image of the fracture surface of the specimen S5 (set 128) halve demonstrated on the right-hand side in figure 34.....	46
Figure 37. Macro-photographic image of the region where rupture occurred in specimen S5 (set 128).....	46

Figure 38. Photographic image of the entirety of specimen S5 (set 821) in the post-ruptured state.....	47
Figure 39. Macro-photographic image of the fracture surface of the specimen S5 (set 821) halve demonstrated on the right-hand side in figure 38.....	48
Figure 40. Macro-photographic image of the fracture surface of the specimen S5 (set 821) halve demonstrated on the right-hand side in figure 38.....	48
Figure 41. Macro-photographic image of the region where rupture occurred in specimen S5 (set 821).....	49
Figure 42. Photographic image of the entirety of specimen S7 in the post-ruptured state.....	50
Figure 43. Macro-photographic image of the fracture surface of the specimen S7 halve demonstrated on the right-hand side in figure 42.....	50
Figure 44. Macro-photographic image of the fracture surface of the specimen S7 halve demonstrated on the right-hand side in figure 42.....	51
Figure 45. Macro-photographic image of the region where rupture occurred in specimen S7.....	51
Figure 46. Figure 46. Photographic image of the entirety of specimen S9 in the post-ruptured state.....	52
Figure 47. Macro-photographic image of the fracture surface of the specimen S9 halve demonstrated on the right-hand side in figure 46.....	53
Figure 48. Macro-photographic image of the fracture surface of the specimen S9 halve demonstrated on the right-hand side in figure 46.....	53
Figure 49. Macro-photographic image of the region where rupture occurred in specimen S9.....	54

Figure 50. Comparison of creep-rupture data derived from wrought/sheet [6] and cast specimens (Sulzer Turbo Services, personal communication, October 2 nd , 2012), and from creep-rupture specimens that were tested as part of research investigation.....	57
Figure 51. Plot of S1 deformation (inches) as a function of time to rupture (hours).....	58
Figure 52. Plot of S2 deformation (inches) as a function of time to rupture (hours).....	59
Figure 53. Plot of S4 deformation (inches) as a function of time to rupture (hours).....	60
Figure 54. Plot of S5 (set 128) deformation (inches) as a function of time rupture (hours).....	61
Figure 55. Plot of S5 (set 821) deformation (inches) as a function of time rupture (hours).....	62
Figure 56. Plot of S7 deformation (inches) as a function of time rupture (hours).....	63
Figure 57. Plot of S9 (set 128) deformation (inches) as a function of time rupture (hours).....	64
Figure 58. Etched microstructure of specimen 1 (as-received); original magnification: 100X...	136
Figure 59. Etched microstructure of specimen 1 (as-received); original magnification: 100X...	137
Figure 60. Etched microstructure of specimen 1 (as-received); original magnification: 500X...	137
Figure 61. Etched microstructure of specimen 1 (as-received); original magnification: 1000X.....	138
Figure 62. Etched microstructure of specimen 2 (as-received); original magnification: 100X...	138
Figure 63. Etched microstructure of specimen 2 (as-received); original magnification: 200X...	139
Figure 64. Etched microstructure of specimen 2 (as-received); original magnification: 500X...	139
Figure 65. Etched microstructure of specimen 2 (as-received); original magnification: 1000X.....	140
Figure 66. Etched microstructure of specimen 3 (as-received); original magnification: 100X...	140
Figure 67. Etched microstructure of specimen 3 (as-received); original magnification: 200X...	141

Figure 68. Etched microstructure of specimen 3 (as-received); original magnification: 500X...	141
Figure 69. Etched microstructure of specimen 3 (as-received); original magnification: 1000X.....	142
Figure 70. Etched microstructure of specimen 4 (as-received); original magnification: 100X...	142
Figure 71. Etched microstructure of specimen 4 (as-received); original magnification: 200X...	143
Figure 72. Etched microstructure of specimen 4 (as-received); original magnification: 500X...	143
Figure 73. Etched microstructure of specimen 4 (as-received); original magnification: 1000X.....	144
Figure 74. Etched microstructure of specimen 5 (as-received); original magnification: 100X...	144
Figure 75. Etched microstructure of specimen 5 (as-received); original magnification: 200X...	145
Figure 76. Etched microstructure of specimen 5 (as-received); original magnification: 500X...	145
Figure 77. Etched microstructure of specimen 5 (as-received); original magnification: 1000X.....	146
Figure 78. Etched microstructure of specimen 6 (as-received); original magnification: 100X...	146
Figure 79. Etched microstructure of specimen 6 (as-received); original magnification: 200X...	147
Figure 80. Etched microstructure of specimen 6 (as-received); original magnification: 500X...	147
Figure 81. Etched microstructure of specimen 6 (as-received); original magnification: 1000X.....	148
Figure 82. Etched microstructure of specimen 7 (as-received); original magnification: 100X...	148
Figure 83. Etched microstructure of specimen 7 (as-received); original magnification: 200X...	149
Figure 84. Etched microstructure of specimen 7 (as-received); original magnification: 500X...	149

Figure 85. Etched microstructure of specimen 7 (as-received); original magnification: 1000X.....	150
Figure 86. Etched microstructure of specimen 8 (as-received); original magnification: 100X...	150
Figure 87. Etched microstructure of specimen 8 (as-received); original magnification: 200X...	151
Figure 88. Etched microstructure of specimen 8 (as-received); original magnification: 500X...	151
Figure 89. Etched microstructure of specimen 8 (as-received); original magnification: 1000X.....	152
Figure 90. Etched microstructure of specimen 9 (as-received); original magnification: 100X...	152
Figure 91. Etched microstructure of specimen 9 (as-received); original magnification: 200X...	153
Figure 92. Etched microstructure of specimen 9 (as-received); original magnification: 500X...	153
Figure 93. Etched microstructure of specimen 9 (as-received); original magnification: 1000X.....	154
Figure 94. Etched microstructure of specimen 10 (as-received); original magnification: 100X.....	154
Figure 95. Etched microstructure of specimen 10 (as-received); original magnification: 200X.....	155
Figure 96. Etched microstructure of specimen 10 (as-received); original magnification: 500X.....	155
Figure 97. Etched microstructure of specimen 10 (as-received); original magnification: 1000X.	
Microconstituents identified for metallographic reference purposes.....	67, 156
Figure 98. Etched microstructure of specimen 11 (as-received); original magnification: 100X.....	156

Figure 99. Etched microstructure of specimen 11 (as-received); original magnification: 200X.....	157
Figure 100. Etched microstructure of specimen 11 (as-received); original magnification: 500X.....	157
Figure 101. Etched microstructure of specimen 11 (as-received); original magnification: 1000X. Microconstituents identified for metallographic reference purposes.....	68, 158
Figure 102. Etched microstructure of specimen 12 (as-received); original magnification: 100X.....	158
Figure 103. Etched microstructure of specimen 12 (as-received); original magnification: 200X.....	159
Figure 104. Etched microstructure of specimen 12 (as-received); original magnification: 500X.....	159
Figure 105. Etched microstructure of specimen 12 (as-received); original magnification: 1000X.....	160
Figure 106. Laves plates (with MC and M6C carbides) in S-816; original magnification: 5950X [2]. Labeling of the different microconstituents was performed for the purposes of this research investigation, as the original reference <i>did not</i> include any labeling within the micrograph.....	69
Figure 107. Un-etched microstructure of specimen S1 (rupture surface); magnification: 500X.....	161
Figure 108. Un-etched microstructure of specimen S1 (rupture surface); magnification: 500X.....	162
Figure 109. Un-etched microstructure of specimen S1 (at core); magnification: 500X.....	162

Figure 110. Un-etched microstructure of specimen S1 (rupture surface); magnification: 1000X.....	163
Figure 111. Un-etched microstructure of specimen S1 (rupture surface); magnification: 1000X.....	163
Figure 112. Un-etched microstructure of specimen S1 (at core); magnification: 1000X.....	164
Figure 113. Un-etched microstructure of specimen S2 (rupture surface); magnification: 500X.....	164
Figure 114. Un-etched microstructure of specimen S2 (rupture surface); magnification: 500X.....	165
Figure 115. Un-etched microstructure of specimen S2 (rupture surface); magnification: 1000X.....	165
Figure 116. Un-etched microstructure of specimen S2 (rupture surface); magnification: 1000X.....	166
Figure 117. Un-etched microstructure of specimen S2 (at core); magnification: 1000X.....	166
Figure 118. Un-etched microstructure of specimen S2 (at core); magnification: 1000X.....	167
Figure 119. Un-etched microstructure of specimen S4 (rupture surface); magnification: 500X.....	167
Figure 120. Un-etched microstructure of specimen S4 (at core); magnification: 500X.....	168
Figure 121. Un-etched microstructure of specimen S4 (at core); magnification: 500X.....	168
Figure 122. Un-etched microstructure of specimen S4 (rupture surface); magnification: 1000X.....	169

Figure 123. Un-etched microstructure of specimen S4 (rupture surface); magnification: 1000X.....	169
Figure 124. Un-etched microstructure of specimen S4 (at core); magnification: 1000X.....	170
Figure 125. Un-etched microstructure of specimen S5, set 128 (rupture surface); magnification: 500X.....	170
Figure 126. Un-etched microstructure of specimen S5, set 128 (rupture surface); magnification: 500X.....	171
Figure 127. Un-etched microstructure of specimen S5, set 128 (core); magnification: 500X....	171
Figure 128. Un-etched microstructure of specimen S5, set 128 (rupture surface); magnification: 1000X.....	172
Figure 129. Un-etched microstructure of specimen S5, set 128 (at core); magnification: 1000X.....	172
Figure 130. Un-etched microstructure of specimen S5, set 128 (at core); magnification: 1000X.....	173
Figure 131. Un-etched microstructure of specimen S5, set 821 (rupture surface); magnification: 500X.....	173
Figure 132. Un-etched microstructure of specimen S5, set 821 (rupture surface); magnification: 500X.....	174
Figure 133. Un-etched microstructure of specimen S5, set 821 (at core); magnification: 500X.....	174
Figure 134. Un-etched microstructure of specimen S5, set 821 (rupture surface); magnification: 1000X.....	175

Figure 135. Un-etched microstructure of specimen S5, set 821 (rupture surface); magnification: 1000X.....	175
Figure 136. Un-etched microstructure of specimen S5, set 821 (at core); magnification: 1000X.....	176
Figure 137. Un-etched microstructure of specimen S7 (rupture surface); magnification: 500X.....	176
Figure 138. Un-etched microstructure of specimen S7 (rupture surface); magnification: 500X.....	177
Figure 139. Un-etched microstructure of specimen S7 (at core); magnification: 500X.....	177
Figure 140. Un-etched microstructure of specimen S7 (rupture surface); magnification: 1000X.....	178
Figure 141. Un-etched microstructure of specimen S7 (rupture surface); magnification: 1000X.....	178
Figure 142. Un-etched microstructure of specimen S7 (at core); magnification: 1000X.....	179
Figure 143. Un-etched microstructure of specimen S9 (rupture surface); magnification: 500X.....	179
Figure 144. Un-etched microstructure of specimen S9 (rupture surface); magnification: 500X.....	180
Figure 145. Un-etched microstructure of specimen S9 (at core); magnification: 500X.....	180
Figure 146. Un-etched microstructure of specimen S9 (rupture surface); magnification: 1000X.....	181

Figure 147. Un-etched microstructure of specimen S9 (rupture surface); magnification: 1000X.....	181
Figure 148. Un-etched microstructure of specimen S9 (at core); magnification: 1000X.....	182
Figure 149. Etched microstructure of specimen S1 (rupture surface); magnification: 500X.....	183
Figure 150. Etched microstructure of specimen S1 (at core); magnification: 500X.....	184
Figure 151. Etched microstructure of specimen S1 (rupture surface); magnification: 1000X....	184
Figure 152. Etched microstructure of specimen S1 (rupture surface); magnification: 1000X....	185
Figure 153. Etched microstructure of specimen S1 (at core); magnification: 1000X.....	185
Figure 154. Etched microstructure of specimen S1 (at core); magnification: 1000X.....	186
Figure 155. Etched microstructure of specimen S2 (rupture surface); magnification: 500X.....	186
Figure 156. Etched microstructure of specimen S2 (at core); magnification: 500X.....	187
Figure 157. Etched microstructure of specimen S2 (rupture surface); magnification: 1000X....	187
Figure 158. Etched microstructure of specimen S2 (at core); magnification: 1000X.....	188
Figure 159. Etched microstructure of specimen S2 (at core); magnification: 1000X.....	188
Figure 160. Etched microstructure of specimen S4 (rupture surface); magnification: 500X.....	189
Figure 161. Etched microstructure of specimen S4 (at core); magnification: 500X.....	189
Figure 162. Etched microstructure of specimen S4 (rupture surface); magnification: 1000X....	190
Figure 163. Etched microstructure of specimen S4 (rupture surface); magnification: 1000X....	190
Figure 164. Etched microstructure of specimen S4 (at core); magnification: 1000X.....	191
Figure 165. Etched microstructure of specimen S5, set 128 (rupture surface); magnification: 500X.....	191
Figure 166. Etched microstructure of specimen S5, set 128 (at core); magnification: 500X.....	192

Figure 167. Etched microstructure of specimen S5, set 128 (rupture surface); magnification: 1000X.....	192
Figure 168. Etched microstructure of specimen S5, set 128 (at core); magnification: 1000X....	193
Figure 169. Etched microstructure of specimen S5, set 128 (at core); magnification: 1000X....	193
Figure 170. Etched microstructure of specimen S5, set 821 (rupture surface); magnification: 500X.....	194
Figure 171. Etched microstructure of specimen S5, set 821 (rupture surface); magnification: 500X.....	194
Figure 172. Etched microstructure of specimen S5, set 821 (at core); magnification: 500X.....	195
Figure 173. Etched microstructure of specimen S5, set 821 (rupture surface); magnification: 1000X.....	195
Figure 174. Etched microstructure of specimen S5, set 821 (rupture surface); magnification: 1000X.....	196
Figure 175. Etched microstructure of specimen S5, set 821 (rupture surface); magnification: 1000X.....	196
Figure 176. Figure 176. Etched microstructure of specimen S5, set 821 (at core); magnification: 1000X.....	197
Figure 177. Etched microstructure of specimen S7 (rupture surface); magnification: 500X.....	197
Figure 178. Etched microstructure of specimen S7 (at core); magnification: 500X.....	198
Figure 179. Figure 179. Etched microstructure of specimen S7 (rupture surface); magnification: 1000X.....	198
Figure 180. Etched microstructure of specimen S7 (rupture surface); magnification: 1000X....	199

Figure 181. Etched microstructure of specimen S7 (at core); magnification: 1000X.....	199
Figure 182. Etched microstructure of specimen S7 (at core); magnification: 1000X.....	200
Figure 183. Etched microstructure of specimen S9 (rupture surface); magnification: 500X.....	200
Figure 184. Etched microstructure of specimen S9 (at core); magnification: 500X.....	201
Figure 185. Etched microstructure of specimen S9 (rupture surface); magnification: 1000X....	201
Figure 186. Etched microstructure of specimen S9 (rupture surface); magnification: 1000X....	202
Figure 187. Etched microstructure of specimen S9 (at core); magnification: 1000X.....	202
Figure 188. Etched microstructure of specimen S9 (at core); magnification: 1000X.....	203
Figure 189. Etched microstructure of specimen S1 (rupture surface); magnification: 1000X....	204
Figure 190. Etched microstructure of specimen S1 (rupture surface); magnification: 1000X....	205
Figure 191. Etched microstructure of specimen S1 (at core); magnification: 500X.....	205
Figure 192. Etched microstructure of specimen S1 (at core); magnification: 2000X. Numbered ovals indicate where EDS analyses were conducted.....	74, 206
Figure 193. Etched microstructure of specimen S2 (rupture surface); magnification: 1000X. Microconstituents identified for metallographic reference purposes.....	72, 206
Figure 194. Etched microstructure of specimen S2 (rupture surface); magnification: 2000X....	207
Figure 195. Etched microstructure of specimen S2 (at core); magnification: 2000X.....	207
Figure 196. Etched microstructure of specimen S2 (at core); magnification: 2000X. Numbered ovals indicate where EDS analyses were conducted.....	79, 208
Figure 197. Etched microstructure of specimen S4 (rupture surface); magnification: 1000X. Numbered ovals indicate where EDS analyses were conducted.....	84, 208
Figure 198. Etched microstructure of specimen S4 (rupture surface); magnification: 1000X....	209

Figure 199. Etched microstructure of specimen S4 (at core); magnification: 1000X.	
Microconstituents identified for metallographic reference purposes.....	27, 209
Figure 200. Etched microstructure of specimen S4 (at core); magnification: 1000X.	
Microconstituents identified for metallographic reference purposes.....	73, 210
Figure 201. Etched microstructure of specimen S5, set 128 (rupture surface); magnification: 1000X.....	210
Figure 202. Etched microstructure of specimen S5, set 128 (rupture surface); magnification: 1000X.....	211
Figure 203. Etched microstructure of specimen S5, set 128 (at core); magnification: 1000X....	211
Figure 204. Etched microstructure of specimen S5, set 128 (at core); magnification: 1000X. A numbered oval indicates where an EDS analysis was conducted.....	89, 212
Figure 205. Etched microstructure of specimen S5, set 821 (rupture surface); magnification: 1000X.....	212
Figure 206. Etched microstructure of specimen S5, set 821 (rupture surface); magnification: 1000X.....	213
Figure 207. Etched microstructure of specimen S5, set 821 (at core); magnification: 1000X. A numbered oval indicates where an EDS analysis was conducted.....	93, 213
Figure 208. Etched microstructure of specimen S5, set 821 (at core); magnification: 1000X. A numbered oval indicates where an EDS analysis was conducted.....	93, 214
Figure 209. Etched microstructure of specimen S7 (rupture surface); magnification: 1000X....	214
Figure 210. Etched microstructure of specimen S7 (rupture surface); magnification: 1000X....	215
Figure 211. Etched microstructure of specimen S7 (at core); magnification: 1000X.....	215

Figure 212. Etched microstructure of specimen S7 (at core); magnification: 1000X.....	216
Figure 213. Etched microstructure of specimen S9 (rupture surface); magnification: 1000X....	216
Figure 214. Etched microstructure of specimen S9 (rupture surface); magnification: 1000X....	217
Figure 215. Etched microstructure of specimen S9 (at core); magnification: 1000X. A numbered oval indicates where an EDS analysis was conducted.....	98, 217
Figure 216. Etched microstructure of specimen S9 (at core); magnification: 1000X. Numbered ovals indicate where EDS analyses were conducted.....	98, 218
Figure 217. Elemental spectrum collected during EDS analysis of location 1 in figure 192.....	76
Figure 218. Elemental spectrum collected during EDS analysis of location 2 in figure 192.....	77
Figure 219. Elemental spectrum collected during EDS analysis of location 3 in figure 192.....	78
Figure 220. Elemental spectrum collected during EDS analysis of location 4 in figure 196.....	81
Figure 221. Elemental spectrum collected during EDS analysis of location 5 in figure 196.....	82
Figure 222. Elemental spectrum collected during EDS analysis of location 6 in figure 197.....	85
Figure 223. Elemental spectrum collected during EDS analysis of location 7 in figure 197.....	86
Figure 224. Elemental spectrum collected during EDS analysis of location 8 in figure 197.....	87
Figure 225. Elemental spectrum collected during EDS analysis of location 9 in figure 197.....	88
Figure 226. Elemental spectrum collected during EDS analysis of location 10 in figure 204.....	91
Figure 227. Elemental spectrum collected during EDS analysis of location 11 in figure 207.....	95
Figure 228. Elemental spectrum collected during EDS analysis of location 12 in figure 208.....	96
Figure 229. Elemental spectrum collected during EDS analysis of location 13 in figure 215....	100
Figure 230. Elemental spectrum collected during EDS analysis of location 14 in figure 216....	101
Figure 231. Elemental spectrum collected during EDS analysis of location 15 in figure 216....	102

Figure 232. SE image of rupture surface of specimen S1; magnification: 100X.....	106
Figure 233. SE image of rupture surface of specimen S1; magnification: 500X.....	106
Figure 234. SE image of rupture surface of specimen S2; magnification: 250X.....	107
Figure 235. SE image of rupture surface of specimen S2; magnification: 500X.....	108
Figure 236. SE image of rupture surface of specimen S2; magnification: 1000X.....	108
Figure 237. BSE image of rupture surface of specimen S2 (same location as demonstrated in figure 236); magnification 1000X.....	109
Figure 238. SE image of rupture surface of specimen S4; magnification: 500X.....	110
Figure 239. SE image of rupture surface of specimen S4; magnification: 1000X.....	110
Figure 240. BSE image of rupture surface of specimen S4 (same location as demonstrated in figure 240); magnification: 1000X.....	111
Figure 241. SE image of rupture surface of specimen S5, set 128; magnification: 250X.....	112
Figure 242. SE image of rupture surface of specimen S5, set 128; magnification: 500X.....	112
Figure 243. SE image of rupture surface of specimen S5, set 128; magnification: 1000X.....	113
Figure 244. SE image of rupture surface of specimen S5, set 128; magnification: 2000X.....	113
Figure 245. BSE image of rupture surface of specimen S5, set 128 (approximately same location as demonstrated in figure 244); magnification: 2000X.....	114
Figure 246. SE image of rupture surface of specimen S5, set 821; magnification: 250X.....	115
Figure 247. SE image of rupture surface of specimen S5, set 821; magnification: 500X.....	115
Figure 248. SE image of rupture surface of specimen S5, set 821; magnification: 1000X.....	116
Figure 249. SE image of rupture surface of specimen S5, set 821; magnification: 2000X.....	116
Figure 250. SE image of rupture surface of specimen S7; magnification: 250X.....	117

Figure 251. SE image of rupture surface of specimen S7; magnification: 500X.....	118
Figure 252. SE image of rupture surface of specimen S7; magnification: 1000X.....	118
Figure 253. SE image of rupture surface of specimen S7; magnification: 2000X.....	119
Figure 254. SE image of rupture surface of specimen S9; magnification: 250X.....	120
Figure 255. SE image of rupture surface of specimen S9; magnification: 500X.....	120
Figure 256. SE image of rupture surface of specimen S9; magnification: 500X.....	121
Figure 257. SE image of rupture surface of specimen S9; magnification: 1000X.....	121
Figure 258. SE image of rupture surface of specimen S9; magnification: 1000X.....	122

Chapter 1: Introduction

1.1 History and Background

The cobalt-based superalloy, S-816, was developed in conjunction with the earliest Vitallium-derivative superalloys in the late 1940's; Vitallium, an alloy developed for dental and biomedical applications in the 1930's, provided the alloy base for the development of several superalloys during this era. S-816 was developed primarily as a gas turbine blade material that could withstand higher stresses and eventually became known for its excellent creep and creep-rupture properties [1].

A national incentive to develop superalloys with no amounts of cobalt in the late 1970's, as a consequence of the global cobalt shortage that was precipitated by the political insurrection in Zaire, hindered the number of new Co-base superalloys that have been developed in the past 60 years; at the time, the United States considered cobalt a strategic material and wanted to greatly diminish the impact on stockpile quantities, as cobalt resources were (and still are) globally abundant only in the mid-African continent. Additionally, the lack of an ordered, coherent, precipitation-hardenable phase (such as gamma prime in Ni-base superalloys) limited this superalloy system to solid-solution strengthening and non-coherent carbides as sources of mechanical strength. These two key factors have historically placed Co-base superalloys in a secondary position in the superalloys market for the past 60 years. Despite these developmental issues, cast and wrought Co-base superalloys continue to be used for the following reasons [2]:

1. Cobalt alloys exhibit higher melting temperatures and correspondingly flatter stress rupture curves, providing useful stress capability to a higher absolute temperature than nickel- or iron-base alloys.
2. Cobalt alloys offer superior hot-corrosion resistance to contaminated gas turbine atmospheres due to their higher chromium contents.

3. In general, cobalt alloys exhibit superior thermal fatigue resistance and weldability to nickel alloys.

1.2 Research Incentive

This superalloy material system has continued to provide reliable performance in lower pressure, higher temperature regions (as compared to Ni-base components) for industrial, end-user corporations, for service hours up to 66% more than the manufacturer's recommended service life ~personal correspondence~. This exhibited material behavior creates an opportunity for an increase in the cost-effectiveness of S-816 turbine buckets, as their time before overhaul (TBO) could be increased. Additionally, given the excellent weldability of this superalloy, the possibility of reusing these components after additive laser-clad welding and CNC machining (depending on the severity of geometrical alterations to the used turbine buckets), and rejuvenation via appropriate heat treatment, represents an opportunity for material recyclability and additional cost-effectiveness. Assessments of residual, post-service (i.e. past the manufacturer's warranty life) creep-rupture properties, as well as rejuvenation and re-usability capabilities, of superalloy components are scarce, limited, or proprietary; hence, the end-user interest is significant and understood, as safer, economical, and more educated risk assessments are always needed regarding the societal and industrial demand for increased turbine component performance.

The specimens used in this research project emanate from two sets of turbine buckets (sets 128 and 821) which had been overhauled after experiencing over 100,000 hours of service,. Both sets were employed as second-stage turbine buckets within General Electric® Frame 3 land-

based gas turbines; these turbines operated within a range of 6000 to 6500 rpm (S. Stafford, personal communication, May 5th, 2011).

1.3 Overview of Co-base Superalloy System and S-816

Cobalt-base superalloys, like the other Ni- and Fe-base superalloy systems, are complex chemical and crystallographic material systems consisting of an austenitic matrix and a variety of precipitated phases, such as carbides and intermetallic compounds. These intermetallic compounds can be of the geometrically close-packed (GCP) or the topologically close-packed (TCP) type structures [2]. In the dynamic service environment that this material system is exposed to, the effects of stress, temperature, time, and surface-atmosphere interactions induce a state of compositional and microstructural flux in superalloy components. It is imperative, then, that these components maintain the austenitic matrix polymorph at elevated service temperatures, as pure cobalt will exhibit an allotropic phase transformation from the high-temperature, face-centered-cubic (FCC) austenitic crystal structure (γ) to the low-temperature, hexagonal-close-packed (HCP) structure (ϵ) at 783 °F (417 °C) [2]. The great capability of the Co-Ni-Fe polymorph is summarized in the following passage [3]:

[The] close-packed FCC lattice has the capability to maintain relatively high and reliable tensile, rupture, creep, and thermomechanical fatigue properties to homologous temperatures that are much higher than for equivalent body-centered-cubic (BCC) systems. Contributing factors are the high modulus of the FCC lattice, its many slip systems, and its low diffusivity for secondary elements. Further, of utmost importance are the broad solubility of secondary elements in the austenitic matrix and their physiochemical characteristics enabling precipitation...for strength. Strengthening effects can also be obtained by solid-solution hardening, carbide precipitation, and grain boundary control[.]

The athermal, martensitic γ -to- ϵ transformation can be suppressed by alloying element additions so that it occurs at lower temperatures, effectively reducing the risk of transformation during elevated temperature service. Chromium, molybdenum, tungsten, and silicon additions stabilize the HCP polymorph while carbon, niobium, iron, manganese, and nickel stabilize the FCC polymorph. Figure 1 graphically portrays a summary of the effect of different alloying additions on the γ -to- ϵ transformation temperature, as a function of atomic weight percent (a/o) solubility in FCC cobalt [2].

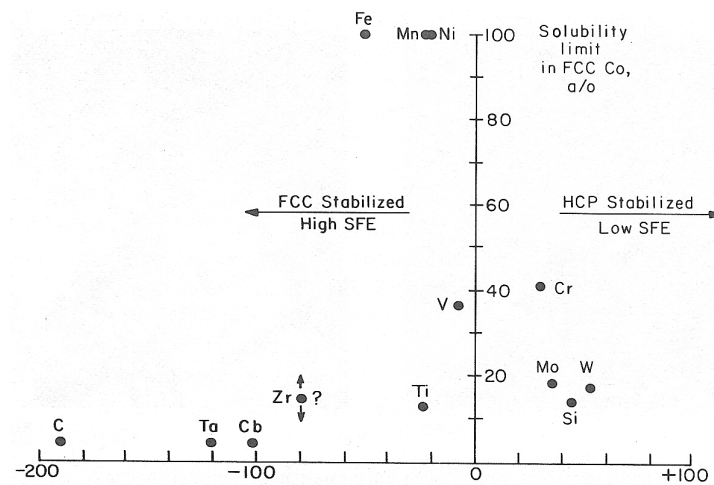


Figure 1. Change in γ -to- ϵ transformation temperature ($^{\circ}\text{C}$) by 1.0 a/o addition of different alloying elements.

The S-816 alloy was first manufactured by the Allegheny-Ludlum Steel Corporation; its chemical composition is demonstrated in Table 1 [4].

Table 1. Range of elemental weight percentages in S-816 chemical composition [4].

Element	Weight (%)
Carbon	0.32-0.42

Element	Weight (%)
Manganese	1.00-2.00
Silicon	0.20-0.60
Phosphorus	0.030 max
Sulfur	0.030 max
Chromium	19.0-21.0
Nickel	19.0-21.0
Molybdenum	3.50-4.50
Tungsten	3.50-4.50
Niobium	3.50-4.50
Iron	5.00 max
Cobalt	Balance

The roles of different alloying additions in defining the chemical composition, microstructural features, and mechanical properties of S-816 (and Co-base superalloys in general) are varied and compounded. The chromium addition plays a key part in aiding resistance to hot corrosion and high-temperature oxidation via the formation of the Cr_2O_3 oxide scale; additionally, it can form different types of carbides (M_{23}C_6 , M_7C_3 , and M_3C_2) and provides some solid-solution strengthening. Cr_2O_3 is the most stable oxide that can be formed by the S-816 alloy and its development during service preserves component functionality by preventing the oxidation of other alloying additions, as their oxides do not compare to the stability of Cr_2O_3 . Molybdenum and tungsten are the primary solid-solution strengtheners in S-816, as chromium and niobium have a higher affinity for performing other chemical functions; both of these elements allow formation of M_6C carbides, and tungsten is also the only addition that increases

the melting point of S-816 [2]. Niobium, the third refractory element addition to S-816, is a stronger MC carbide former than molybdenum or tungsten and hence forms the very stable MC carbide in S-816; figure 2 provides testament to this statement, as large blocky MC carbides are identified as CbC (NbC) in a representative micrograph of an S-816 specimen that was solutionized and subsequently aged [5].



Figure 2. S-816 solution annealed at 2150 °F (1177 °C), aged for 16 hrs. at 1400 °F (760 °C), and air cooled. The FCC matrix contains blocky, primary MC carbides in the form of CbC (NbC) and grain-boundary precipitates primarily in the form of Cr_{23}C_6 . Etched with a solution of 92 mL HCl, 5 mL H_2SO_4 , and 3 mL HNO_3 . 500 X original magnification [5].

Nickel and iron are added to enhance the stability of the austenitic FCC cobalt matrix (γ) at high temperatures (above 783 °F (417 °C)) and to suppress the transformation to HCP cobalt at low temperatures [2]. Manganese and silicon are added to enhance the castability of this superalloy, in terms of alloy fluidity, melt deoxidation practices, and sulfur control. Even though

manganese can form Mn_7C_3 , its concentration is too diluted for this to be noticeable; similarly, silicon can produce its own oxide scale to assist in resistance to high temperature oxidation but its concentration is too diluted for this to occur. Finally, as S-816 depends heavily on carbide precipitation for its strength, the carbon content is on the higher-end of the spectrum, in comparison to Ni- or Fe-base superalloys.

S-816 can be manufactured in wrought, forged, and cast forms; it was designed for service in the 1200-1500 °F (649-816 °C) temperature range. The majority of the documented mechanical property data on the S-816 superalloy emanates from specimens in the wrought or forged condition that underwent solutionization, rapidly cooling, and aging; heat treatment was generally omitted on cast buckets, although preliminary data on experimental engines indicated that aging improved the properties of cast buckets [6]. This is an important distinction, as the specimens for this research investigation emanate from cast turbine buckets, which are not *exactly* representative of the manufactured form from which most of the available mechanical property data on the S-816 superalloy emanates. Figure 3 demonstrates an SEM micrograph of the un-etched microstructure of the platform section of a turbine bucket from set 128; the dendritic structure indicates that the bucket was indeed cast—it is unknown whether either of the two bucket sets underwent an aging heat treatment procedure after they were originally cast.

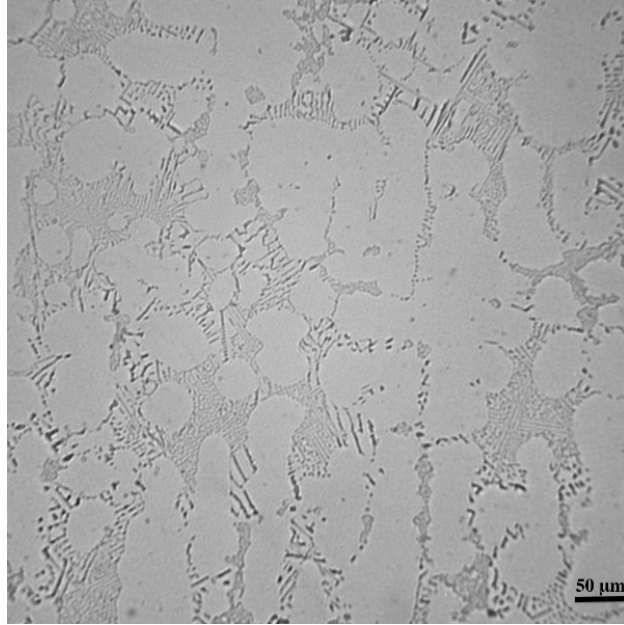


Figure 3. S-816 micrograph from the platform (dovetail) section of a turbine bucket from set 128. Original magnification: 200X.

With this issue taken in consideration, figures 4-8 demonstrate a compilation of mechanical properties of S-816 in the wrought or forged forms [4]. Table 2 demonstrates a compilation of hardness data that emanated from the only two literature sources that were found to contain hardness data on the S-816 alloy.

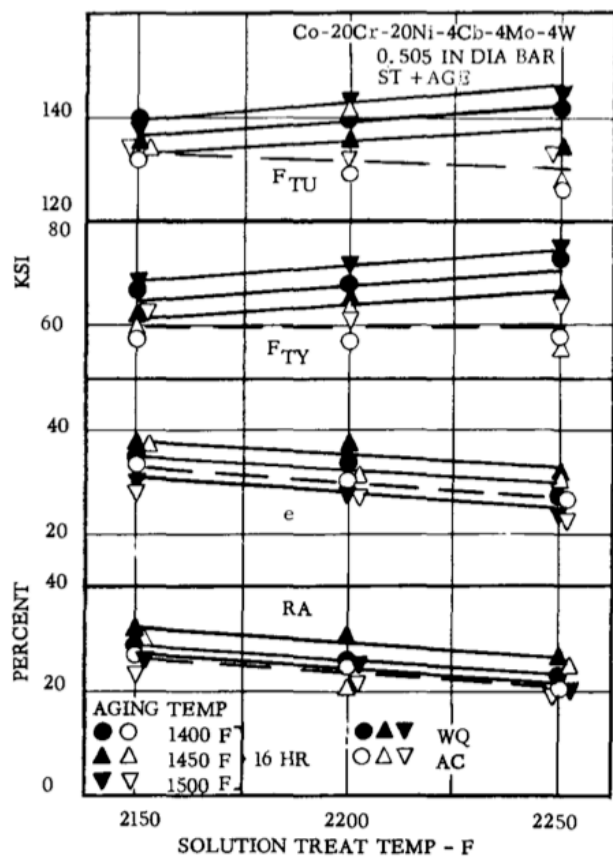


Figure 4. Effect of solutionization temperature, cooling method, and tempering temperature on tensile properties of S-816 bar [4].

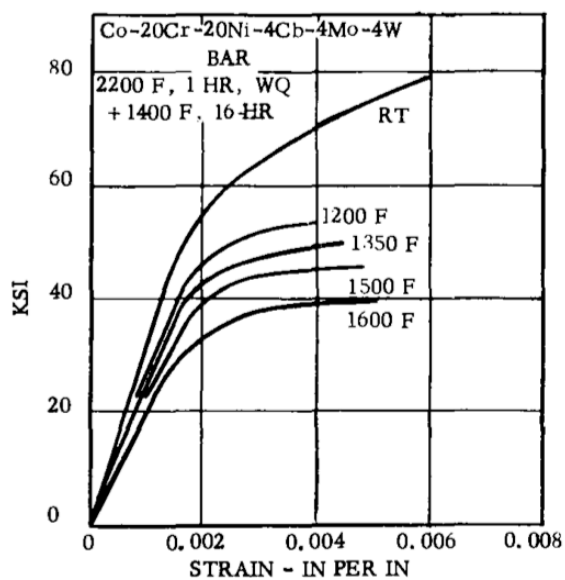


Figure 5. Stress-strain curves at room and elevated temperatures for aged S-816 bar [4].

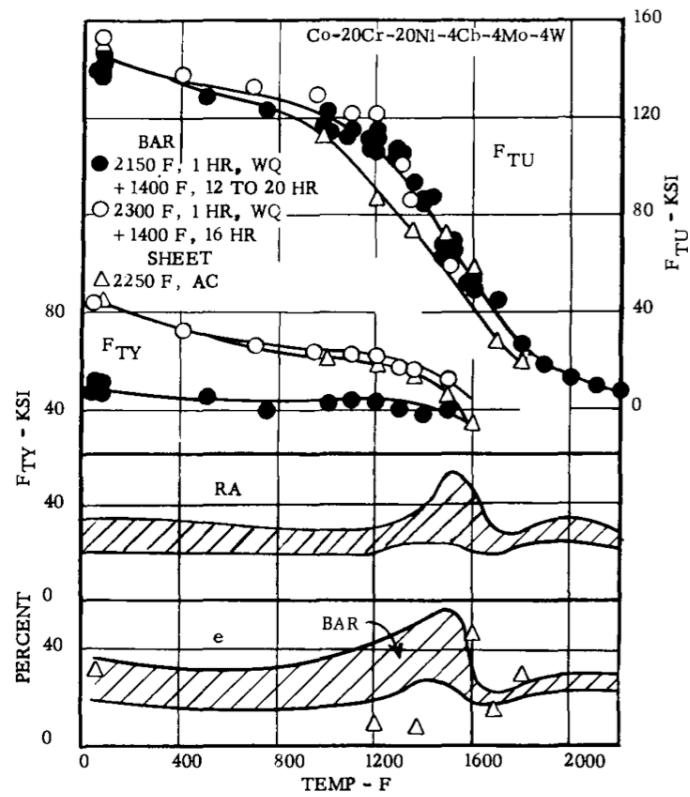


Figure 6. Effect of test temperature on tensile properties of aged S-816 bar and solutionized S-816 sheet [4].

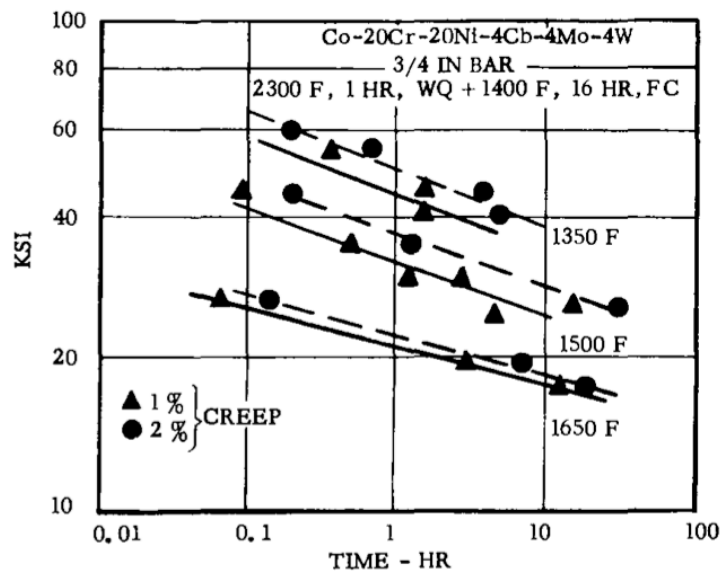


Figure 7. Creep curves at 1350, 1500, and 1650 °F for aged S-816 bar [4].

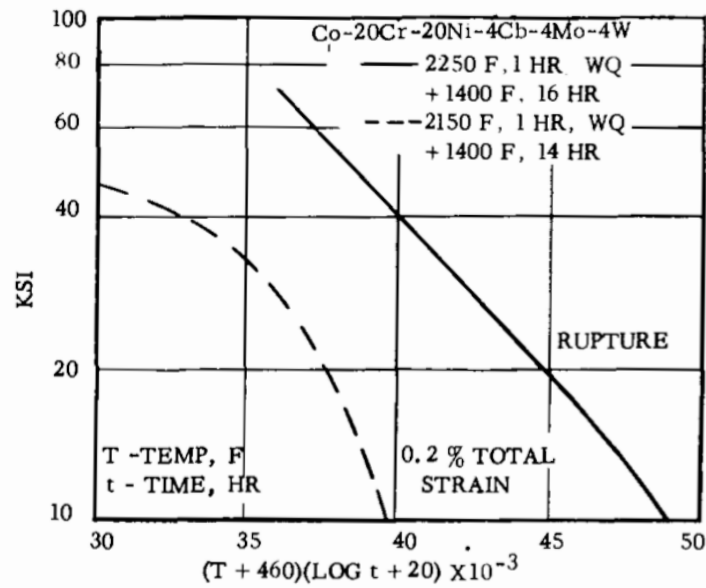


Figure 8. Master curves for total strain and creep rupture of aged S-816 alloy [4].

Table 2. Compilation of reference hardness data of the S-816 alloy in different material forms.

Material Condition	Heat Treatment	Hardness	Reference
Wrought	2150 °F for 1 hr., water quenched 1400 °F for 16 hrs., air cooled	HRA 65 (HRC 30)	[6]
Wrought	2300 °F for 1 hr., water quenched	HRB 101 (HRC 23)	[6]
Bar stock, 0.505 in. outer diameter	2150 °F for 1 hr., water quenched 1400 °F for 12 hrs.	269 - 352 BHN (24 - 35 HRC)	[6]
1.5 in. round wrought bar	2150 °F for 1 hr., water quenched 1400 °F for 16 hrs.	355 VPN (36 HRC)	[6]
Sheet, strip, plate	2130 - 2170 °F for 1 hr., air cooled	35 HRC max	[4]
Bar, forgings	2130 - 2170 °F for 1 hr., water quenched 1390 - 1410 °F for 12 - 16 hrs.	24 HRC min 25 HRC max	[4]

Material Condition	Heat Treatment	Hardness	Reference
5/8 in. - 3/4 in. bar	Hot-worked	25 - 35 HRC	[4]
5/8 in. - 3/4 in. bar	Solution-treated	17 - 25 HRC	[4]
5/8 in. - 3/4 in. bar	Solution-treated 1400 °F for 16 hrs.	24 - 37 HRC	[4]

1.4 The Creep Phenomenon

Creep can be defined as plastic deformation that can occur when the stress and temperature of a component are maintained constant; that is, the strain within the component is time-dependent. This mechanical behavior can occur in any material system and occurs due to the fact that the flow stress in a rigid body contains a component that responds to thermal activation [7]. The seminal equation that has been used as the basis for the many creep models that have been developed over the past sixty years simply expresses that the strain rate in a material is thermally activated and temperature-dependent via an Arrhenius-type relationship [7]:

$$\dot{\varepsilon} = Ae^{-\frac{q}{kT}}$$

Creep strain is the fundamental issue by which creep is understood and characterized, as creep curves (depicting creep strain vs. time) are used to conceptualize the basic aspects of this phenomenon. Creep curves for different materials are obtained by testing a specimen in constant uniaxial load or stress and recording the resulting strain as a function of time. There are three characteristic stages within a typical creep curve (primary, secondary, and tertiary) which are defined by differing rates of creep and controlled by equally different mechanical behavior phenomena. Primary creep behavior is characterized by a decelerating creep rate after the initial

onset of instantaneous strain; secondary creep behavior is characterized by a steady-state creep rate; tertiary creep behavior is characterized by an accelerating creep rate, which ultimately leads to fracture. Figure 9 [14] demonstrates a schematic illustration of generalized creep curves, which depicts the effect of increasing stress and temperature on creep behavior, with the three stage boundaries separated by dashed lines.

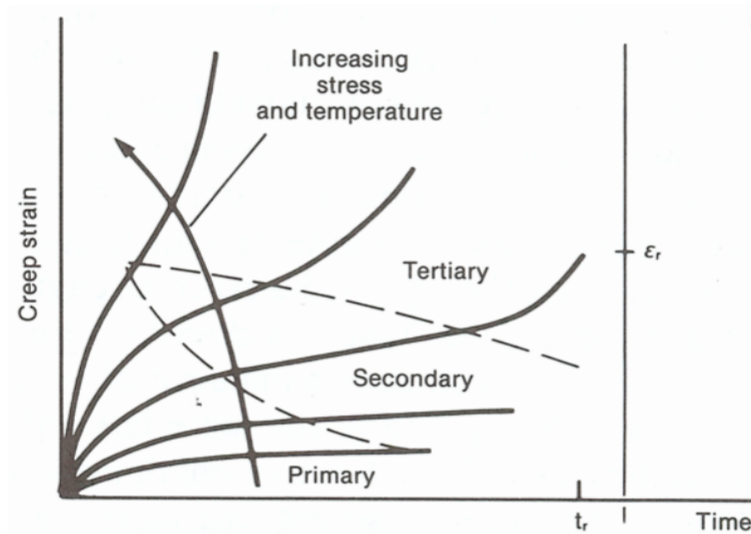


Figure 9. Schematic illustration of creep-curve shapes; ϵ_r and t_r represent the strain and total time at which rupture occurs, respectively [14].

The underlying creep deformation mechanisms which compound when practical scenarios are considered, and which have led to many different creep models for practical use, can be summarized by something they all hold in common: thermal energy assisting dislocation motion.

However, despite the many models used to predict creep behavior in structural components, these models are insufficient when used in predictive life assessments of components due to the operational and environmental effects that exacerbate the damage mechanisms by which high-temperature components degrade and ultimately fail; the effects of oxidation, corrosion, and thermal cycling are just some of the factors that must be considered in

addition to any creep modeling equations. A combinatory solution of modeling, non-destructive evaluation, historical referencing of case histories, and prior empirical work is ultimately used in assessing the effect of the creep phenomenon on structural components.

1.5 Degradation and Failure Mechanisms of Co-base Superalloys

The hot, corrosive, and stressed environment under which turbine bucket components operate places them in a state of compositional and microstructural flux. The creep-rupture properties of Co-base superalloys can be diminished by the formation and growth of creep voids, grain boundary sliding, and the modification of carbide morphology and composition. The creep resistance and thermal fatigue strength of this material system are derived from incoherent carbide precipitation and refractory element solid-solution strengthening. Mechanisms of grain boundary sliding, grain growth, and dislocation mobility are inhibited by a combination of the following carbide groups: MC, M₃C₂, M₆C, M₇C₃, and M₂₃C₆. However, the *lack* of a high-temperature, ordered, coherent particle-strengthening mechanism (such as γ' in Ni-based superalloys), produces lower strengths at elevated temperatures in these superalloys.

Creep void nucleation and growth

Ashby et. al. [8] identify three different fracture mechanisms for polycrystalline solids that operate above creep temperatures, which is generally considered to be above 0.3T_m or 0.4T_m; these three mechanisms are transgranular, intergranular, and diffusional creep fracture. As noted by Goods and Brown [9], “The ductile fracture of metals and alloys generally occurs by the formation and subsequent growth and coalescence of voids or cavities.” The heterogeneous nucleation of surfaces or cavities during plastic deformation occurs at regions where the deformation is inhomogeneous [9], such as in grain boundaries and regions around incoherent

particles, whether they be inclusions or precipitates; these are interfacial regions that have relatively higher energies due to their larger amounts of free volume and subsequent lattice strain, as compared to the matrix.

Grain boundary cavitation appears more readily under conditions that favor a change in deformation mode, from bulk deformation to grain boundary sliding, such as intermediate temperatures (generally accepted in the literature as being from 1000-1400°F) and lower strain rates [9]. When grain boundary sliding is blocked by triple points, ledges or particles in the boundaries, nucleation of cavities can occur due to the resulting increased stress and strain concentrations at these interfaces. The growth of the cavities, however, can be attributed to mechanisms that involve both the coalescence of cavities during plastic deformation as well the diffusion of matter away from cavities and into the grain boundaries (diffusional creep); intergranular creep embodies the aforementioned mechanisms of cavity growth and nucleation. The diffusional creep mechanism is controlled by the interfacial energy differentiation between the stressed grain boundaries and the void surfaces, as indicated by Ashby et. al. [8]:

The tensile traction σ_n acting across a grain boundary lowers the chemical potential of atoms or ions there by the amount $\sigma_n\Omega$, [where Ω denotes the volume per atom]. If the chemical potential difference ($\sigma_n\Omega - 2\Gamma_s\Omega/r_h$) between sites on the boundary and those on the void surfaces is negative, then matter flows out of the holes (usually by grain boundary diffusion) and deposits on to the boundary causing the grains on either side to move apart [Γ_s denotes the surface energy within the voids and r_h denotes the radius of the holes].

Figure 10 [8] demonstrates a schematic of the mechanism described above, along with indications of where the equations apply in the schematic.

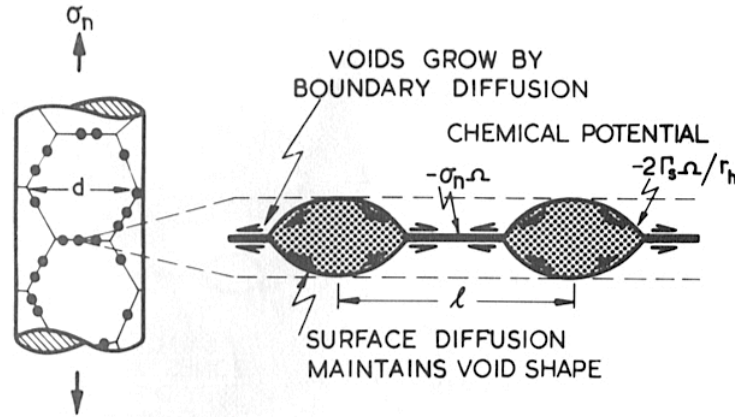


Figure 10. Schematic of the diffusional void growth mechanism [8].

Cavity nucleation around particles can occur due to a separation of the particle-matrix interface or by fracture of the particles themselves. The local state of deformation at these interfaces is controlled by a number of factors, such as particle geometry and orientation relative to the applied stress in the system.

Particles that are roughly equiaxed will generally undergo internal decohesion from the matrix after some amount of plastic strain [9]; these spherical particles do not inhibit elastic or plastic deformation in any orientation, which thus allows for a triaxial state of stress to exist locally. In contrast, particles that are irregularly shaped or those with large aspect ratios often fail by internal fracture [9]; these irregularly shaped particles inhibit elastic or plastic deformation in a specific orientation (based upon their irregular geometry), which thus creates a local biaxial state of stress. There is little to no relative orientation of roughly equiaxed particles to the applied stress in a system; however, the orientation of irregularly shaped particles, relative to the applied stress in a system, can make them fracture preferentially if their major axes lie at small angles to the applied stress direction.

The lack of a controlled microstructural architecture is inherent to cast, polycrystalline materials, even if they have undergone hot isostatic pressing during processing, have been investment cast, or have been made from material that was vacuum melted or re-melted. The prevalence of interfacial regions where cavity growth and nucleation may occur in the creep-rupture specimens used for this research investigation cannot go understated.

Grain boundary sliding

Grain boundary sliding, as mentioned briefly in the context of the nucleation of cavities at grain boundaries, “is thought of as a surface that can slide upon itself in a continuous matter, totally ignoring atomistic structure, and avoiding the complexity that appears when dislocations, ledges, protrusions, facets, and other structural features at the boundaries are introduced” [10]. Even though it may appear macroscopically simple as the translation of two grains over a common planar interface (as demonstrated in figure 11 [10]), as a result of resolved shear stresses acting parallel to the interface, it can occur microscopically only by the systematic displacements on the atomic level involving the structural features of grain boundaries [10].

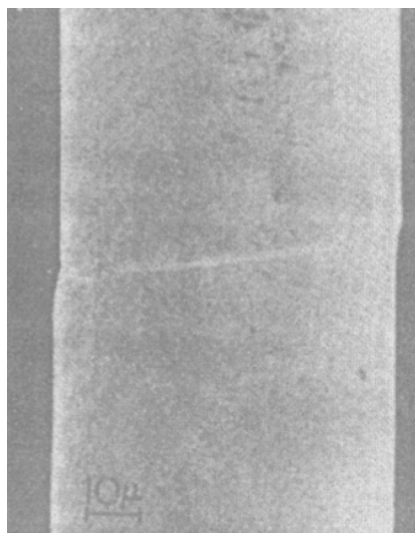


Figure 11. Scanning electron image of grain boundary sliding in a nickel wire [10].

The total creep process inherently involves grain boundary sliding either as “deformation by grain boundary sliding with diffusion maintaining the integrity of the interface, or as deformation by mass transport with grain boundary sliding accommodating the incompatibilities which would otherwise appear in the interfaces” [10]; this description of creep is applicable to the phenomenology of the aforementioned fracture mechanisms that can occur at creep temperatures. Figure 12 [10] exhibits a schematic of this description of the creep process, which illustrates a rigid translation (sliding) along the grain boundary and migration (or transport of matter) into the voids created at the interfaces; the μ parameter denotes the sliding displacement between the grains.

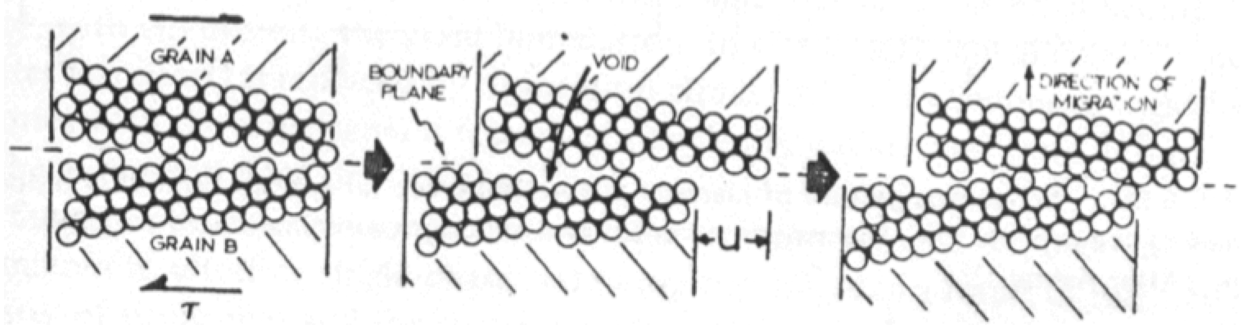


Figure 12. Idealized schematic of the creep process [10].

In comparing the phenomena of the translation of solid matter by grain boundary sliding with stress-induced slip of a perfect crystalline matrix, Murr [10] concludes that as grain boundaries possess unique interfacial dislocations (which gives them their characteristic structural features), then grain boundary sliding can be described by the movement of grain boundary dislocations in the interfaces; this is phenomenologically comparable to the manner by which crystal lattice dislocations can account for the systematic sliding of the boundary plane.

Modification of carbide morphology and composition

It is generally accepted that all turbine bucket or blade alloys form two types of carbide precipitates: primary and secondary. As Benac and Swaminathan [11] indicate, primary carbides form when carbon reacts with strong carbide-forming elements, such as chromium, niobium, molybdenum, or tungsten, during the solidification of the molten alloy; these carbides will usually have the formula MC, where M is the metallic element that is forming the carbide. These carbides tend to have blocky or Chinese-script morphologies, as well as large sizes, as seen in the micrograph of figure 13 [2]. Secondary carbides tend to form at lower temperatures (during the solidification of the molten alloy) from the remaining carbon that is dissolved in the matrix as well as from the dissolution of primary MC carbides.

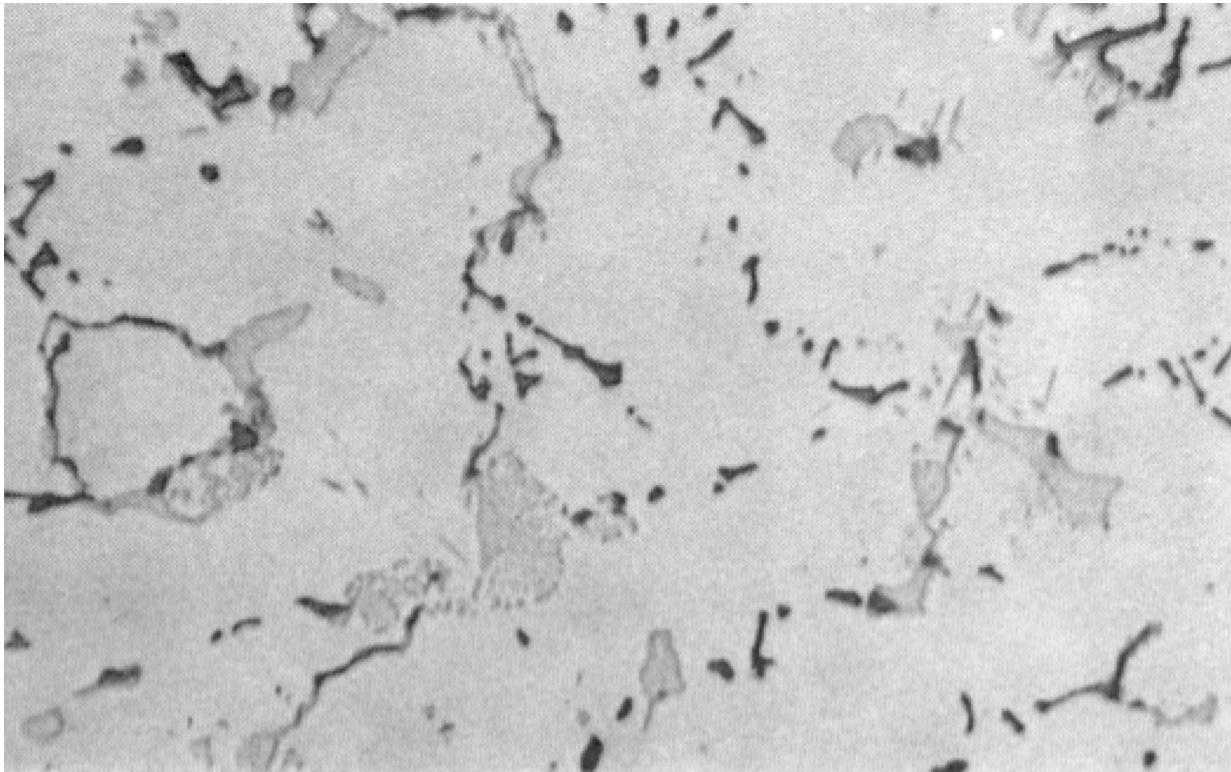


Figure 13. Characteristic MC carbides in as-cast MM-509 Co-base superalloy; original magnification: 375X [2].

The incoherency of the metastable primary carbides with the matrix (which is of the FCC structure for the S-816 Co-base superalloy) will eventually lead to their degradation as they transform into M_6C or $M_{23}C_6$ carbides. The increased magnitude of coherency strains in these carbide-matrix interfacial regions induces the required presence of larger concentrations of dislocations (which leads to an interfacial energy increase), as compared to coherent precipitates that induce coherency strains which are magnitudes smaller. The chemical composition incoherencies in these carbide-matrix interfacial regions also add to the interfacial energy increase. According to Porter et. al. [12], the lattice distortion and strain field associated with dislocations can assist the nucleation of precipitates by reducing the positive change in the Gibbs free energy associated with the total strain energy of the precipitates. Even as coherent nuclei, precipitates are still structurally and chemically different from the matrix; a region that is strained or that has a higher energy associated with it (as compared to the matrix) is preferential for habitation, as the precipitates have to expend less energy in creating their own perturbation of the matrix lattice. It is energetically favorable for precipitates to “use” what dislocations or any other lattice defects have to offer: energetically free space. As a result, MC carbides can transform into M_6C and $M_{23}C_6$ carbides at dendrite boundaries after long-term exposure to elevated-temperature service conditions, as grain boundaries offer increased amounts of free volume and an increased probability for compositional heterogeneity. The eventual agglomeration and filming phenomena exhibited by secondary carbides substantially reduces the impact properties as well as the stress-rupture life of components made from these alloys, as the continuity of these hard intermetallic phases throughout the grain/dendrite boundaries offers easy paths for crack propagation and creep void nucleation.

1.6 Creep-rupture Testing

The objective of this research is to qualitatively define the remnant service capabilities of overhauled turbine components with supporting qualitative and quantitative data; it is fitting, then, that the type of testing conducted should stress the specimens (made from these components) to rupture in an environment that closely mimics the actual service environment within the turbine section in which they were used. Creep, creep-rupture, and stress-rupture testing are three different testing methods which can be used to assess the mechanical properties of materials used in elevated temperature applications. The following definitions from ASTM Standard E139-11 illustrate the key differences between these testing methods [13]:

3.2.4 *creep-rupture test*—a test in which progressive specimen deformation and the time for rupture are measured. In general, deformation is much larger than that developed during a creep test.

3.2.5 *creep test*—a test that has the objective of measuring creep and creep rates occurring at stresses usually well below those which would result in fracture during the time of testing. Since the maximum deformation is only a few percent, a sensitive extensometer is required.

3.2.11 *stress-rupture test*—a test in which time for rupture is measured, no deformation measurements being made during the test.

Creep-rupture testing encompasses aspects from both creep and stress-rupture testing that will be of use in the overall assessment of residual service capabilities of these components, such as the monitoring of specimen deformation and testing specimens to rupture.

Chapter 2: Experimental Procedure

2.1 Creep-Rupture Testing Apparatus

The loading frame and furnace of a SATEC™ (now owned by Instron®) creep testing machine (CE model) were used in the creep-rupture testing that was performed for this research investigation. The antiquated systems of the machine were replaced by modern, calibrated equipment, such as a new temperature controller for control of the furnace temperature and a new linear variable differential transformer (LVDT) for measurement of specimen deformation. The different components of the creep-rupture testing apparatus will be discussed below; ASTM Standard E139-11 was used as a technical reference for the experimental procedure that was followed in the course of this research investigation.

Loading and Specimen-Holding Assembly

The application of the desired uniaxial tensile *load* (constant load, static stress testing) was accomplished via the following loading assembly: dead weights on a weight pan, a weight train which connected the pan to a lever arm with a mechanical advantage ratio of 20:1, an upper pull rod that screwed into the lever arm, a specimen holder assembly that connected both upper and lower pull rods, and a stationary lower pull rod. Calibrated dead weights in increments of 5, 10, 20, and 30 lbf were incrementally added (to avoid shock loading) in order to create the desired load for each test; 15% of the test force was applied during the one hour pre-heat period of testing in order to mitigate the effect of non-axial forces on the pull rods from the packed-in furnace insulation. Figure 14 demonstrates a schematic of the entire testing apparatus [14].

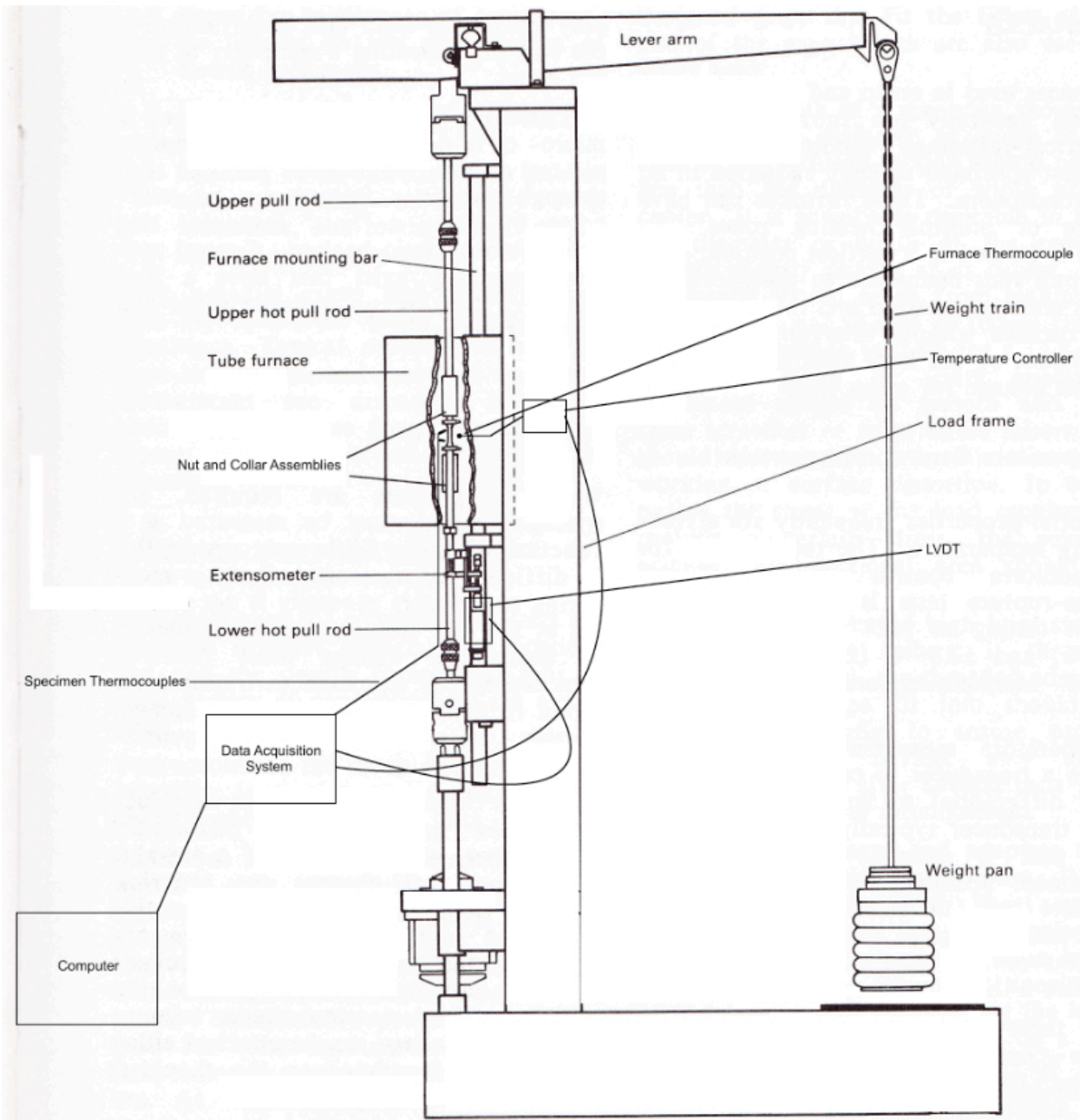


Figure 14. Schematic drawing of creep-rupture testing apparatus [14]; modified from original to depict actual testing assembly used in this research investigation.

The specimen-holding assembly consisted of a collar and a specimen-retaining nut (figure 15); B. Patterson [15] developed this scheme in order to prolong the re-use of the collars, as these and the retaining nuts had to necessarily be made from superalloy material (Inconel 718) in

order for them to perform adequately at the elevated test temperatures. Via this scheme, the collars were preserved in that if the end of a specimen seized, the retaining nuts could be tapped and sacrificed (instead of the collars) in order to remove the seized specimen. It was much more feasible and economical to make these small retaining nuts than to acquire and thread entire cylinders/bars for new collars.

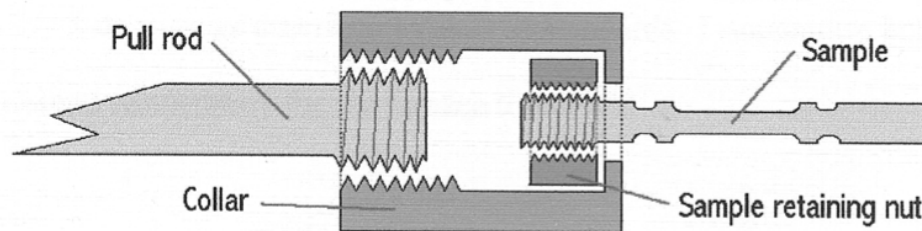


Figure 15. Schematic drawing demonstrating cross-sectional view (along longitudinal orientation) of specimen-holding assembly [15].

Data Acquisition System

A new Omega® iNet-100 data acquisition system was used in order to digitize and record the various streams of test data from the temperature controller, the LVDT, and two thermocouples. All four differential channel inputs for the four aforementioned data streams were programmed to collect 1 data point per second. The DAQ system interfaced with a stationary desktop (Windows® XP Professional operating system) via an Omega® iNet-240 USB 2.0 controller, which allowed for the Omega® iNet-iWPLUS software to enable real-time display of data acquisition during testing. The Direct To Excel program (part of the iNet-iWPLUS software) was used to directly digitize and record real-time data to the Microsoft Excel™ spreadsheet program.

Furnace, Temperature Controller, and Thermocouples

The three-stage furnace that was originally part of the SATEC™ creep testing machine was modified and used for creep-rupture testing in this research investigation; modifications included installation of a new K-type furnace thermocouple and converting the furnace into a single-stage furnace in order to reduce temperature variations along specimen gauge lengths. Fiberglass insulation was used to cover and insulate the top and bottom of the furnace prior to furnace operation.

As mentioned earlier, a new Omega® temperature controller with automatic tuning capabilities was installed on the creep testing machine in order to further mitigate furnace temperature variations; data output from the controller to the data acquisition system occurred via an analog, isolated 0 -10 V (DC) signal. Preliminary test trials of the creep-rupture testing apparatus demonstrated furnace temperature fluctuations to vary by ± 10 °F (± 6 °C) during furnace ramping; however, after reaching the temperature set-point, the furnace temperature held consistently within $\pm 3 - 4$ °F (1 - 2 °C).

Two Super OMEGACLAD® XL, K-type thermocouple probes were purchased in order to mitigate the effect of furnace heat on the quality of thermocouple data streams and to improve ease of use in the confines of the furnace.

Extensometer

The extensometer consisted of a rod-and-tube bracket which attached onto a specimen's shoulders and correlated a change in specimen length by transmitting relative displacement to an adjustable micrometer that impinged on the LVDT, thus digitizing specimen deformation into a mV output that was recorded by the DAQ system. The mV output of the LVDT was converted

into inches via an inch to mV ratio (0.04 thousandths of an inch per millivolt), which was calculated from the calibrated LVDT range (- 4993 mV to + 4983 mV) and the actual deformation range of the extensometer (0.391 inches). This ratio was also empirically derived by plotting extensometer measurements and the corresponding LVDT mV output data; both methods of ratio determination yielded the same result. Figure 16 demonstrates the plot of the extensometer measurements and the corresponding LVDT mV output data. Figure 17 demonstrates an image of a rod-and-tube type extensometer, which is similar to the one used in this research investigation [16].

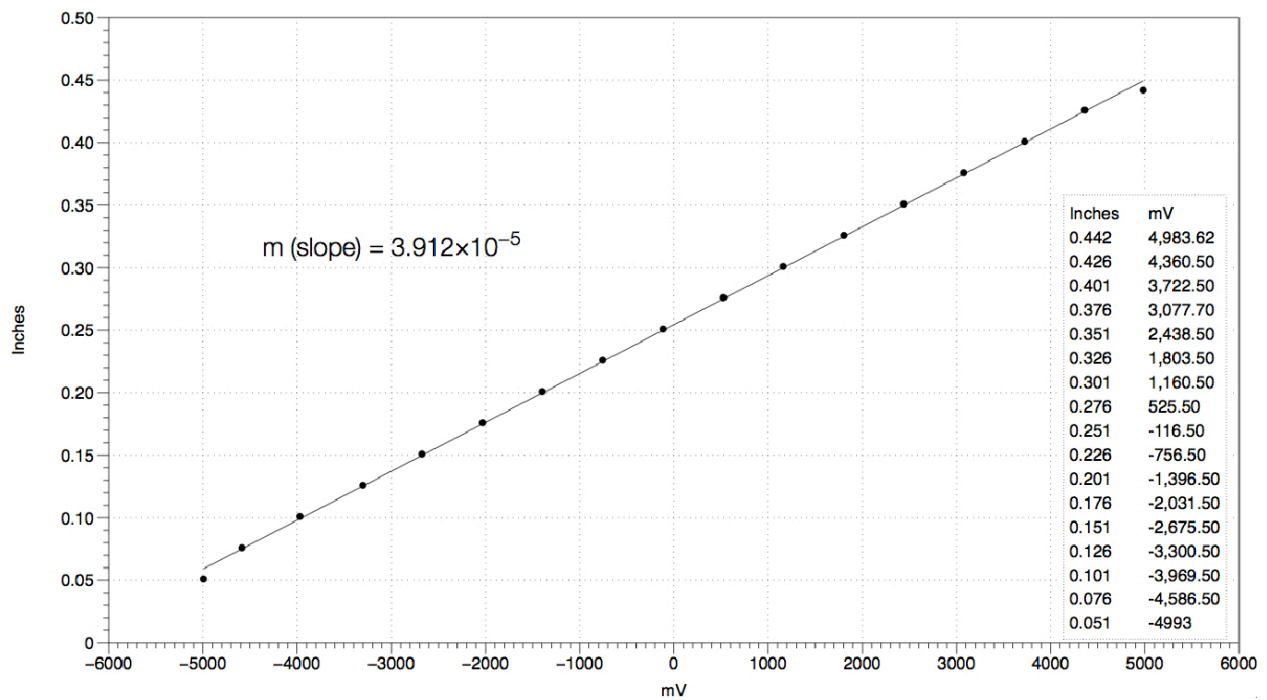


Figure 16. Plot of data used for empirical determination of extensometer's inch to mV ratio.

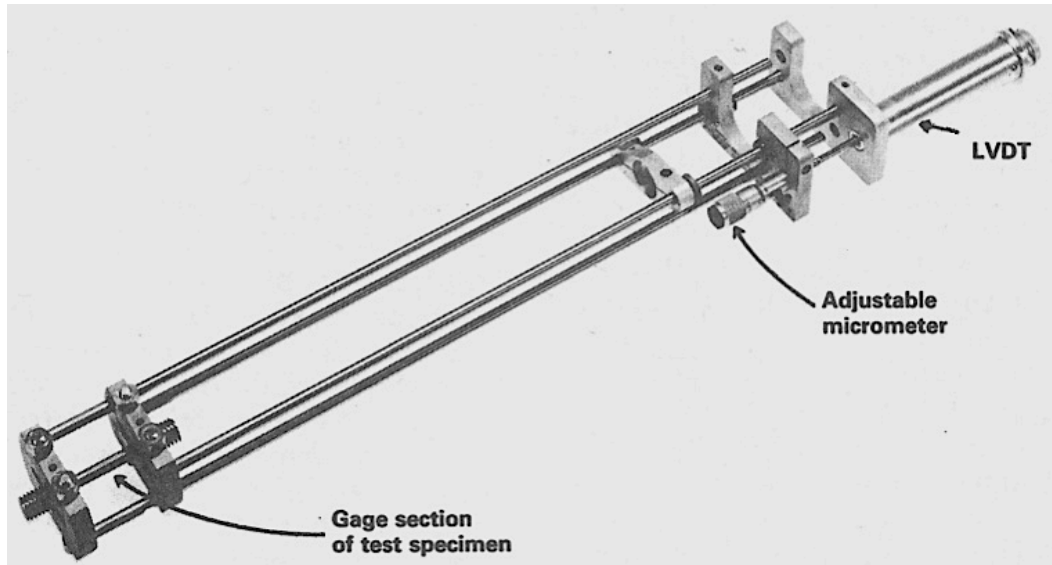


Figure 17. Rod-and-tube type extensometer typically used in elevated-temperature creep testing [16].

As noted earlier, a new Omega[®] LVDT was purchased in order to replace the original LVDT that was part of the SATEC[™] creep testing machine, which had a loose, broken transducer. Preliminary test trials of the creep-rupture testing apparatus demonstrated noise fluctuations of 50 to 100 mV (0.004 to 0.008 inches, or 1 to 2% of the total calibrated range) in the output of the new LVDT, which placed its performance below the acceptable noise level of 5% (of the total calibrated range) for extensometer systems in creep-rupture testing of metallic materials, according to ASTM Standard E139-11. An EPSCO (model D-612T) filtered DC power source was used to power the LVDT in order to mitigate power-source signal fluctuations, as a conventional DC power source led to noise fluctuations of more than 5% in LVDT mV output during preliminary test trials of the extensometer system.

2.2 Creep-Rupture Specimen Preparation

The specimens used for this research investigation were prepared in accordance with ASTM Standard E139-06 [13] and ASTM Standard E8/E8M-11 [17]. Given the physical

constraints of the turbine buckets' geometry, the specimens were sub-size (relative to the standard specimen size listed in the aforementioned ASTM standards) and had the following dimensions: an overall length of 4.5 inches, a gauge length of 1.0 inches, and a gauge diameter of 0.252 inches. Figure 18 demonstrates a turbine bucket from set 128, prior to it being sectioned, with sectioning lines drawn; a lubricated, continuously-cooled band saw was used to perform all of the sectioning of turbine buckets that were used to produce specimens. The following describes the different steps taken in order to prepare a specimen for the creep-rupture testing that is the subject of this research investigation:

1. Sectioned top of bucket, in a transverse orientation, approximately 4.75 inches from the bottom of the bucket; the upper portion of this cross-section was too thin and variable in thickness for derivation of a specimen.
2. Sectioned sides of bucket, in longitudinal orientations, approximately 1.25 inches from the side ends of the bucket platform.
3. The core of turbine bucket material produced as a result of steps 1 and 2 (as seen in figure 19) was placed on a lathe, rounded, and machined to the specimen dimensions demonstrated in figure 20. It was possible to derive only one creep-rupture specimen from every one core of turbine bucket material.

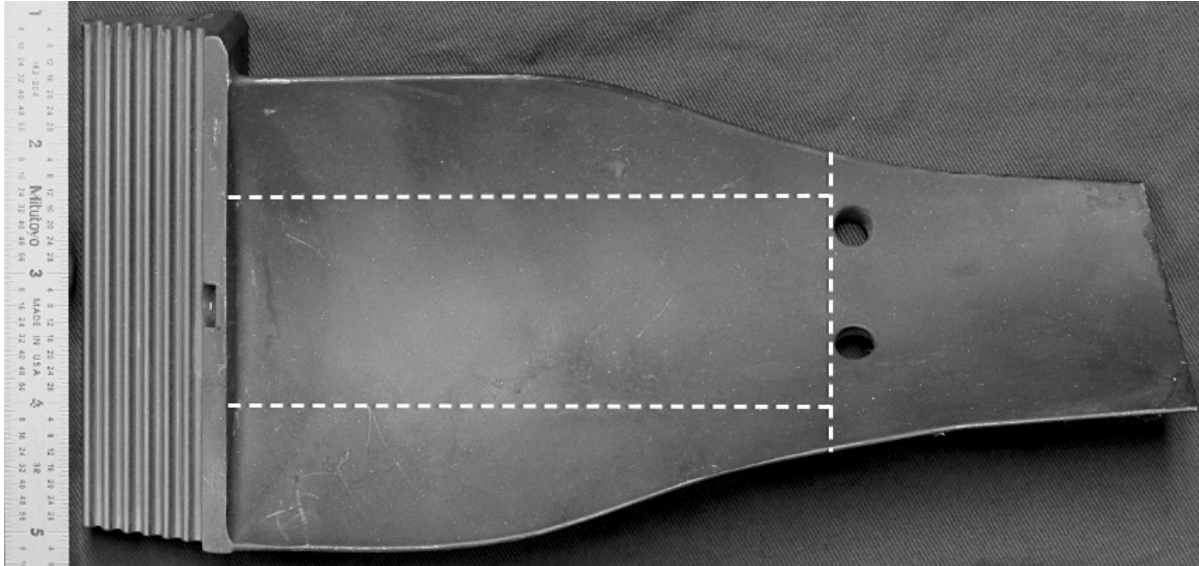


Figure 18. Turbine bucket from set 128; dashed lines demonstrate where sectioning was conducted.



Figure 19. Core produced from sectioning of turbine bucket.

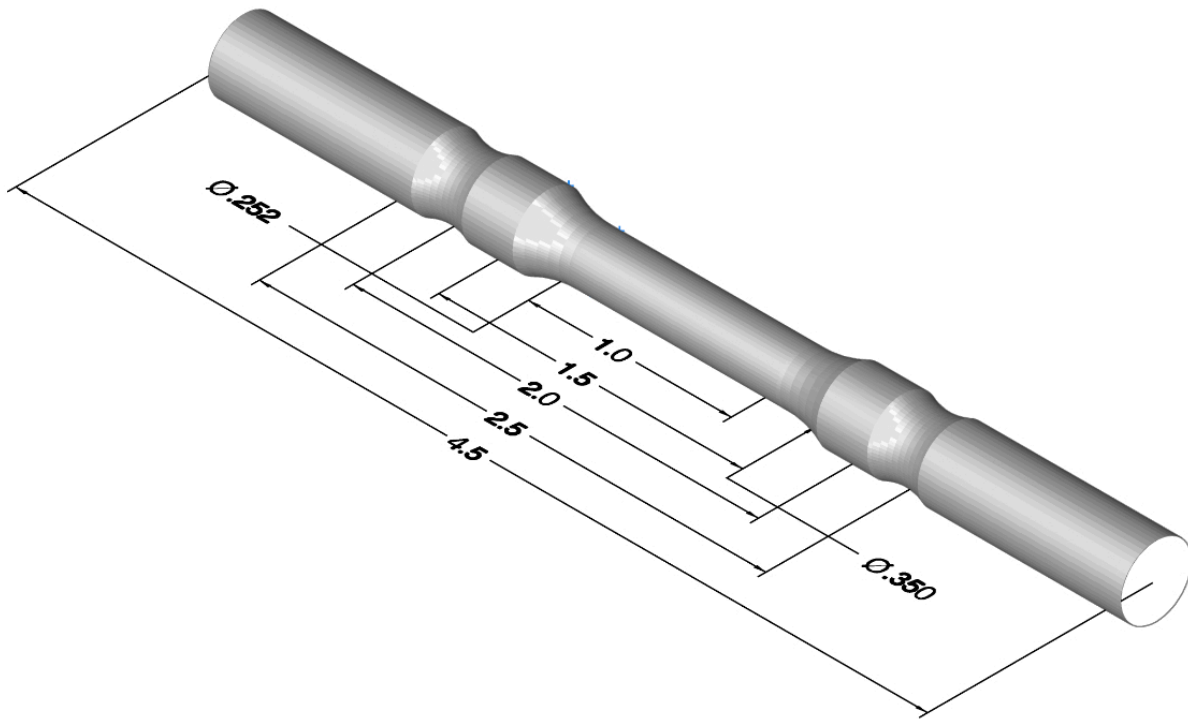


Figure 20. Schematic drawing of creep-rupture specimen produced for this research investigation; specimen dimensions are in inches.

2.3 Testing Parameters

The literature regarding the mechanical properties of S-816 is consistent in demonstrating that creep and creep-ruptures tests on this material were limited to the following temperatures: 1200, 1350, 1500, and 1650 °F. However, as the turbine buckets used for this research investigation did not experience normal operating temperatures in excess of 1500 °F, only the 1200, 1350, and 1500 °F temperatures were used in the testing scheme that was developed for this research investigation.

Two sources of data [4,5] were reviewed regarding the different stresses that were used in the creep-rupture testing of this material; it was discovered that each of the three aforementioned test temperatures were limited to creep and creep-rupture testing within the following

(approximate) stress ranges: 20 - 40 ksi (1500 °F), 25 - 45 ksi (1350 °F), and 45 - 65 ksi (1200 °F). Table 3 demonstrates the testing scheme that was developed for this research investigation.

Table 3. Creep-rupture testing scheme used in research investigation.

Parameter	1200 °F	1350 °F	1500 °F
$20 \leq 30$ ksi			S1 (24 ksi)
$31 \leq 40$ ksi		S4 & S5 (36 & 40 ksi)	S2 & S3 (36 & 40 ksi)
$41 \leq 50$ ksi		S6 (44 ksi)	
$51 \leq 60$ ksi	S7 & S8 (56 & 60 ksi)		
$61 \leq 70$ ksi	S9 (64 ksi)		

At the onset of this research investigation, five specimens from set 821 had already been machined according to the specimens dimensions demonstrated in figure 20; at that time, no other turbine buckets from set 821 were available in order to produce additional creep-rupture specimens from set 821. Three of these five specimens from set 821 were improperly loaded and accidentally broken at the onset of this research investigation, as no equipment manual and few records were available regarding the operation of the antiquated creep testing machine. The fourth of these five specimens was designated to be S4 (according to table 3) and was supposed to have been tested at 1350 °F and 36 ksi; unfortunately, prior to this specimen being tested, the furnace thermocouple had undergone maintenance and was not placed deep within the confines of the furnace upon replacement. Hence, the specimen temperature far exceeded the readings of the furnace thermocouple, which led to the specimen temperature achieving equilibrium at an unintended 1650 °F. The fifth of these five specimens was designated as S5 and was successfully tested at 1350 °F and 40 ksi.

Despite the setbacks experienced with the specimens from set 821, five of the nine specimens prepared from turbine buckets from set 128 were successfully tested; the three unsuccessfully tested specimens from set 128 consisted of the S3 (40 ksi, 1500 °F), S5 (40 ksi, 1350 °F), S6 (44 ksi, 1350 °F), and S8 (60 ksi, 1200 °F) specimens. The S3 specimen was unsuccessfully tested due to a power outage that occurred at the university during the time that the specimen was being tested; the extensometer (specimen deformation) data for this specimen was irretrievably lost during this outage. The S5, S6, and S8 specimens experienced failure at one of their threaded ends in the course of being tested; this was attributed to improper engagement by the specimen-retaining nuts as the nuts' threads had worn down from being re-used multiple times in different tests.

In total, seven (out of a possible fourteen) specimens were successfully tested; six of these specimens emanated from turbine bucket set 128 and one of these specimens emanated from turbine bucket set 821.

The creep machine's frame allowed the application of static stress to a specimen via a lever arm; with a mechanical advantage ratio of 20:1 (M_A), this lever arm was mechanically loaded by calibrated weights (W) and applied stress (P) to a creep-rupture specimen (with a cross-sectional surface area of 0.05 in², A_s) via the following equation:

$$P = \frac{M_A \cdot W}{A_s}$$

2.4 Post-Rupture Specimen Characterization

The distance between the shoulders of a ruptured specimen (after *carefully* re-connecting the two fractured halves) was recorded for each specimen, after being retrieved from the creep-rupture testing machine. After these dimensions were recorded, the post-rupture state of the

specimens and their fracture surfaces were photographically documented (with a dimensional reference). After this documentation, the two halves of the ruptured specimens were sorted into two different groups, one for metallographic analysis and another for fractographic analysis.

2.5 Creep-Rupture Data Analysis

DataGraph (a Macintosh program) was used to compile and statistically analyze the specimen deformation data that was gathered during the different creep-rupture tests.

Specimen elongation percentages (using ruptured specimen lengths from both measured and extensometer data sets) were calculated in accordance with ASTM Standard E139-11; this specification indicates that if the specimens' gage length included fillets and shoulders (as in the specimens used this research investigation), then change in gage length should be expressed as a percentage of the length of the specimens' reduced section (in this case, 1.00 inches).

Specimen deformation (in inches) as a function of time to rupture (in hours) was plotted for each of the different specimens.

A comparative logarithm-logarithm plot between the creep-rupture data gathered in this research investigation and historical reference data on the S-816 alloy was created. The creep-rupture curves from historical data (derived from wrought and sheet specimens) were created by plotting an average of the different rupture stresses for 100, 1,000, and 10,000-hour creep-rupture lives at 1200, 1350, and 1500 °F, respectively. Historical data derived from cast specimens only yielded data for 1,000-hour creep-rupture life; hence, these rupture stresses were individually plotted as 1,000-hour points at 1200, 1350, and 1500 °F. The creep-rupture curves from the experimental specimens' data were created by plotting the individual rupture stresses for the different times to rupture at 1200, 1350, and 1500 °F.

2.6 Metallographic Analysis

At the onset of this research investigation, a bucket from set 128 was longitudinally sectioned via water-jet cutting; the resulting piece was transversely sectioned along eleven different planes in order to produce specimens for metallographic analysis of the as-received state of a bucket from set 128. Figure 21 demonstrates the twelve metallographic specimens that were produced as a result of these sectioning procedures, which were longitudinally mounted in resin, except for the dovetail section (specimen 12 in figure 21); the size of this specimen allowed for grinding and polishing to be conducted without the need of a mount.

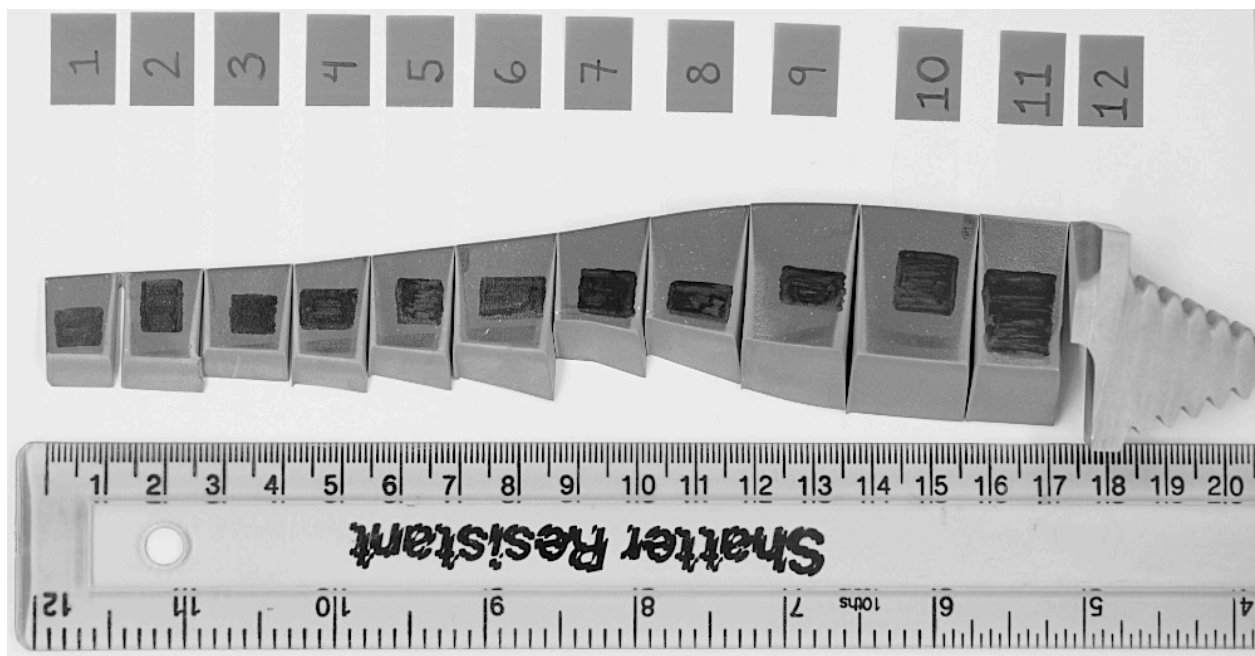


Figure 21. Photographic image of the twelve specimens used for metallographic analysis of a bucket from set 128; the longitudinally-cut specimen surfaces (light grey in coloration) were mounted face-down in resin and metallographically prepared.

The halves of the ruptured specimens that were selected for metallographic analysis were transversely sectioned at approximately 0.25 inches from their fracture surfaces with a continuously-cooled abrasive saw. These resulting sections were longitudinally mounted in resin

and ground until the specimens' longitudinal, cross-sectional surfaces were at least 0.15 inches in width.

Specimen grinding was conducted with silicon carbide pads, from 60 through 600 grit; specimen polishing was conducted with 1 μm diamond paste in a colloidal suspension. After being polished to a mirror finish, the metallographic specimens were viewed in the un-etched state via an optical microscope. After being metallographically characterized in the un-etched state, the metallographic specimens were immersed for thirty seconds for optical microscopy (OM) and sixty seconds for scanning electron microscopy (SEM) in an etchant with the following composition: 92 mL HCl, 5 mL H₂SO₄, 3 mL HNO₃; the etchant emanated from the only literature source that was found to contain metallographic data on the S-816 alloy: Atlas of Microstructures etc. After being etched, the metallographic specimens were viewed in the etched state via optical and scanning electron microscopic methods. The equipment used for OM of the metallographic specimens was a Leitz MM 6 largefield metallographic microscope. The equipment used for SEM of the metallographic specimens was an FEI™ Quanta 600i environmental scanning electron microscope with a tungsten cathode and a PGT energy dispersive spectrometer.

2.7 Energy Dispersive X-ray Spectroscopy

The elemental composition of four morphologically different phases, and microstructural matrix, observed in the metallographic specimens produced from the seven creep-rupture specimens was determined via energy dispersive X-ray spectroscopy (EDS). The operational parameters of the SEM/EDS equipment, at the time that the analyses were conducted, were as follows: variable working distances in between 10-15 mm (due to differences in the size of the

metallographic specimen mounts), high vacuum, and an accelerating voltage of 20.0 kV. The equipment used for EDS microanalysis of the metallographic specimens was an FEI™ Quanta 600i environmental scanning electron microscope with a tungsten cathode and a PGT energy dispersive spectrometer.

2.8 Microhardness Testing

After characterization of the metallographic specimens via optical and scanning electron microscopic methods, and EDS, Vickers microhardness testing was conducted on these specimens. Fifteen randomly chosen hardness tests were conducted on each specimens' matrix; care was taken during the microhardness testing in order to avoid testing any *visibly large* microconstituents and boundary/interfacial regions in the specimens' microstructures, such as dendrite boundaries or microconstituent-matrix boundaries.

2.9 Fractographic Analysis

The halves of the ruptured specimens that were selected for fractographic analysis were transversely sectioned at approximately 0.25 inches from their fracture surfaces with a continuously-cooled abrasive saw. The resulting sections were then cleaned in an ultrasonic bath, within a 2% solution of Alconox® surfactant and de-ionized water, for differing lengths of time (one to three hours), as the degree of oxidation on the fracture surfaces varied; these variations were attributed to the differing test temperatures that the specimens were exposed to after rupturing—hence, specimens that had been tested at relatively higher temperatures developed a greater amount of oxidation on their fracture surfaces and had to be cleaned for longer lengths of time.

After being cleaned, the fracture surface sections of the ruptured specimens were viewed and documented via scanning electron microscopy. The equipment used for SEM fractographic analysis of the different fracture surfaces of the seven creep-rupture specimens was an FEI™ Quanta 600i environmental scanning electron microscope with a tungsten cathode and a PGT energy dispersive spectrometer.

Chapter 3: Results

3.1 Post-Rupture Specimen Characterization

Figures 22-49 are macro-photographic images of the seven creep-rupture specimens in the post-ruptured state. Figures 22-25 correspond to specimen S1, figures 26-29 correspond to specimen S2, figures 30-33 correspond to specimen S4, figures 34-37 correspond to specimen S5 (set 128), figures 38-41 correspond to specimen S5 (set 821), figures 42-45 correspond to specimen S7, and figures 46-49 correspond to specimen S9.



Figure 22. Photographic image of the entirety of specimen S1 in the post-ruptured state.

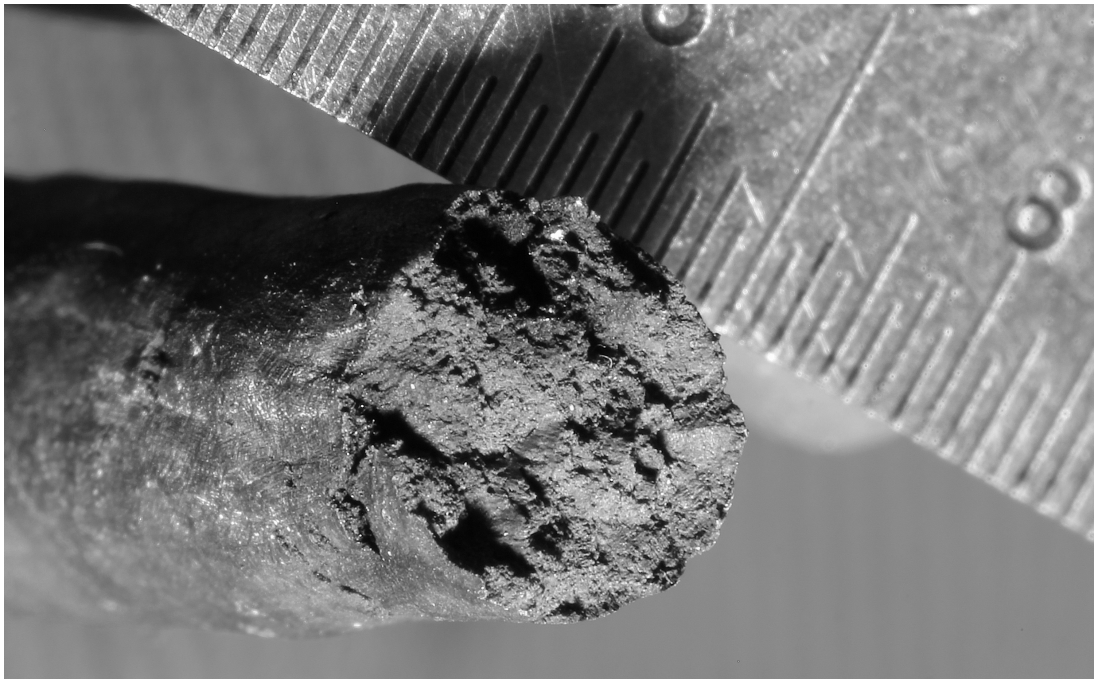


Figure 23. Macro-photographic image of the fracture surface of the specimen S1 halve demonstrated on the left-hand side in figure 22.



Figure 24. Macro-photographic image of the fracture surface of the specimen S1 halve demonstrated on the left-hand side in figure 22.

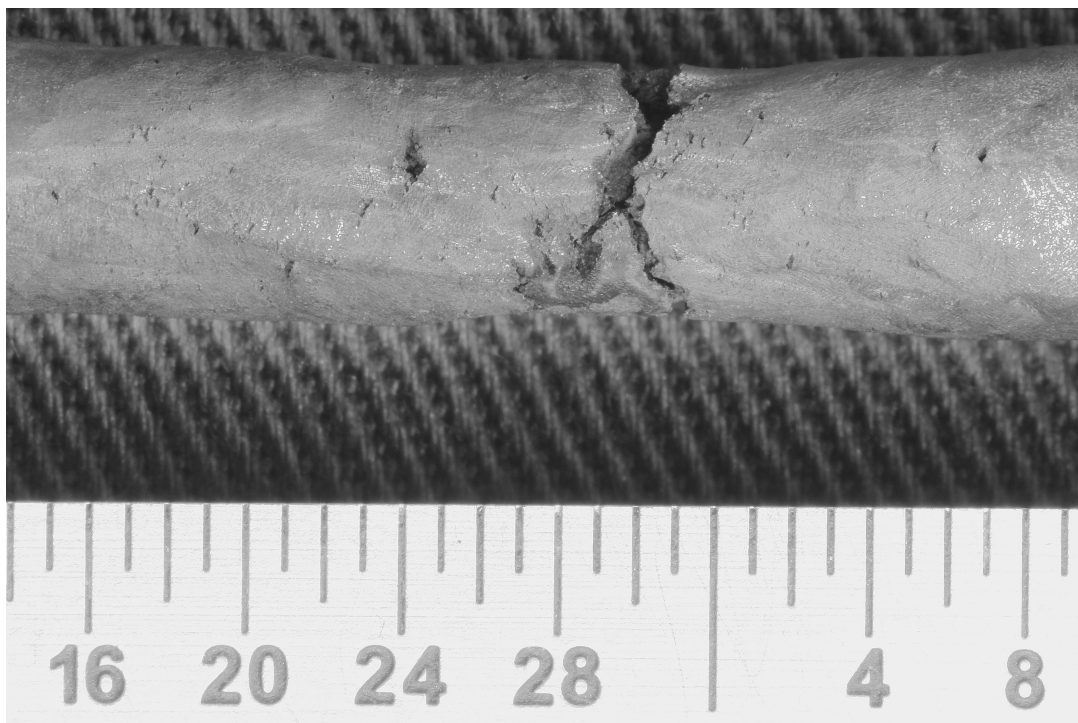


Figure 25. Macro-photographic image of the region where rupture occurred in specimen S1.

Figures 22 and 25 demonstrate that the outer surface of the gauge length in specimen S1 exhibits features that are indicative of plastic deformation that occurred during creep-rupture testing; these features consist of a textured elongation of the specimen's body and exposed ruptures or bursts along the specimen's body. Figures 23 and 24 demonstrate that the fracture surface of specimen S1 exhibits large cratering and appears topographically irregular; these large macroscopic features are consistently seen throughout the entirety of the surface.



Figure 26. Photographic image of the entirety of specimen S2 in the post-ruptured state.

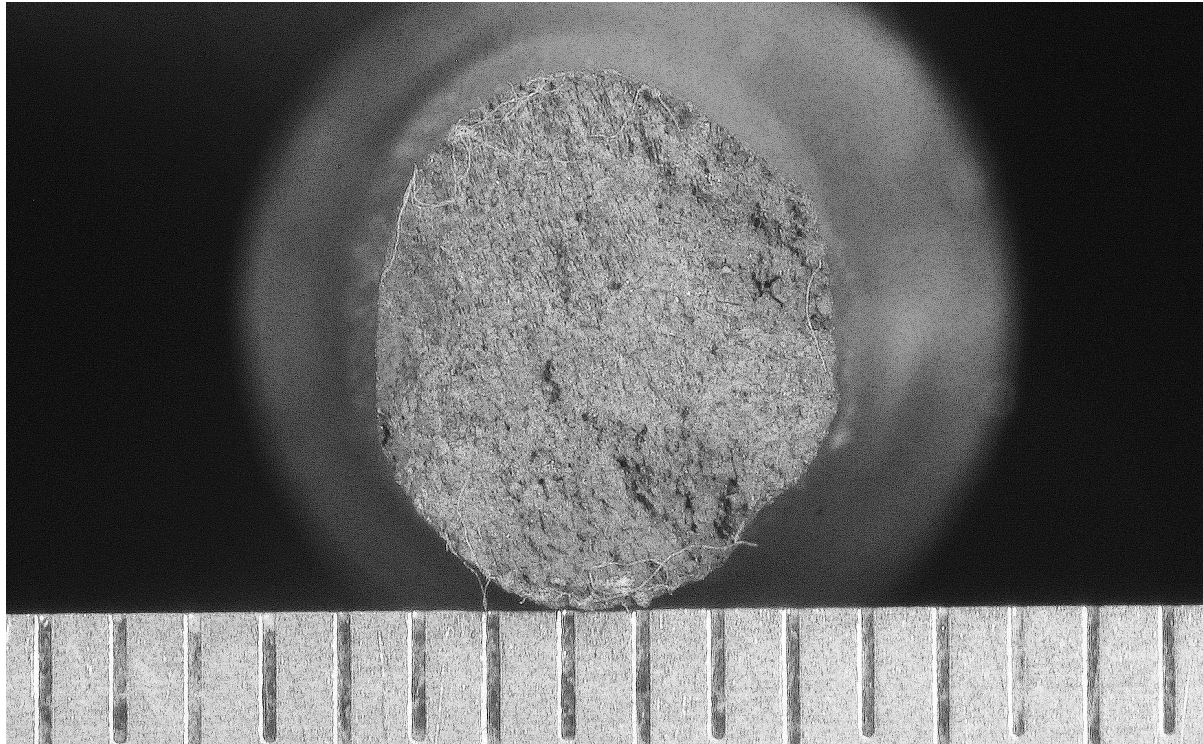


Figure 27. Macro-photographic image of the fracture surface of the specimen S2 halve demonstrated on the left-hand side in figure 26.



Figure 28. Macro-photographic image of the fracture surface of the specimen S2 halve demonstrated on the right-hand side in figure 26.

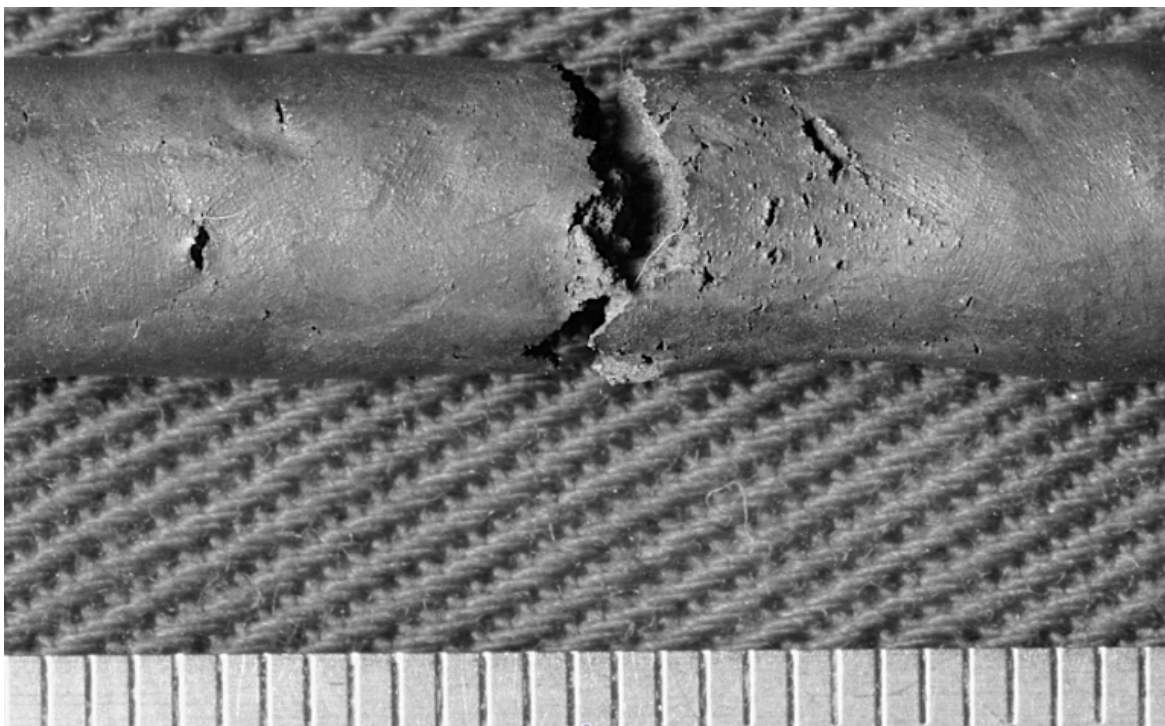


Figure 29. Macro-photographic image of the region where rupture occurred in specimen S2.

Figures 26 and 29 demonstrate that the outer surface of the gauge length in specimen S2 exhibits features that are indicative of plastic deformation that occurred during creep-rupture testing; these features consist of a textured elongation of the specimen's body and exposed ruptures or bursts along the specimen's body. The degree of textured elongation is *less* than that exhibited by specimen S1; the presence and size of exposed ruptures or bursts along the specimen's body is observed to be *more or less equal* to that exhibited by specimen S1. Figures 27 and 28 demonstrate that the fracture surfaces of specimen S2 appear granular and are less topographically diverse than the fracture surface of specimen S1; these macroscopic features are consistently seen throughout the entirety of both surfaces.



Figure 30. Photographic image of the entirety of specimen S4 in the post-ruptured state.



Figure 31. Macro-photographic image of the fracture surface of the specimen S4 halve demonstrated on the left-hand side in figure 30.

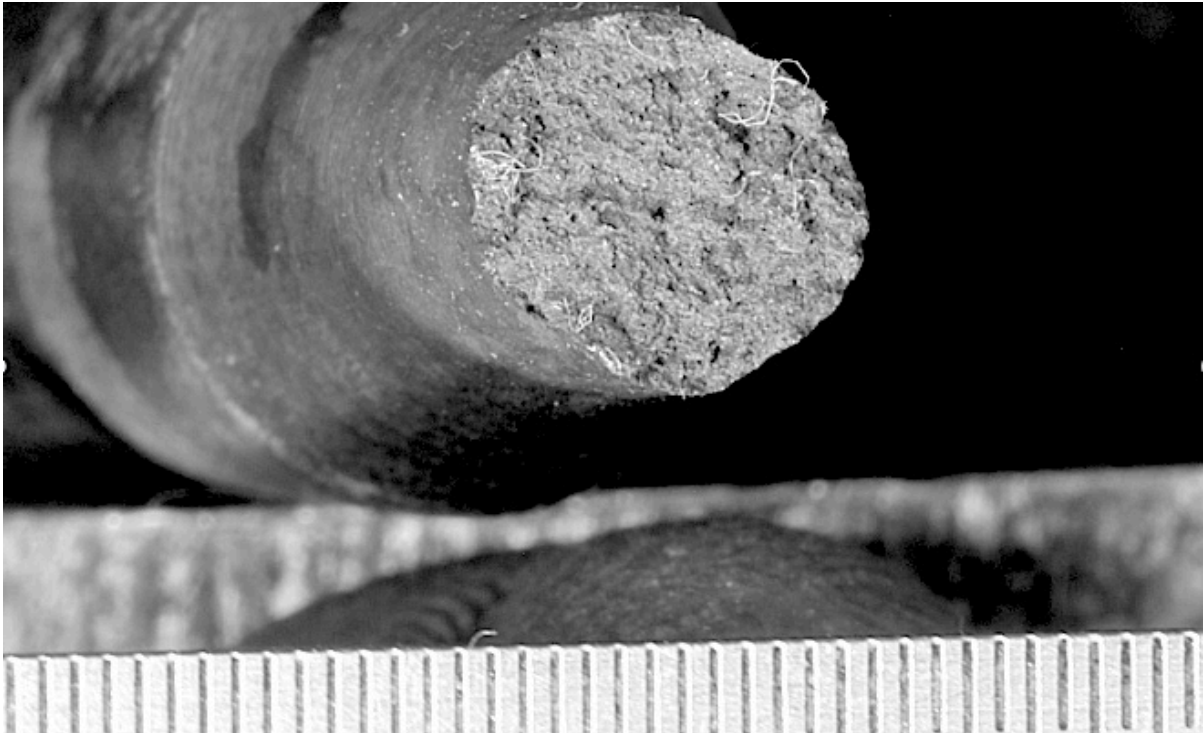


Figure 32. Macro-photographic image of the fracture surface of the specimen S4 halve demonstrated on the left-hand side in figure 30.

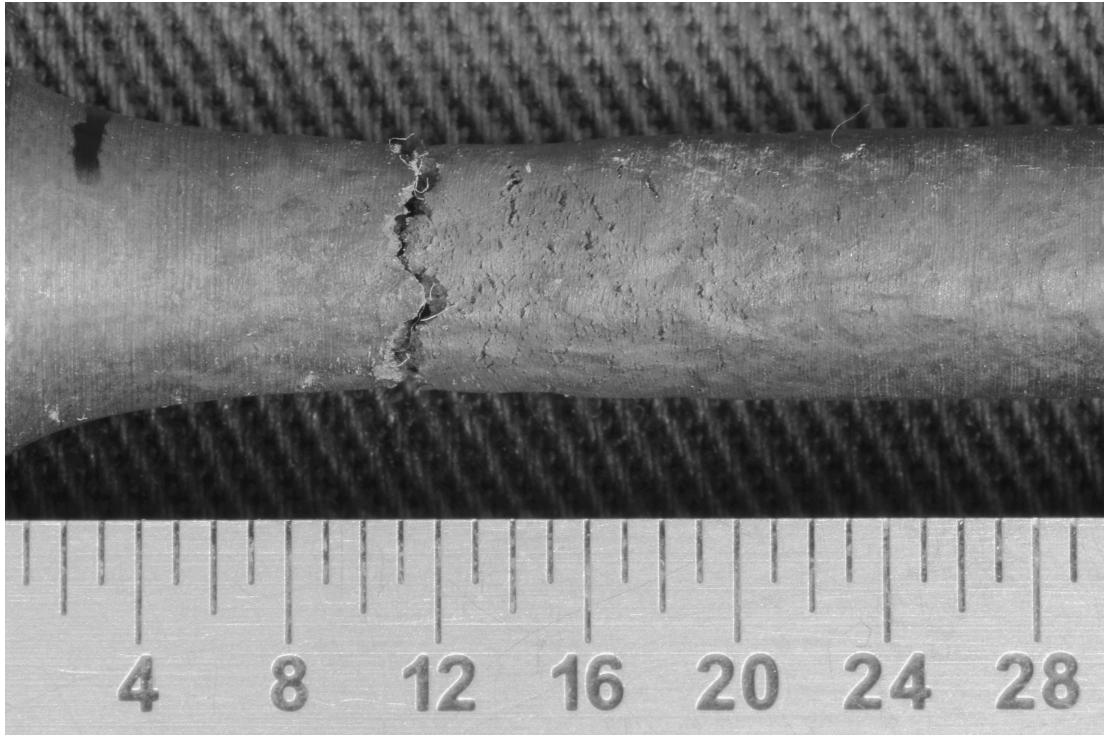


Figure 33. Macro-photographic image of the region where rupture occurred in specimen S4.

Figures 30 and 33 demonstrate that the outer surface of the gauge length in specimen S4 exhibits features that are indicative of plastic deformation that occurred during creep-rupture testing; these features consist of a textured elongation of the specimen's body and exposed ruptures or bursts along the specimen's body. The degree of textured elongation is comparable to that exhibited by specimen S1; the presence of exposed ruptures or bursts along the specimen's body is observed to be *greater* than that exhibited by specimens S1 and S2, while the size of these features is *smaller* than those exhibited by specimens S1 and S2. Figures 31 and 32 demonstrate that the fracture surface of specimen S4 exhibits large cratering and appears topographically irregular, in a manner similar to the fracture surface of specimen S1; these macroscopic features are consistently seen throughout the entirety of the surface.

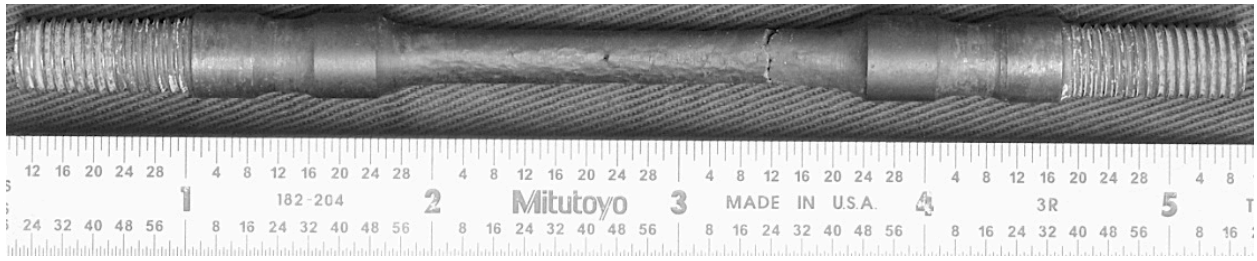


Figure 34. Photographic image of the entirety of specimen S5 (set 128) in the post-ruptured state.

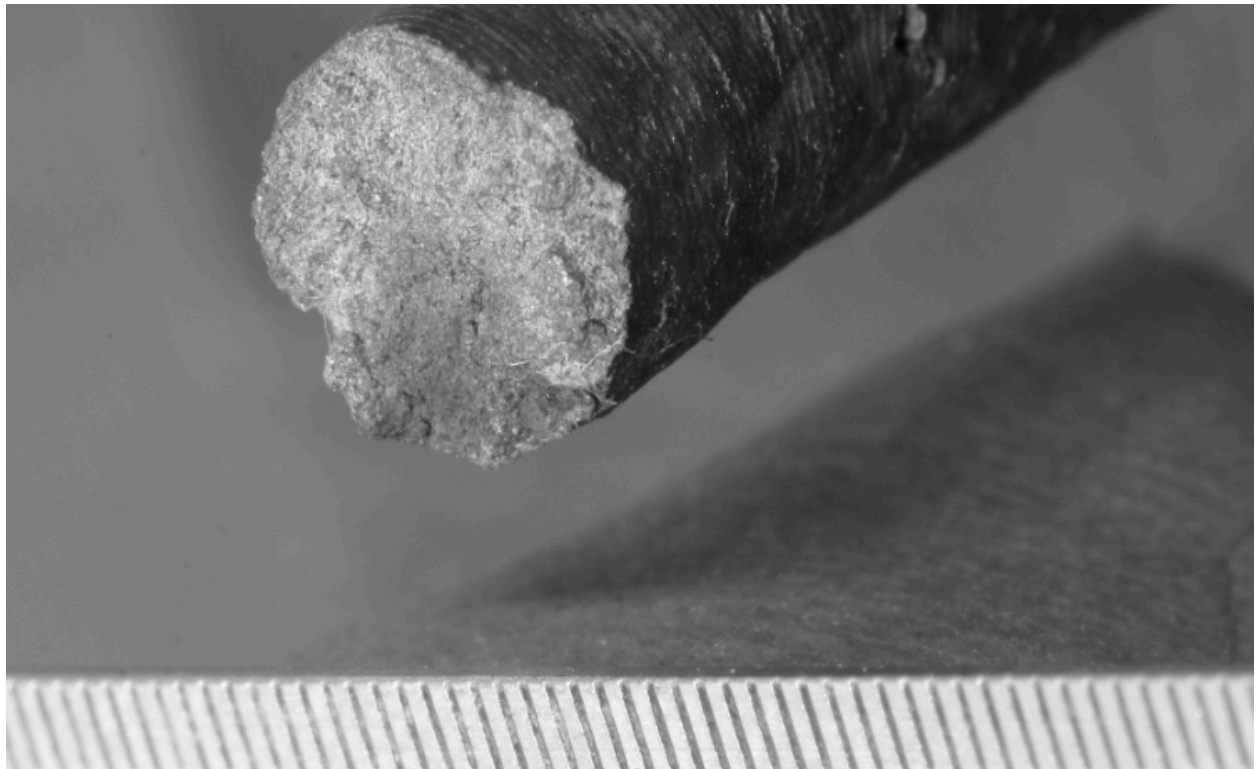


Figure 35. Macro-photographic image of the fracture surface of the specimen S5 (set 128) halve demonstrated on the left-hand side in figure 34.

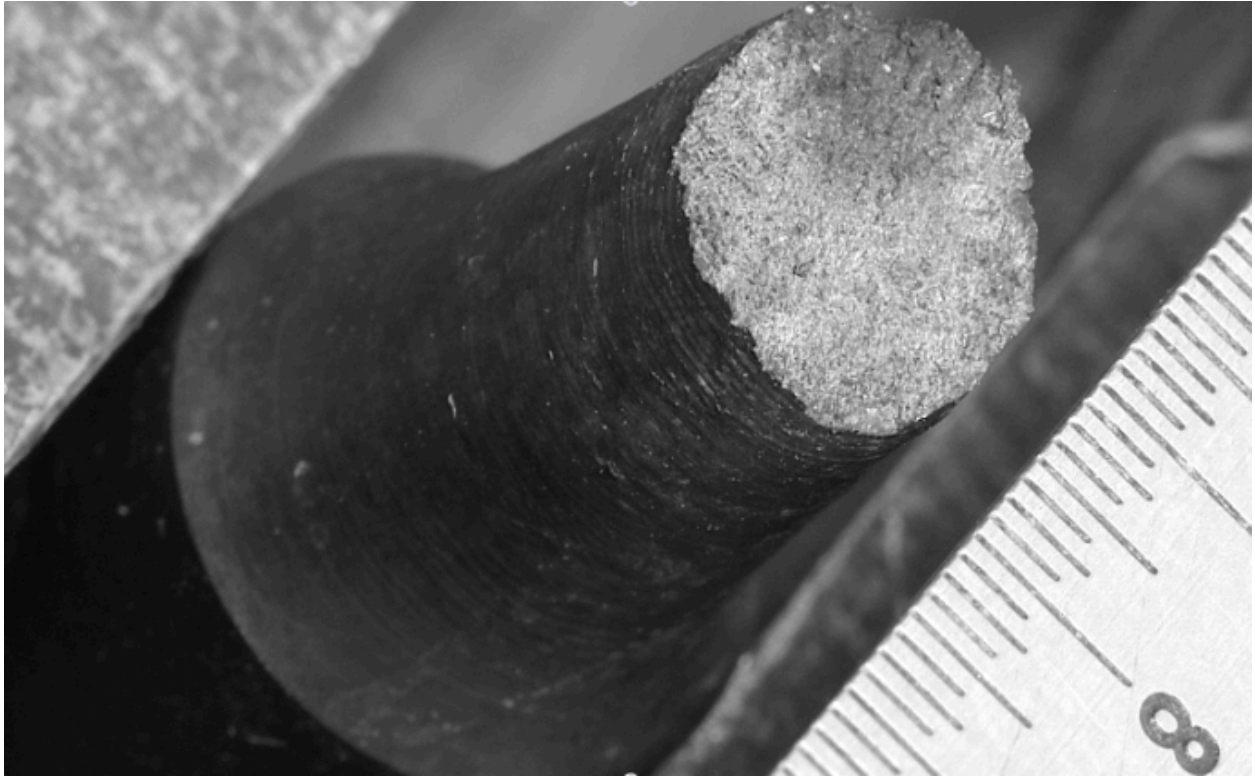


Figure 36. Macro-photographic image of the fracture surface of the specimen S5 (set 128) halve demonstrated on the right-hand side in figure 34.

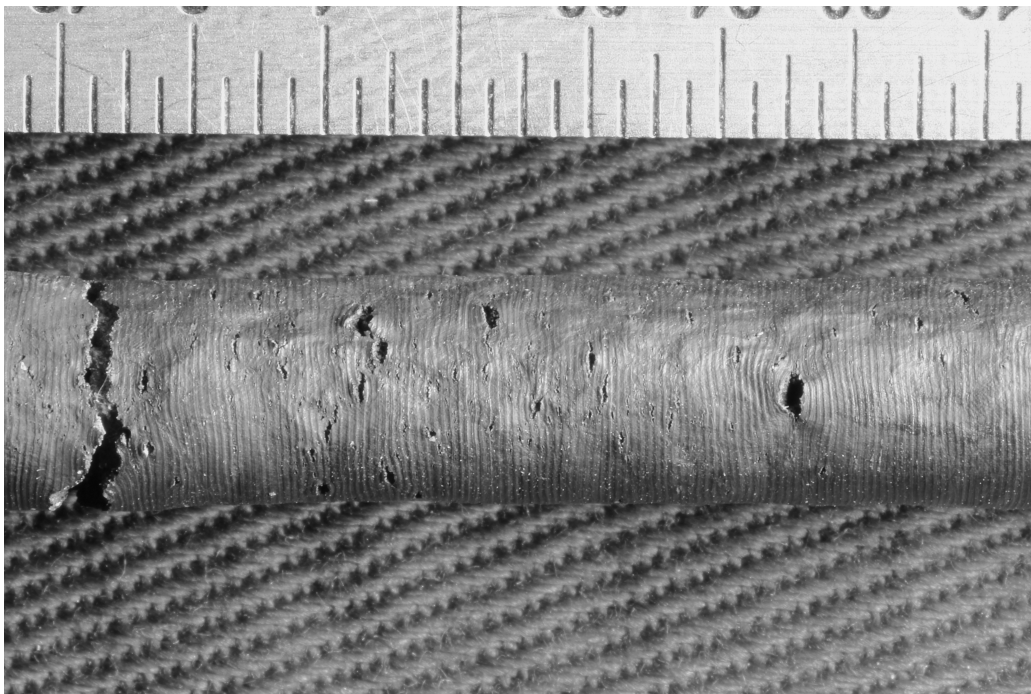


Figure 37. Macro-photographic image of the region where rupture occurred in specimen S5 (set 128).

Figures 34 and 37 demonstrate that the outer surface of the gauge length in specimen S5 (set 128) exhibits features that are indicative of plastic deformation that occurred during creep-rupture testing; these features consist of a textured elongation of the specimen's body and exposed ruptures or bursts along the specimen's body. The degree of textured elongation is comparable to that exhibited by specimens S1 and S4; the presence and size of exposed ruptures or bursts along the specimen's body is observed to be *more or less equal* to that exhibited by specimens S1 and S2. Figures 35 and 36 demonstrate that the fracture surfaces of specimen S5 (set 128) appear granular and are less topographically diverse than the fracture surfaces of specimens S1 and S4, but comparable to the fracture surfaces of specimen S2; these macroscopic features are consistently seen throughout the entirety of both surfaces.

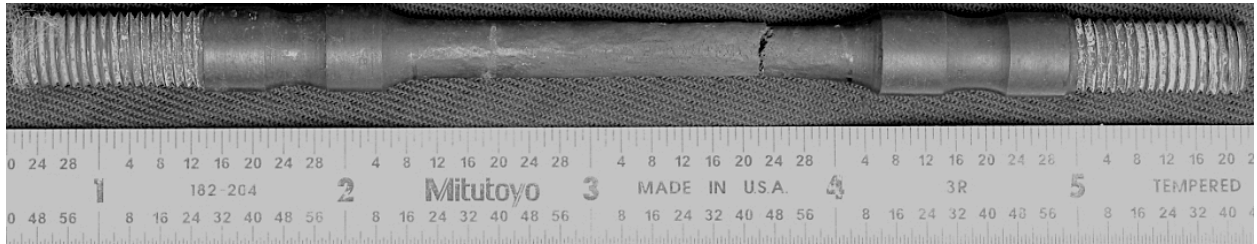


Figure 38. Photographic image of the entirety of specimen S5 (set 821) in the post-ruptured state.

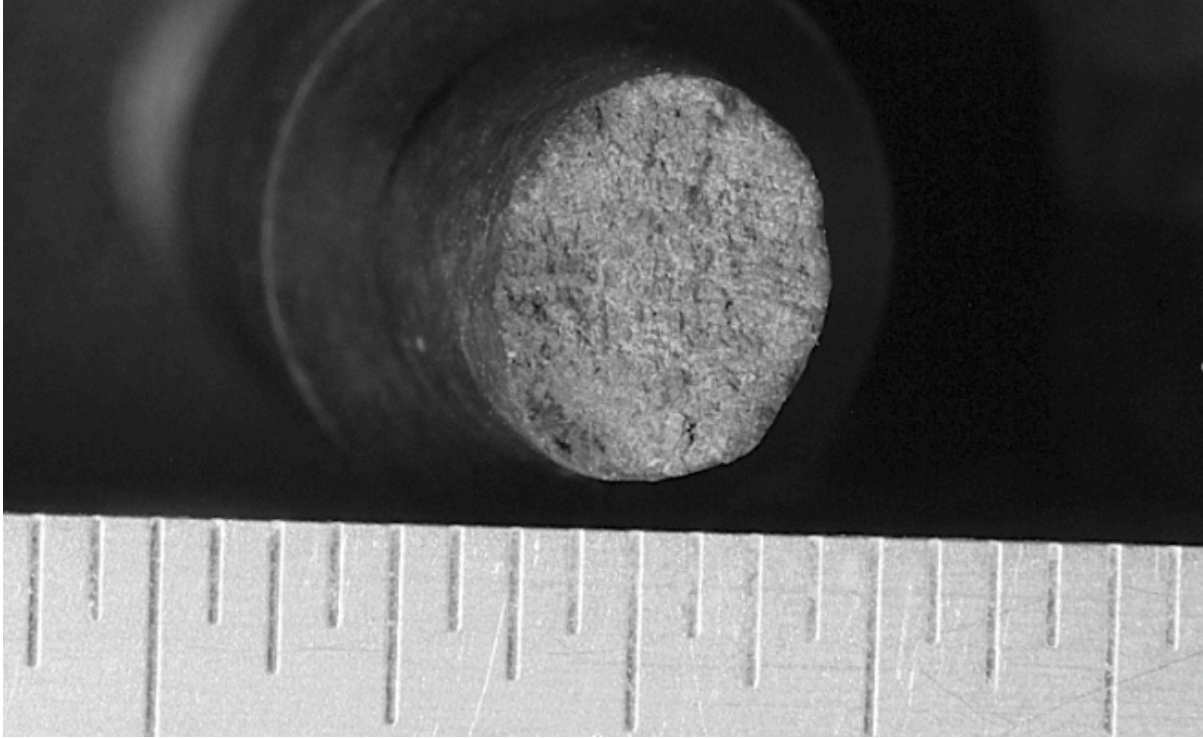


Figure 39. Macro-photographic image of the fracture surface of the specimen S5 (set 821) halve demonstrated on the right-hand side in figure 38.



Figure 40. Macro-photographic image of the fracture surface of the specimen S5 (set 821) halve demonstrated on the right-hand side in figure 38.

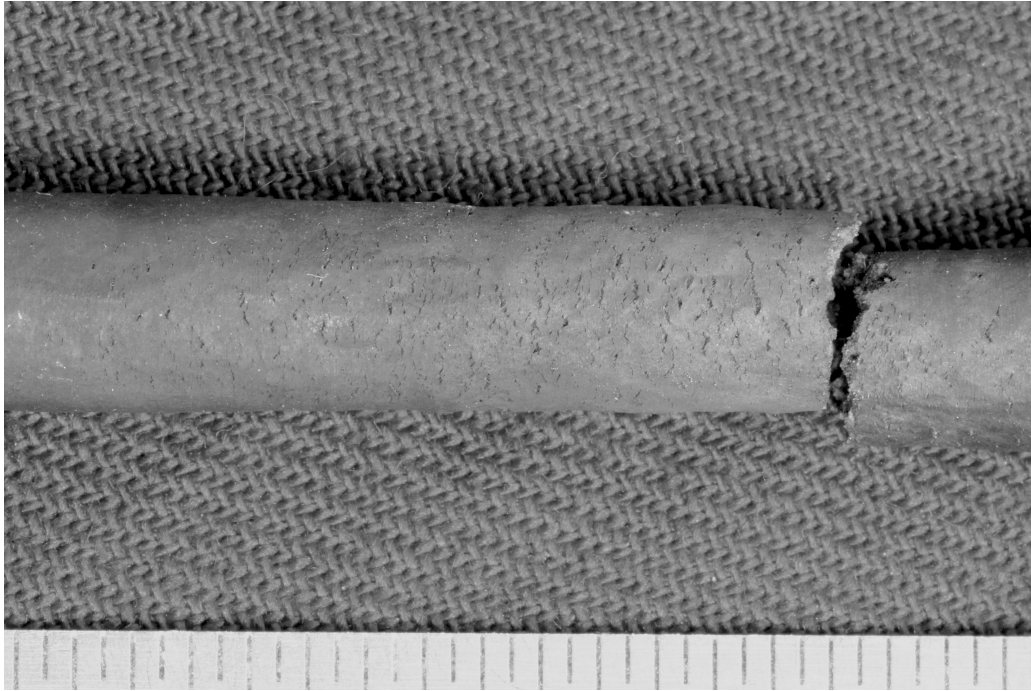


Figure 41. Macro-photographic image of the region where rupture occurred in specimen S5 (set 821).

Figures 38 and 41 demonstrate that the outer surface of the gauge length in specimen S5 (set 821) exhibits features that are indicative of plastic deformation that occurred during creep-rupture testing; these features consist of a textured elongation of the specimen's body and exposed ruptures or bursts along the specimen's body. The degree of textured elongation is comparable to that exhibited by specimens S, S4, and S5 (set 128); the presence and size of exposed ruptures or bursts along the specimen's body is observed to be *more or less equal* to that exhibited by specimen S4. Figures 39 and 40 demonstrate that the fracture surfaces of specimen S5 (set 821) appear granular and are less topographically diverse than the fracture surfaces of specimens S1 and S4, but comparable to the fracture surfaces of specimens S2 and S5 (set 128); these macroscopic features are consistently seen throughout the entirety of the surface.

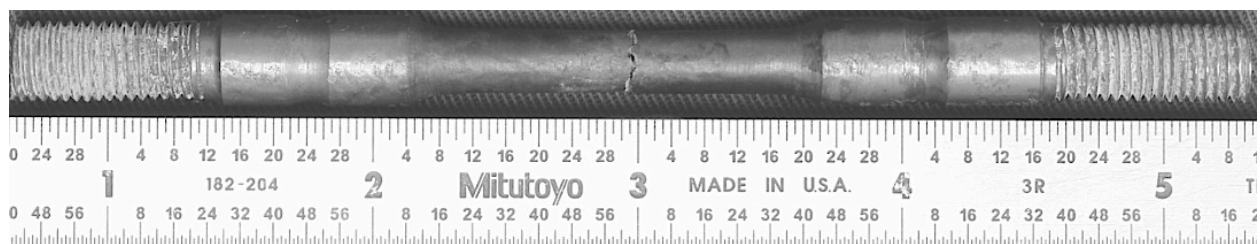


Figure 42. Photographic image of the entirety of specimen S7 in the post-ruptured state.

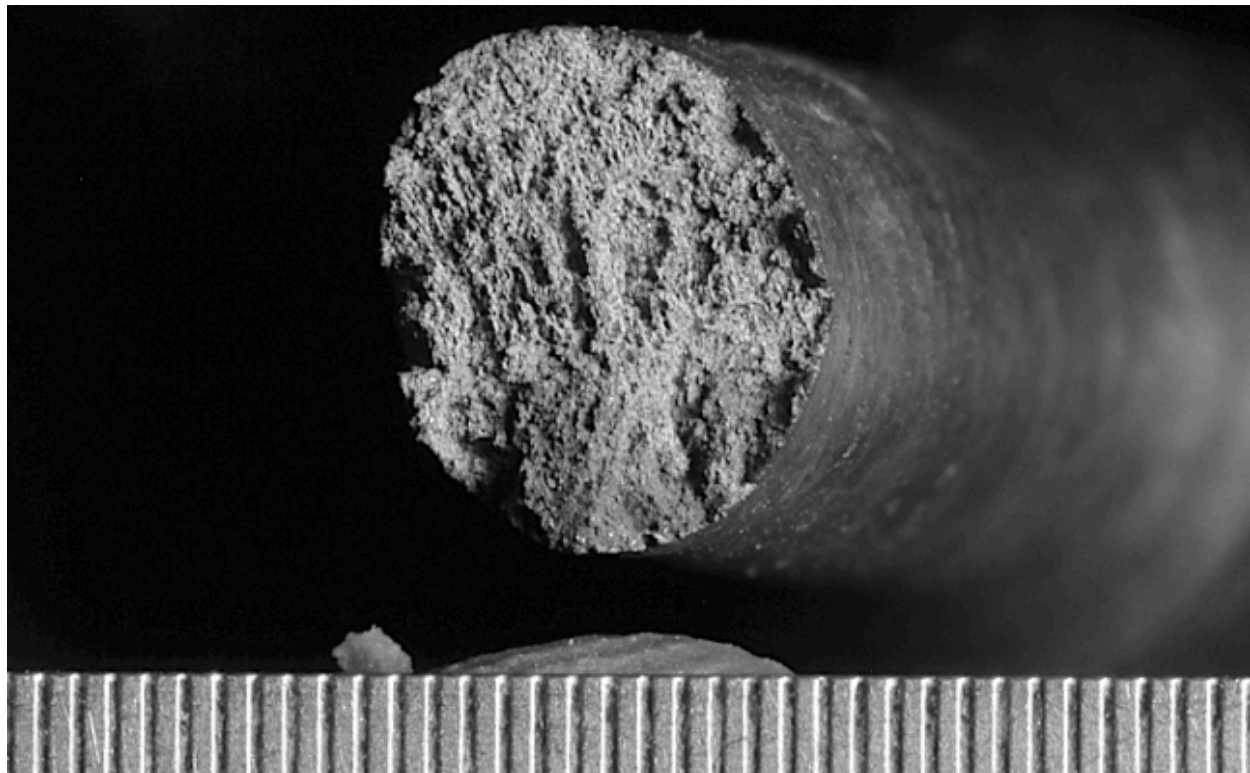


Figure 43. Macro-photographic image of the fracture surface of the specimen S7 halve demonstrated on the right-hand side in figure 42.

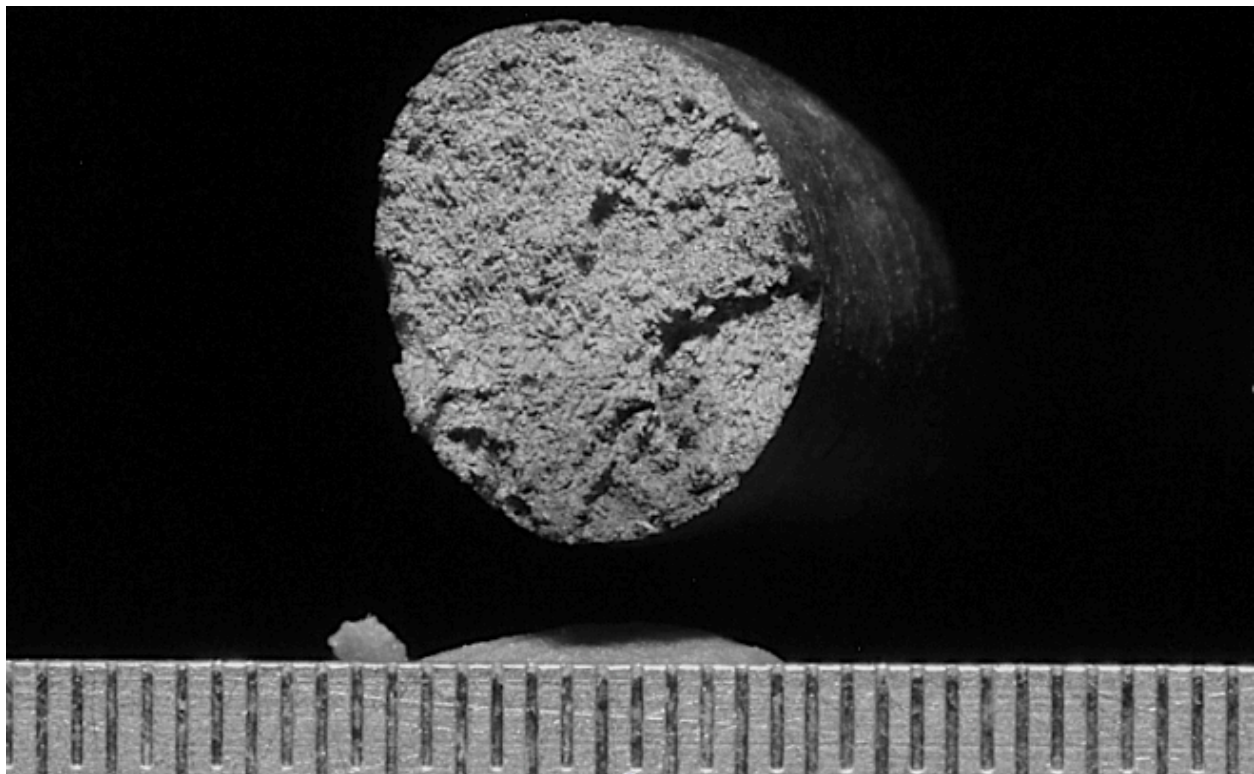


Figure 44. Macro-photographic image of the fracture surface of the specimen S7 halve demonstrated on the right-hand side in figure 42.

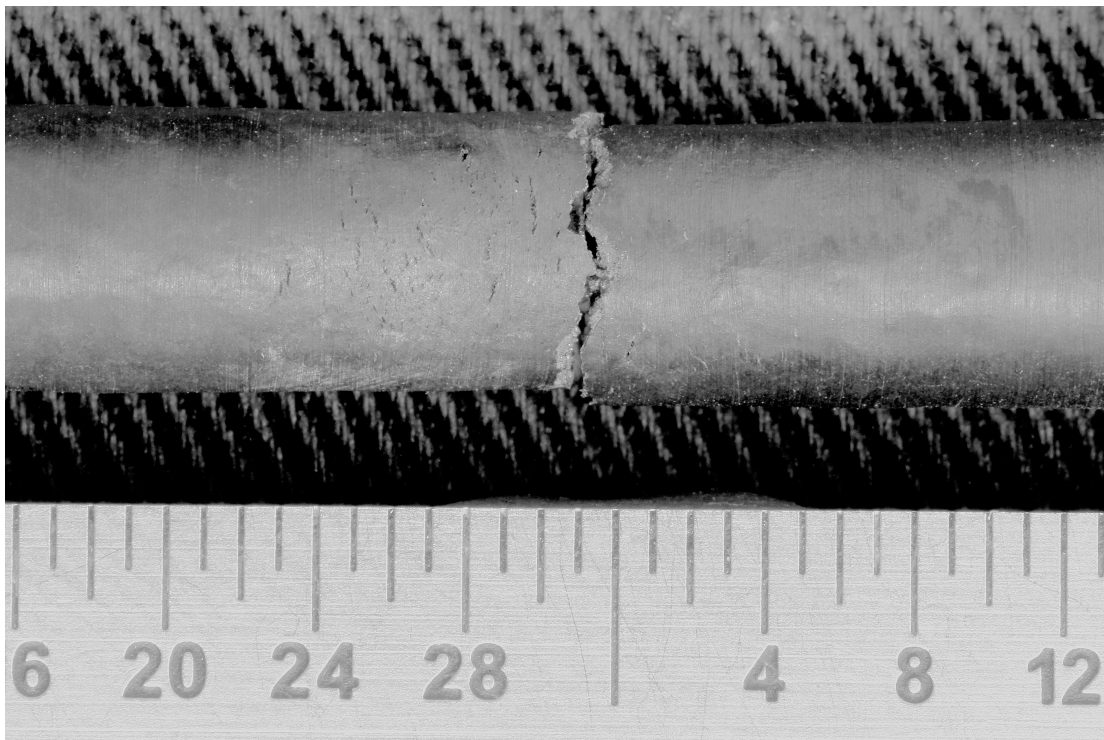


Figure 45. Macro-photographic image of the region where rupture occurred in specimen S7.

Figures 42 and 45 demonstrate that the outer surface of the gauge length in specimen S7 exhibits features that are indicative of abrupt rupture and *diminished* plastic deformation that occurred during creep-rupture testing; these features consist of subtle textured elongation of the specimen's body and fine exposed ruptures or bursts along the specimen's body—the presence of these features is considered relatively diminished when compared to that exhibited by specimens S1, S2, S4, S5 (set 128), and S5 (set 821). Figures 43 and 44 demonstrate that the fracture surface of specimen S7 appears granular and is less topographically diverse than the fracture surfaces of specimens S1 and S4, but more textured than the fracture surfaces of specimens S2 and S5 (set 128), and the fracture surface of specimen S5 (set 821); these macroscopic features are consistently seen throughout the entirety of the surface.

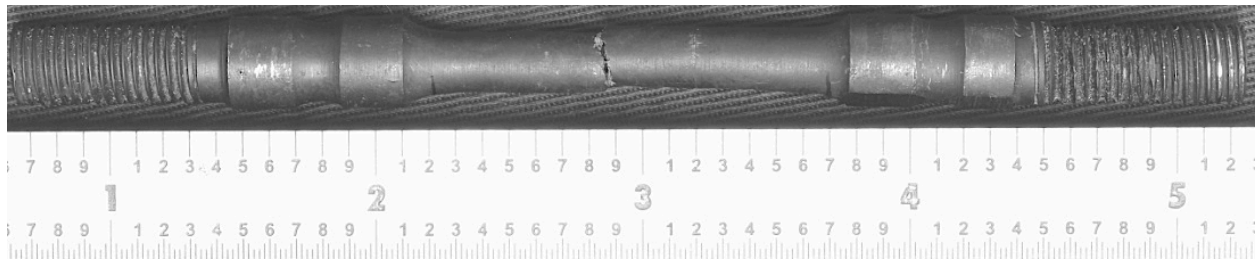


Figure 46. Photographic image of the entirety of specimen S9 in the post-ruptured state.

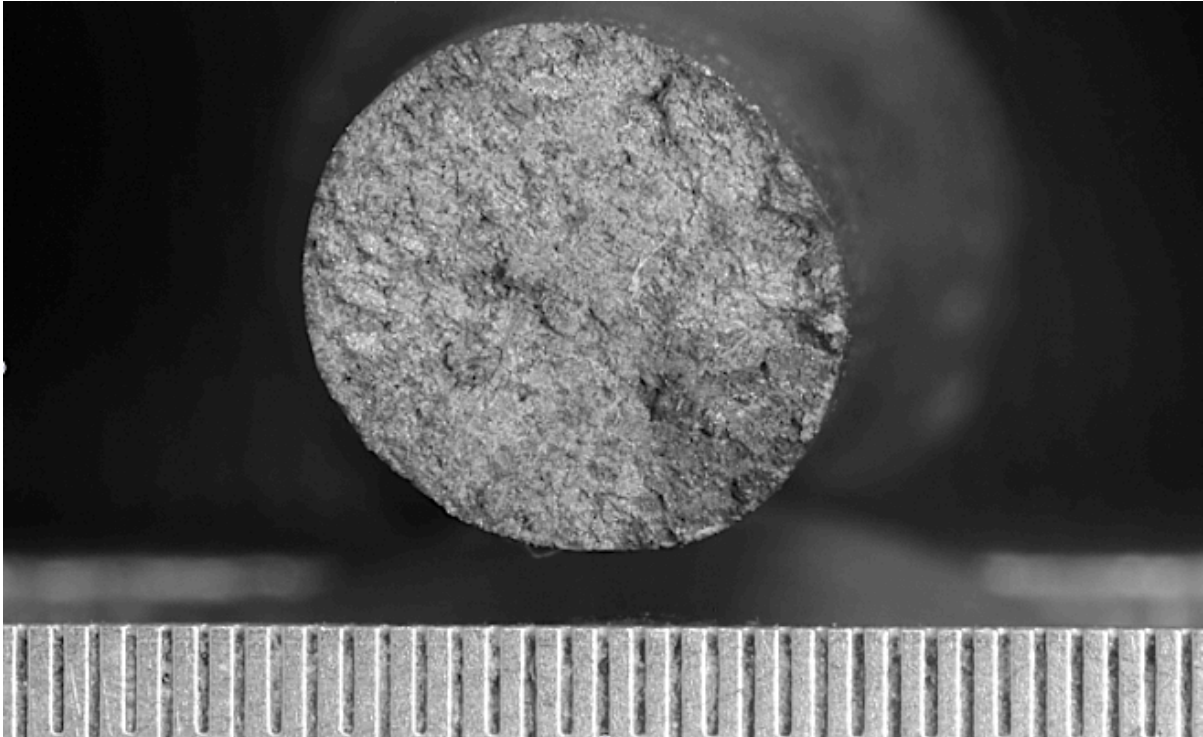


Figure 47. Macro-photographic image of the fracture surface of the specimen S9 halve demonstrated on the right-hand side in figure 46.



Figure 48. Macro-photographic image of the fracture surface of the specimen S9 halve demonstrated on the right-hand side in figure 46.

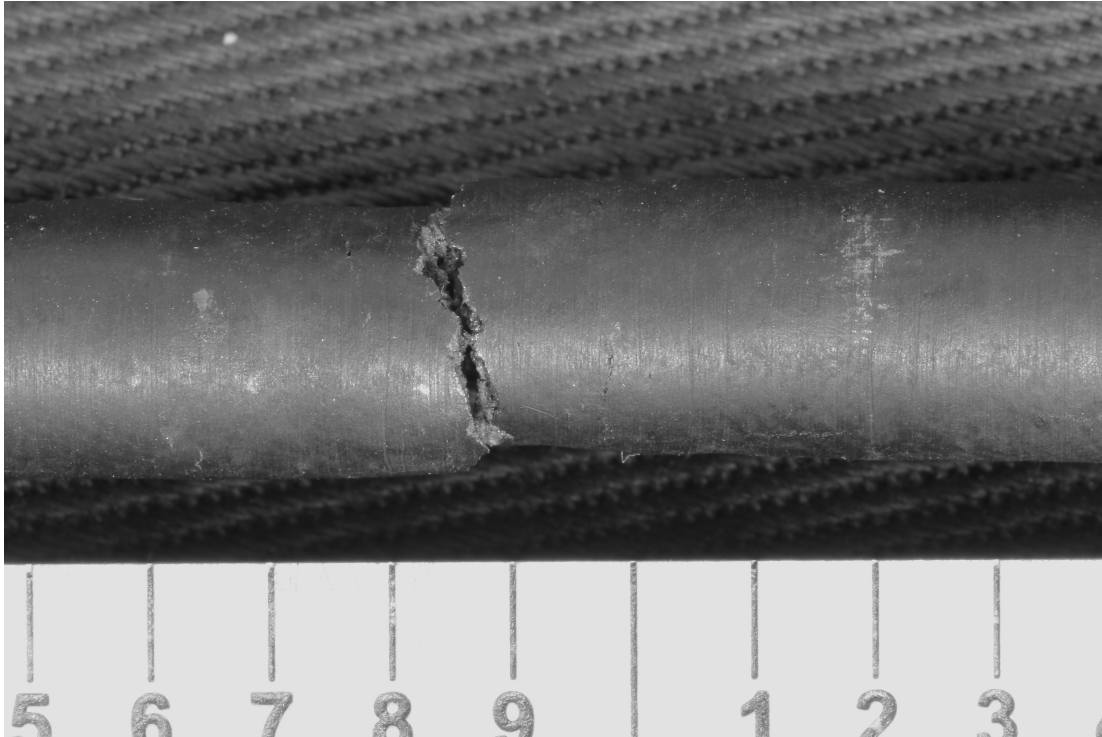


Figure 49. Macro-photographic image of the region where rupture occurred in specimen S9.

Figures 46 and 49 demonstrate that the outer surface of the gauge length in specimen S9 exhibits features that are indicative of abrupt rupture and *diminished* plastic deformation that occurred during creep-rupture testing; these features consist of subtle textured elongation (barely discernible) of the specimen's body and fine exposed ruptures or bursts (barely present or discernible) along the specimen's body—the presence of these features is considered relatively diminished when compared to that exhibited by specimens S1, S2, S4, S5 (set 128), and S5 (set 821). Figures 47 and 48 demonstrate that the fracture surface of specimen S9 appears granular and is less topographically diverse than the fracture surfaces of specimens S1 and S4, but comparable to the fracture surface of specimen S7; these macroscopic features are consistently seen throughout the entirety of the surface.

3.2 Creep-Rupture Data Analysis

Specimen elongation percentages, which were determined from both the extensometer data stream that was collected during the different tests and the specimens' dimensions that were measured at the conclusion of said tests, are demonstrated in table 4; the different lengths of time that it took for each of the different specimens to rupture (once their respective test temperatures had been reached) are also demonstrated in table 4.

Table 4. Time to rupture and elongation percentage data gathered from creep-rupture testing of seven creep-rupture specimens; test parameters and specimen designations also exhibited.

Specimen	Temperature (°F)	Stress (ksi)	Time to Rupture (hrs.)	Elongation % (extensometer)	Elongation % (measured)
S1 (set 128)	1500 °F	24	149.6	25.2	29.0
S2 (set 128)	1500 °F	36	5.4	24.4	30.0
S4 (set 821)	1650 °F	36	0.083	22.6	17.4
S5 (set 128)	1350 °F	36	187.1	3.0	55.0
S5 (set 821)	1350 °F	40	61.3	24.8	53.6
S7 (set 128)	1200 °F	56	259.0	8.6	7.6
S9 (set 128)	1200 °F	64	240.5	22.4	7.5

As demonstrated in table 4, the correlation in between the measured and extensometer elongation percentages of the different specimens is varied; it is suspected that these discrepancies are related to the final moments of specimen rupture, as abrupt movement of the creep bracket may have led to erroneous data output by the LVDT. The specimen elongation percentages that will be referenced in this manuscript are those derived from post-rupture measurements of the specimens.

Figure 50 demonstrates a comparative plot between the creep-rupture data gathered in this research investigation and historical reference data on the S-816 alloy. The blue curves correspond to the 1200 °F temperature regime, the green curves correspond to the 1350 °F temperature regime, and the red curves correspond to the 1500 °F temperature regime. The solid curves and black-colored data points correspond to historical reference data derived from wrought/sheet specimens, the white-colored data points correspond to historical reference derived from cast specimens, and the dashed curves and red-colored data points correspond to the creep-rupture data that was gathered in the course of this research investigation. The only literature source that was found to contain S-816 creep-rupture data (of wrought/sheet specimens) in the 1200, 1350, and 1500 °F temperature regimes was ASTM Special Technical Publication No. 160 [6]. The only source that allowed for an establishment of creep-rupture properties of cast S-816 specimens was personal communication from Sulzer Turbo Services (Sulzer Turbo Services, personal communication, October 2nd, 2012).

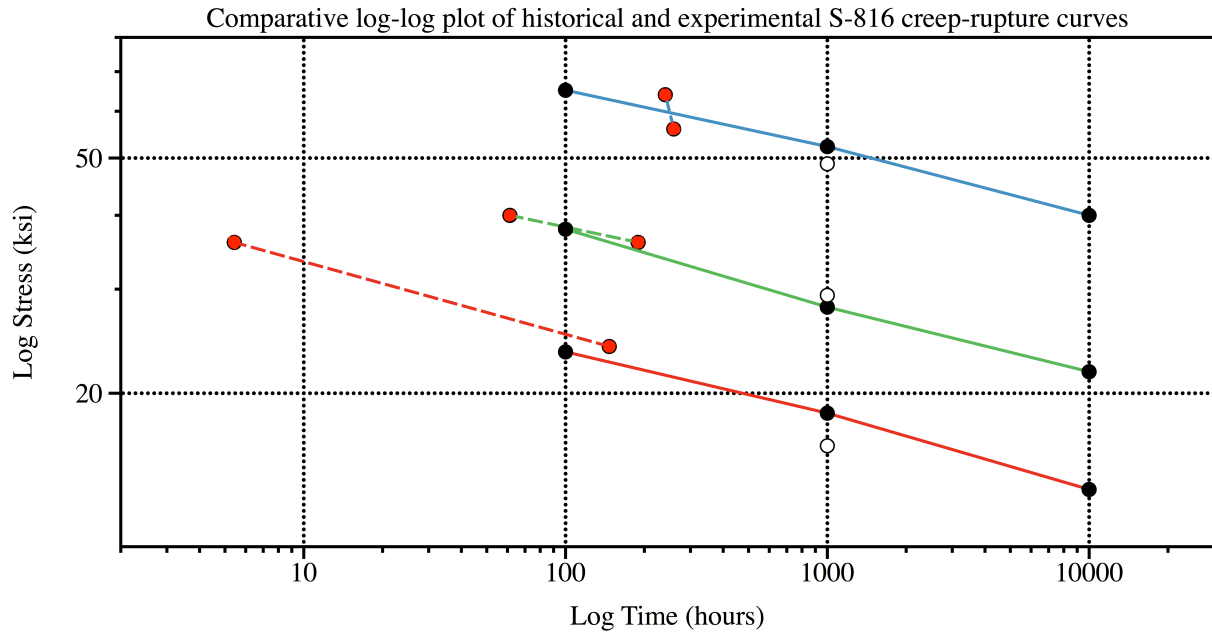


Figure 50. Comparison of creep-rupture data derived from wrought/sheet [6] and cast specimens (Sulzer Turbo Services, personal communication, October 2nd, 2012), and from creep-rupture specimens that were tested as part of research investigation.

Figures 51-58 demonstrate the seven specimens' deformation as a function of time to rupture.

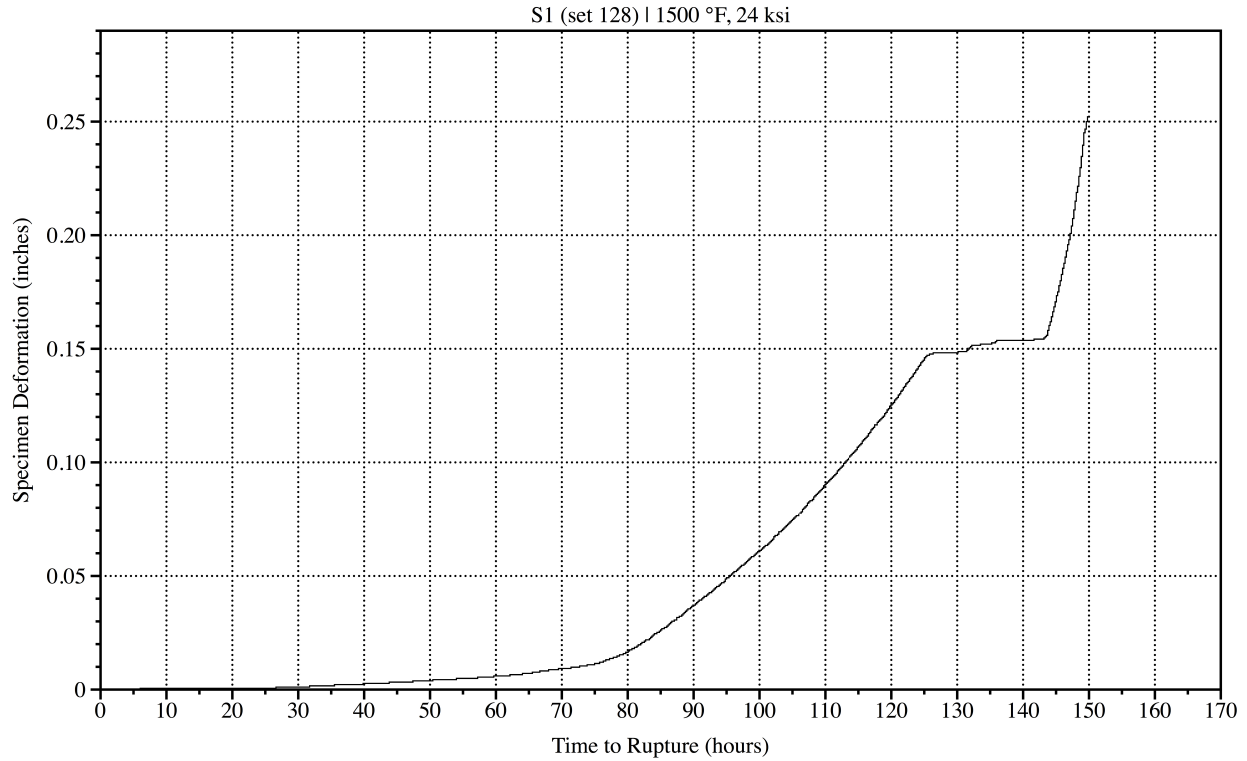


Figure 51. Plot of S1 deformation (inches) as a function of time to rupture (hours).

Figure 51 demonstrates that specimen S1 did not exhibit any primary creep behavior at the onset of the testing procedure; instead, it initially demonstrated secondary creep behavior and then transitioned into tertiary creep behavior after approximately 79.6 hours of testing. The specimen then transitioned from tertiary creep behavior back into secondary creep behavior after approximately 125 hours of testing; then, a second shift from secondary creep behavior back into tertiary creep behavior occurred after approximately 144 hours of testing. The specimen sustained this second phase of tertiary creep behavior for approximately 6 hours before finally rupturing after a total of 149.6 hours at 1500 °F and under a constant load of 24 ksi.

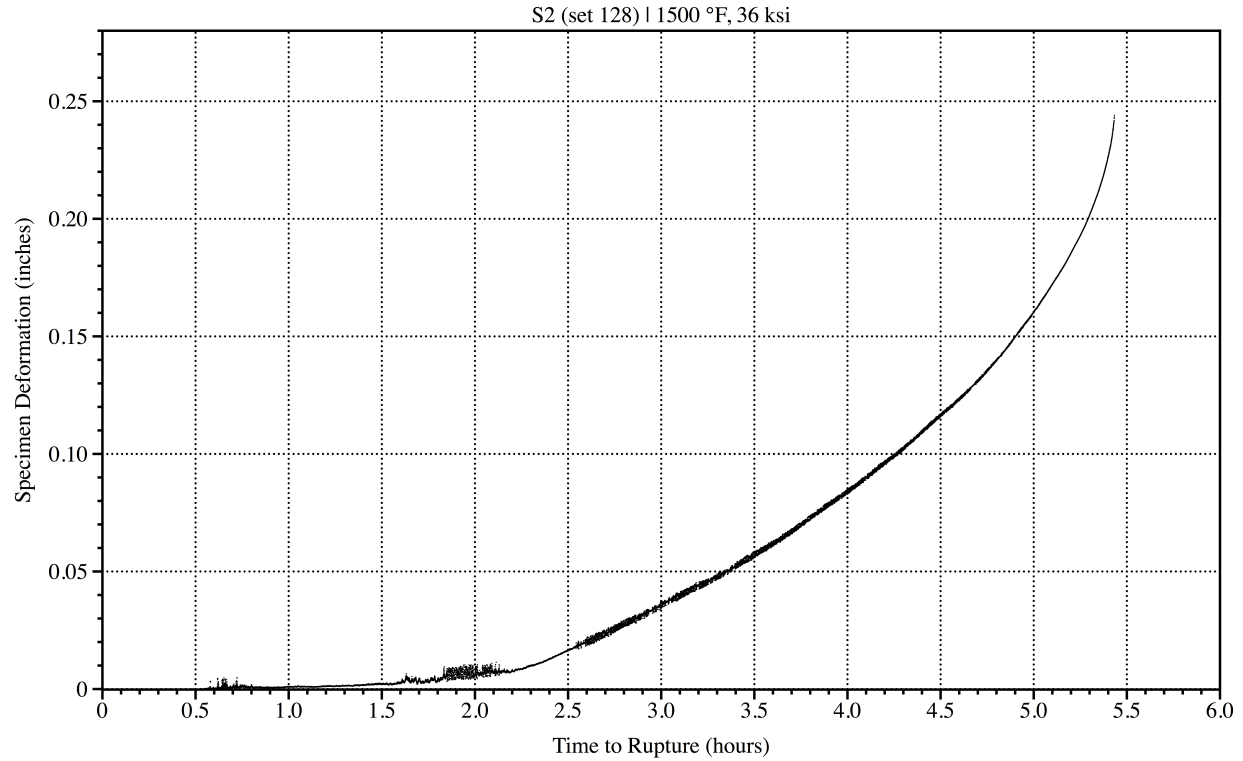


Figure 52. Plot of S2 deformation (inches) as a function of time to rupture (hours).

Figure 52 demonstrates that specimen S2 did not exhibit any primary creep behavior at the onset of the testing procedure; instead, it initially demonstrated secondary creep behavior and then transitioned into tertiary creep behavior after approximately 2.3 hours of testing. The specimen sustained tertiary creep behavior for approximately 3.1 hours before finally rupturing after a total of 5.4 hours at 1500 °F and under a constant load of 36 ksi.

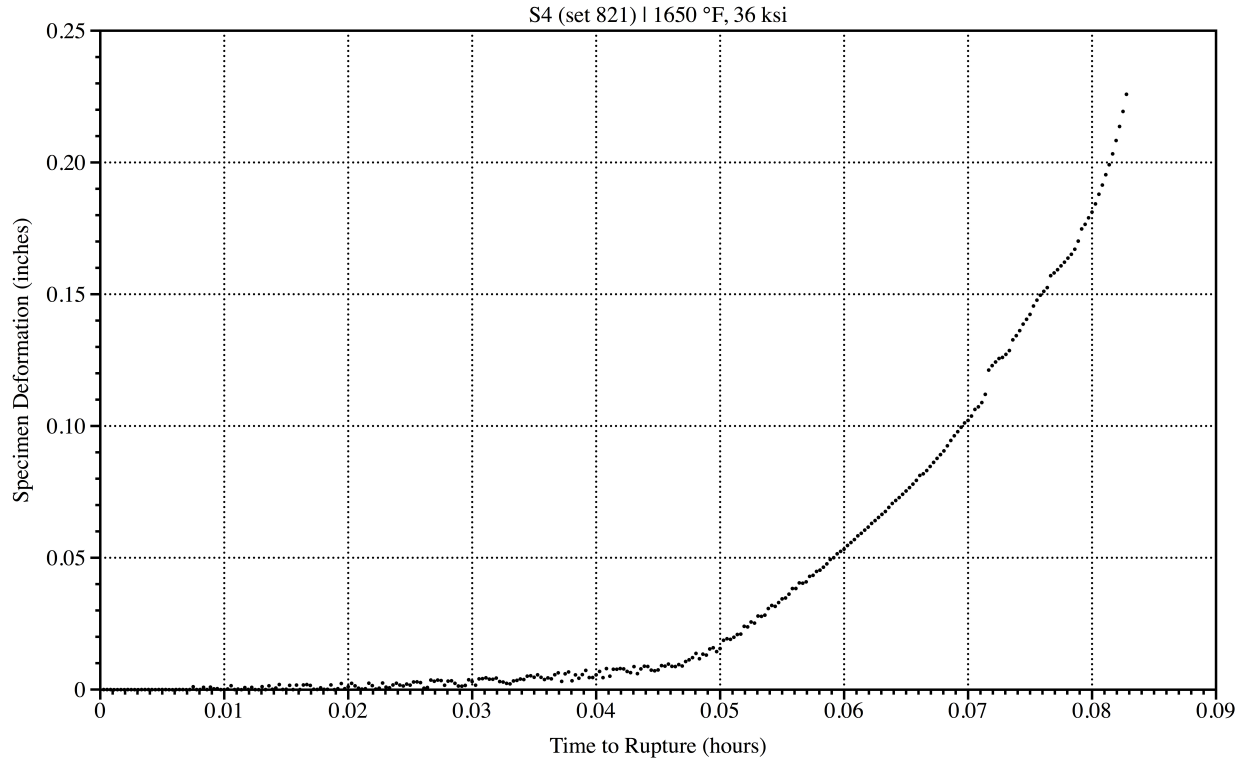


Figure 53. Plot of S4 deformation (inches) as a function of time to rupture (hours).

Figure 53 demonstrates that specimen S4 did not exhibit any primary creep behavior at the onset of the testing procedure; instead, it initially demonstrated secondary creep behavior and then transitioned into tertiary creep behavior after approximately 0.047 hours (169.2 seconds) of testing. The specimen sustained tertiary creep behavior for approximately 0.036 hours (129.6 seconds) before finally rupturing after a total of 0.083 hours (298.8 seconds) at 1650 °F and under a constant load of 36 ksi.

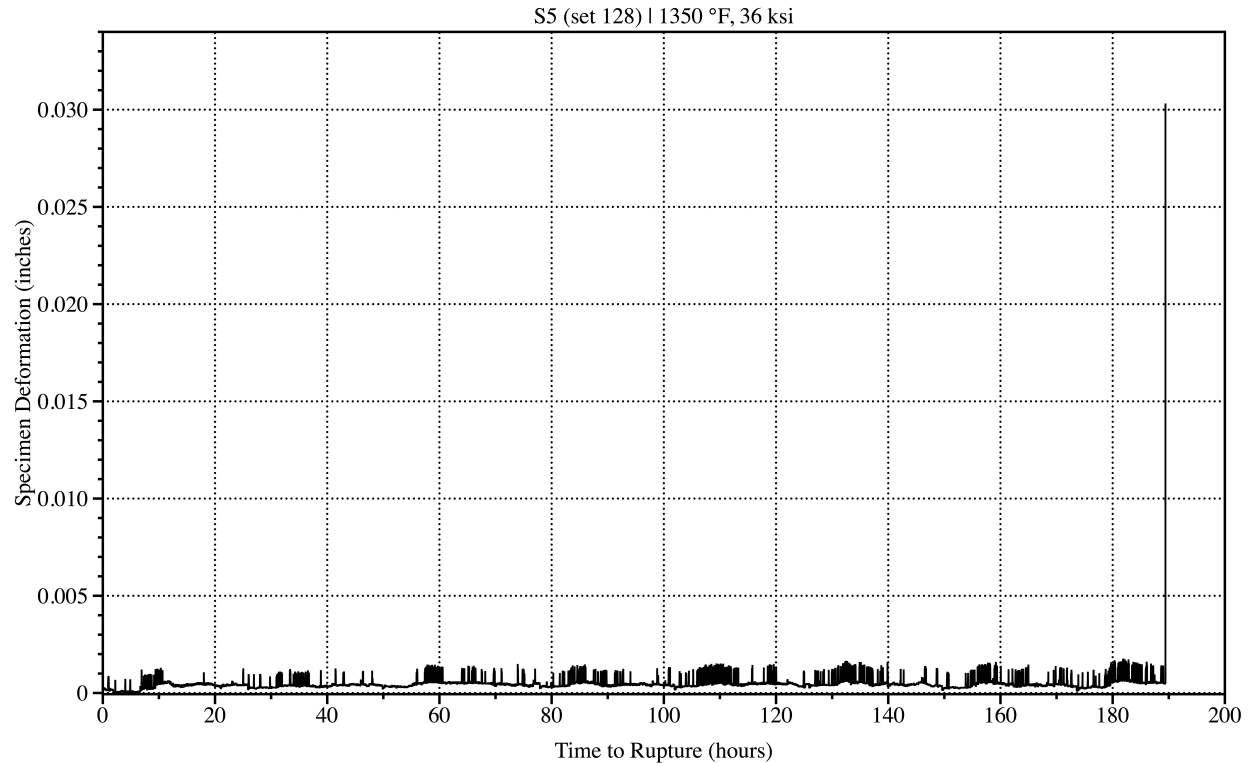


Figure 54. Plot of S5 (set 128) deformation (inches) as a function of time rupture (hours).

Figure 54 appears to demonstrate that specimen S5 (set 128) did not exhibit any classical creep behavior; instead, acceptable LVDT output noise (ranging between 0.001 to 0.002 inches) is demonstrated to have occurred before the specimen finally ruptured after a total of 187.1 hours at 1350 °F and under a constant load of 36 ksi. However, given that the specimen's elongation was measured to be 55%, and that the recorded specimen elongation was only 3%, it is suspected that the LVDT was not fully engaged or activated during the testing procedure. The accuracy of the time to rupture recorded for specimen S5 (set 128) is not suspected to have been compromised by this lack of LVDT engagement, as the creep bracket fully extends upon a specimen's rupture; the final seconds of the figure 54 plot indicate that the LVDT was successfully engaged upon the specimen's rupture.

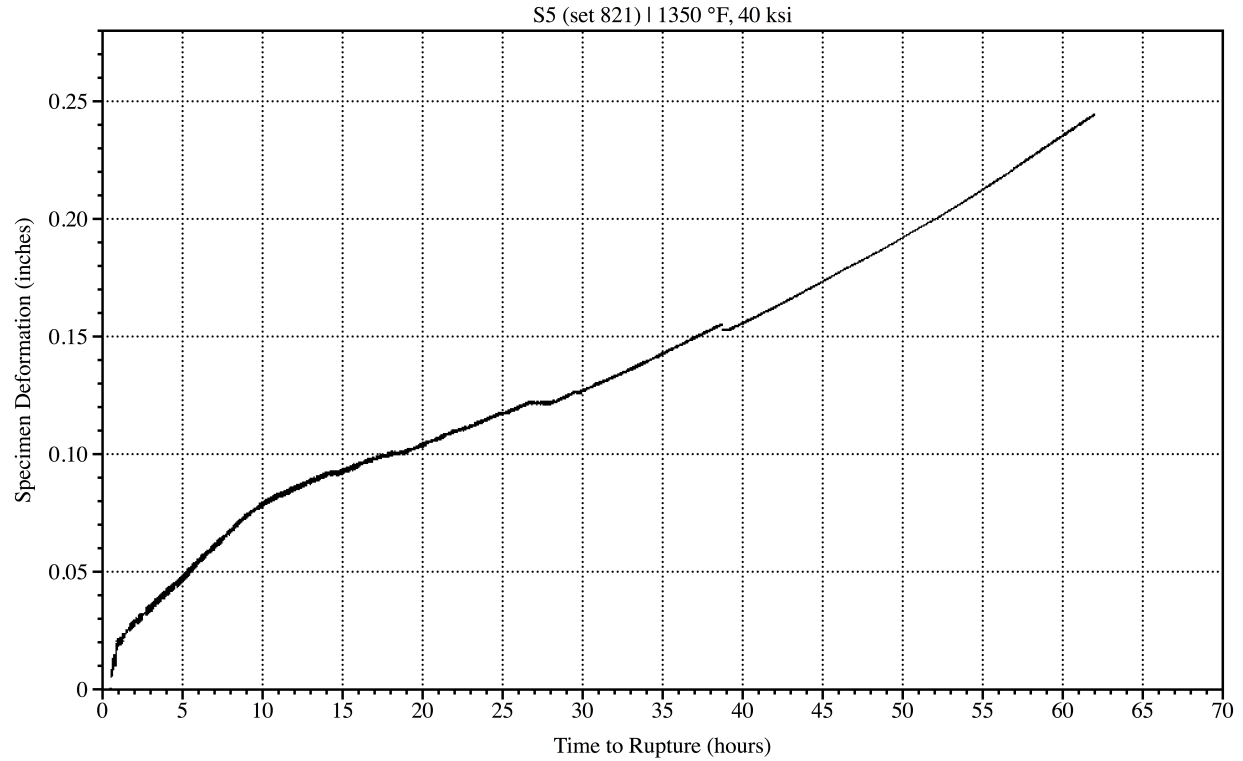


Figure 55. Plot of S5 (set 821) deformation (inches) as a function of time rupture (hours).

Figure 55 demonstrates that specimen S5 (set 821) exhibited all three stages of classically defined creep behavior. Primary creep behavior occurred at the onset of the testing procedure and then transitioned into steady-state, secondary creep behavior after approximately 10 hours of testing; secondary creep behavior was maintained for approximately 17 hours, as the specimen transitioned into tertiary creep behavior after approximately 27 hours of testing. The specimen sustained tertiary creep behavior for approximately 34.3 hours before finally rupturing after a total of 61.3 hours at 1350 °F and under a constant load of 40 ksi.

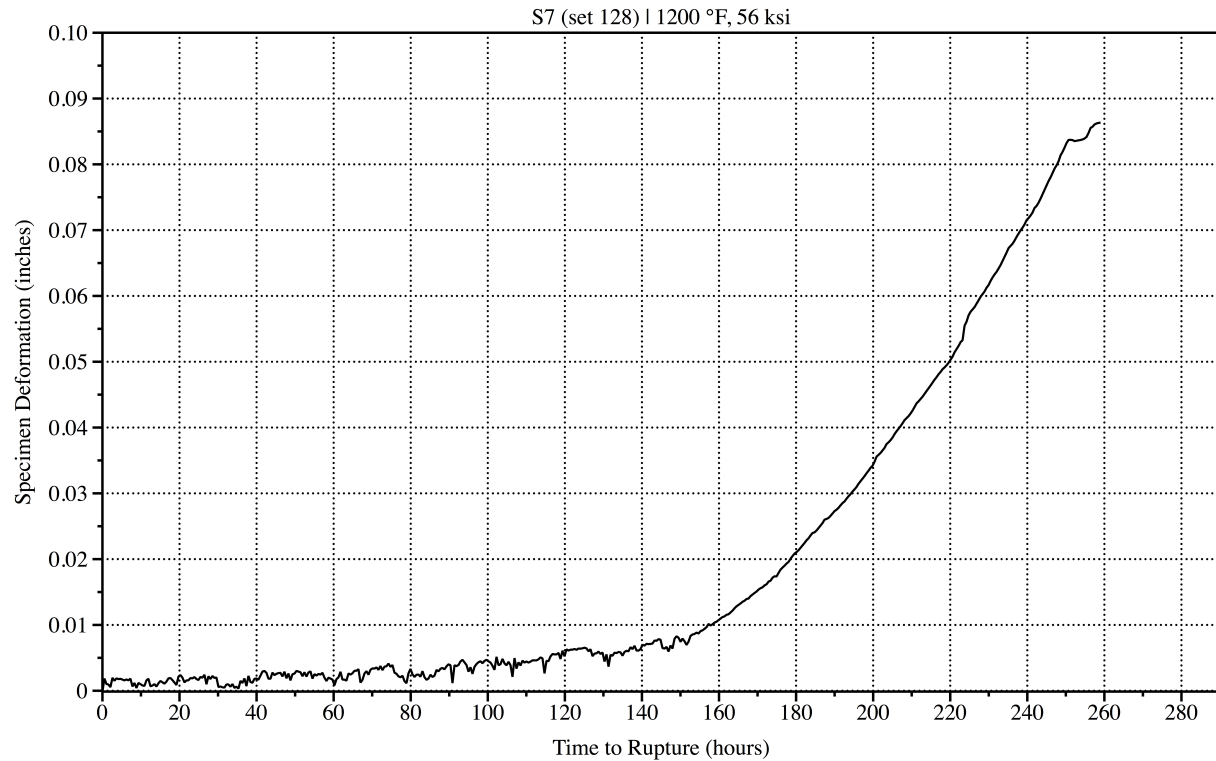


Figure 56. Plot of S7 deformation (inches) as a function of time rupture (hours).

Figure 56 demonstrates that specimen S7 did not exhibit any primary creep behavior at the onset of the testing procedure; instead, it initially demonstrated secondary creep behavior and then transitioned into tertiary creep behavior after approximately 85 hours of testing. The specimen sustained tertiary creep behavior for approximately 174 hours before finally rupturing after a total of 259 hours at 1200 °F and under a constant load of 56 ksi.

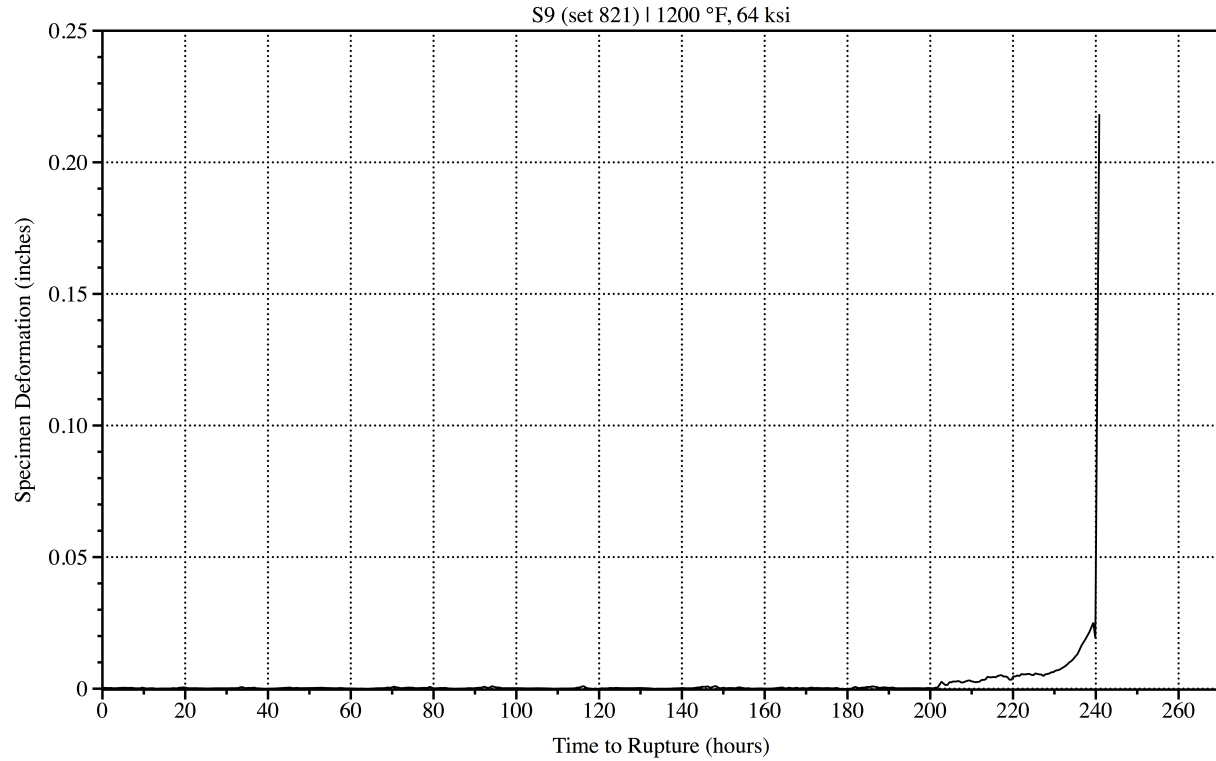


Figure 57. Plot of S9 (set 128) deformation (inches) as a function of time rupture (hours).

Figure 57 demonstrates that specimen S9 exhibited all three stages of classically defined creep behavior. Primary creep behavior occurred at the onset of the testing procedure and then transitioned into steady-state, secondary creep behavior after approximately 202 hours of testing; secondary creep behavior was maintained for approximately 26 hours, as the specimen transitioned into tertiary creep behavior after approximately 228 hours of testing. The specimen sustained tertiary creep behavior for approximately 12.5 hours before finally rupturing after a total of 240.5 hours at 1200 °F and under a constant load of 64 ksi.

3.3 Metallographic Analysis

Figures 58-105 are optical micrographs at 100, 200, 500, and 1000X magnifications of the twelve metallographic specimens (demonstrated in figure 17) that were produced for metallographic analysis of the *as-received* state of a bucket from set 128; these figures are located in Appendix A. Figures 58-61 correspond to specimen 1, figures 62-65 correspond to specimen 2, figures 66-69 correspond to specimen 3, figures 70-73 correspond to specimen 4, figures 74-77 correspond to specimen 5, figures 78-81 correspond to specimen 6, figures 82-85 correspond to specimen 7, figures 86-89 correspond to specimen 8, figures 90-93 correspond to specimen 9, figures 94-97 correspond to specimen 10, figures 98-101 correspond to specimen 11, and figures 102-105 correspond to specimen 12.

The lower magnification micrographs (100X and 200X) of the twelve, as-received metallographic specimens serve to demonstrate that there is an inter-specimen dendrite size gradient; the dendrite size increases steadily from the thinner cross-sections at the leading-edge end of the bucket to the thicker cross-sections along the main body of the bucket. This is not an unexpected phenomenon, as the turbine buckets used for this research investigation are cast components. The thinner regions of a cast component experience faster cooling rates, as heat dissipation is more readily achieved throughout a volumetrically reduced region; therefore, the time that thinner regions of a casting have to reach equilibrium is diminished, relative to thicker regions. As a result, grain growth via Ostwald ripening occurs more readily in thicker regions and not as readily in thinner regions of a cast component.

The higher magnification micrographs (500X and 1000X) of the twelve, as-received metallographic specimens serve to identify and characterize the different microconstituents

exhibited by the S-816 turbine bucket from set 128. These different microconstituents were identified and categorized in figures 97 and 101 (reproduced at the end of this paragraph) in order to establish metallographic references for interpretation of the many etched OM micrographs in this manuscript. The following discusses the morphological and locational differences in between the *five* microconstituents that were consistently demonstrated in the etched OM micrographs of this manuscript:

- large, blocky carbides, which are characteristic of the MC carbides that should exist in the S-816 microstructure, as demonstrated in figure 106; this phase is labeled as MC in figures 97, 101, and 106.
- Chinese-script carbides, which occur readily as a variant form of MC carbides in cast Co-base superalloys [2]; this phase is labeled as C-script in figures 97 and 101.
- agglomerated, interdendritic carbides, which are characteristic of M_6C carbides that should exist in the S-816 microstructure, as demonstrated in figure 106; this phase is labeled as M_6C in figures 101 and 106.
- fine, acicular microconstituents, which are characteristic of the topologically close-packed (TCP) Laves phase in Co-base superalloys, as demonstrated in figure 106. TCP phases can occur when the solubility limit of the austenitic FCC matrix is exceeded by a combination of chromium and refractory-element additions [2]; this phase is labeled as Laves in figures 97, 101, and 106.
- carbides that exist as films along dendritic boundaries and as cellular or lath precipitates in a pseudoeutectic phase that occurs intradendritically and is composed of alternating layers of austenitic matrix and carbide are all characterized as $M_{23}C_6$, as their morphological and

locational features are consistent with what has been documented of $M_{23}C_6$ carbides in Co-base superalloys [2]; this phase is labeled as $M_{23}C_6$ in figures 97 and 101.

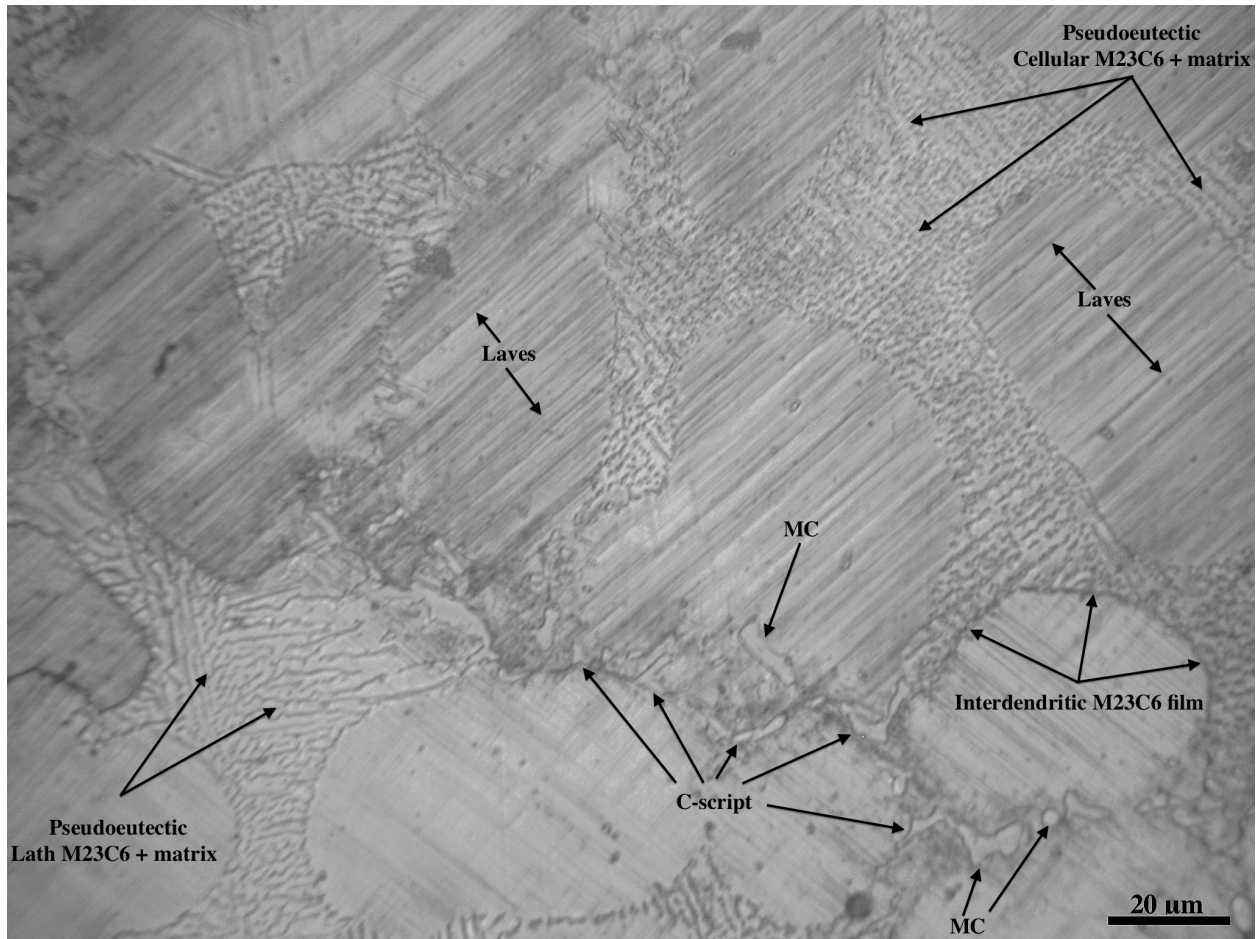


Figure 97. Etched microstructure of specimen 10 (as-received); original magnification: 1000X. Microconstituents identified for metallographic reference purposes.

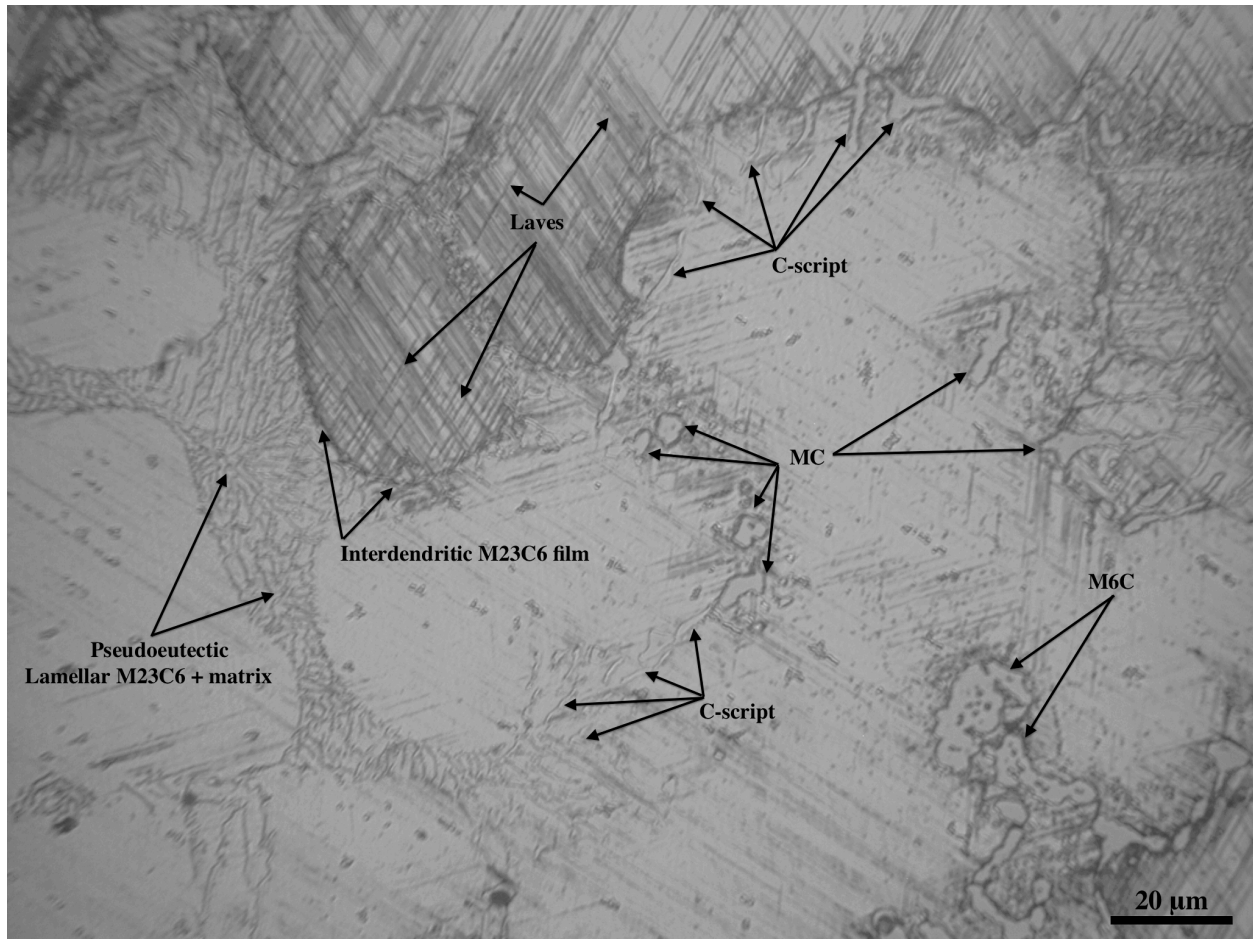


Figure 101. Etched microstructure of specimen 11 (as-received); original magnification: 1000X.
Microconstituents identified for metallographic reference purposes.

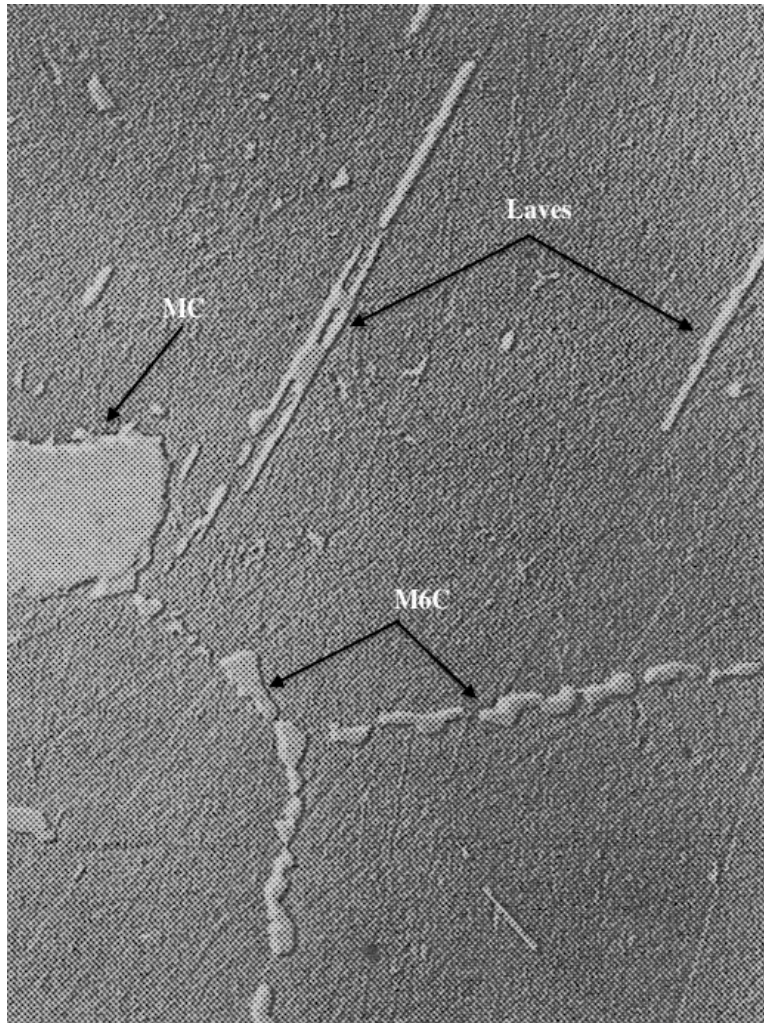


Figure 106. Laves plates (with MC and M_6C carbides) in S-816; original magnification: 5950X [2]. Labeling of the different microconstituents was performed for the purposes of this research investigation, as the original reference *did not* include any labeling within the micrograph.

An inter-specimen difference in the presence of the different microconstituents (relative to one another) is not readily observed for specimens 1-11; rather, specimens 1-11 are consistent in demonstrating the presence of all five different microconstituents. Specimen 12 only demonstrates the presence of MC, Chinese-script, M_6C carbides, and $M_{23}C_6$ carbides; the acicular Laves phase is not observed in its microstructure.

Figures 107-148 are optical micrographs at 500 and 1000X magnifications of the metallographic specimens (in the un-etched state) produced from longitudinal cross-sections of the seven creep-rupture specimens; these figures are located in Appendix B. Figures 107-112 correspond to specimen S1, figures 113-118 correspond to specimen S2, figures 119-124 correspond to specimen S4, figures 125-130 correspond to specimen S5 (set 128), figures 131-136 correspond to specimen S5 (set 821), figures 137-142 correspond to specimen S7, and figures 143-148 correspond to specimen S9.

The figures in Appendix B demonstrate that creep voids and ruptures formed within all seven creep-rupture specimens. The presence of creep voids and ruptures is relatively increased in specimen S4, and relatively decreased in specimens S7 and S9, when compared to the rest of the specimens; by inference, specimens S1, S2, S5 (set 128), and S5 (set 821) are relatively equal in terms of the presence of creep voids and ruptures. These figures also consistently demonstrate the presence of creep voids and/or ruptures directly adjacent to the rupture surfaces of the seven creep-rupture specimens; additionally, the rupture surfaces of all seven specimens are jagged and geometrically diverse in morphology.

Figures 149-188 are optical micrographs at 500 and 1000X magnifications of the metallographic specimens (in the etched state) produced from longitudinal cross-sections of the seven creep-rupture specimens; these figures are located in Appendix C. Figures 149-154 correspond to specimen S1, figures 155-159 correspond to specimen S2, figures 160-164 correspond to specimen S4, figures 165-169 correspond to specimen S5 (set 128), figures 170-176 correspond to specimen S5 (set 821), figures 177-182 correspond to specimen S7, and figures 183-188 correspond to specimen S9.

Figures 189-216 are back-scattered electron (BSE) micrographs at various magnifications of the metallographic specimens (in the etched state) produced from longitudinal cross-sections of the seven creep-rupture specimens; these figures are located in Appendix D. Figures 189-192 correspond to specimen S1, figures 193-196 correspond to specimen S2, figures 197-200 correspond to specimen S4, figures 201-204 correspond to specimen S5 (set 128), figures 205-208 correspond to specimen S5 (set 821), figures 209-212 correspond to specimen S7, and figures 213-216 correspond to specimen S9.

The figures in Appendices C and D demonstrate that *very few* of the observed creep voids and ruptures formed in regions where the matrix was solely present; rather, most of the observed creep voids and ruptures formed along interfacial regions, such as interdendritic or carbide-matrix interfaces. Additionally, as demonstrated in these figures, the jagged, geometrically diverse morphology of the specimens' rupture surfaces (as observed in the figures of Appendix B) is attributed to rupture having occurred along interdendritic or interfacial carbide-matrix interfaces.

The *five* different microconstituents exhibited in the figures of Appendix D were identified and categorized in figures 193, 199, and 200 (reproduced at the end of this paragraph) in order to establish metallographic references for interpretation of the etched BSE micrographs in this manuscript; these five microconstituents are the same as those described previously for etched OM micrographs.

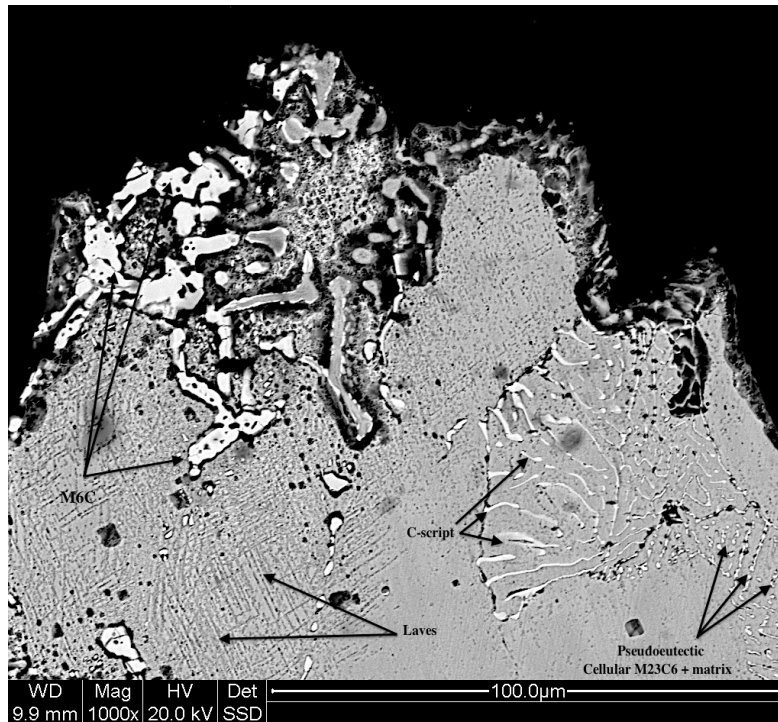


Figure 193. Etched microstructure of specimen S2 (rupture surface); magnification: 1000X. Microconstituents identified for metallographic reference purposes.

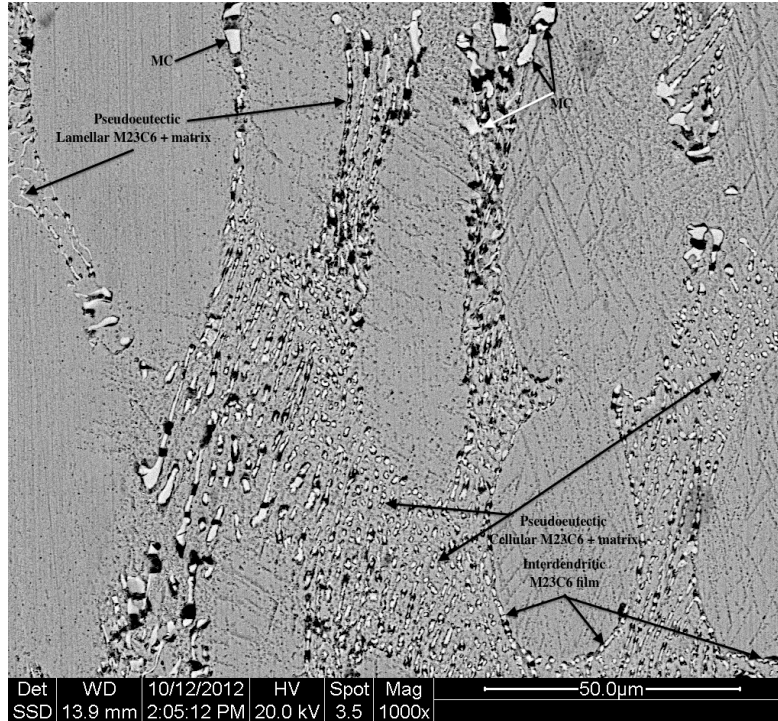


Figure 199. Etched microstructure of specimen S4 (at core); magnification: 1000X. Microconstituents identified for metallographic reference purposes.

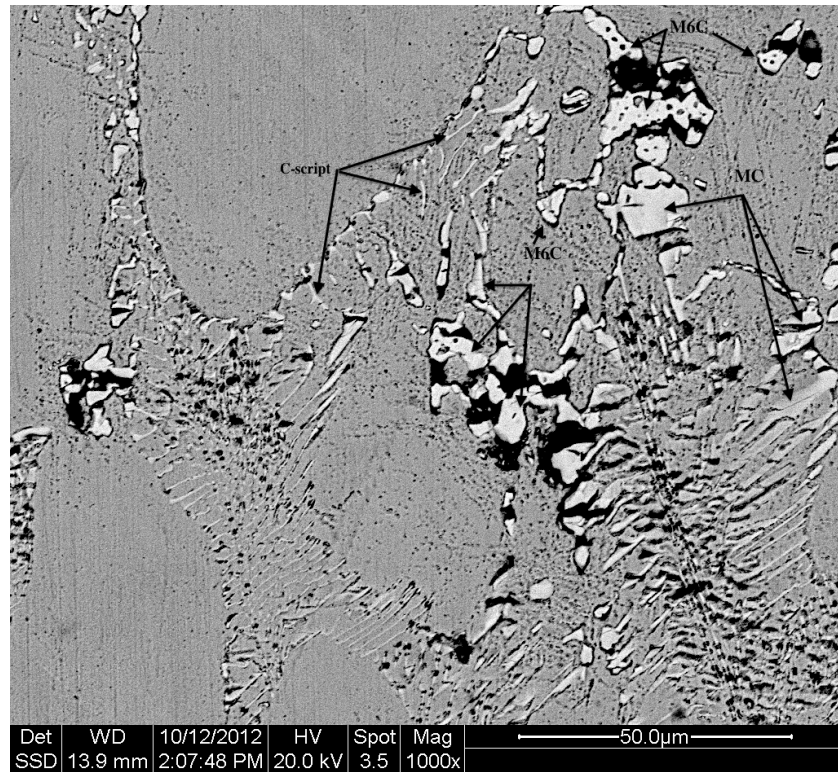


Figure 200. Etched microstructure of specimen S4 (at core); magnification: 1000X.
Microconstituents identified for metallographic reference purposes.

The figures in Appendices C and D are consistent in demonstrating that the *largest* creep ruptures formed at regions adjacent to agglomerated M_6C carbides. Physical deterioration of the MC, Chinese-script, and M_6C carbides was also consistently observed in these figures. The M_6C carbides demonstrated a larger propensity for the formation of voids within themselves (as opposed to crack formation), while the MC and Chinese-script carbides demonstrated a larger propensity for the formation of cracks within themselves (as opposed to void formation).

3.4 Energy Dispersive X-ray Spectroscopy

Table 5 demonstrates the approximate chemical composition of the microconstituents identified with numbered ovals in figure 192 (reproduced below); location 1 corresponds to a Chinese-script carbide while locations 2 and 3 correspond to MC carbides. Figures 217-219 demonstrate the qualitative spectrographic data that was also gathered during the elemental microanalysis of these three different locations in the S1 metallographic specimen. Table 5 and figures 217-219 demonstrate that both the MC and Chinese-script carbides in figure 192 are composed primarily of niobium and devoid of molybdenum; other carbide-forming elements, such as chromium and tungsten, are also present in the chemical composition of these carbides. The presence of nickel, iron, and cobalt in the chemical composition of these carbides is considered to have emanated from EDS detection of the microstructural matrix.

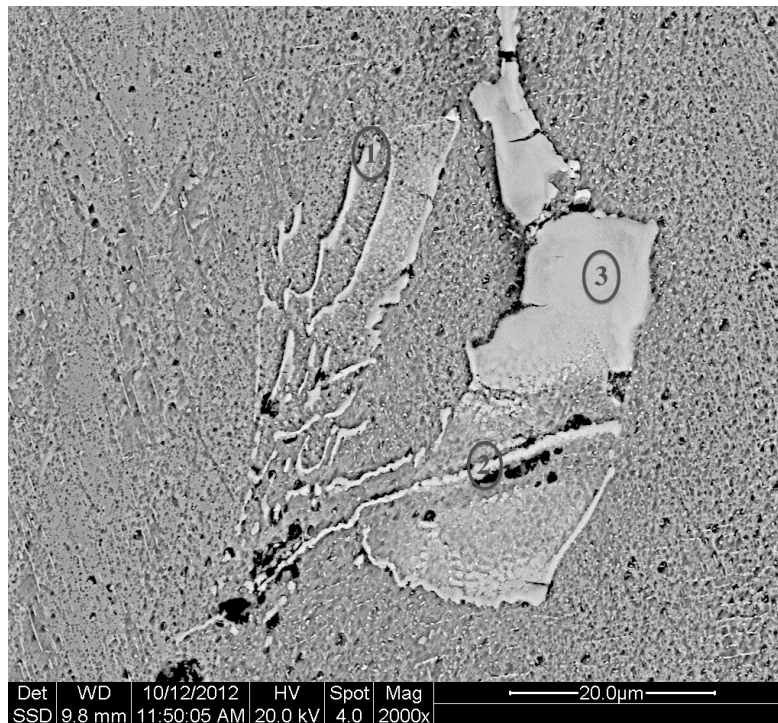


Figure 192. Etched microstructure of specimen S1 (at core); magnification: 2000X. Numbered ovals indicate where EDS analyses were conducted.

Table 5. Approximate chemical composition of microconstituents at three different locations in figure 192.

Element	Wt. (%) Location 1	Wt. (%) Location 2	Wt. (%) Location 3
Manganese	-	-	-
Chromium	10.85	4.58	3.77
Nickel	8.80	3.45	2.90
Molybdenum	-	-	-
Tungsten	12.70	12.74	8.28
Niobium	48.18	73.38	79.99
Iron	1.49	-	-
Cobalt	17.49	5.85	4.65

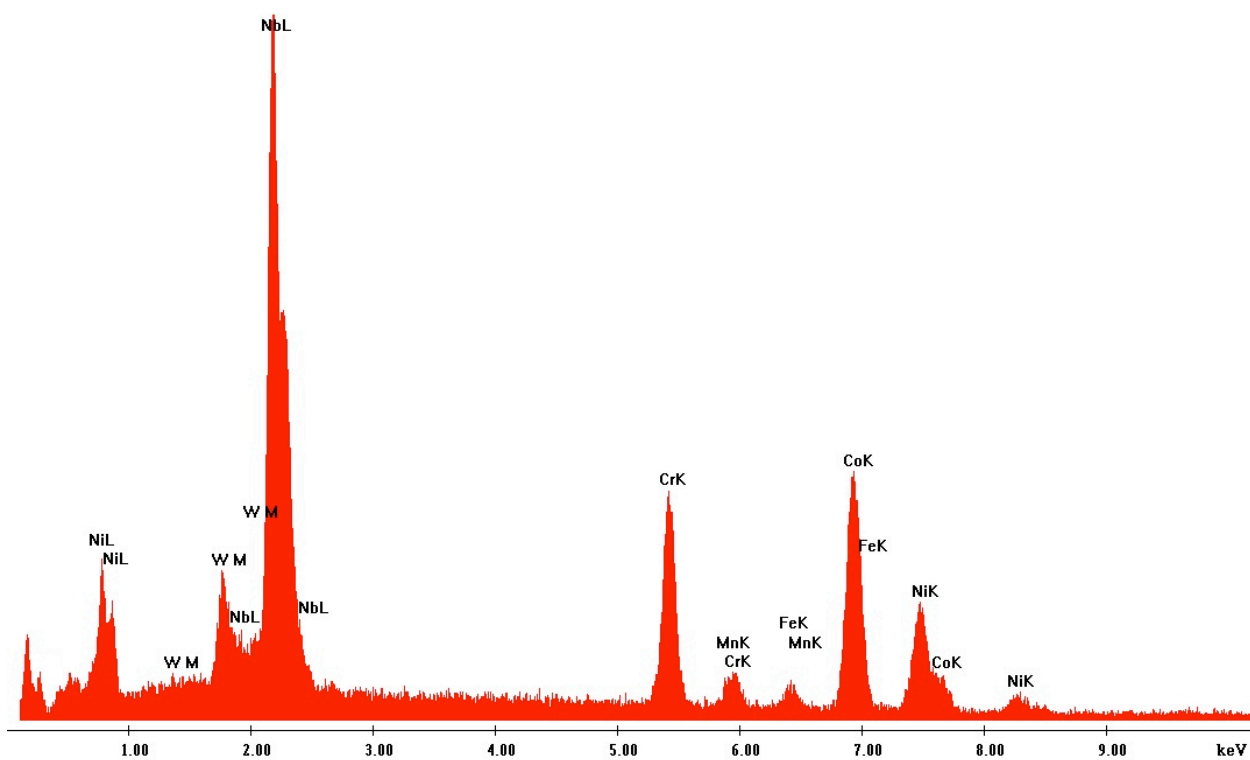


Figure 217. Elemental spectrum collected during EDS analysis of location 1 in figure 192.

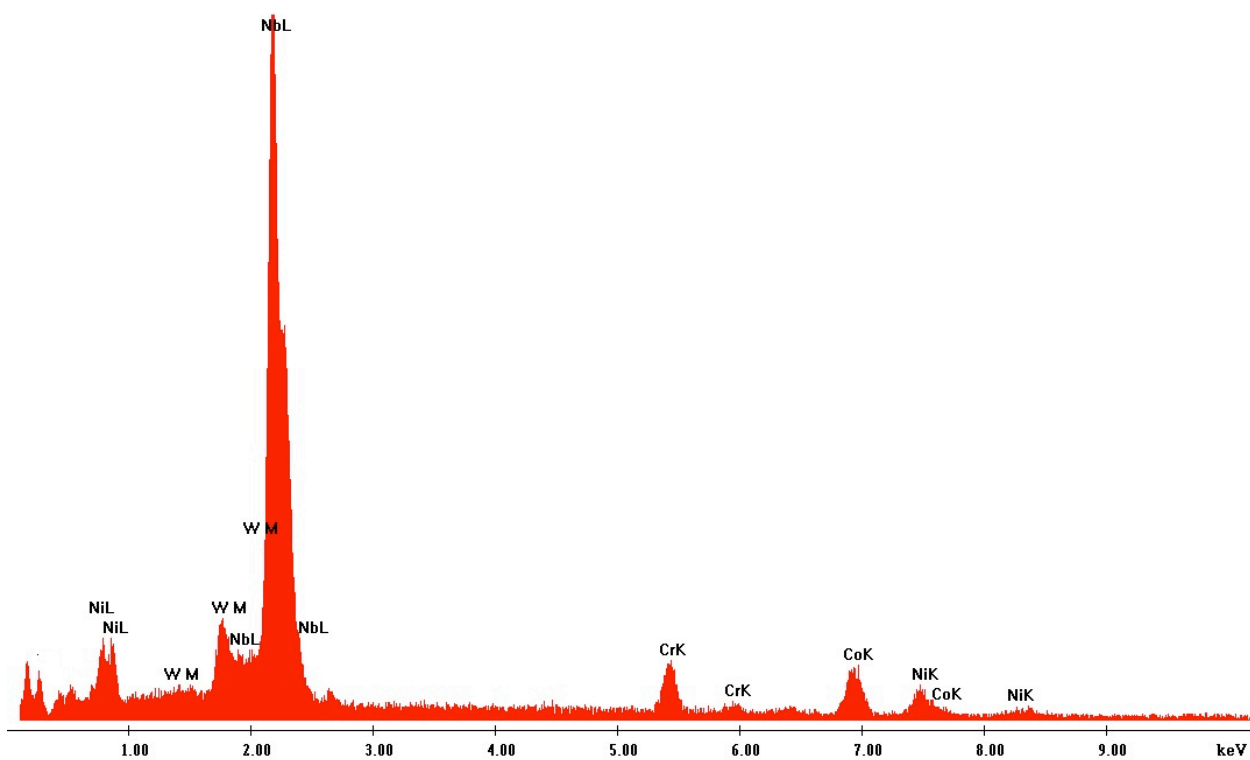


Figure 218. Elemental spectrum collected during EDS analysis of location 2 in figure 192.

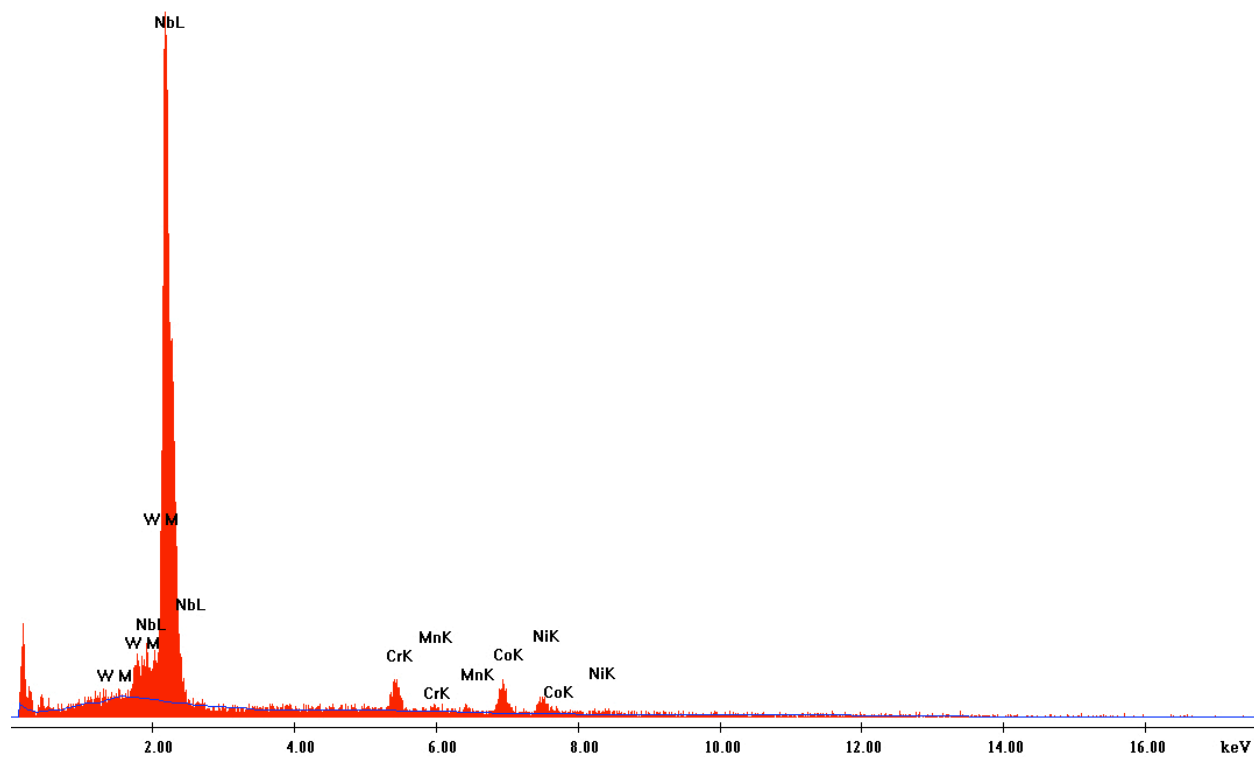


Figure 219. Elemental spectrum collected during EDS analysis of location 3 in figure 192.

Table 6 demonstrates the approximate chemical composition of the microconstituents identified with numbered ovals in figure 196 (reproduced below); locations 4 and 5 correspond to agglomerated M_6C carbides. Figures 220 and 221 demonstrate the qualitative spectrographic data that was also gathered during the elemental microanalysis of these two different locations in the S2 metallographic specimen. Table 6, and figures 220 and 221, demonstrate that the M_6C carbides in figure 196 are devoid of niobium and composed primarily of molybdenum; other carbide-forming elements, such as chromium and tungsten, are also present in the chemical composition of these carbides. The presence of manganese, nickel, iron, and cobalt in the chemical composition of these carbides is considered to have emanated from EDS detection of the microstructural matrix.

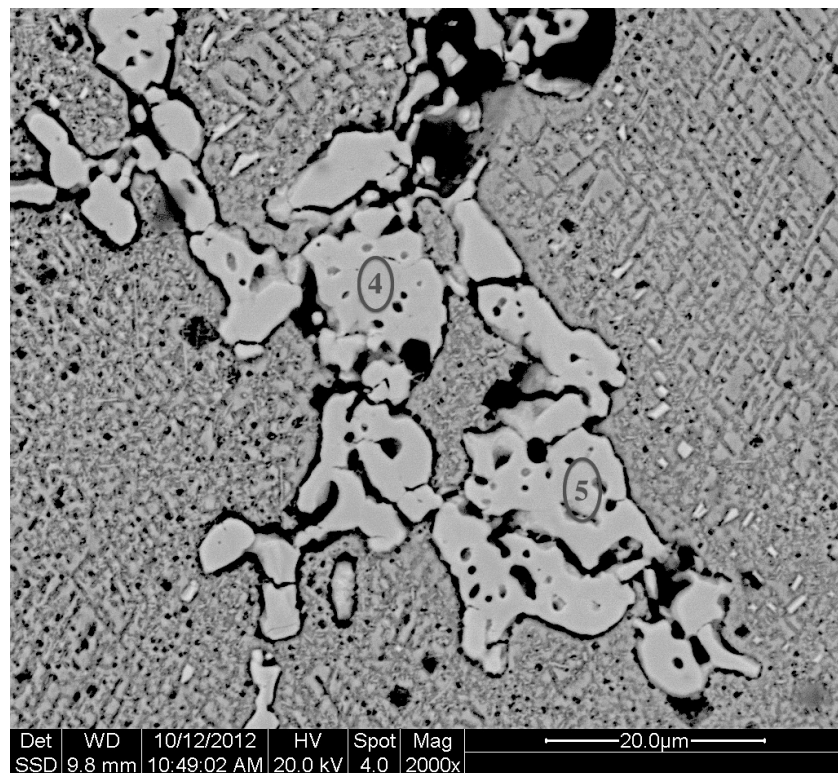


Figure 196. Etched microstructure of specimen S2 (at core); magnification: 2000X. Numbered ovals indicate where EDS analyses were conducted.

Table 6. Approximate chemical composition of microconstituents at two different locations in figure 196.

Element	Wt. (%) Location 4	Wt. (%) Location 5
Manganese	0.50	-
Chromium	15.32	15.31
Nickel	19.45	10.30
Molybdenum	38.95	31.37
Tungsten	11.12	23.78
Niobium	-	-
Iron	-	1.22
Cobalt	14.65	18.03

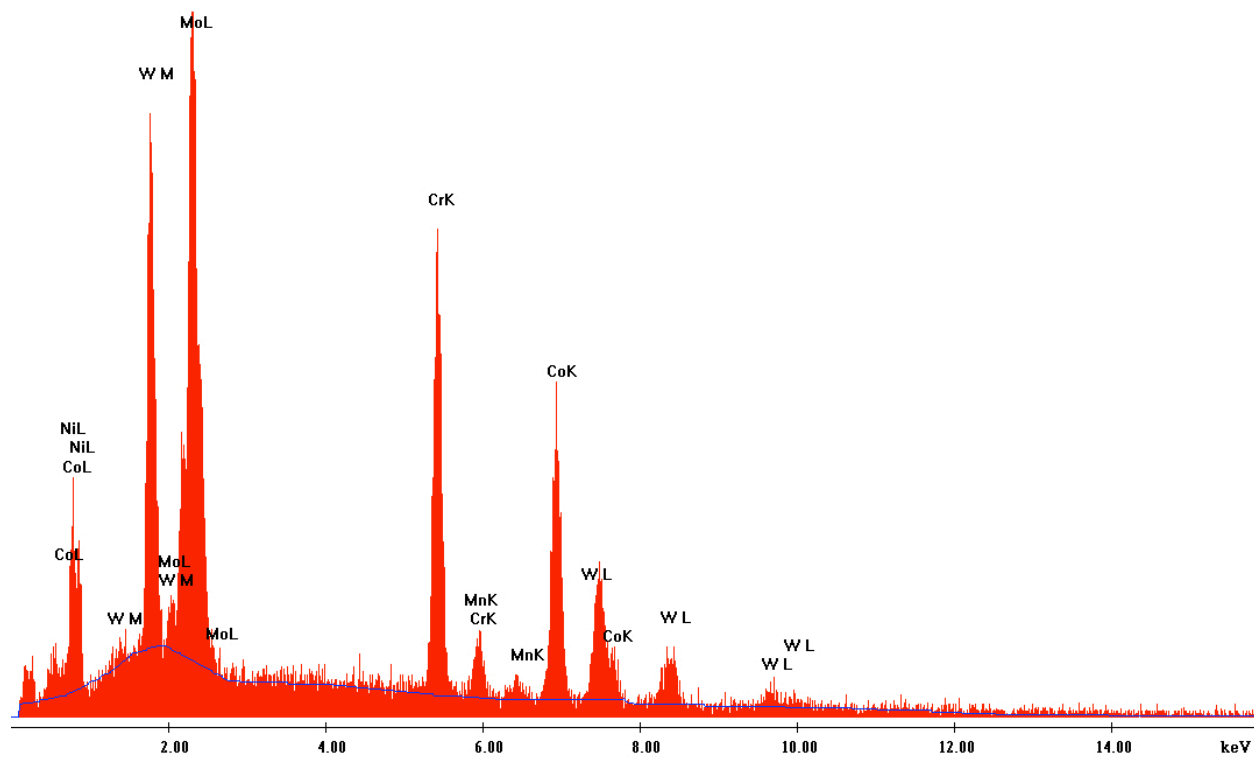


Figure 220. Elemental spectrum collected during EDS analysis of location 4 in figure 196.

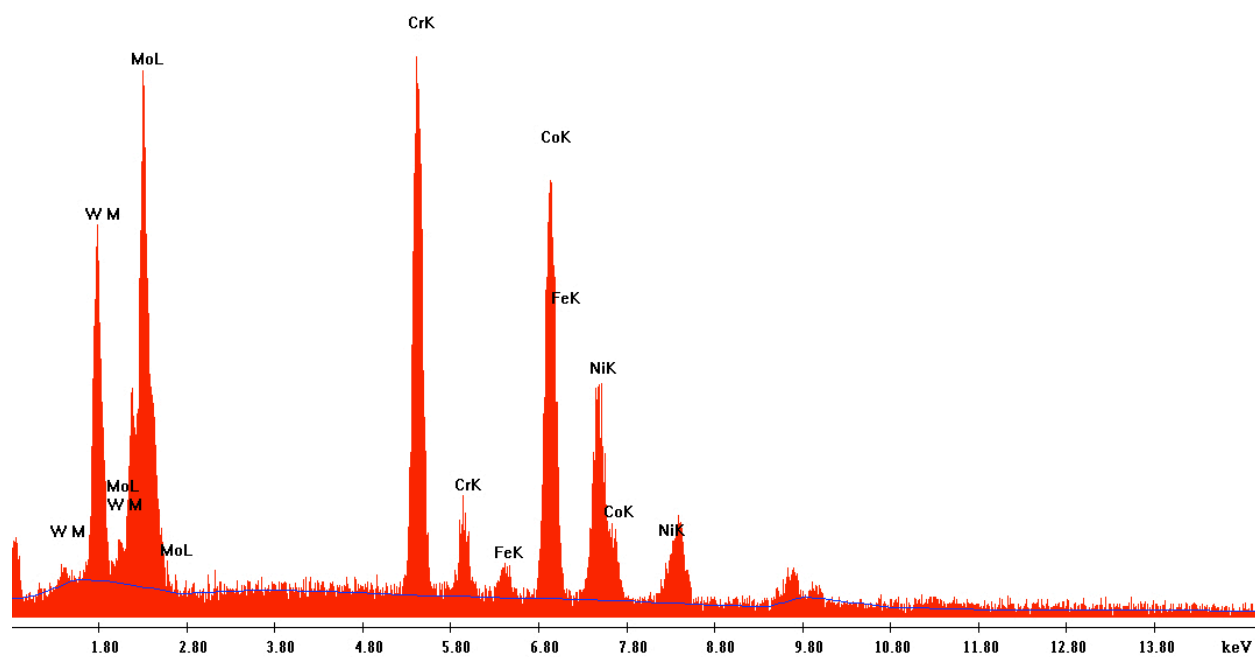


Figure 221. Elemental spectrum collected during EDS analysis of location 5 in figure 196.

Table 7 demonstrates the approximate chemical composition of the microconstituents identified with numbered ovals in figure 197 (reproduced below); location 6 corresponds to an MC carbide, locations 7 and 8 corresponds to dark- and light-colored regions at the core and edge of another MC carbide (respectively), and location 9 corresponds to an agglomerated M_6C carbide that is located directly adjacent to the MC carbide analyzed at locations 7 and 8. Figures 222-225 demonstrate the qualitative spectrographic data that was also gathered during the elemental microanalysis of these four different locations in the S4 metallographic specimen. Columns two and three of table 7, and figures 222 and 223, demonstrate that the MC carbide analyzed at location 6 and the core of the MC carbide analyzed at location 7 in figure 197 (respectively) are composed primarily of niobium and devoid of molybdenum; other carbide-forming elements, such as chromium and tungsten, are also present in the chemical composition of these two locations. Column four of table 7 and figure 224 demonstrate that the edge of the MC carbide analyzed at location 8 in figure 197 is composed primarily of molybdenum, tungsten, and niobium; chromium was also present in the chemical composition of this location, as it too is a carbide-forming element. Column five of table 7 and figure 225 demonstrate that the agglomerated M_6C carbide analyzed at location 9 in figure 197 is composed primarily of molybdenum; other carbide-forming elements, such as chromium, tungsten, and niobium are also present in the chemical composition of this carbide. The presence of manganese, nickel, iron, and cobalt in the chemical composition of these carbides is considered to have emanated from EDS detection of the microstructural matrix.

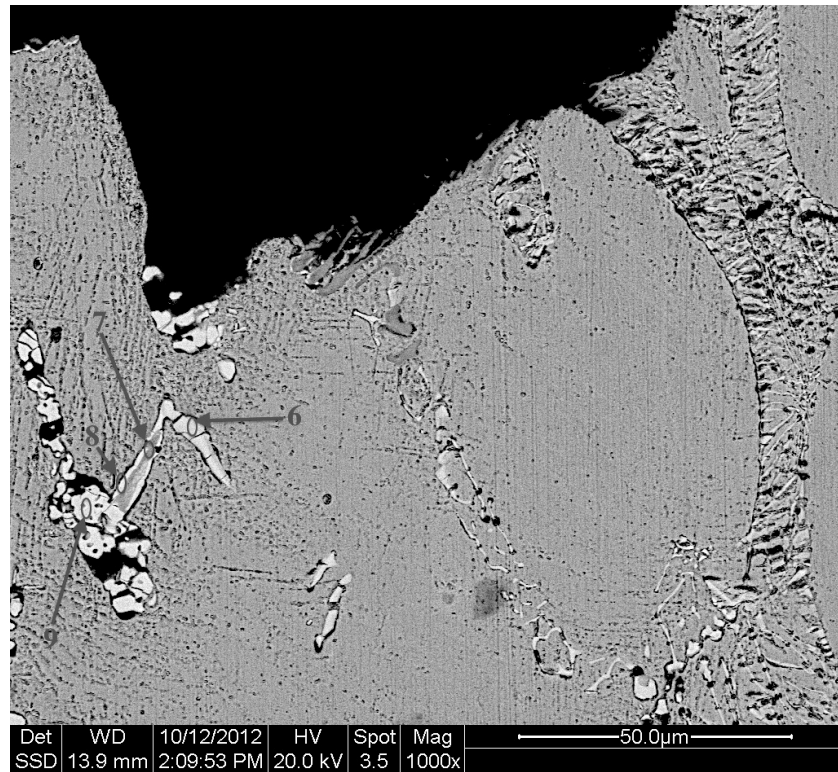


Figure 197. Etched microstructure of specimen S4 (rupture surface); magnification: 1000X. Numbered ovals indicate where EDS analyses were conducted.

Table 7. Approximate chemical composition of microconstituents at four different locations in figure 197.

Element	Wt. (%) Location 6	Wt. (%) Location 7	Wt. (%) Location 8	Wt. (%) Location 9
Manganese	-	2.19	0.69	-
Chromium	3.21	8.67	9.55	15.75
Nickel	1.81	-	5.25	10.62
Molybdenum	-	-	25.97	26.13
Tungsten	9.65	-	26.42	13.52
Niobium	82.24	86.79	22.55	11.07
Iron	-	-	-	4.04
Cobalt	3.10	2.35	9.57	18.88

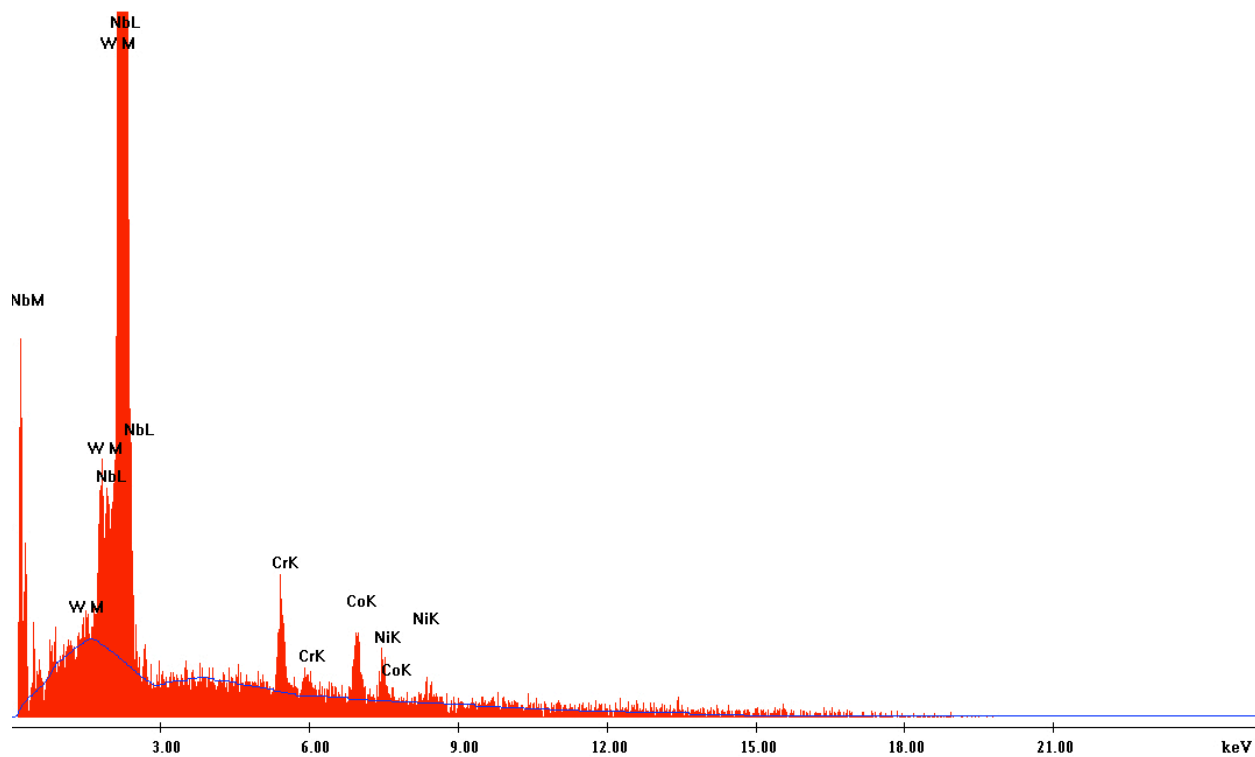


Figure 222. Elemental spectrum collected during EDS analysis of location 6 in figure 197.

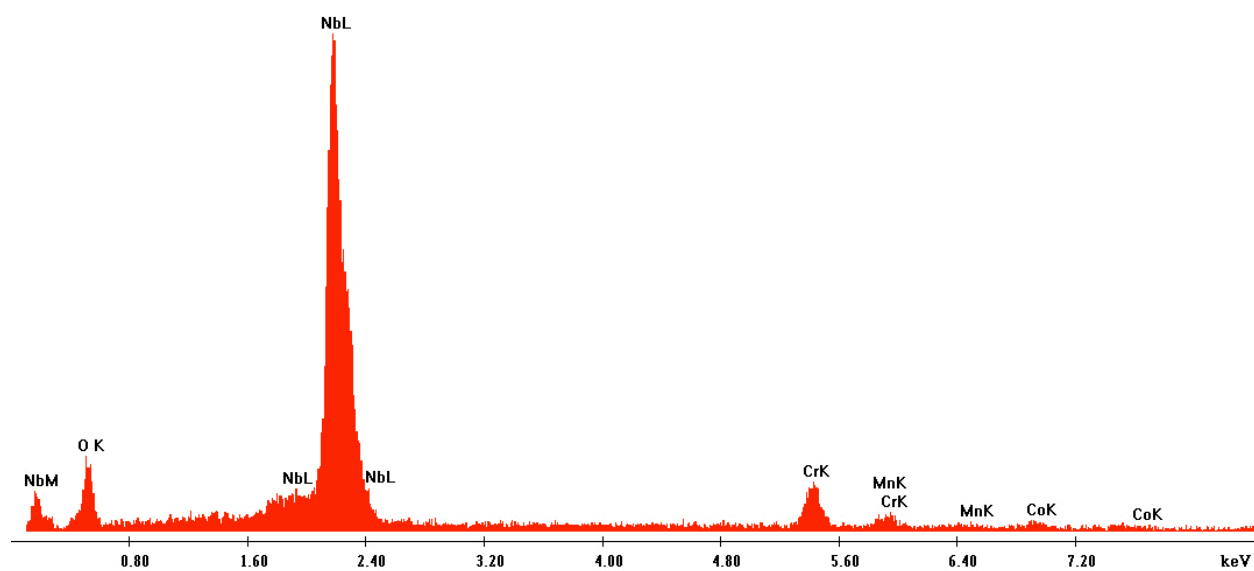


Figure 223. Elemental spectrum collected during EDS analysis of location 7 in figure 197.

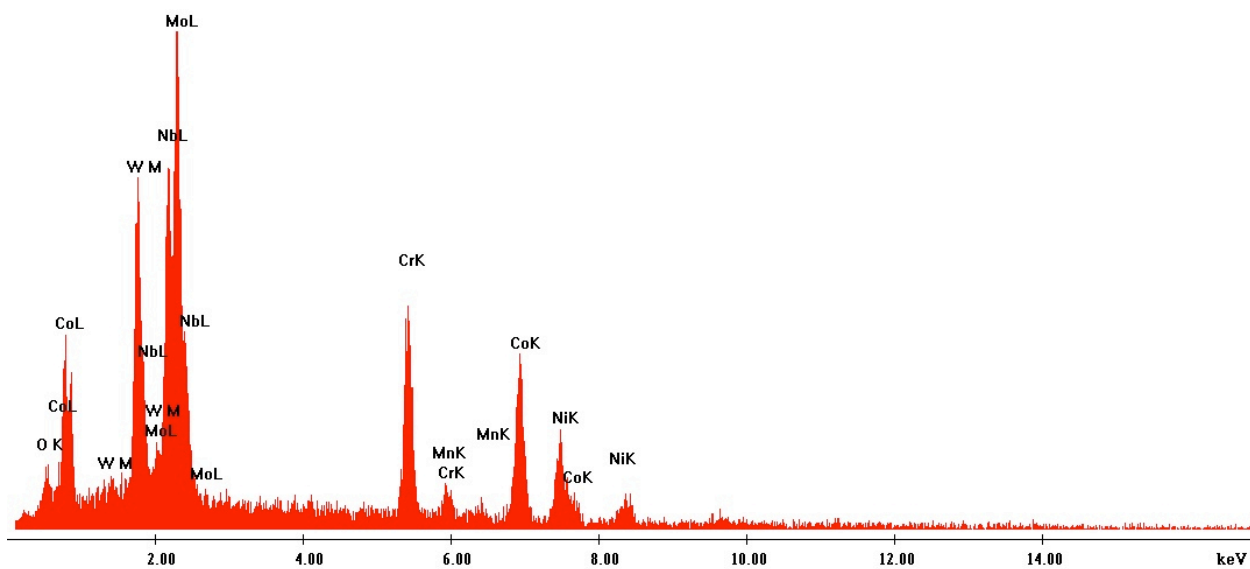


Figure 224. Elemental spectrum collected during EDS analysis of location 8 in figure 197.

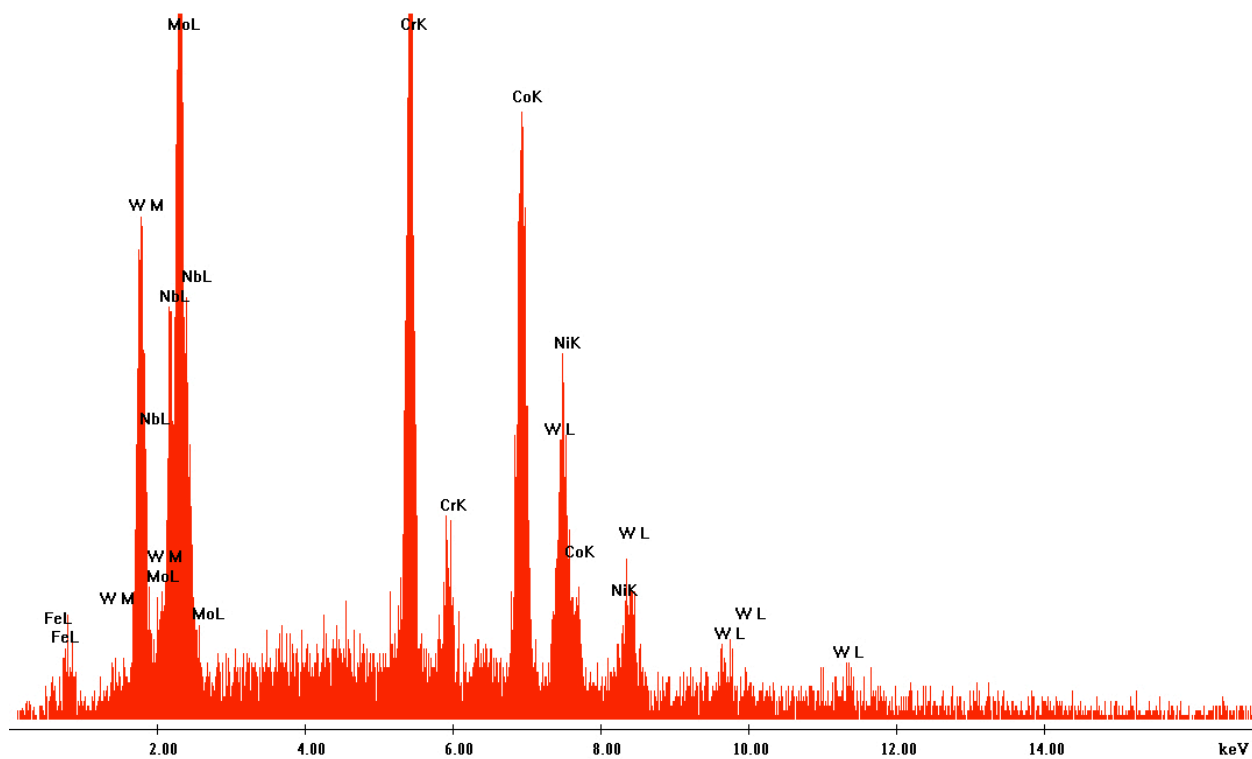


Figure 225. Elemental spectrum collected during EDS analysis of location 9 in figure 197.

Table 8 demonstrates the approximate chemical composition of the microconstituent identified with a numbered oval in figure 204 (reproduced below); location 10 corresponds to an agglomerated M_6C carbide. Figure 226 demonstrates the qualitative spectrographic data that was also gathered during the elemental microanalysis of this one location in the S5 (set 128) metallographic specimen. Table 8 and figure 226 demonstrate that the M_6C carbide in figure 204 is devoid of niobium and composed primarily of molybdenum; other carbide-forming elements, such as chromium and tungsten, are also present in the chemical composition of this carbide. The presence of manganese, nickel, iron, and cobalt in the chemical composition of these carbides is considered to have emanated from EDS detection of the microstructural matrix.

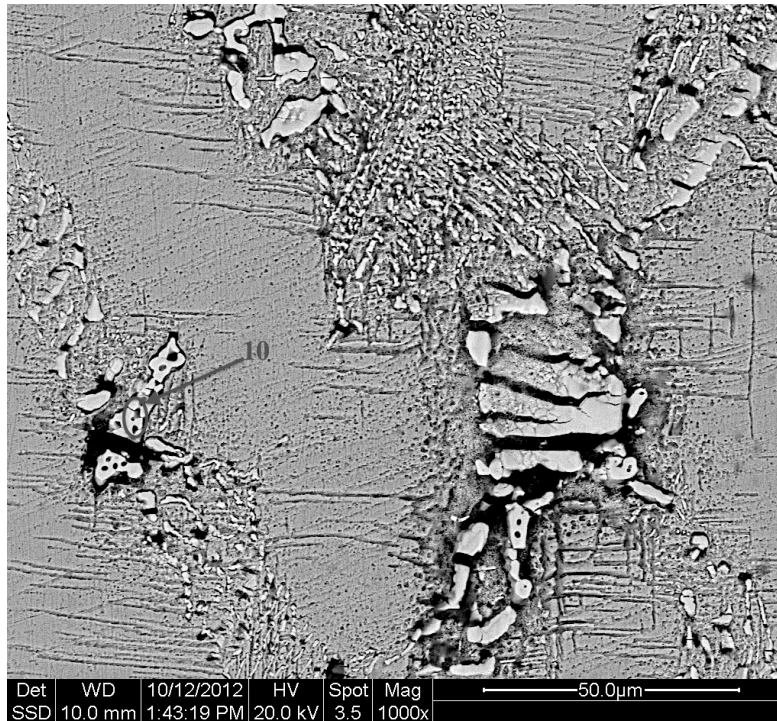


Figure 204. Etched microstructure of specimen S5, set 128 (at core); magnification: 1000X. A numbered oval indicates where an EDS analysis was conducted.

Table 8. Approximate chemical composition of the microconstituent at a single location in figure 204.

Element	Wt. (%) Location 10
Manganese	0.68
Chromium	15.32
Nickel	9.76
Molybdenum	46.17
Tungsten	11.04
Niobium	-
Iron	-
Cobalt	17.03

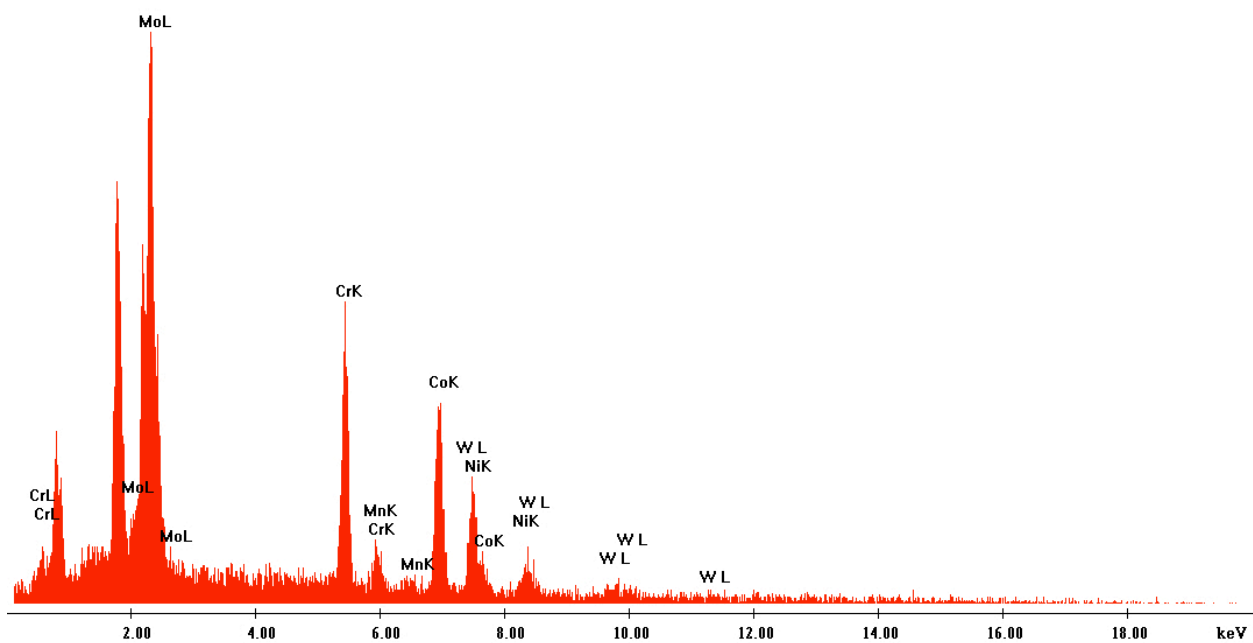


Figure 226. Elemental spectrum collected during EDS analysis of location 10 in figure 204.

Table 9 demonstrates the approximate chemical composition of microstructural matrix regions identified with numbered ovals in figures 207 and 208 (reproduced below); figures 227 and 228 demonstrate the qualitative spectrographic data that was also gathered during the elemental microanalysis of these two locations in the S5 (set 821) metallographic specimen. In comparison to table 1 (reproduced after figures 207 and 208), which demonstrates the chemical composition of S-816, table 9 demonstrates that the chemical composition of locations 11 and 12 in figures 207 and 208 (respectively) lie approximately within the elemental ranges (for chemical species *detectable* by EDS) specified for S-816. This observation is not applicable to molybdenum, niobium, and tungsten, as the differences in their detected concentrations (relative to those specified for S-816) do not lie approximately close (within 5 - 10%) to those specified for S-816. The presence of molybdenum and tungsten (especially) is increased, and the presence of niobium is decreased, with respect to their elemental ranges specified for S-816.

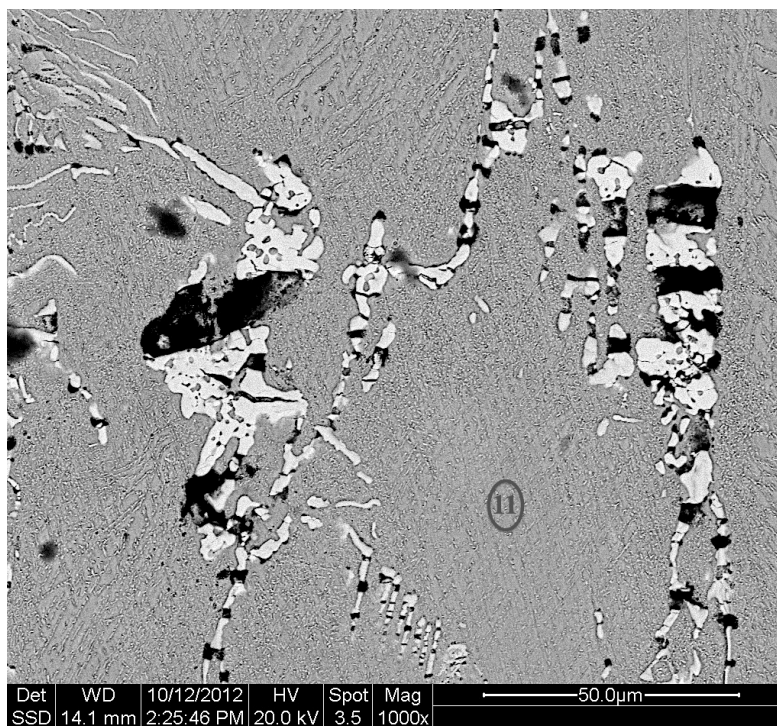


Figure 207. Etched microstructure of specimen S5, set 821 (at core); magnification: 1000X. A numbered oval indicates where an EDS analysis was conducted.

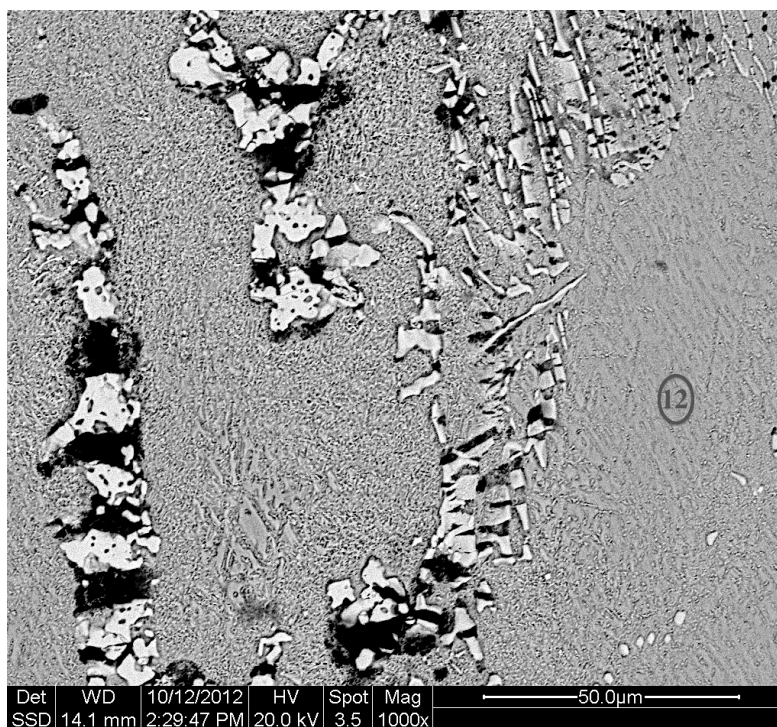


Figure 208. Etched microstructure of specimen S5, set 821 (at core); magnification: 1000X. A numbered oval indicates where an EDS analysis was conducted.

Table 9. Approximate chemical composition of the microstructural matrix at single locations in figures 207 and 208.

Element	Wt. (%) Location 11	Wt. (%) Location 12
Manganese	0.51	0.38
Chromium	21.18	21.20
Nickel	16.74	17.40
Molybdenum	5.70	6.25
Tungsten	14.32	14.21
Niobium	1.33	1.15
Iron	3.64	3.21
Cobalt	36.59	36.21

Table 1. Range of elemental weight percentages in S-816 chemical composition.

Element	Weight (%)
Carbon	0.32-0.42
Manganese	1.00-2.00
Silicon	0.20-0.60
Phosphorus	0.030 max
Sulfur	0.030 max
Chromium	19.0-21.0
Nickel	19.0-21.0
Molybdenum	3.50-4.50
Tungsten	3.50-4.50
Niobium	3.50-4.50
Iron	5.00 max
Cobalt	Balance

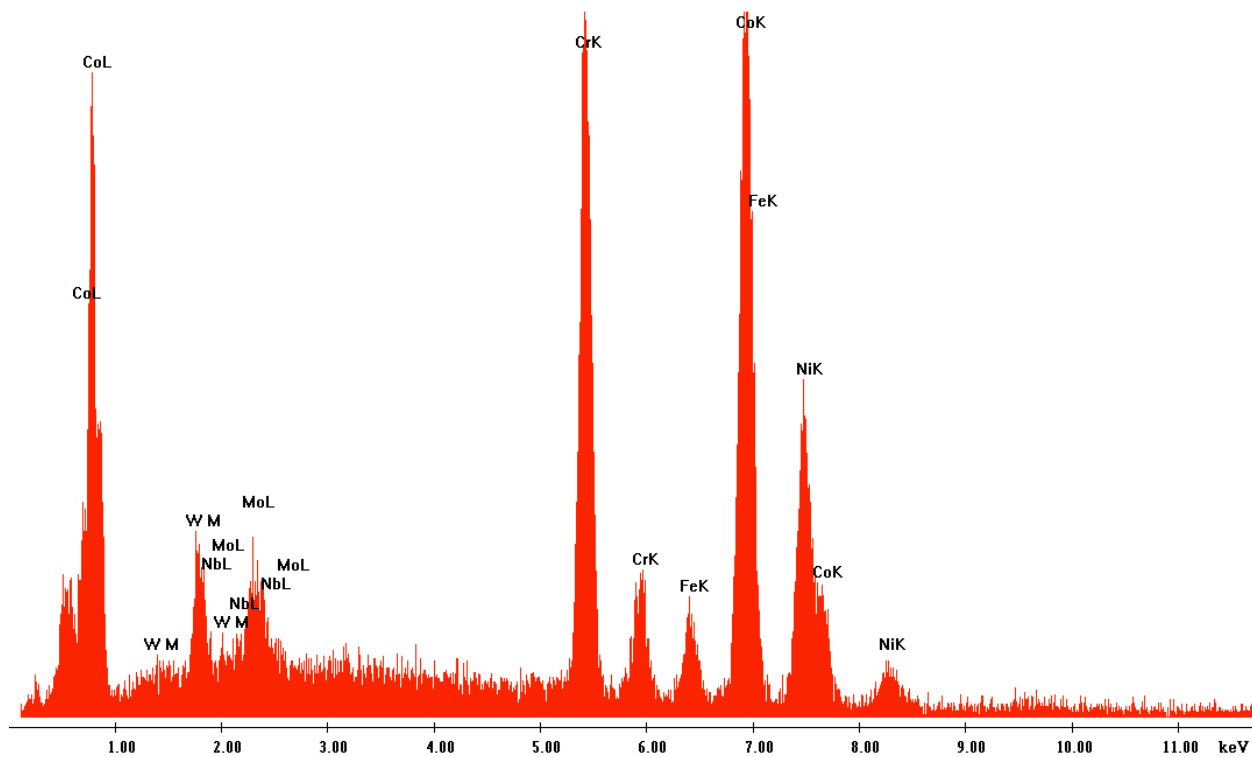


Figure 227. Elemental spectrum collected during EDS analysis of location 11 in figure 207.

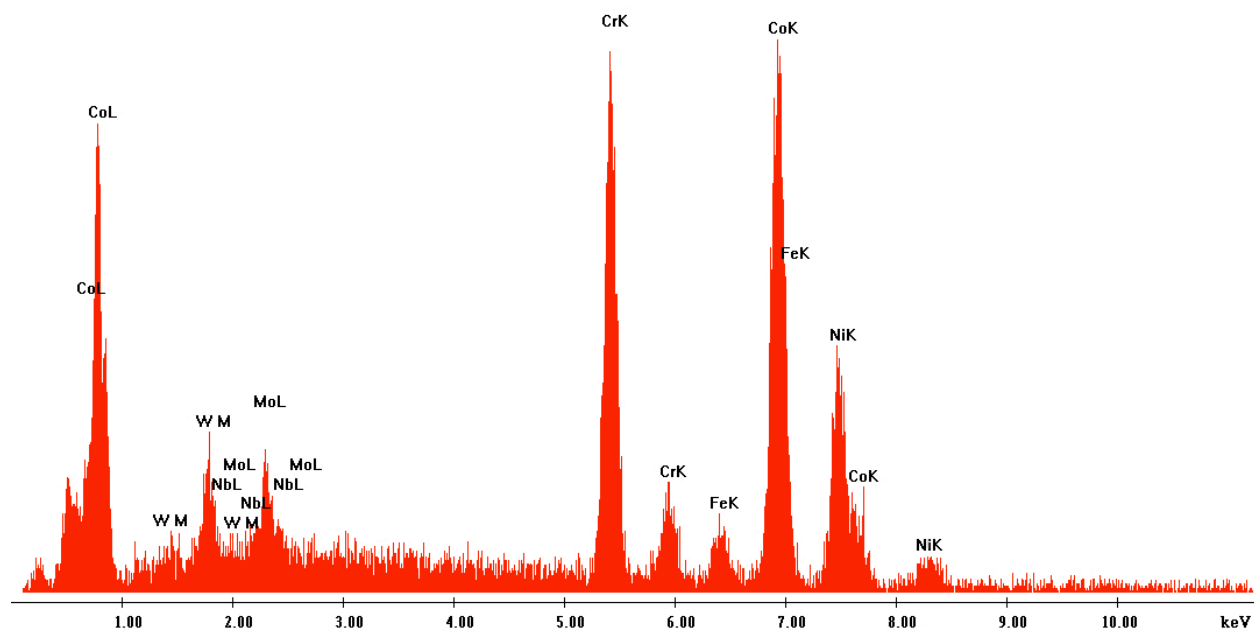


Figure 228. Elemental spectrum collected during EDS analysis of location 12 in figure 208.

Table 10 demonstrates the approximate chemical composition of the microconstituents identified with numbered ovals in figures 215 and 216 (reproduced below); location 13 corresponds to an M_6C carbide, and locations 14 and 15 correspond to Chinese-script carbides. Figures 229-231 demonstrate the qualitative spectrographic data that was also gathered during the elemental microanalysis of these three different locations in the S9 metallographic specimen. Column two of table 10 and figure 229 demonstrate that the M_6C carbide analyzed at location 13 in figure 215 is composed primarily of niobium; other carbide-forming elements, such as chromium, tungsten, and niobium are also present in the chemical composition of this carbide. Columns three and four of table 10, and figures 230 and 231, demonstrate that the Chinese-script carbides analyzed at locations 14 and 15 in figure 216 are composed primarily of niobium and devoid of molybdenum; other carbide-forming elements, such as chromium and tungsten are also present in the chemical composition of these carbides. The presence of manganese, nickel, and cobalt in the chemical composition of these carbides is considered to have emanated from EDS detection of the microstructural matrix.

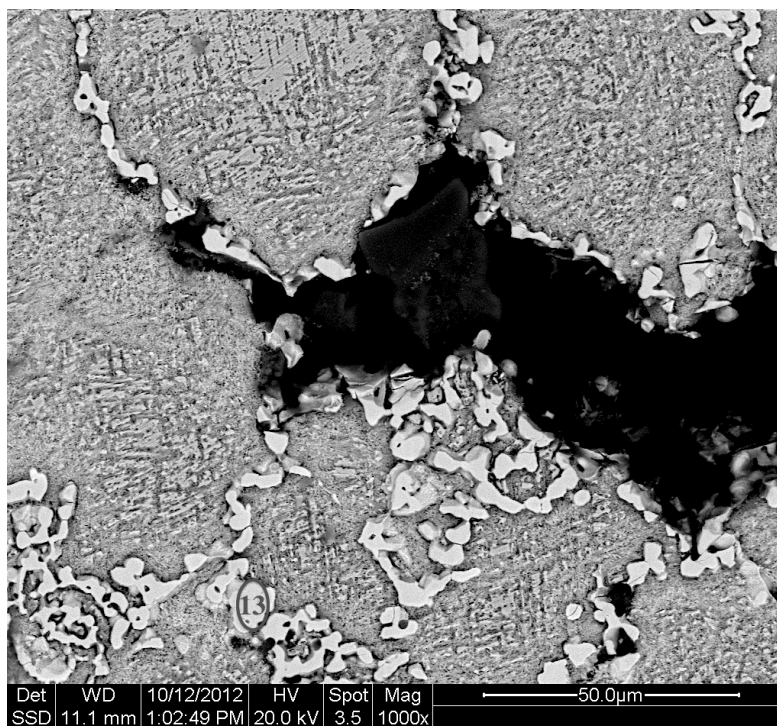


Figure 215. Etched microstructure of specimen S9 (at core); magnification: 1000X. A numbered oval indicates where an EDS analysis was conducted.

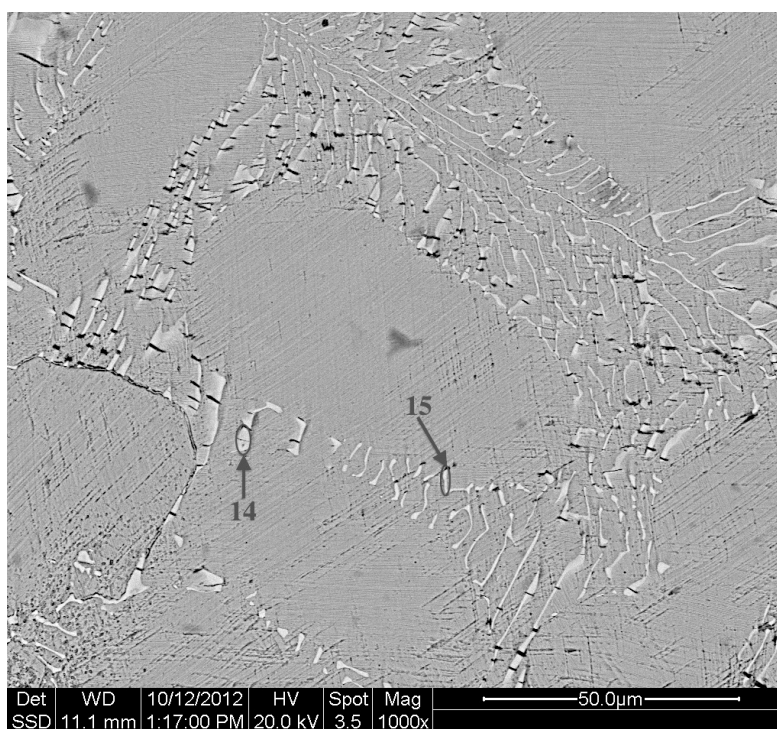


Figure 216. Etched microstructure of specimen S9 (at core); magnification: 1000X. Numbered ovals indicate where EDS analyses were conducted.

Table 10. Approximate chemical composition of microconstituents at different locations in figures 215 and 216.

Element	Wt. (%) Location 13	Wt. (%) Location 14	Wt. (%) Location 15
Manganese	0.52	-	-
Chromium	13.38	2.19	3.84
Nickel	8.87	-	-
Molybdenum	33.44	-	-
Tungsten	10.95	8.08	13.72
Niobium	17.84	87.40	79.36
Iron	-	-	-
Cobalt	15.00	2.34	3.08

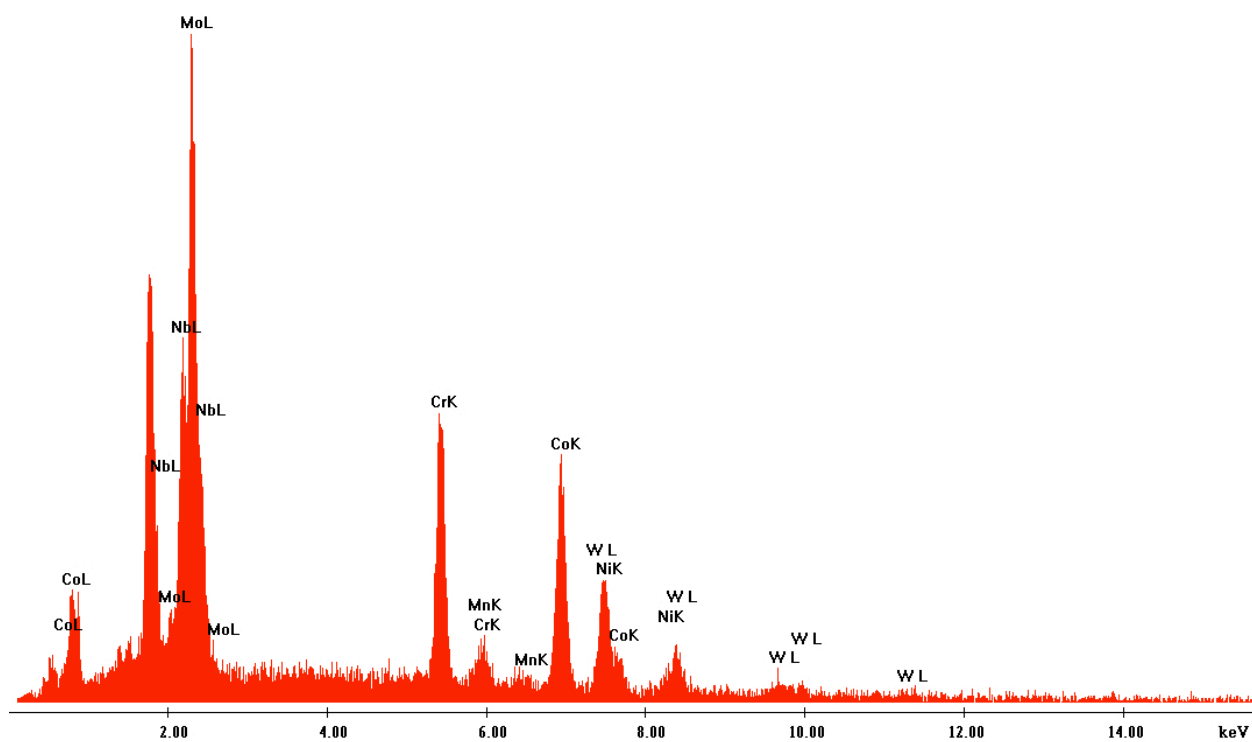


Figure 229. Elemental spectrum collected during EDS analysis of location 13 in figure 215.

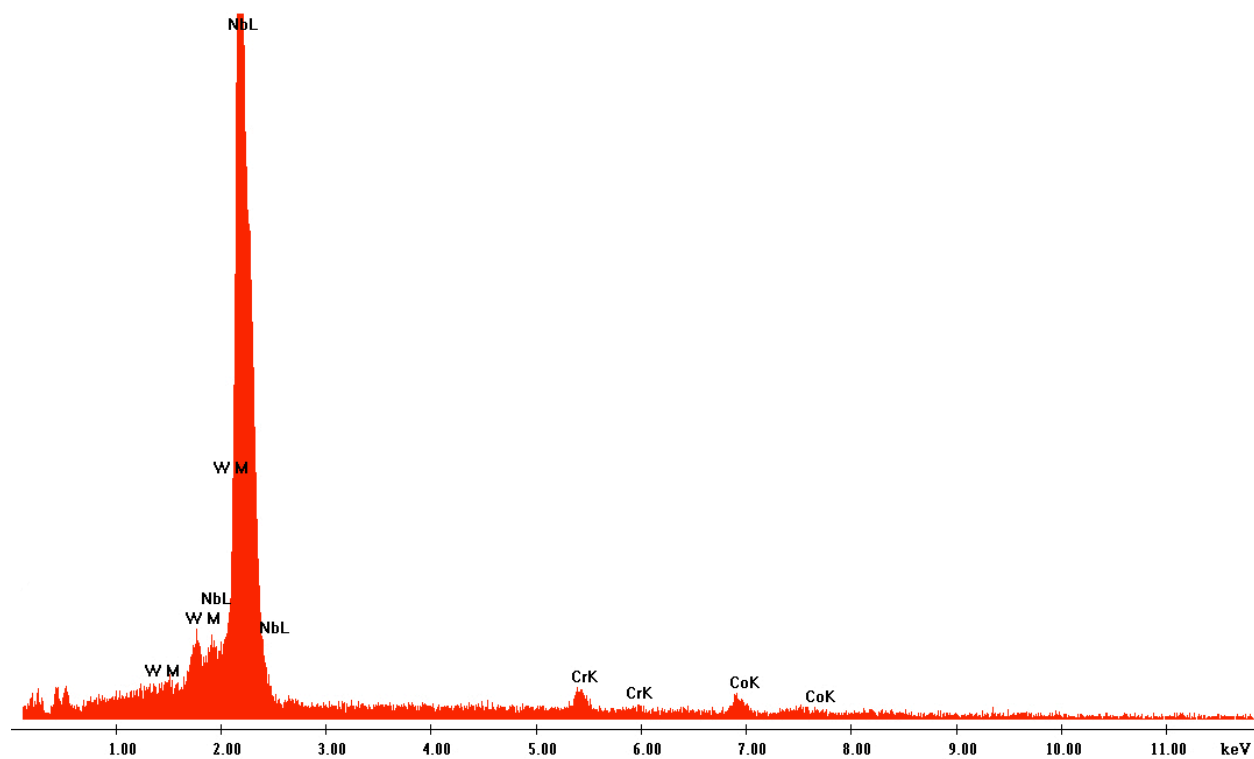


Figure 230. Elemental spectrum collected during EDS analysis of location 14 in figure 216.

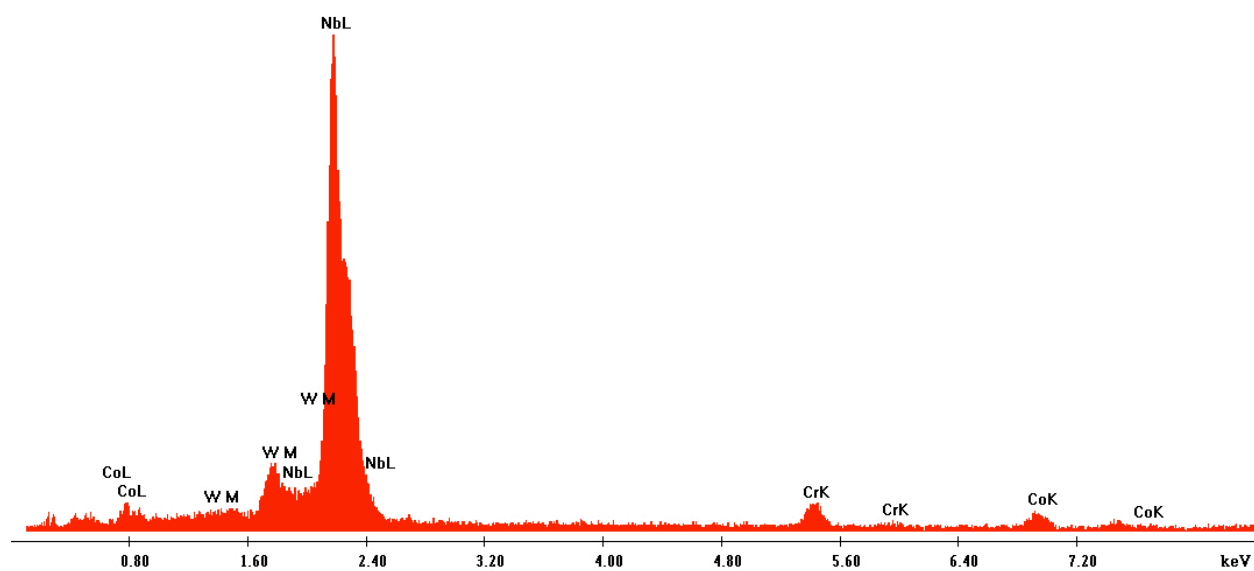


Figure 231. Elemental spectrum collected during EDS analysis of location 15 in figure 216.

3.5 Microhardness Testing

Tables 11 and 12 demonstrates a compilation of the average hardness values (fifteen hardness readings per specimen) of the nineteen metallographic specimens used in this research investigation; table 11 corresponds to the twelve as-received metallographic specimens and table 12 corresponds to metallographic specimens produced from the seven creep-rupture specimens.

Table 11. Compilation of average hardness values of twelve, as-received, metallographic specimens used in research investigation.

Specimen	Hardness (HRC)
1	34.0
2	34.0
3	34.0
4	34.0
5	34.0
6	34.5
7	36.0
8	36.0
9	34.5
10	36.0
11	36.0
12	21.0

Table 11 demonstrates that there is a slight average hardness gradient throughout the longitudinal length of the as-received turbine bucket from set 128. As demonstrated in the figures of Appendix A, this turbine bucket also demonstrated an inter-specimen dendrite size gradient, as specimens from thinner sections exhibited smaller dendrite sizes relative to specimens from

thicker sections. However, as hardness and dendrite/grain size are inversely related, it is interesting that the hardness of specimens from thinner sections (smaller dendrite size) was *slightly less than* the hardness of specimens from thicker sections (larger dendrite size). These observations do not apply to specimen 12, as it demonstrated an average hardness value that was approximately 15 HRC lower than any of the other specimens' average hardness values. This decrease in hardness is consistent with the aforementioned dendrite/grain size-hardness relationship, as specimen 12 demonstrated the largest dendrite size of any of the as-received metallographic specimens (demonstrated in figures 102-105 of Appendix A).

Table 12. Compilation of average hardness values of metallographic specimens produced from seven creep-rupture specimens used in research investigation.

Specimen	Hardness (HRC)	Δ from 35.5 HRC (average hardness of specimens 6-11)
S1	38.0	+ 2.5
S2	36.5	+ 1.0
S4	35.0	-0.5
S5, set 128	41.5	+ 6.0
S5, set 821	44.0	+ 8.5
S7	42.0	+ 6.5
S9	46.0	+ 10.5

Table 12 demonstrates that the average hardnesses of the creep-rupture specimens that were tested at relatively higher temperatures (specimens S1, S2, and S4) are *lower* than the average hardnesses of the creep-rupture specimens that were tested at relatively lower temperatures (specimens S5 (set 128), S5 (set 821), S7, and S9).

The average hardnesses of the creep-rupture specimens (except for specimen S4) were greater than any of the average hardnesses of the as-received metallographic specimens. As the creep-rupture specimens were derived from the same turbine bucket region as that represented by specimens 6-11, column three of table 12 demonstrates the hardness differential in between each of the creep-rupture specimens and the average hardness of specimens 6-11 (calculated to be 35.5 HRC).

3.6 Fractographic Analysis

Figures 232-258 are secondary electron (SE) and back-scattered electron (BSE) images at various magnifications of the fracture surfaces of the seven creep-rupture specimens. Figures 232 and 233 correspond to specimen S1, figures 234-237 correspond to specimen S2, figures 238-240 correspond to specimen S4, figures 241-245 correspond to specimen S5 (set 128), figures 246-249 correspond to specimen S5 (set 821), figures 250-253 correspond to specimen S7, and figures 254-258 correspond to specimen S9.

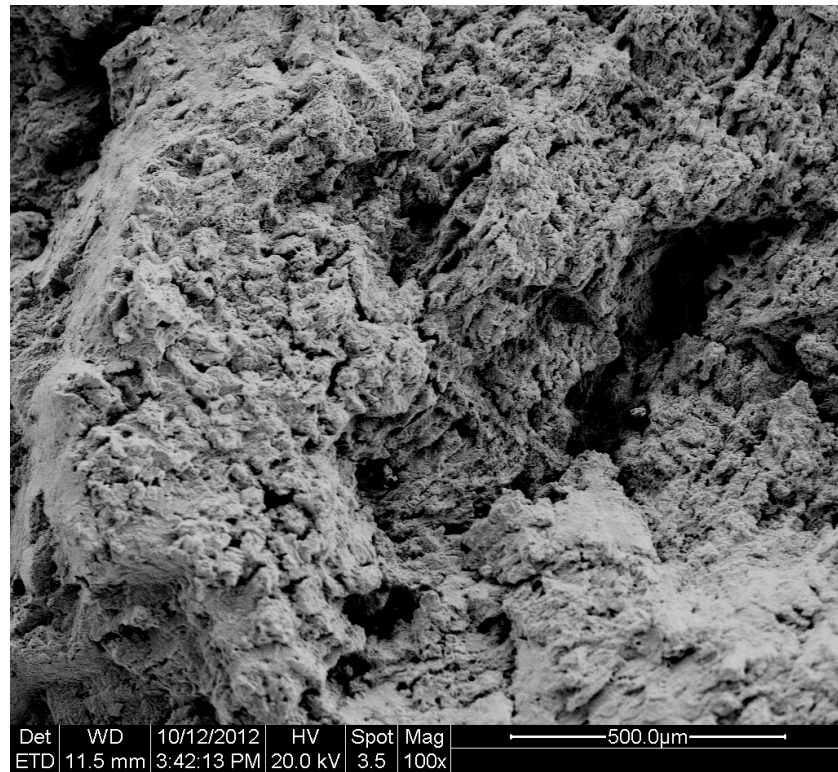


Figure 232. SE image of rupture surface of specimen S1; magnification: 100X.

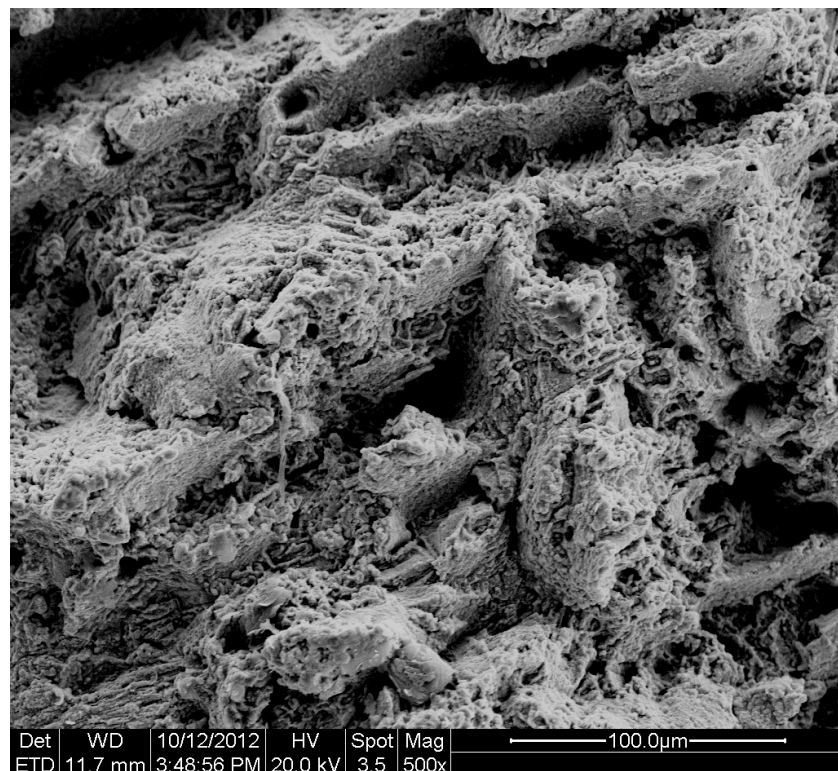


Figure 233. SE image of rupture surface of specimen S1; magnification: 500X.

Figures 232 and 233 demonstrate that specimen S1 fractured along interfacial regions (such as interdendritic and carbide-matrix interfaces), as the rupture surface of the specimen consists mainly of deep, cavernous arrays; this observation is consistent with the results of the metallographic analysis of specimen S1. It is suspected that the resolvability of rupture surface features is diminished in these fractographs as a result of insufficient cleaning prior to SEM viewing of the rupture surface.

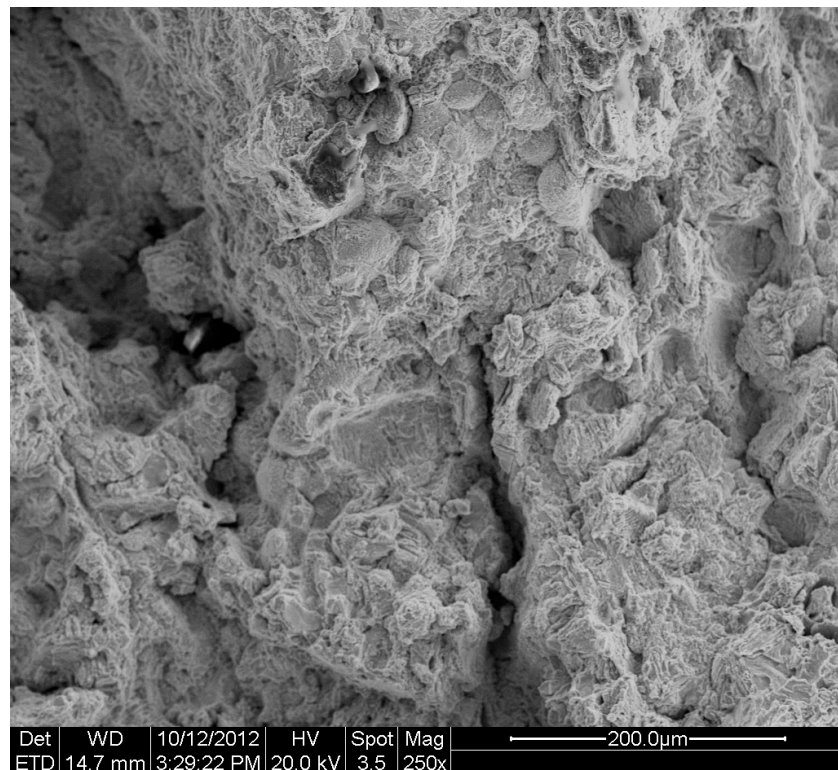


Figure 234. SE image of rupture surface of specimen S2; magnification: 250X.

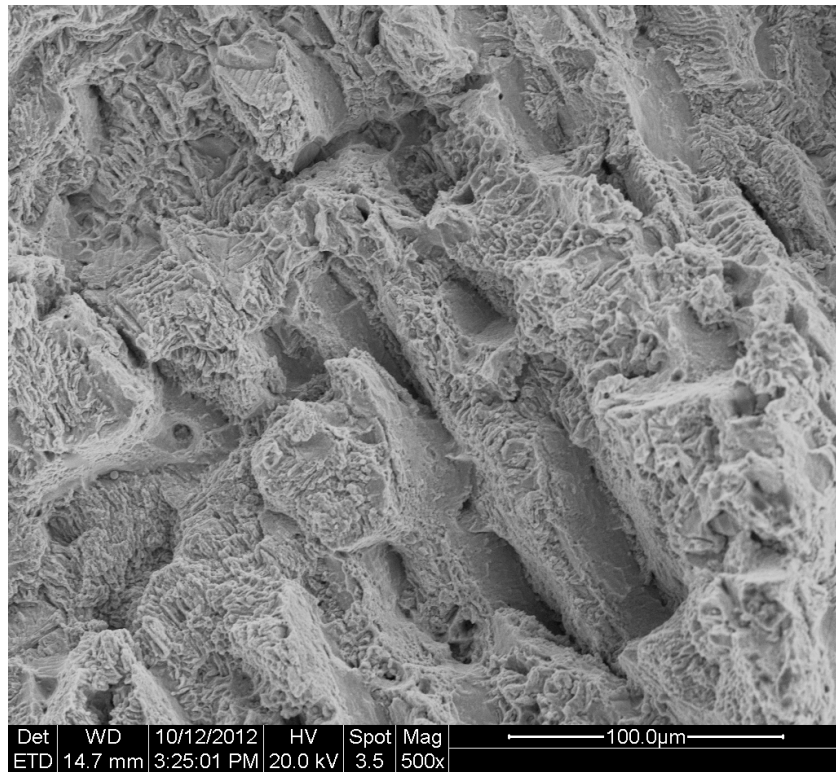


Figure 235. SE image of rupture surface of specimen S2; magnification: 500X.

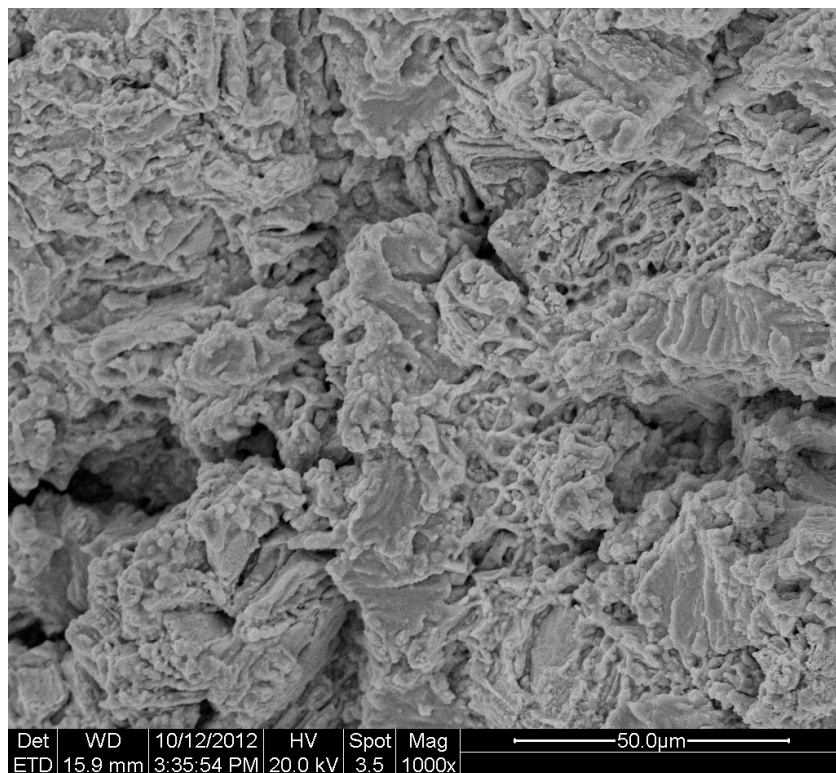


Figure 236. SE image of rupture surface of specimen S2; magnification: 1000X.

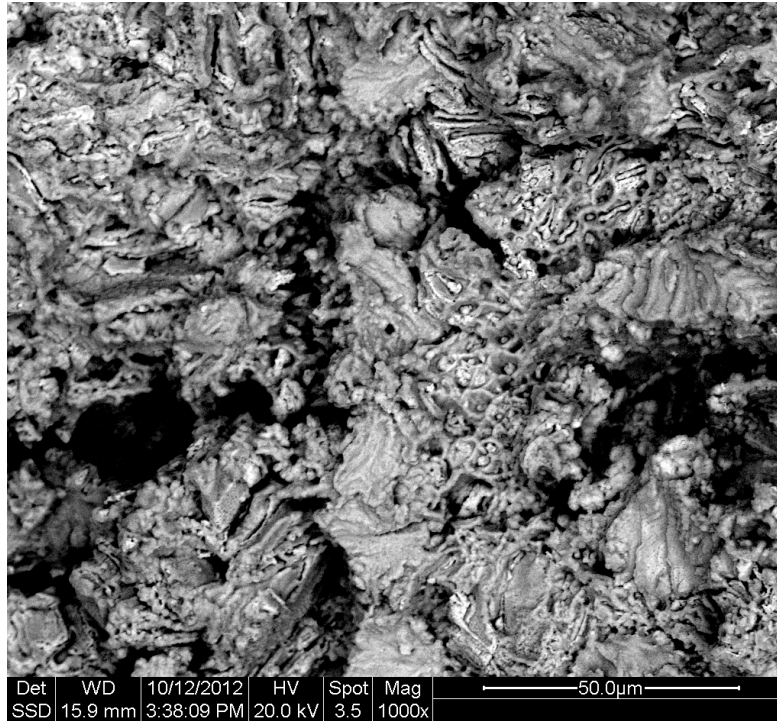


Figure 237. BSE image of rupture surface of specimen S2 (same location as demonstrated in figure 236); magnification 1000X.

Figures 234-237 demonstrate that specimen S2 fractured along interfacial regions (such as interdendritic and carbide-matrix interfaces), as the rupture surface of the specimen consists mainly of deep, cavernous arrays; this observation is consistent with the results of the metallographic analysis of specimen S2. The rupture surface features of specimen S2 are reflective of the various morphologies exhibited by the five different carbides and carbide arrays that were observed metallographically. Figure 237 supports this observation, as atomically-heavy carbides are demonstrated to exist within the cavernous arrays of the rupture surface.

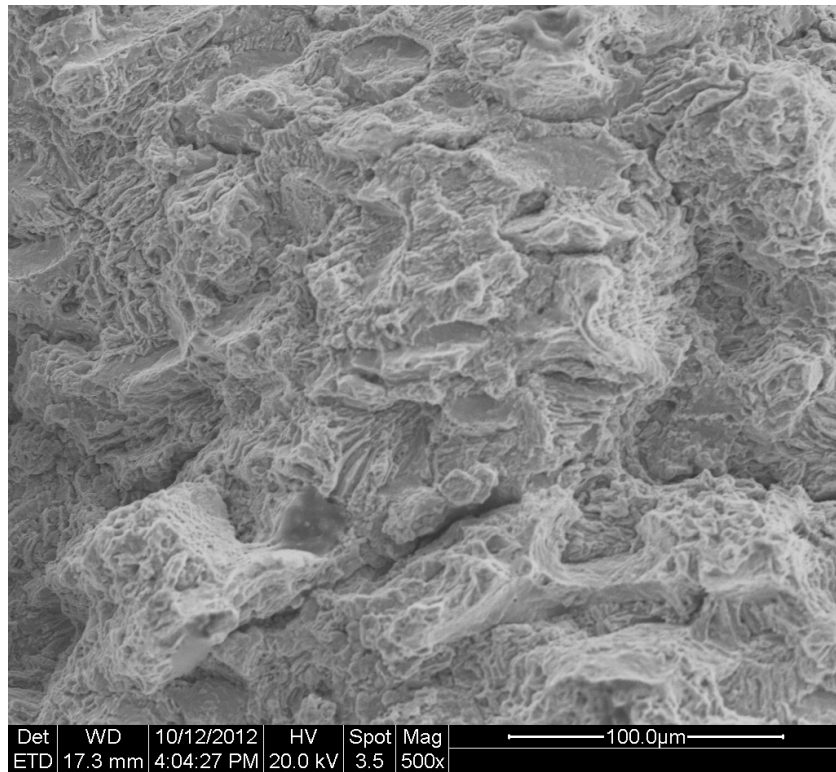


Figure 238. SE image of rupture surface of specimen S4; magnification: 500X.

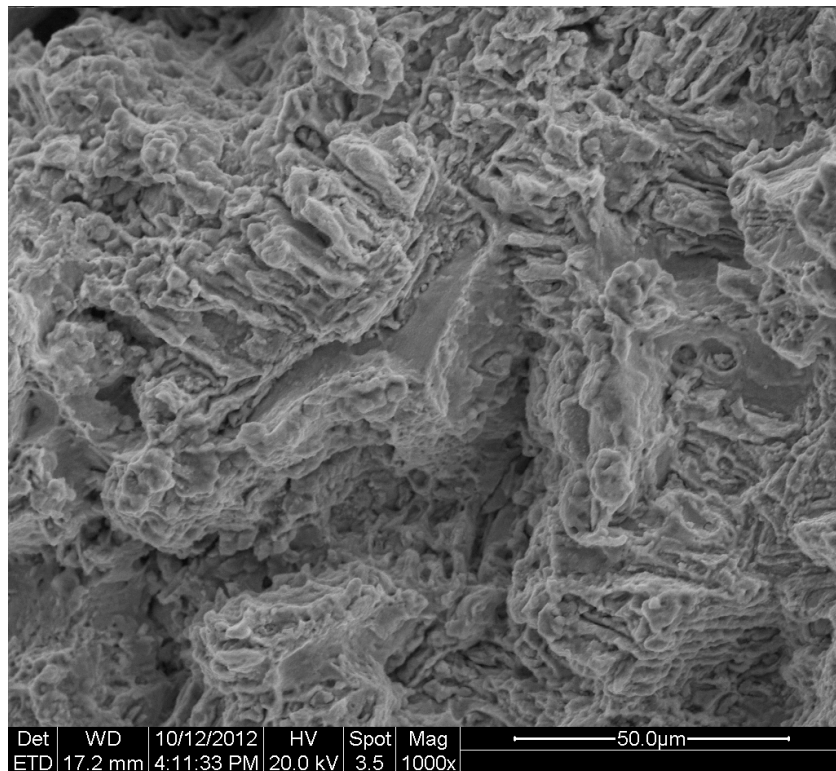


Figure 239. SE image of rupture surface of specimen S4; magnification: 1000X.

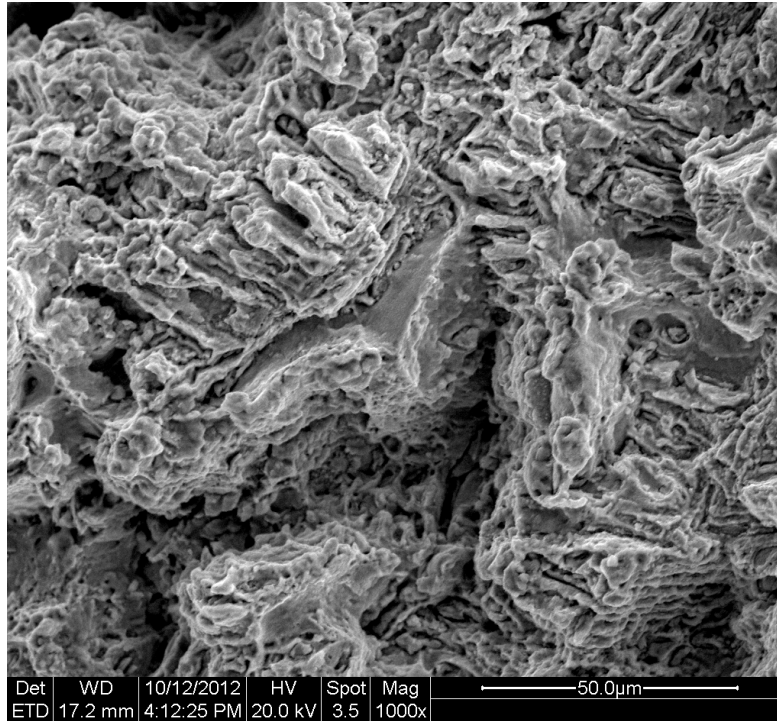


Figure 240. BSE image of rupture surface of specimen S4 (same location as demonstrated in figure 240); magnification: 1000X.

Figures 238-240 demonstrate that specimen S4 fractured along interfacial regions (such as interdendritic and carbide-matrix interfaces), as the rupture surface of the specimen consists mainly of deep, cavernous arrays; this observation is consistent with the results of the metallographic analysis of specimen S4. It is suspected that the resolvability of rupture surface features is diminished in these fractographs as a result of insufficient cleaning prior to SEM viewing of the rupture surface.

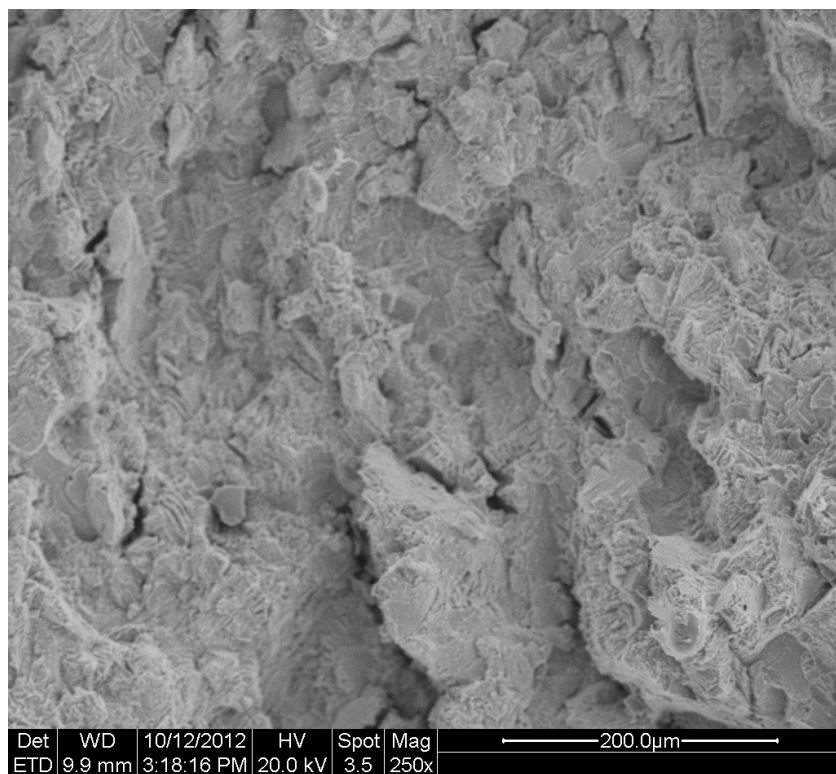


Figure 241. SE image of rupture surface of specimen S5, set 128; magnification: 250X.

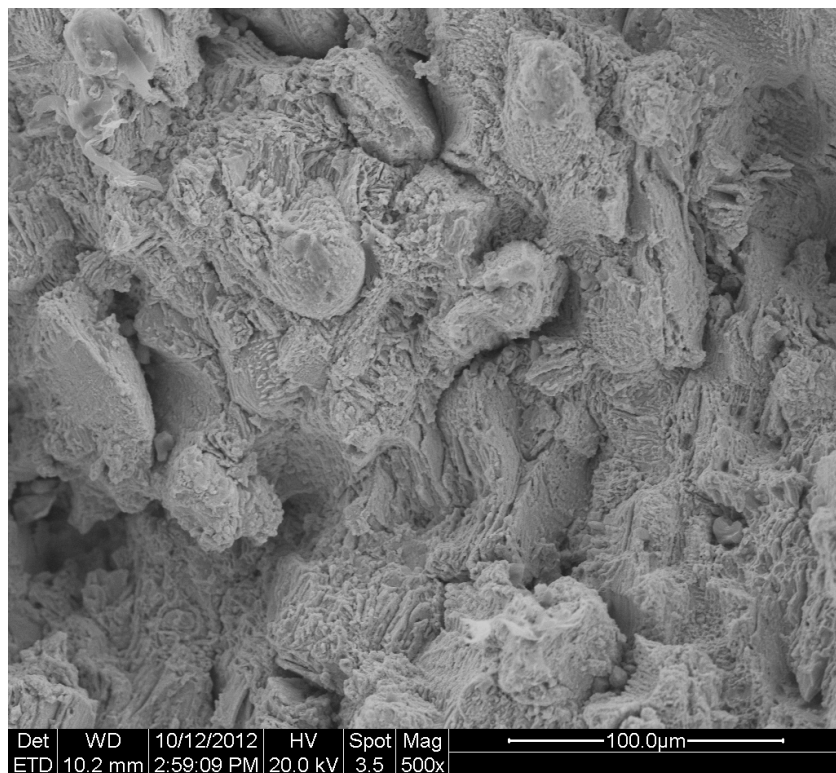


Figure 242. SE image of rupture surface of specimen S5, set 128; magnification: 500X.

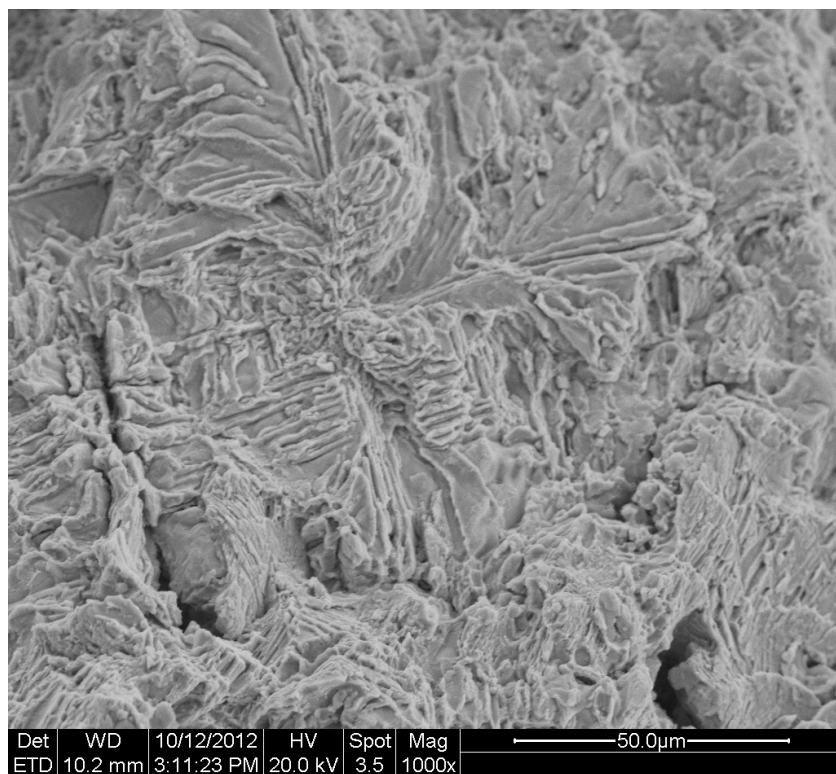


Figure 243. SE image of rupture surface of specimen S5, set 128; magnification: 1000X.

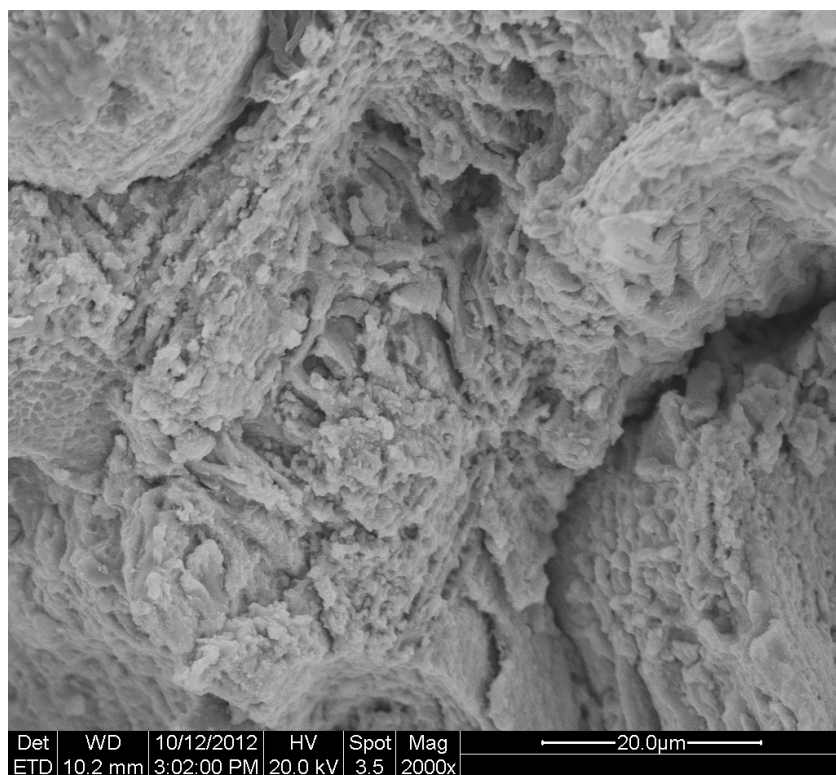


Figure 244. SE image of rupture surface of specimen S5, set 128; magnification: 2000X.

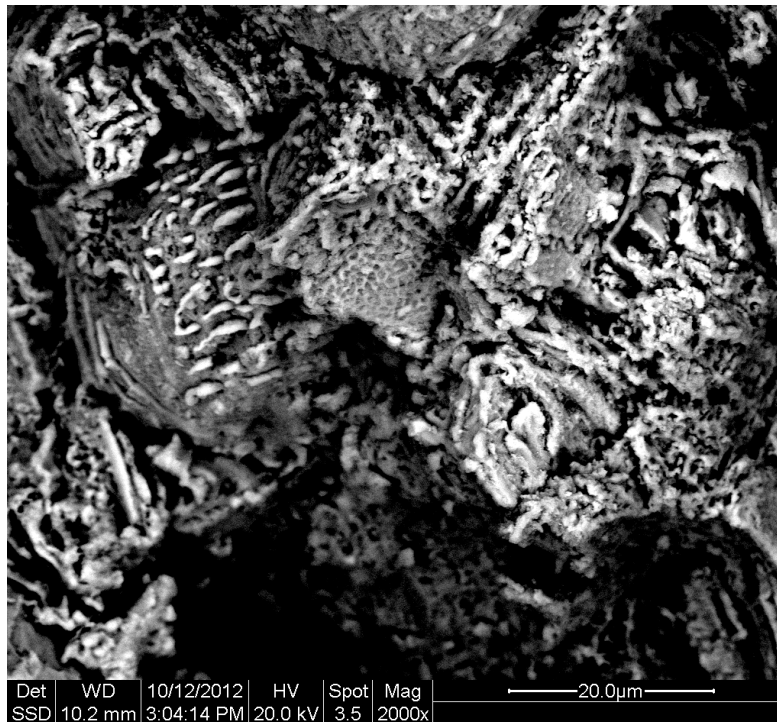


Figure 245. BSE image of rupture surface of specimen S5, set 128 (approximately same location as demonstrated in figure 244); magnification: 2000X.

Figures 241-245 demonstrate that specimen S5 (set 128) fractured along interfacial regions (such as interdendritic and carbide-matrix interfaces), as the rupture surface of the specimen consists mainly of deep, cavernous arrays; this observation is consistent with the results of the metallographic analysis of specimen S5 (set 128). The rupture surface features of specimen S5 (set 128) are reflective of the various morphologies exhibited by the five different carbides and carbide arrays that were observed metallographically. Figure 245 supports this observation, as atomically-heavy carbides are demonstrated to exist within the cavernous arrays of the rupture surface. Additionally, figure 245 demonstrates a small region of dimple rupture at the center of the image, which is indicative of ductile mechanical behavior on behalf of the microstructural matrix.

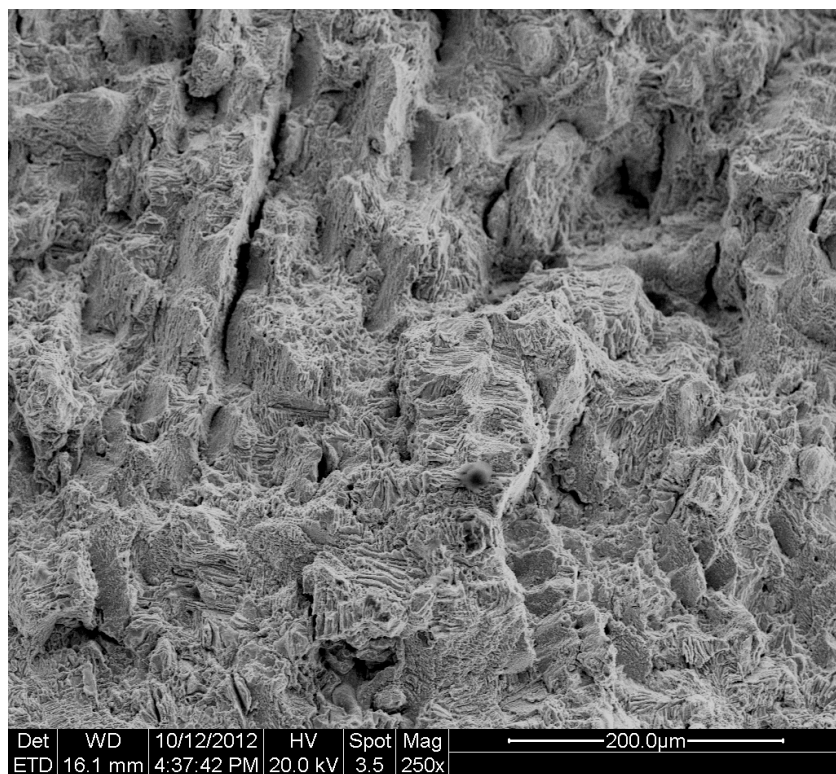


Figure 246. SE image of rupture surface of specimen S5, set 821; magnification: 250X.

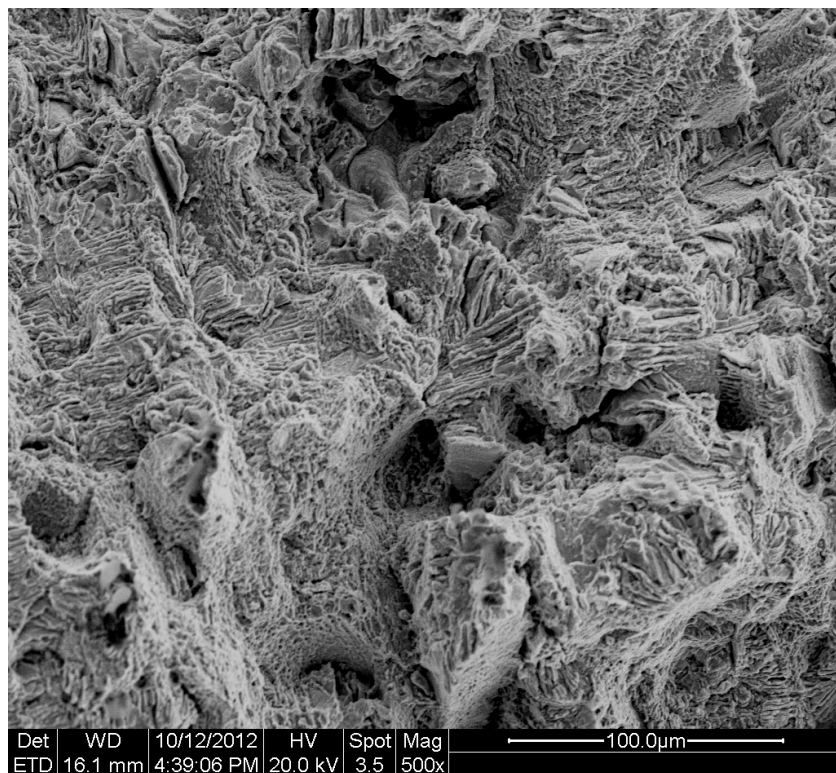


Figure 247. SE image of rupture surface of specimen S5, set 821; magnification: 500X.

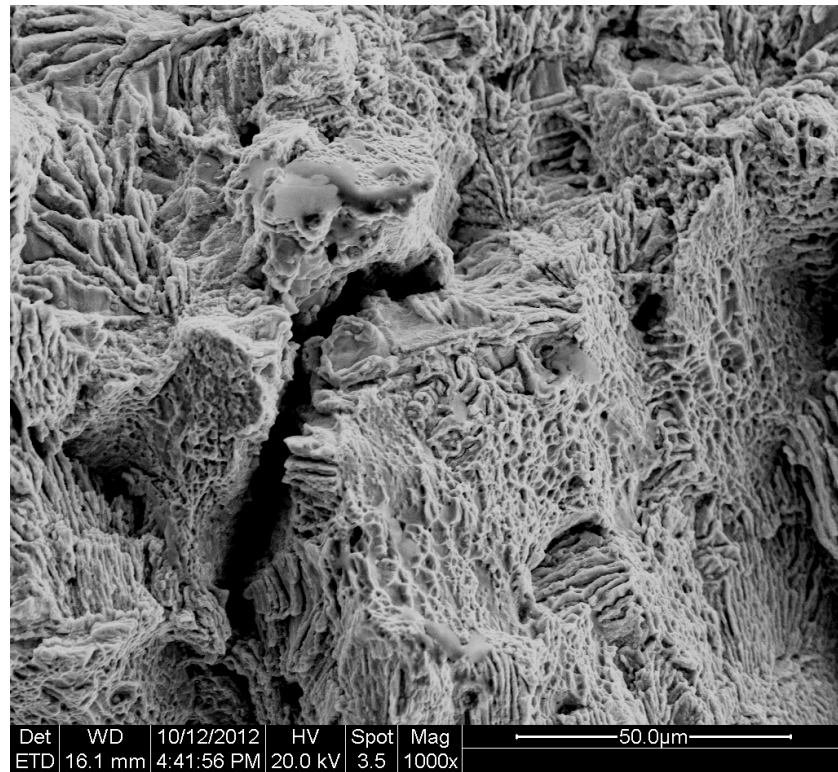


Figure 248. SE image of rupture surface of specimen S5, set 821; magnification: 1000X.

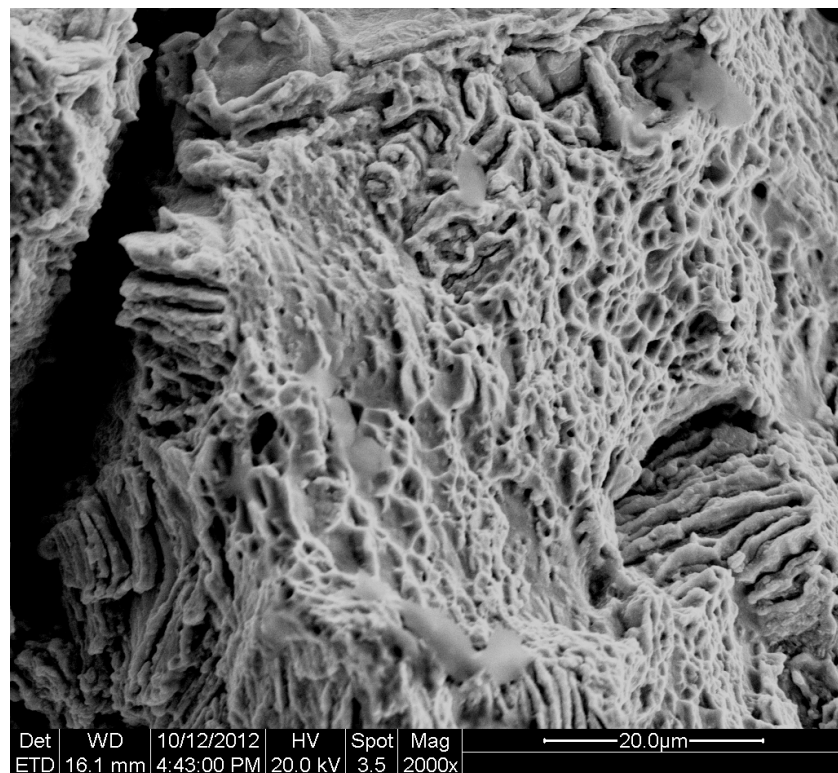


Figure 249. SE image of rupture surface of specimen S5, set 821; magnification: 2000X.

Figures 246-249 demonstrate that specimen S5 (set 821) fractured along interfacial regions (such as interdendritic and carbide-matrix interfaces), as the rupture surface of the specimen consists mainly of deep, cavernous arrays; this observation is consistent with the results of the metallographic analysis of specimen S5 (set 821). The rupture surface features of specimen S5 (set 821) are reflective of the various morphologies exhibited by the five different carbides and carbide arrays that were observed metallographically. Figure 249 explicitly demonstrates a region of dimple rupture, which is indicative of ductile mechanical behavior on behalf of the microstructural matrix.

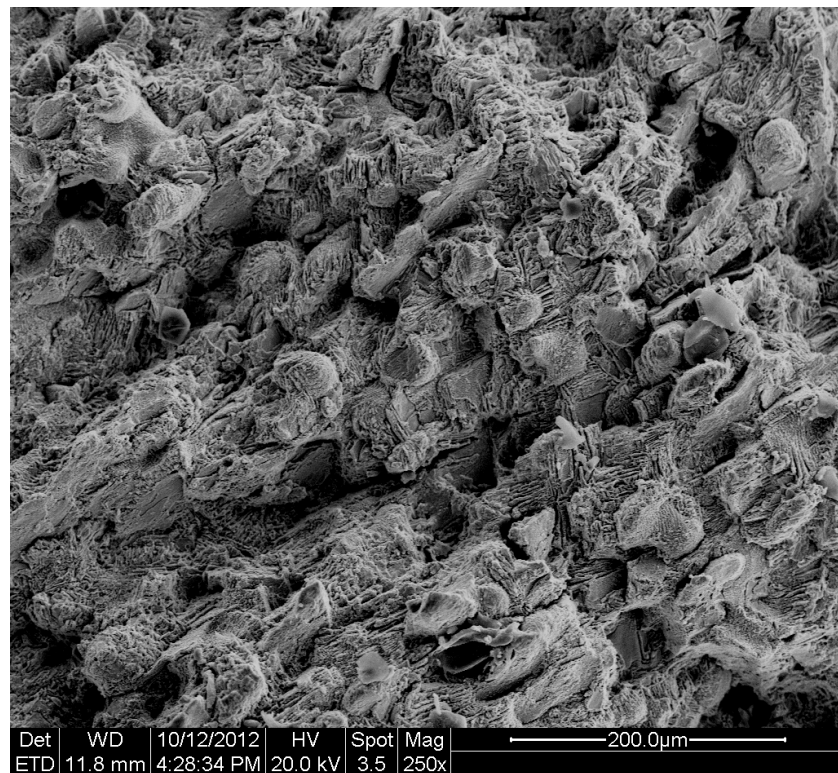


Figure 250. SE image of rupture surface of specimen S7; magnification: 250X.



Figure 251. SE image of rupture surface of specimen S7; magnification: 500X.

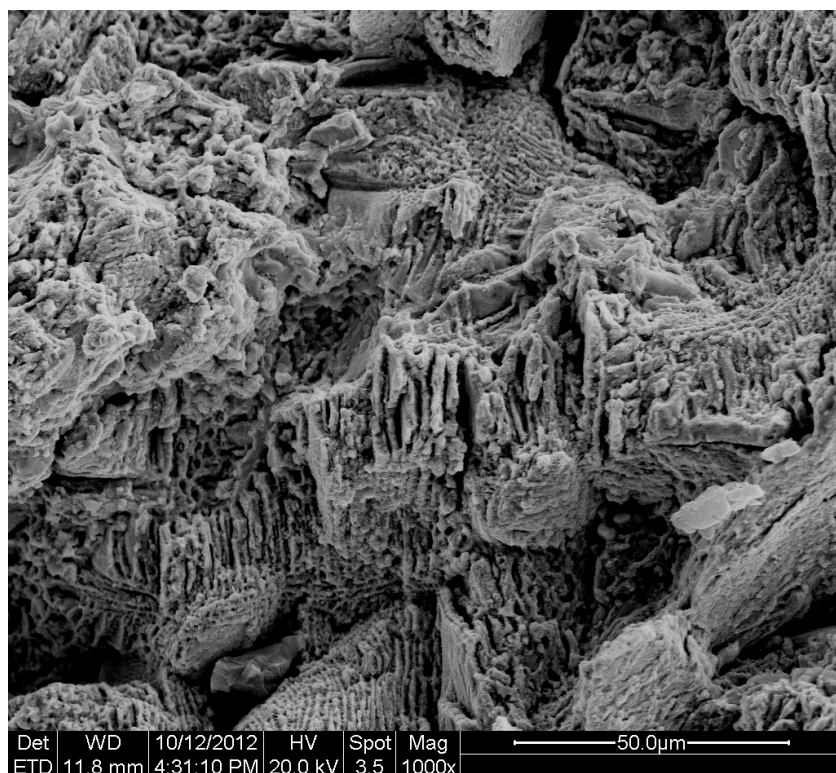


Figure 252. SE image of rupture surface of specimen S7; magnification: 1000X.



Figure 253. SE image of rupture surface of specimen S7; magnification: 2000X.

Figures 250-253 demonstrate that specimen S7 fractured along interfacial regions (such as interdendritic and carbide-matrix interfaces), as the rupture surface of the specimen consists mainly of deep, cavernous arrays; this observation is consistent with the results of the metallographic analysis of specimen S7. The rupture surface features of specimen S7 are reflective of the various morphologies exhibited by the five different carbides and carbide arrays that were observed metallographically.

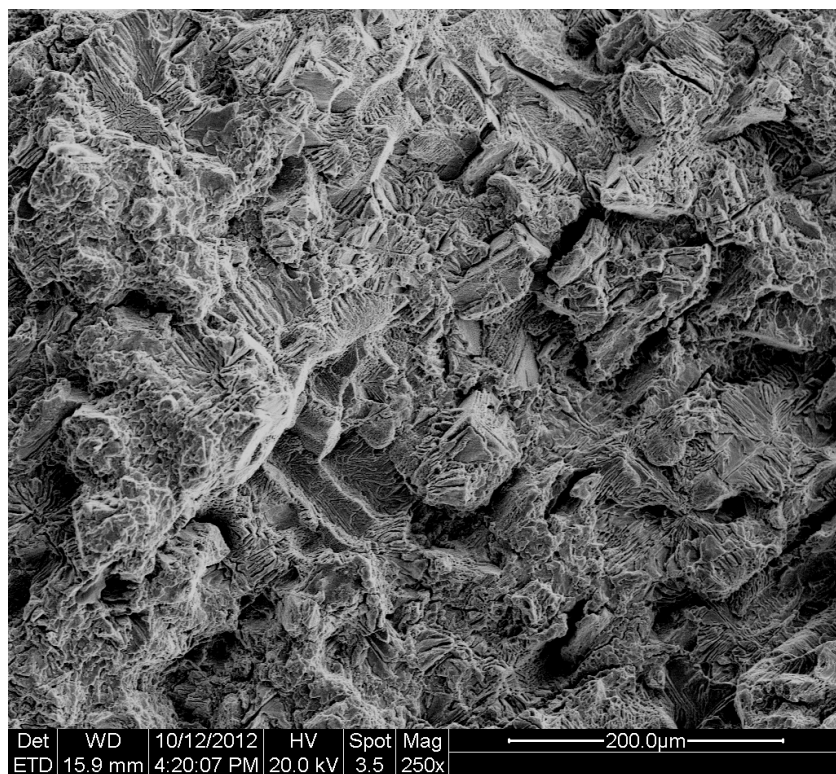


Figure 254. SE image of rupture surface of specimen S9; magnification: 250X.

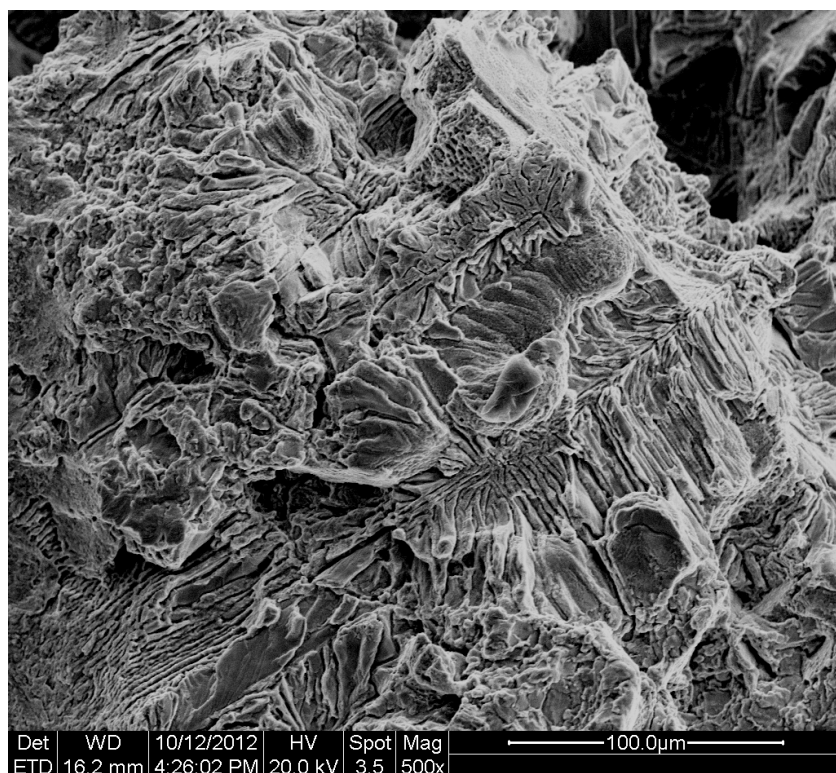


Figure 255. SE image of rupture surface of specimen S9; magnification: 500X.

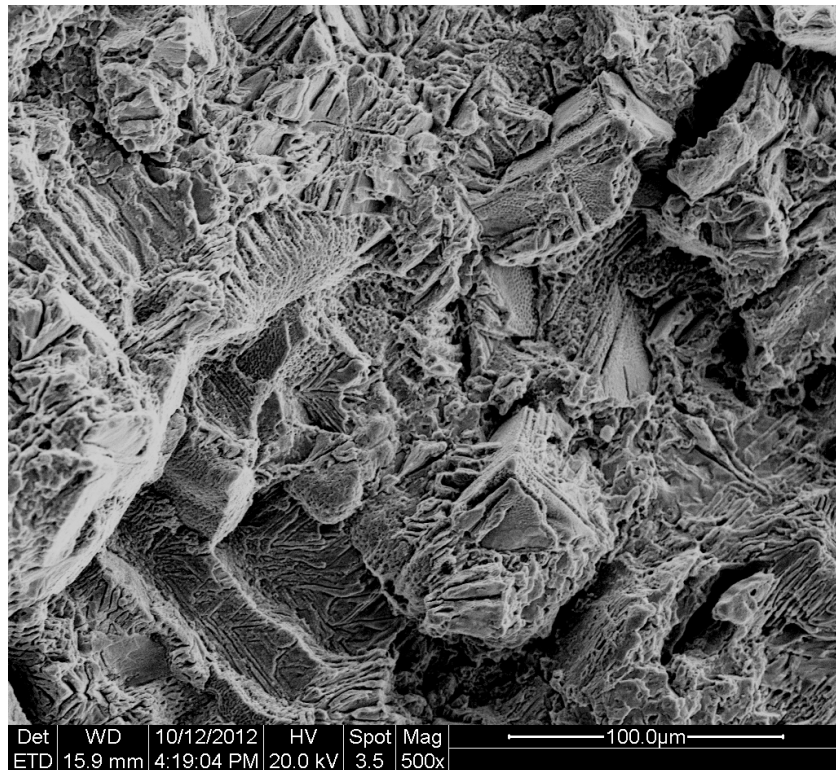


Figure 256. SE image of rupture surface of specimen S9; magnification: 500X.

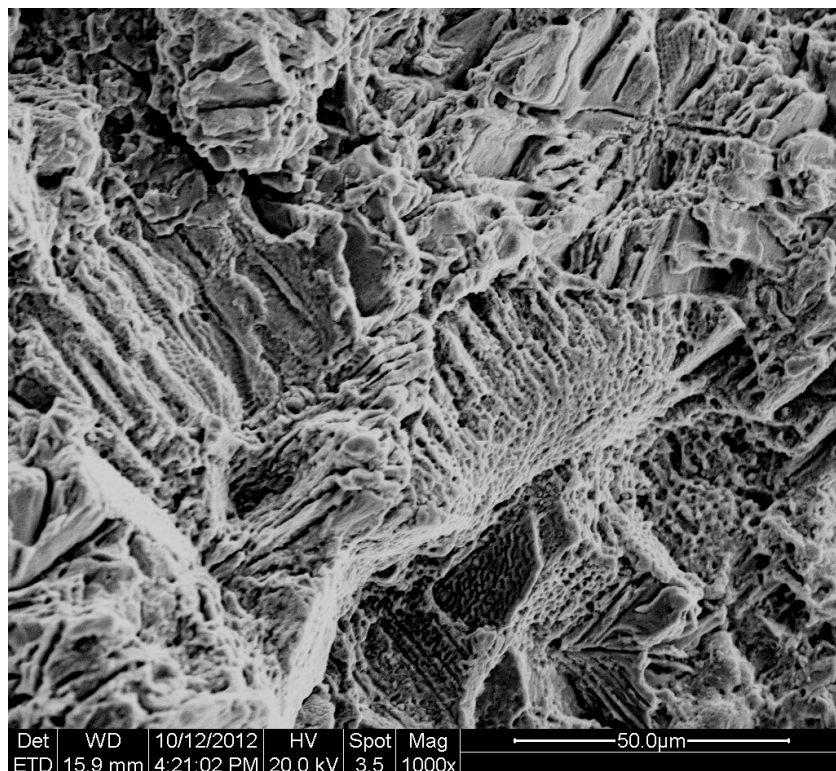


Figure 257. SE image of rupture surface of specimen S9; magnification: 1000X.

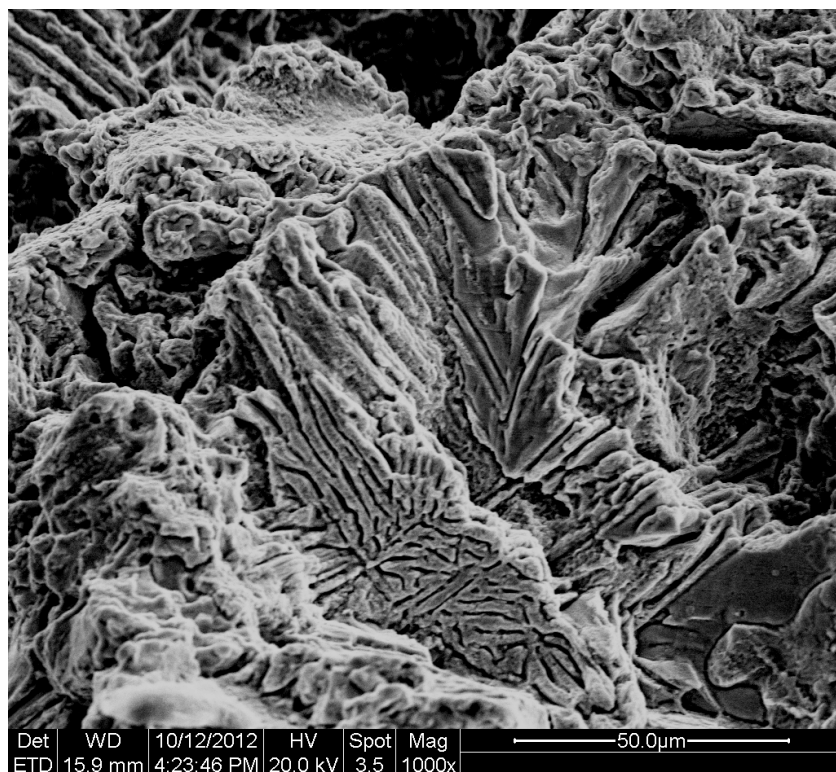


Figure 258. SE image of rupture surface of specimen S9; magnification: 1000X.

Figures 254-258 demonstrate that specimen S9 fractured along interfacial regions (such as interdendritic and carbide-matrix regions), as the rupture surface of the specimen consists mainly of deep, cavernous arrays; this observation is consistent with the results of the metallographic analysis of specimen S9. The rupture surface features of specimen S9 are reflective of the various morphologies exhibited by the five different carbides and carbide arrays that were observed metallographically. Figure 257 demonstrates a region of dimple rupture at the center of the image, which is indicative of ductile mechanical behavior on behalf of the microstructural matrix.

Chapter 4: Discussion

4.1 Post-Rupture Specimen Characterization

All seven creep-rupture specimens demonstrated macroscopic rupture surface features that were granular, textured, and geometrically diverse. As demonstrated in the results of the metallographic and fractographic analysis sections of this manuscript, the topographical diversity of the rupture surfaces emanated from rupture along interfacial regions within the specimens' microstructures, such as interdendritic and carbide-matrix interfaces.

Macro-photographic documentation of the specimens' outer surfaces made it evident that the outer surfaces of the S7 and S9 specimens, which were the specimens that were tested at the lowest of all three temperature regimes (1200 °F), exhibited features that were indicative of abrupt rupture and *diminished* plastic deformation; these features consisted of subtle textured elongation of the specimens' bodies and fine exposed ruptures or bursts along the specimens' bodies. The presence of these features (or lack thereof) was considered relatively diminished when compared to that exhibited by specimens S1, S2, S4, S5 (set 128), and S5 (set 821), which were the specimens that were tested at higher temperature regimes (1350, 1500, and 1650 °F). In a similar fashion, the figures of Appendix B demonstrated that the microstructures of specimens S7 and S9 exhibited a relative decrease in the presence of creep voids and ruptures, when compared to the other specimens' microstructures.

4.2 Creep-Rupture Data Analysis

The reference data from ASTM Special Technical Publication No. 160 [6] emanated from *new* S-816 specimens (no prior exposure to service conditions) that were either in wrought or sheet form; additionally, all of these specimens were solutionized, quenched, and aged, prior to

being tested. As the S-816 turbine buckets that were used to produce the creep-rupture specimens were *cast* components, the appropriateness of comparing the reference data from ASTM Special Technical Publication No. 160 [6] and the data produced as a result of this research investigation was questionable; this was the case until a reference for the creep-rupture properties of new, cast S-816 material was discovered (Sulzer Turbo Services, personal communication, October 2nd, 2012). This reference only allowed for individual data points to be established for creep-rupture life of new, cast S-816 material at 1,000 hours throughout the 1200, 1350, and 1500 °F temperature regimes. Figure 50 establishes that the creep-rupture lives of new, wrought and new, cast S-816 material are not largely different. The 1,000-hour creep-rupture lives of the *cast* S-816 material at 1200 and 1500 °F are slightly decreased, when compared to those of the wrought S-816 material; however, the 1,000-hour creep-rupture life of the cast S-816 material at 1350 °F is slightly increased, when compared to that of the wrought S-816 material.

The creep-rupture data that was produced as result of this research investigation, when compared to the reference creep-rupture data that was derived from new, wrought S-816 material, indicates the following:

- The post-service, creep-rupture life of the turbine buckets, at the 1200 °F temperature regime, is suggested to be severely diminished. Even though two reference points cannot establish a statistically significant observation, the slope of the creep-rupture curve for the 1200 °F temperature regime suggests that the creep-rupture life of the overhauled turbine buckets is compromised at this service temperature.
- The post-service, creep-rupture life of the turbine buckets, at the 1350 and 1500 °F temperature regimes is suggested to be relatively unaffected. Even though two reference points cannot

establish a statistically significant observation, the slopes of the creep-rupture curves for the 1350 and 1500 °F temperature regimes suggests that the creep-rupture life of the overhauled turbine buckets would not be compromised at these service temperatures.

Within the three temperature regimes that were chosen for creep-rupture testing, the specimens' times to rupture decreased upon the application of larger loads; that is, specimen S1 exhibited a longer time to rupture than specimen S2, specimen S5 (set 128) exhibited a longer time to rupture than specimen S5 (set 821), and specimen S7 exhibited a longer time to rupture than specimen S9—this is consistent with classically defined creep-rupture behavior of elevated-temperature components. Additionally, the specimens' deformation vs. time to rupture plots all demonstrated varied degrees of secondary and tertiary creep behavior (except for the specimen S5 (set 128) plot). The classical nature of these results attributes a sense of validity to the creep-rupture testing procedures that were conducted as part of this research investigation.

It is interesting to note that the S5 (set 821) and S9 specimens, which were the specimens that were tested at the highest stresses (relative to the other specimens in their respective temperature regimes), exhibited all three stages of classically defined creep behavior in their deformation vs. time to rupture plots. This, in combination with the fact that all of the other specimens' deformation vs. time to rupture plots (except for the specimen S5 (set 128) plot) demonstrated varied degrees of secondary and tertiary creep behavior, is suggestive of the existence of residual, post-service creep-rupture properties within the turbine buckets used for this research investigation. This observation is put into context if one considers the possibility that all of the creep-rupture specimens (tested at the same varied parameters) could have exhibited tertiary creep behavior at the immediate onset of testing; in this hypothetical scenario,

it would have been quite evident that the turbine buckets contained little to no residual, post-service creep-rupture properties.

Finally, a difference in the specimens' elongation at rupture was observed across the three temperature regimes that were chosen for creep-rupture testing. The largest elongation percentages corresponded to specimens S5 (set 128 and 821), which were tested at 1350 °F. The second-largest elongation percentages corresponded to specimens S1 and S2, which were tested at 1500 °F. The smallest elongation percentages corresponded to specimens S7 and S9, which were tested at 1200 °F.

4.3 Metallographic Analysis

Several aspects of the microstructural phenomena associated with the degradation and alteration of Co-base superalloys as a result of long-term exposure to elevated-temperature service conditions were observed to have occurred in the microstructures of both the as-received and creep-rupture specimens. In particular, the following microstructural features were observed and documented:

- primary MC carbide decomposition in both as-received and creep-rupture specimens, resulting in agglomeration of M_6C and filming of $M_{23}C_6$ carbides along interdendritic regions.
- the formation of two types of intra-dendritic, pseudoeutectic $M_{23}C_6$ carbide + matrix arrays in both as-received and creep-rupture specimens; one type of array exhibited $M_{23}C_6$ with a cellular morphology while the other type of array exhibited $M_{23}C_6$ with a lath morphology.
- the formation of the topologically-close-packed (TCP) Laves phase in both as-received and creep-rupture specimens.

- in the creep rupture specimens, the formation of the largest creep ruptures were observed to have occurred in regions immediately adjacent to agglomerated M_6C carbides. Creep voids and ruptures were observed to have occurred at interfacial carbide-matrix regions.
- internal fracture of and void formation within the MC, Chinese-script, and M_6C carbides (in the creep-rupture specimens.)

The fine, acicular microconstituent that was identified as the TCP Laves phase was characterized by its resemblance to the TCP Laves phase plates that have been documented in the S-816 alloy [2]. However, a more definitive method of characterization could have been performed, such as analysis via transmission electron microscopy; this type of microstructural characterization is suggested to be undertaken by future research investigations. The angled morphology of this fine, acicular microconstituent resembles that of stacking faults, which have been known to exist in Co-base superalloys [2]. However, the size of this acicular microconstituent is not consistent with what is expected of stacking faults, as they are microstructural *lattice* defects that operate on significantly smaller scales.

The prevalence and size of the M_6C carbide agglomeration regions (relative to the other microconstituents) throughout the microstructures of the creep-rupture specimens are the primary factors that induced the formation of the largest creep ruptures in regions immediately adjacent to agglomerated M_6C carbides. As noted earlier in chapter 1, section 1.6 of this manuscript, primary MC and Chinese-script carbides are representative of the most incoherent carbides/precipitates that can exist in an FCC microstructural matrix; additionally, secondary carbides that form as a result of primary carbide decomposition (such as M_6C and $M_{23}C_6$) are representative of carbides/precipitates that are relatively more coherent in an FCC microstructural matrix. Despite

this, however, the *size* of the M_6C carbide agglomeration regions allowed for a greater degree of incoherency (relative to the MC and Chinese-script carbides) in the microstructure of the S-816 creep-rupture specimens, thus allowing for preferential nucleation and growth of creep voids and ruptures at these regions.

Creep rupture of the seven specimens used in this research investigation was metallographically observed to have occurred along interdendritic or interfacial carbide-matrix regions. These high-energy, high-strain regions allowed for the nucleation and growth of creep voids and ruptures, thus providing paths for energetically-favored decohesion and rupture.

4.4 Energy Dispersive X-ray Spectroscopy

The elemental changes of MC and Chinese-script carbides, as they decomposed into M_6C carbides, was documented. It was established that MC and Chinese-script carbides were niobium-rich and contained little to no amounts of molybdenum; in the process of decomposing, the presence of niobium in the MC and Chinese-script carbides was significantly decreased, which was replaced by the increased presence of molybdenum and other carbide-forming elements (such as tungsten and chromium).

Elemental microanalysis of the microstructural matrix at individual locations within two creep-rupture specimens demonstrated that the concentrations of molybdenum and tungsten (especially) were increased, and the presence of niobium was decreased, with respect to their elemental ranges specified for S-816. The relative increase in the presence of tungsten in the matrix, with respect to molybdenum, is suggestive of the effect from the predominance in molybdenum content of the M_6C carbides; that is, as tungsten was not dominant in the chemical composition of the M_6C carbides, it increased its presence in the matrix as a solid-solution

strengtheners. The relative decrease in the presence of niobium is attributed to the fact that it is the primary MC and Chinese-script carbide former in the S-816 alloy, and thus was elementally concentrated in regions adjacent to or on MC and Chinese-script carbides and not isolated regions of the microstructural matrix.

4.5 Microhardness Testing

The peculiar, small hardness differential that was demonstrated to exist across the longitudinal length of the as-received turbine bucket from set 128 is not readily understood. However, as demonstrated in the figures of Appendix A, there were no visible microstructural differences in between the metallographic specimens from the leading edge and those from the thicker end (except for a difference in dendrite size, which was previously established and discussed) that could indicate why this hardness gradient exists.

It is well known that the leading edges of turbine bucket components experience the greatest stresses, temperatures, and temperature gradients; as a result, these sections experience a greater degree of microstructural decay, relative to the thicker sections of turbine bucket components. As established by the metallographic and EDS analysis sections of this manuscript, the microstructural decay of the as-received S-816 turbine bucket manifested itself in the form of carbide decomposition and agglomeration at interdendritic regions, which in turn led to depletion of the microstructural matrix of solid-solution strengthening elements, such as molybdenum and niobium. Hence, systematic, microstructural characterization via EDS of the as-received metallographic specimens is suggested to be undertaken by future research investigations; this would confirm or deny the speculation that the matrix of leading edge sections of the turbine

buckets had been depleted of solid-solution strengthening elements as a consequence of long-term exposure to elevated-temperature service conditions.

The increase in average hardness of the creep-rupture specimens (except for specimen S4) relative to the average hardness of specimens 6-11 (which is representative of the turbine bucket section from which the specimens were derived), indicates that creep-rupture testing induced microstructural changes that subsequently increased the hardness of the creep-rupture specimens (except for specimen S4). Given the short duration of the different creep-ruptures tests, relative to the 100,000 service hours experienced by the creep-rupture specimens, it is not expected that a significant degree of carbide agglomeration and precipitation occurred during testing, which could account for the observed increase in hardness of the creep-rupture specimens. However, it is expected that dislocation densities increased within the creep-rupture specimens, as result of dendrite boundary sliding , and the nucleation and growth of creep voids/ruptures, during testing.

4.6 Fractographic Analysis

The seven specimens' rupture surfaces were observed to demonstrate that fracture occurred along interfacial regions (such as interdendritic and carbide-matrix interfaces), as the rupture surfaces consisted mainly of deep, cavernous arrays; these observations are consistent with the results of the metallographic analysis sections of this manuscript. The rupture surface features of specimen were reflective of the various morphologies exhibited by the five different carbides and carbide arrays that were observed metallographically. Atomically-heavy carbides were demonstrated to exist within the cavernous arrays of the rupture surfaces of specimens S2 and S5 (set 128) . Additionally, regions of dimple rupture were discernible in the rupture surfaces

of specimens S5 (set 128 and 821) and S9 , which is indicative of ductile mechanical behavior on behalf of the microstructural matrix.

Chapter 5: Conclusions

This research investigation proposed to answer the following questions:

1. what is the actual condition of the turbine buckets that have reached the end of the manufacturer's service life?
2. can the manufacturer's service life be extended?
3. what possibilities exist for re-furbishing the buckets and re-using them?

In order to address the first question, as-received characterization via metallographic analysis and microhardness testing was conducted on specimens produced from an overhauled turbine bucket from set 128. It is concluded that the microstructural state of the turbine bucket was altered and degraded, as a result of long-term exposure to elevated-temperature service conditions. It is also concluded that the average hardness of this turbine bucket was in keeping with expected values for the S-816 alloy.

In order to address the second question, creep-rupture testing was conducted on specimens derived from overhauled turbine buckets from bucket sets 128 and 821, both of which had experienced more than 100,000 hours in elevated-temperature service conditions. Post-rupture specimen characterization was conducted via macro-photographic documentation, metallographic analysis via OM, SEM, and EDS, and fractographic analysis via SEM; the creep-rupture data that was gathered during the testing of the different specimens was also analyzed. It is concluded that the creep-rupture data gathered in the course of this research investigation is *suggestive* of the existence of residual, post-service creep-rupture properties within the turbine buckets used for this research investigation.

The metallographic, EDS, and fractographic methods used to characterize the creep-rupture specimens establish the conclusion that the specimens did indeed fail by creep rupture; additionally, creep void nucleation and growth, and creep rupture, occurred along interfacial regions within the specimens' microstructures (such as interdendritic and carbide-matrix interfaces). In particular, metallographic analysis of the as-received and creep-rupture specimens was conclusive in characterizing and documenting the following microstructural features, which are indicative of the deleterious effects (and associated microstructural phenomena) of long-term exposure to elevated-temperature service conditions:

- primary MC carbide decomposition, which resulted in the agglomeration of M_6C and $M_{23}C_6$ carbides along interdendritic regions.
- the formation of two types of intra-dendritic, pseudoeutectic $M_{23}C_6$ carbide + matrix arrays.
- the formation of the TCP Laves phase.
- internal fracture of and void formation within the MC, Chinese-script, and M_6C carbides (in the creep-rupture specimens.)

The largest creep ruptures within the creep-rupture specimens' microstructures occurred adjacent to regions of carbide decomposition/agglomeration; the preponderance of these regions throughout the specimens' microstructures is directly attributed to the aforementioned, degraded microstructural state of the specimens' as-received condition.

As the manufacturer's service life for the turbine buckets used in this research investigation was 60,000 service hours, the fact that they were in use for more than 100,000 service hours is a testament to the excellent elevated-temperature properties of the Co-base, S-816 superalloy. The creep-rupture data gathered in the course of this research investigation is

conclusive in demonstrating that the manufacturer's service life *can be* extended to a maximum of 100,000 service hours, as the specimens tested did not exhibit extremely diminished creep-rupture properties.

The possibilities that exist for refurbishment and re-use of the turbine buckets used in this research investigation (those that were not tested) involve adequate application of resolutionization and aging heat treatments; these heat-treatment practices, in combination with dimensional and fluorescent dye inspections, have been extensively used by companies that are in the business of providing refurbished turbine components (S. Stafford, personal communication, May 5th, 2011). However, refurbishment and re-use of these turbine buckets would be recommended only once, as the work by E. Lvova [18] indicates that the same level of achievable elevated-temperature properties cannot be consistently produced upon the application of multiple rejuvenation procedures to the same components. In this work, the microstructural degradation and alteration of a rejuvenated component is demonstrated to have occurred more rapidly, relative to a new component that was exposed to the same service conditions. The accelerated aging exhibited by the rejuvenated component was directly correlated to the increased presence of carbon and carbide-forming elements in the component's microstructural matrix; during the application of the rejuvenation heat treatment, these alterations to the matrix were created due to extensive primary MC carbide decomposition, as carbon and carbide-forming elements were more readily distributed into the matrix after being drawn out during primary MC carbide decomposition. Thus, *as it has been* established that extensive MC carbide decomposition was present in the as-received microstructural state of a turbine bucket from set 128, it is suspected that the same increase in the aging/degradation kinetics exhibited by the

rejuvenated component in the work E. Lvova [18] will also occur for rejuvenated turbine buckets from set 128.

Finally, a statistically significant degree of creep-rupture testing of specimens derived from bucket set 128 is suggested to be undertaken by future research investigations; this would serve to confirm or deny the suggested post-service, residual creep-rupture properties of the components used in this research investigation.

Appendix A

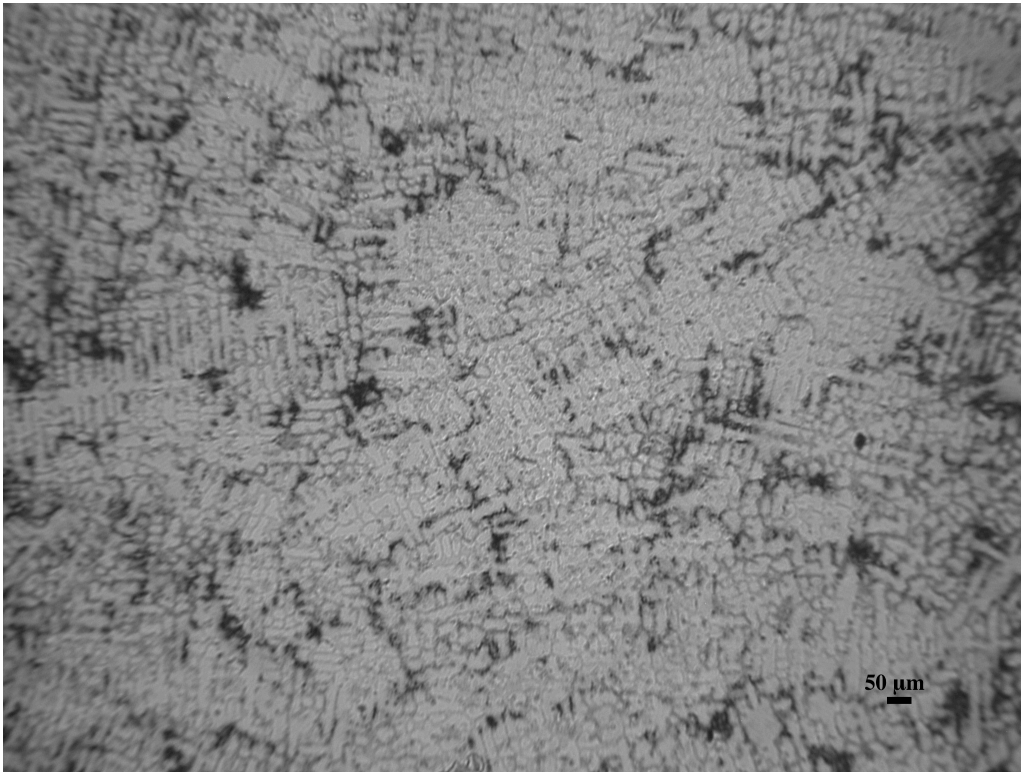


Figure 58. Etched microstructure of specimen 1 (as-received); original magnification: 100X.

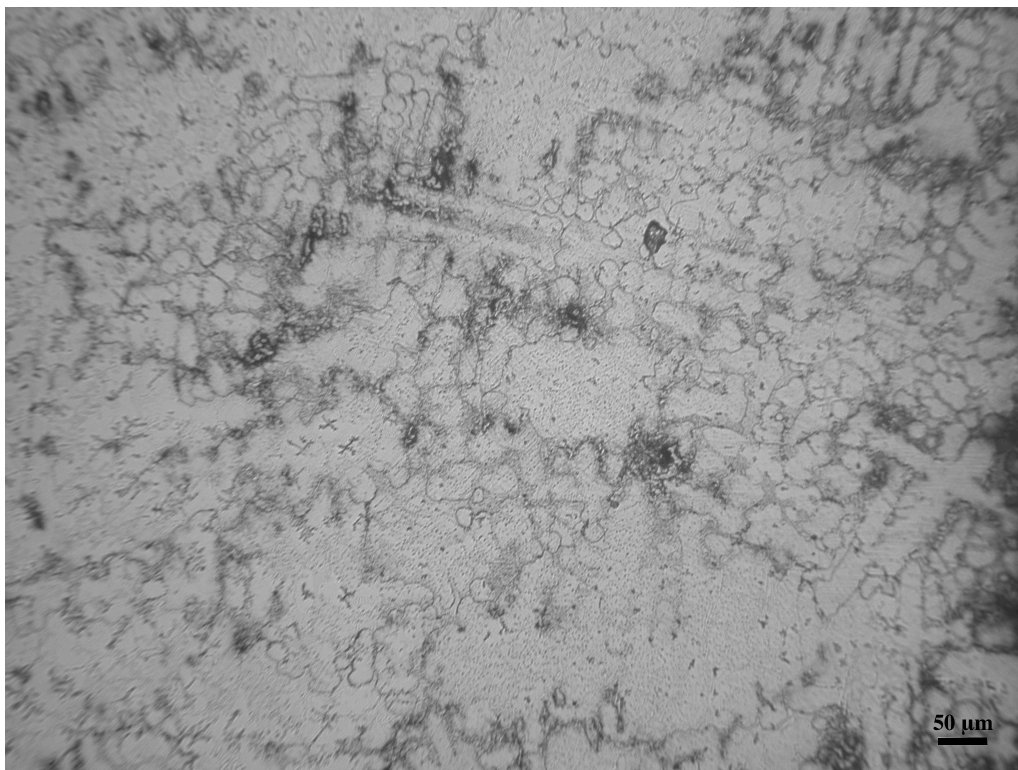


Figure 59. Etched microstructure of specimen 1 (as-received); original magnification: 200X.

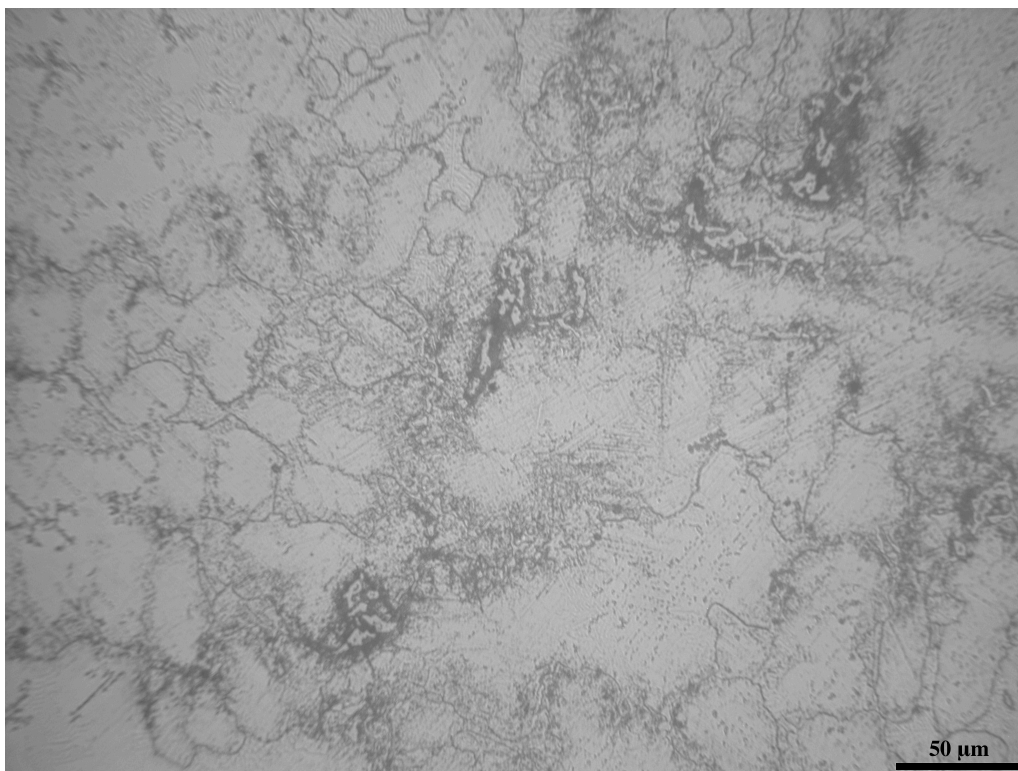


Figure 60. Etched microstructure of specimen 1 (as-received); original magnification: 500X.

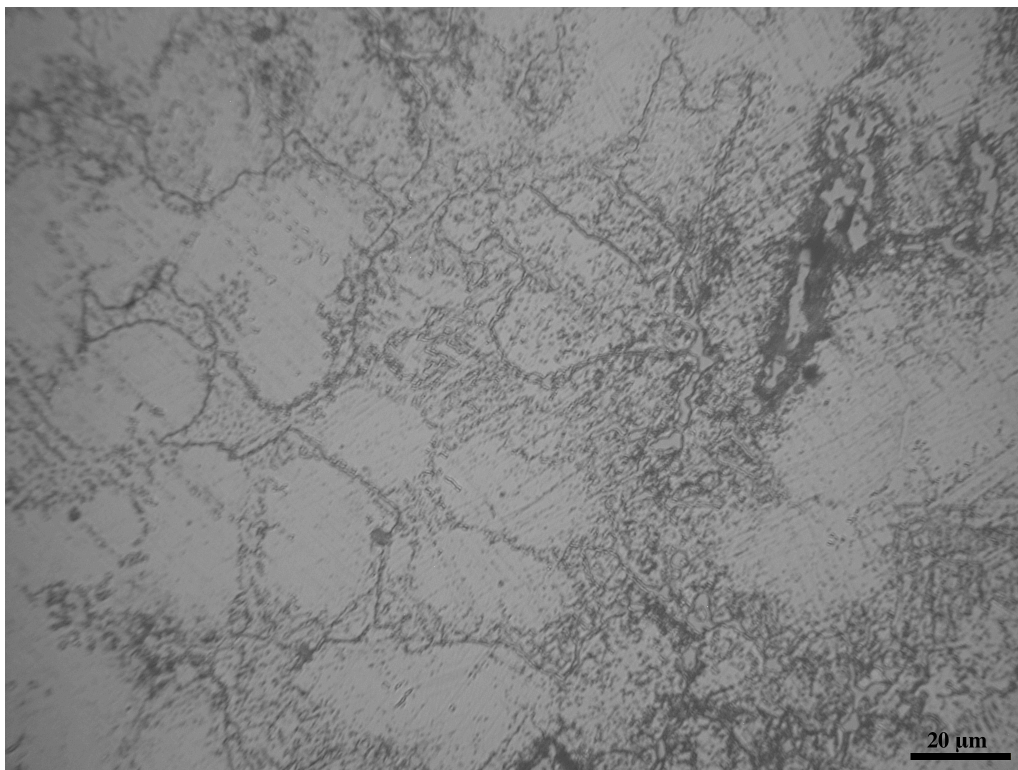


Figure 61. Etched microstructure of specimen 1 (as-received); original magnification: 1000X.



Figure 62. Etched microstructure of specimen 2 (as-received); original magnification: 100X.

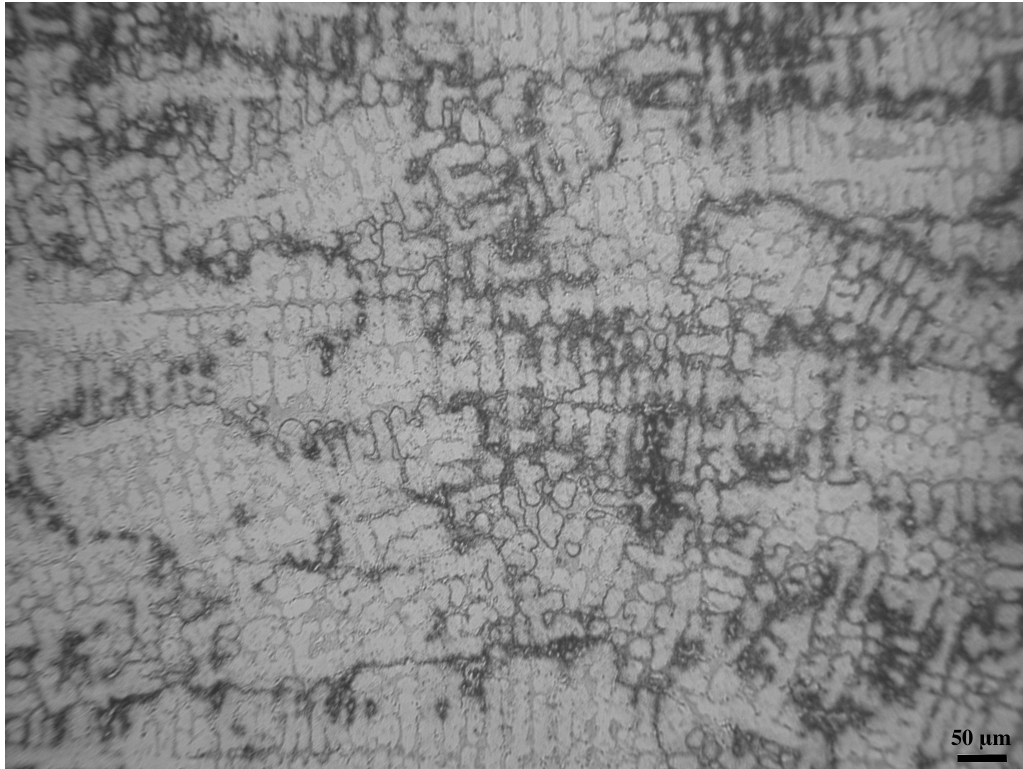


Figure 63. Etched microstructure of specimen 2 (as-received); original magnification: 200X.

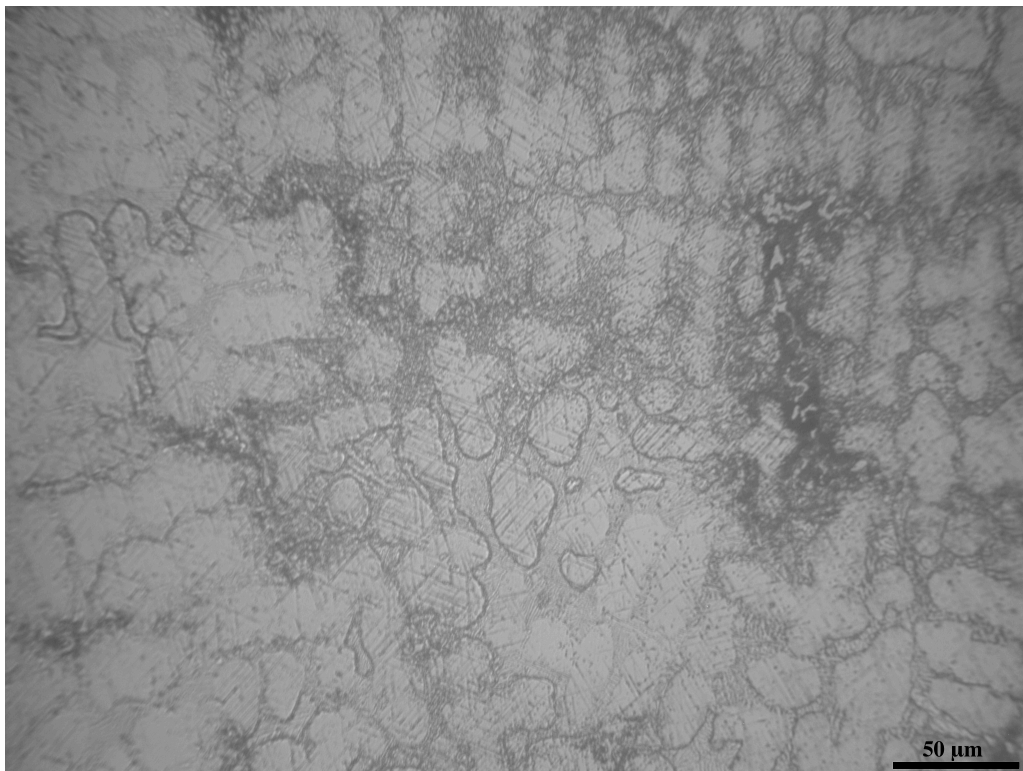


Figure 64. Etched microstructure of specimen 2 (as-received); original magnification: 500X.

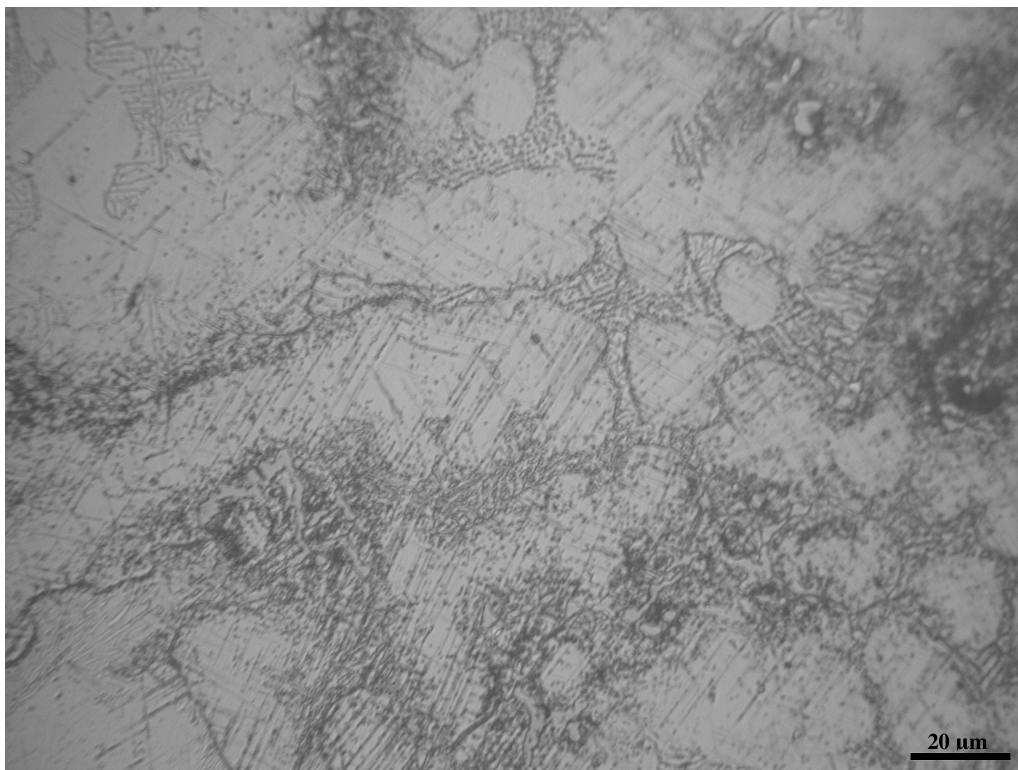


Figure 65. Etched microstructure of specimen 2 (as-received); original magnification: 1000X.



Figure 66. Etched microstructure of specimen 3 (as-received); original magnification: 100X.



Figure 67. Etched microstructure of specimen 3 (as-received); original magnification: 200X.

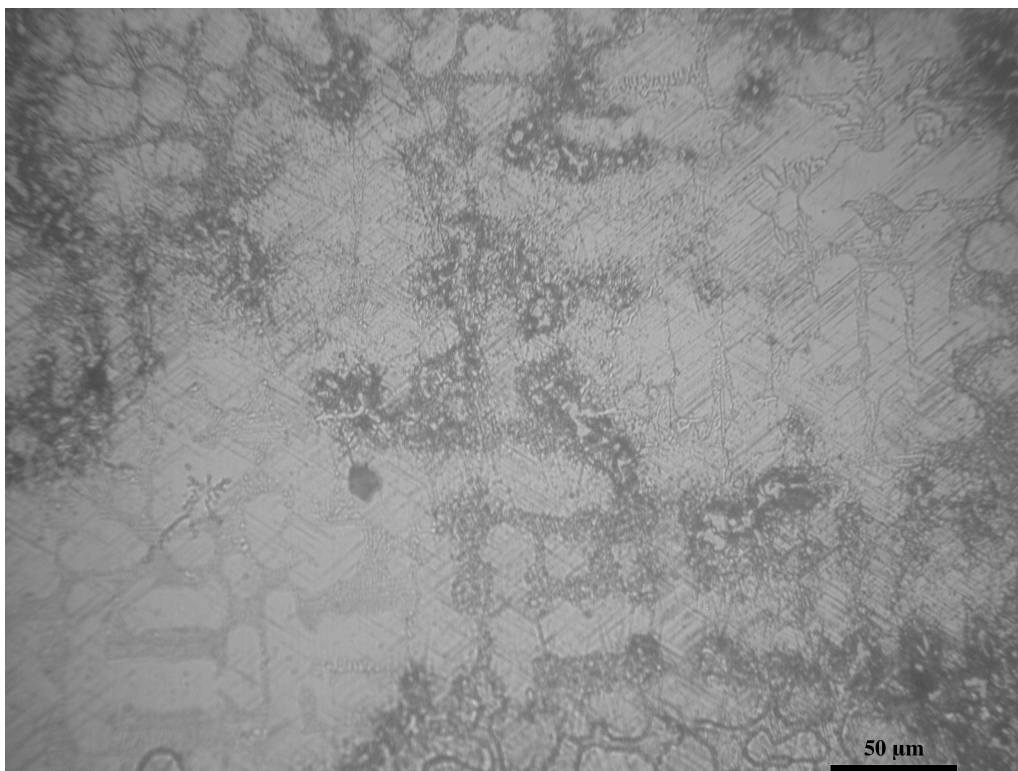


Figure 68. Etched microstructure of specimen 3 (as-received); original magnification: 500X.

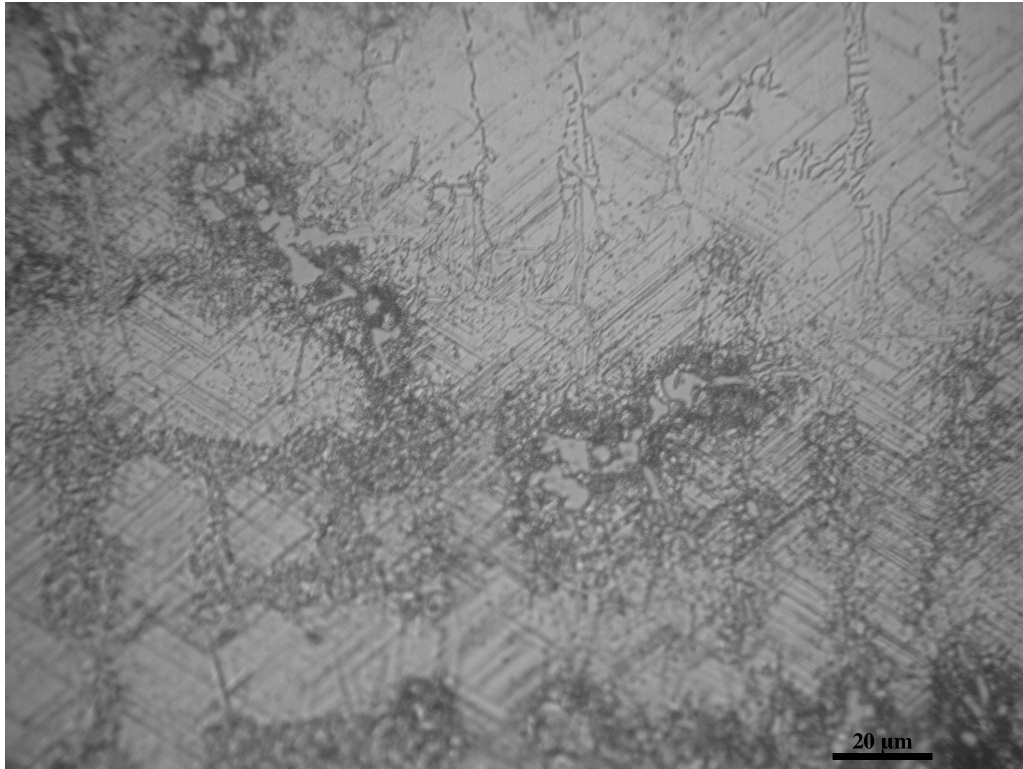


Figure 69. Etched microstructure of specimen 3 (as-received); original magnification: 1000X.

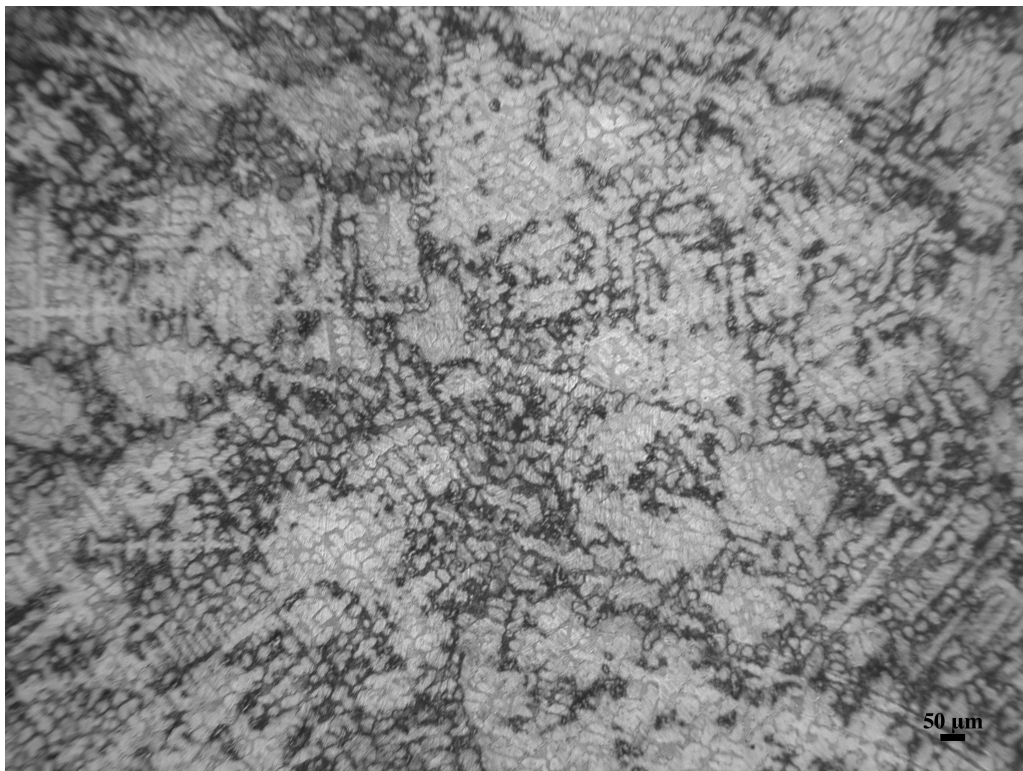


Figure 70. Etched microstructure of specimen 4 (as-received); original magnification: 100X.



Figure 71. Etched microstructure of specimen 4 (as-received); original magnification: 200X.



Figure 72. Etched microstructure of specimen 4 (as-received); original magnification: 500X.



Figure 73. Etched microstructure of specimen 4 (as-received); original magnification: 1000X.



Figure 74. Etched microstructure of specimen 5 (as-received); original magnification: 100X.

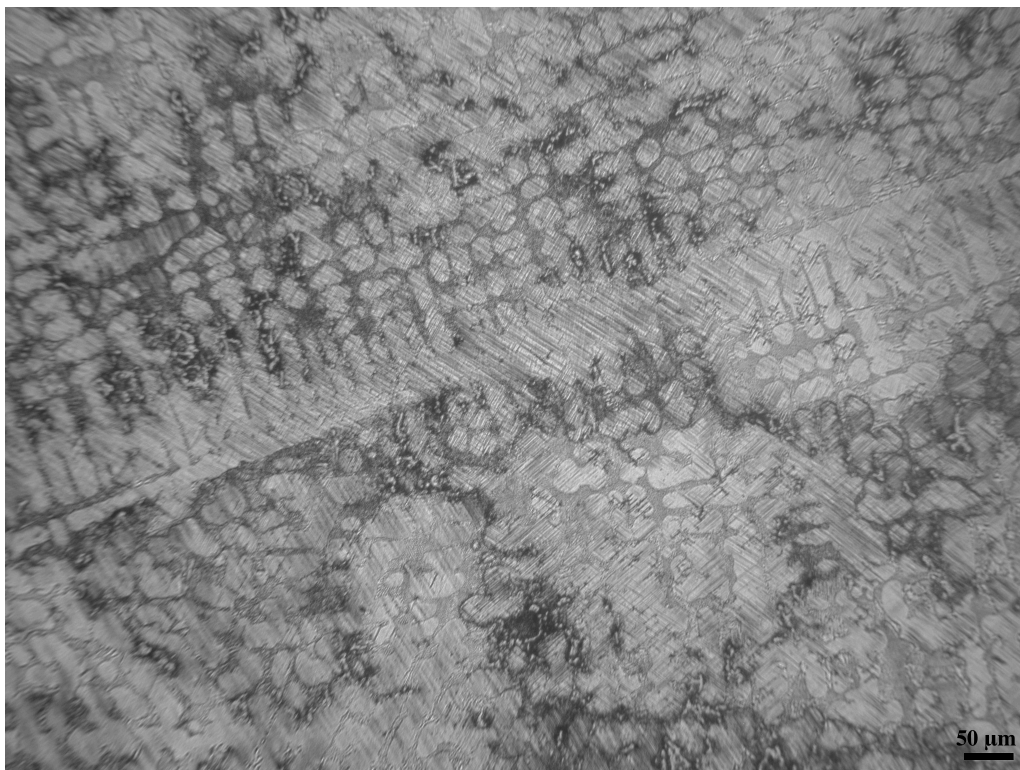


Figure 75. Etched microstructure of specimen 5 (as-received); original magnification: 200X.

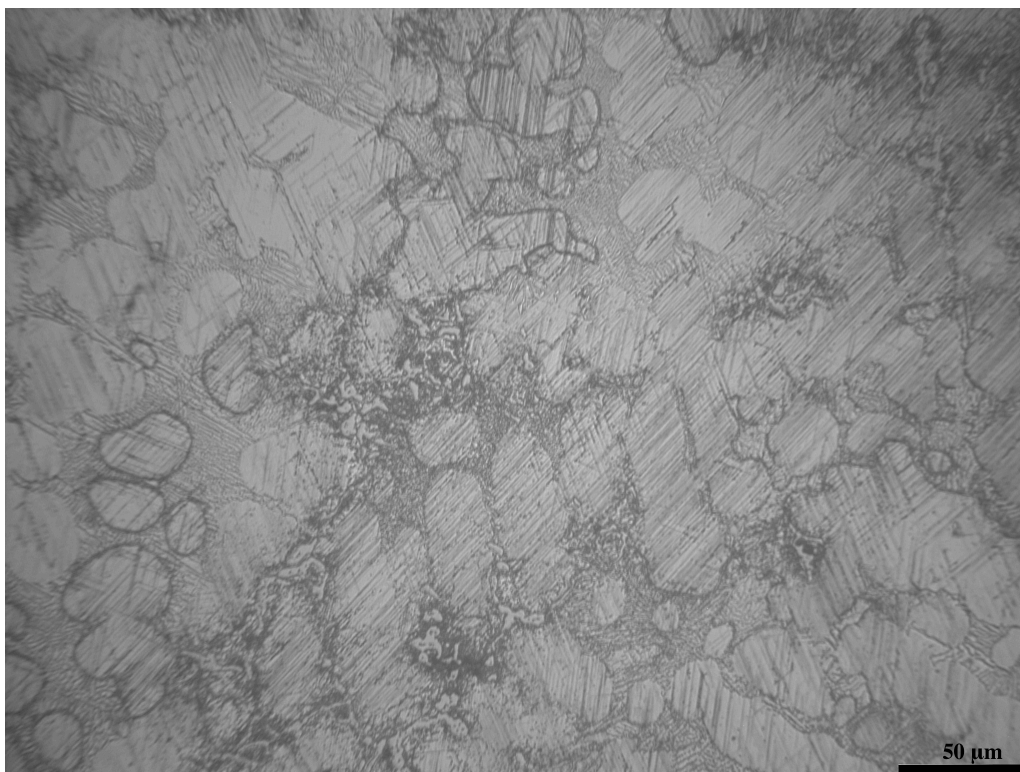


Figure 76. Etched microstructure of specimen 5 (as-received); original magnification: 500X.

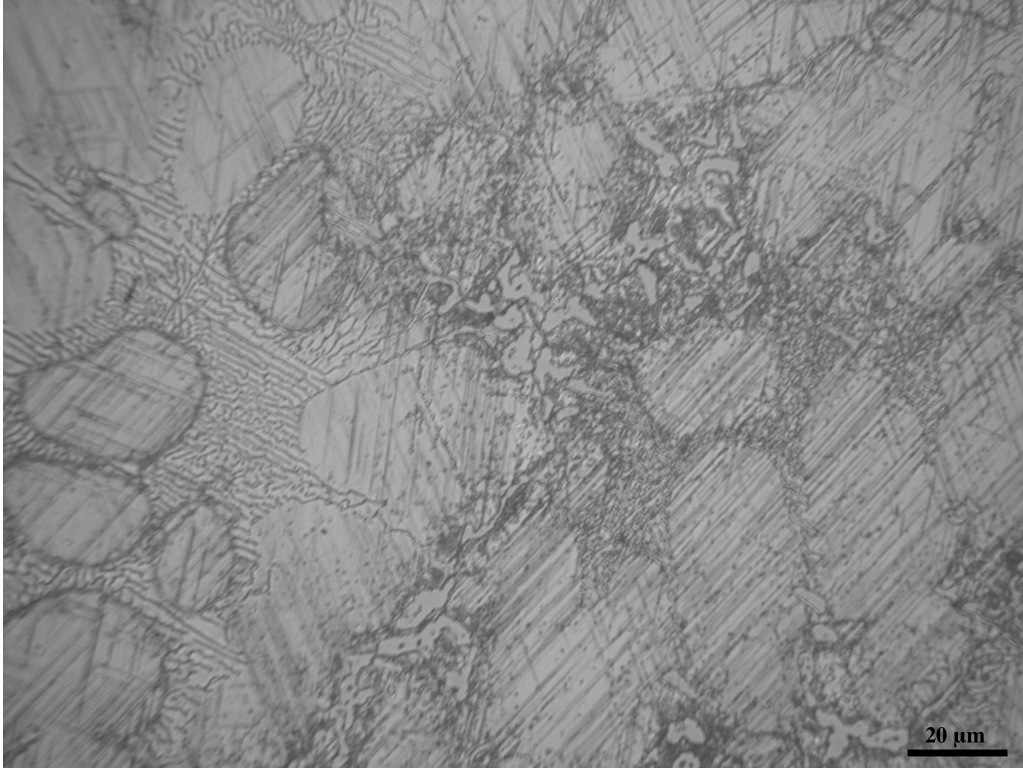


Figure 77. Etched microstructure of specimen 5 (as-received); original magnification: 1000X.

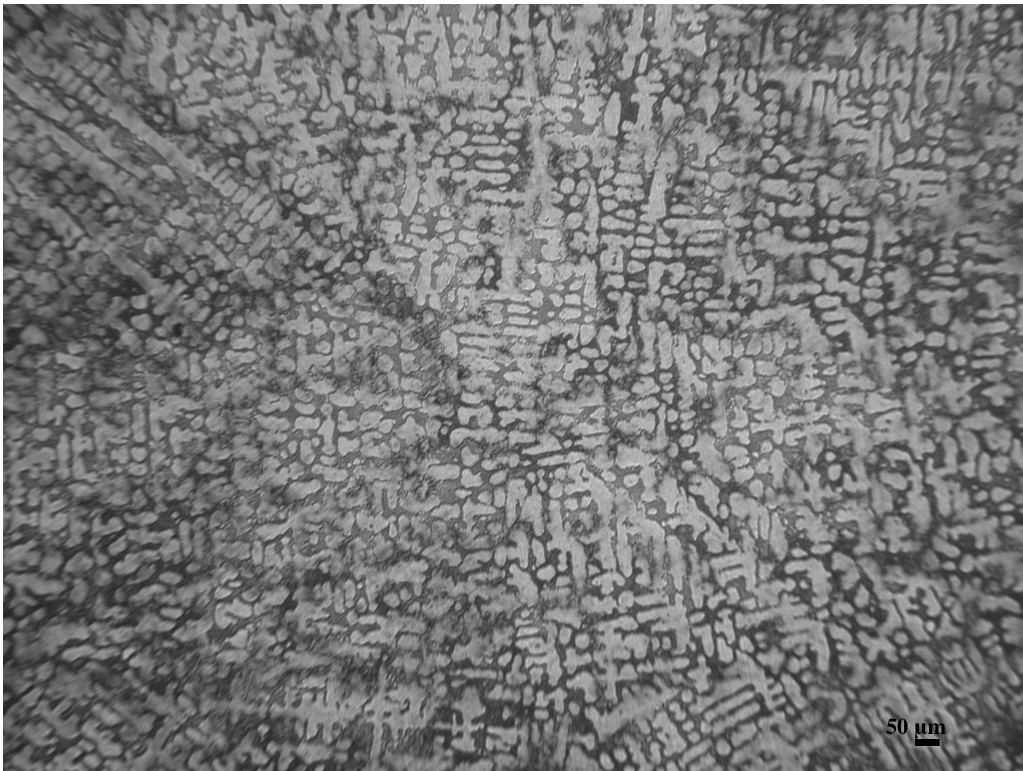


Figure 78. Etched microstructure of specimen 6 (as-received); original magnification: 100X.

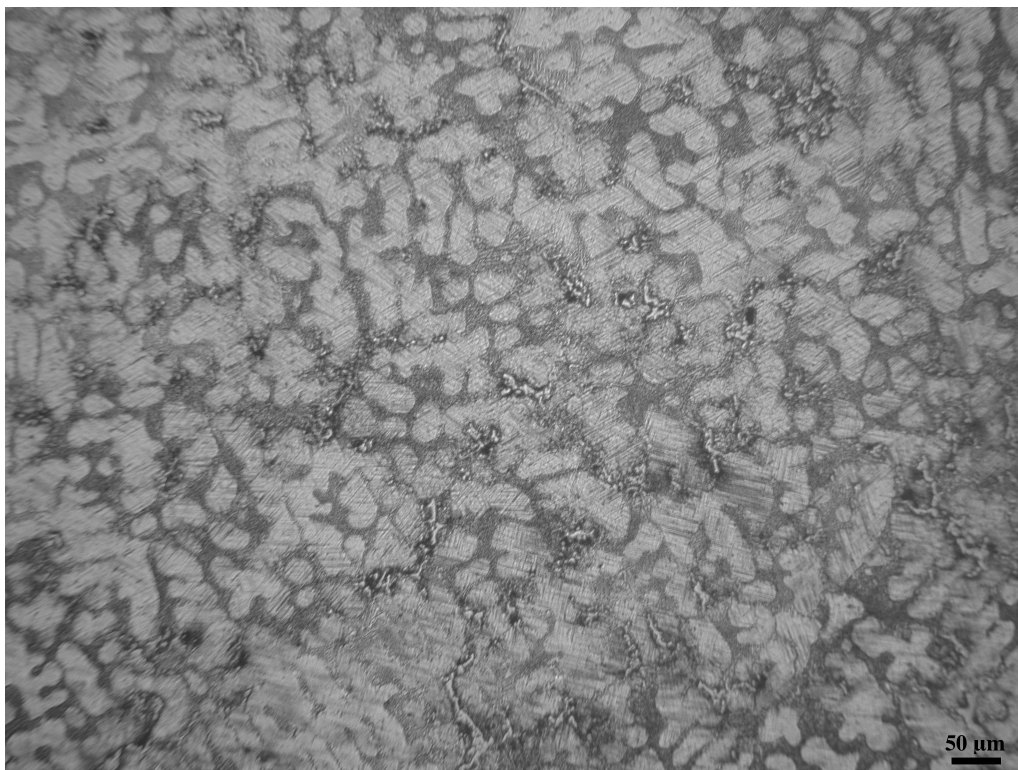


Figure 79. Etched microstructure of specimen 6 (as-received); original magnification: 200X.

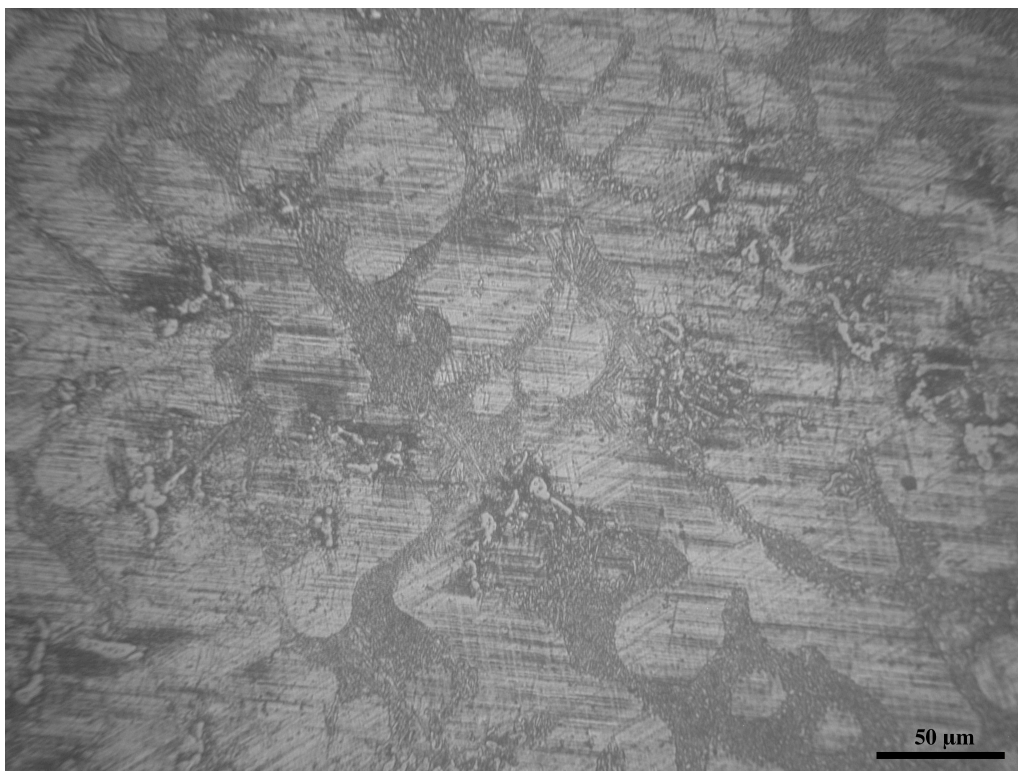


Figure 80. Etched microstructure of specimen 6 (as-received); original magnification: 500X.



Figure 81. Etched microstructure of specimen 6 (as-received); original magnification: 1000X.



Figure 82. Etched microstructure of specimen 7 (as-received); original magnification: 100X.

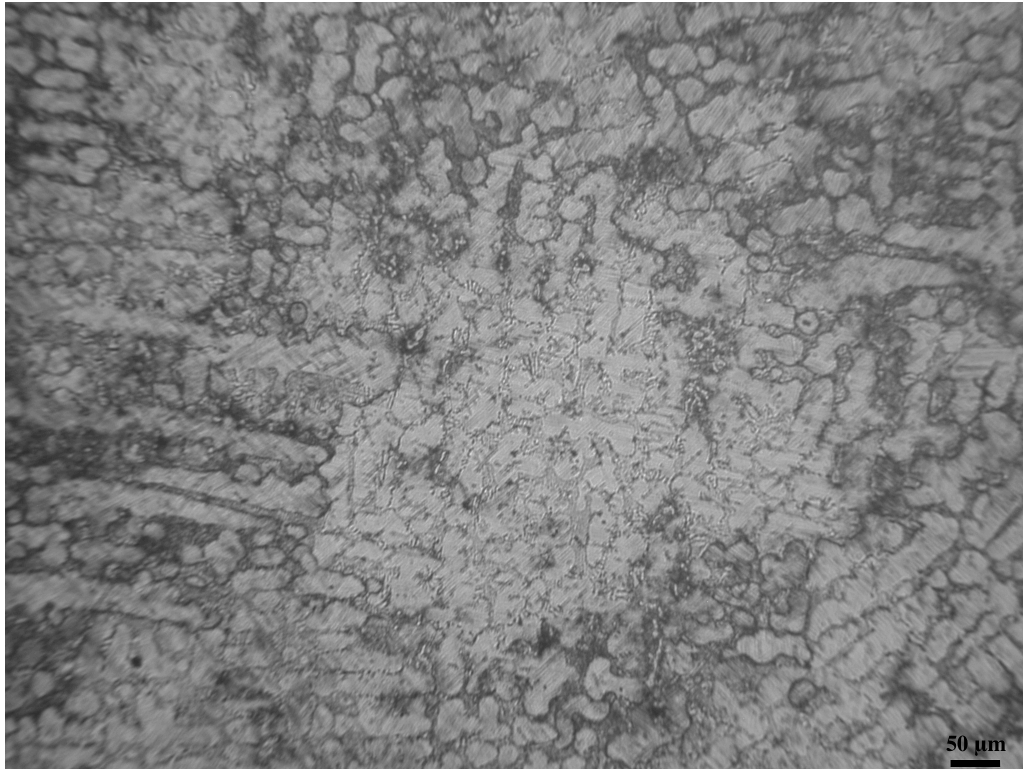


Figure 83. Etched microstructure of specimen 7 (as-received); original magnification: 200X.

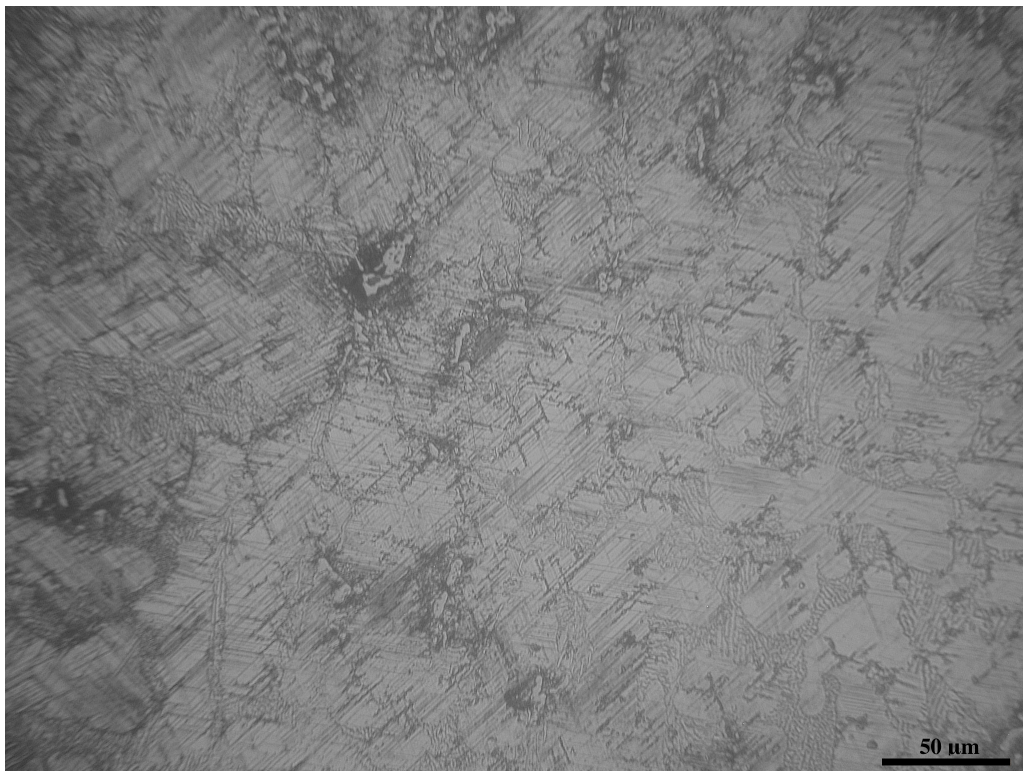


Figure 84. Etched microstructure of specimen 7 (as-received); original magnification: 500X.



Figure 85. Etched microstructure of specimen 7 (as-received); original magnification: 1000X.

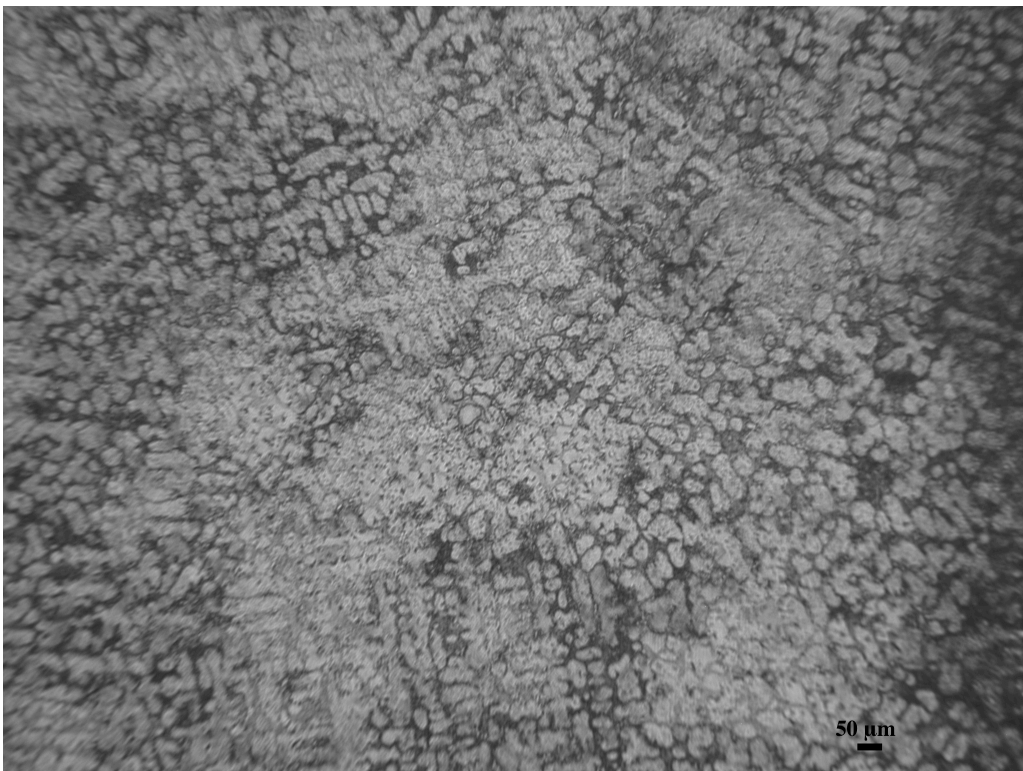


Figure 86. Etched microstructure of specimen 8 (as-received); original magnification: 100X.

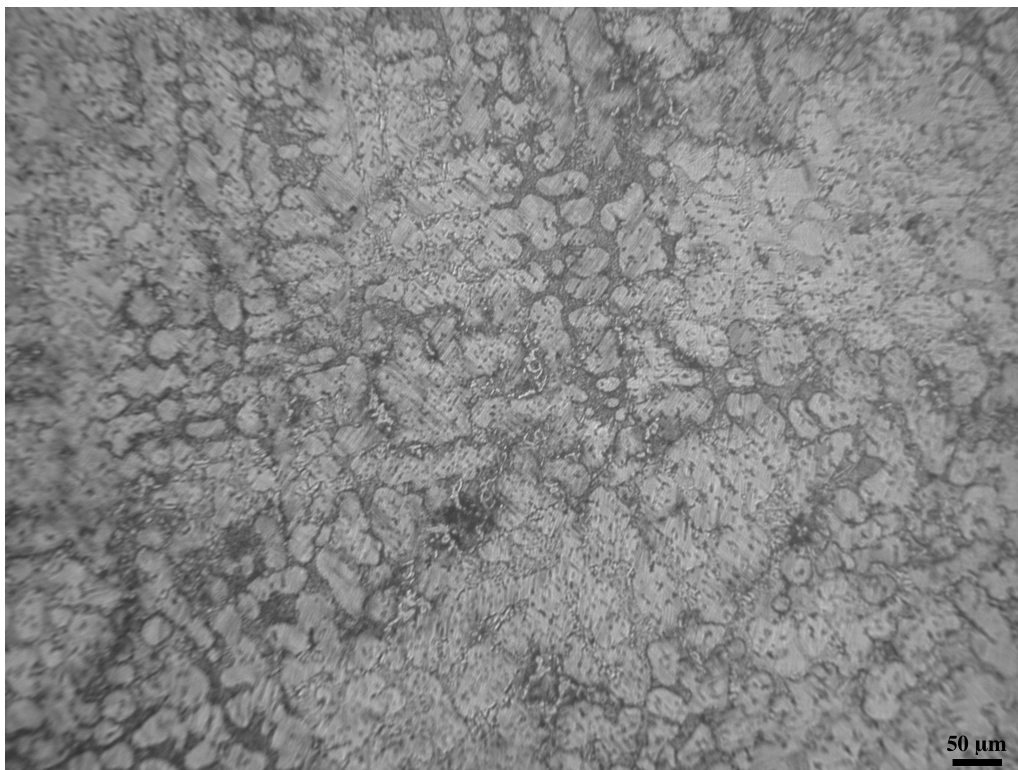


Figure 87. Etched microstructure of specimen 8 (as-received); original magnification: 200X.

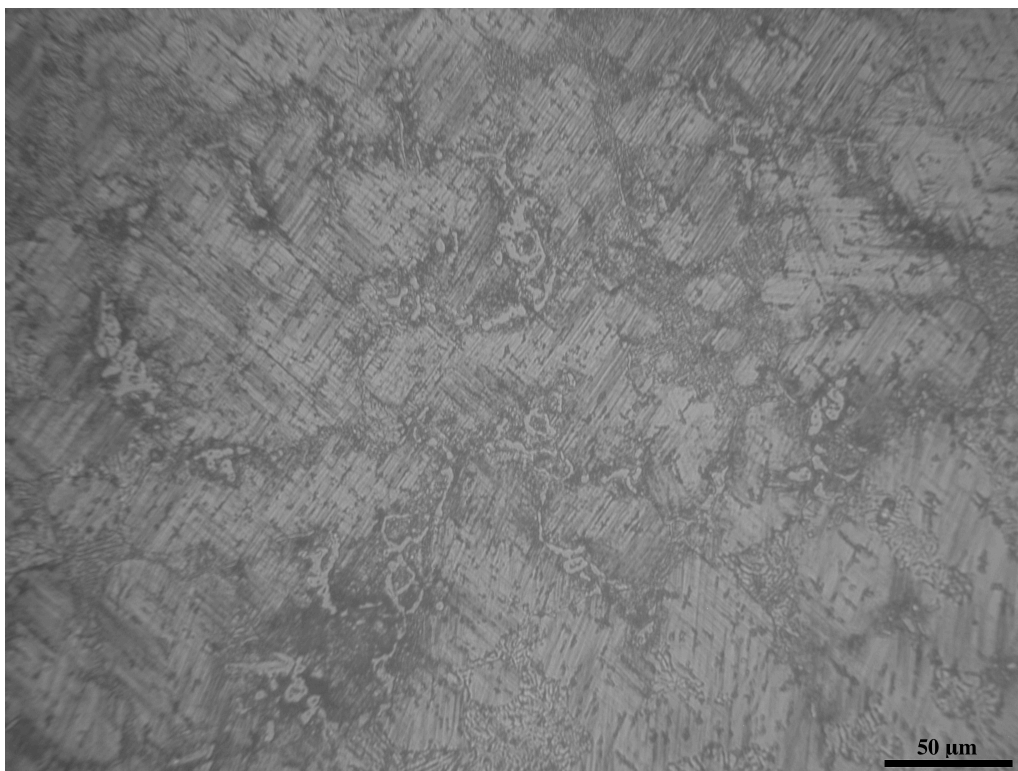


Figure 88. Etched microstructure of specimen 8 (as-received); original magnification: 500X.



Figure 89. Etched microstructure of specimen 8 (as-received); original magnification: 1000X.



Figure 90. Etched microstructure of specimen 9 (as-received); original magnification: 100X.

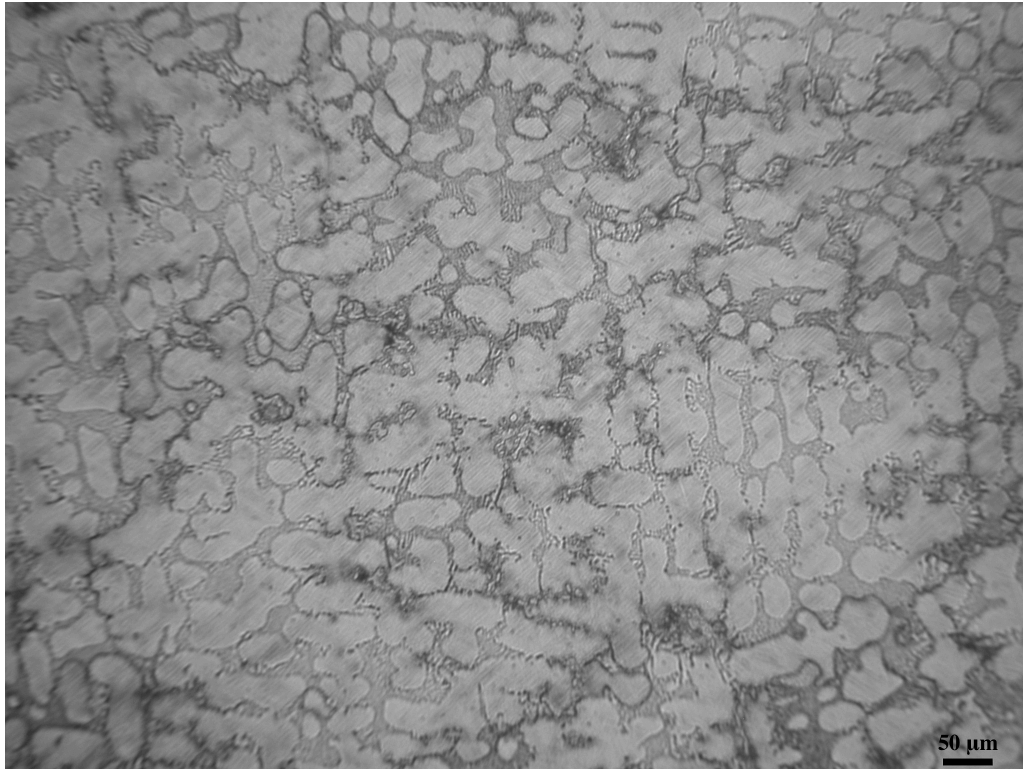


Figure 91. Etched microstructure of specimen 9 (as-received); original magnification: 200X.

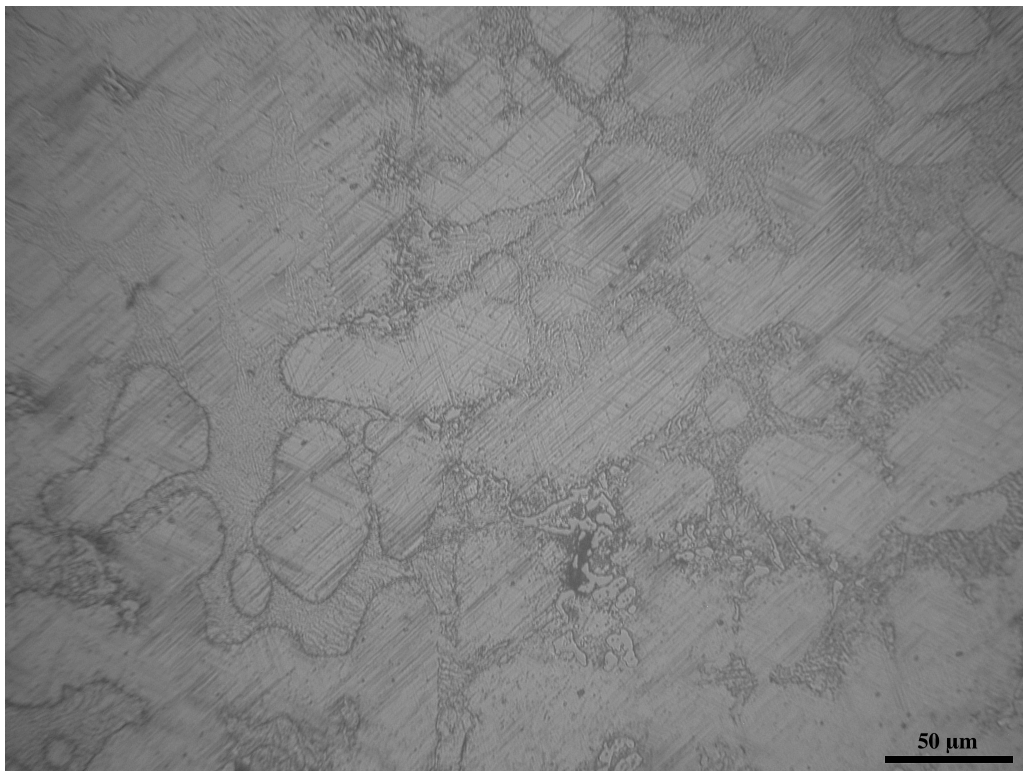


Figure 92. Etched microstructure of specimen 9 (as-received); original magnification: 500X.

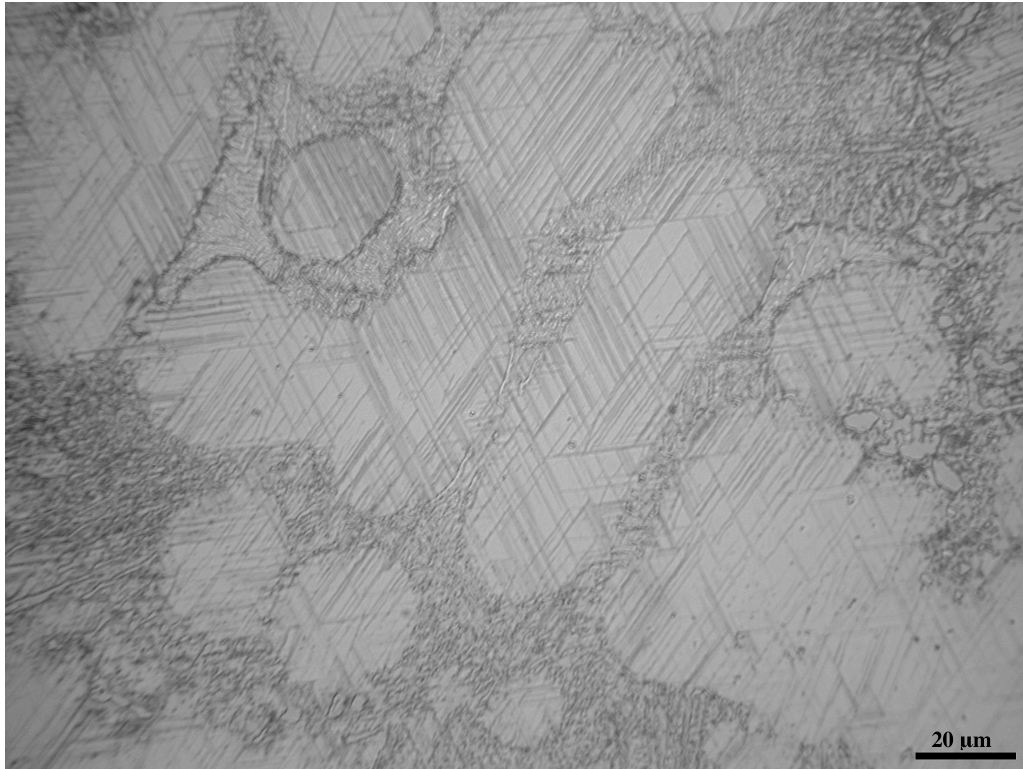


Figure 93. Etched microstructure of specimen 9 (as-received); original magnification: 1000X.

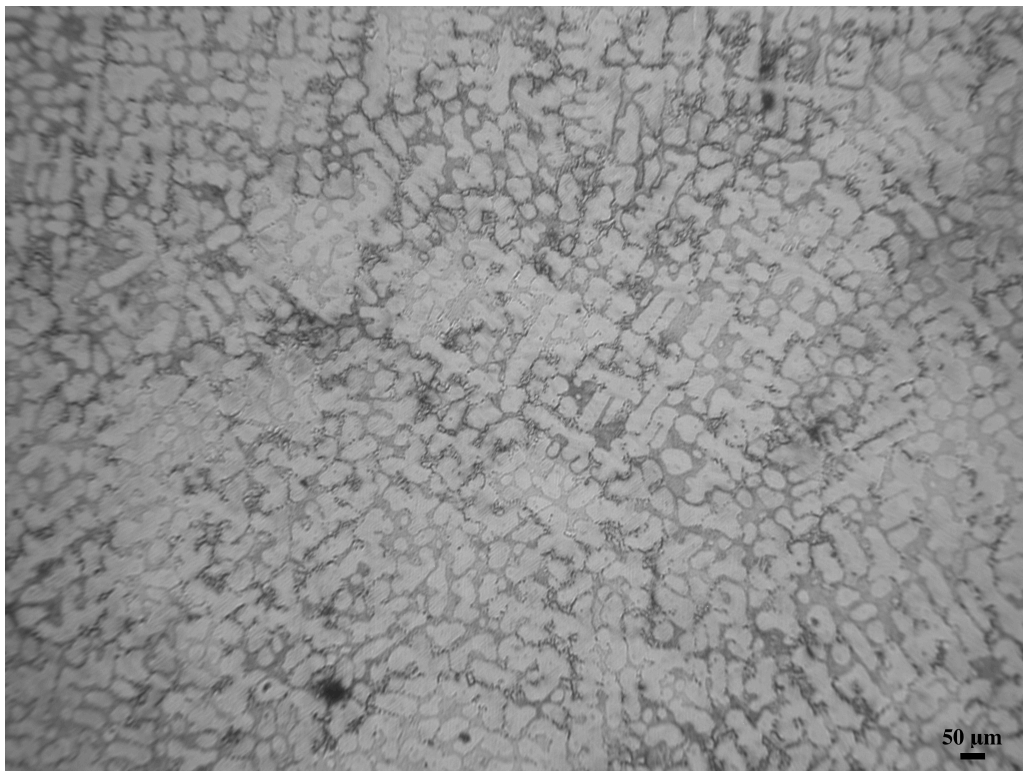


Figure 94. Etched microstructure of specimen 10 (as-received); original magnification: 100X.

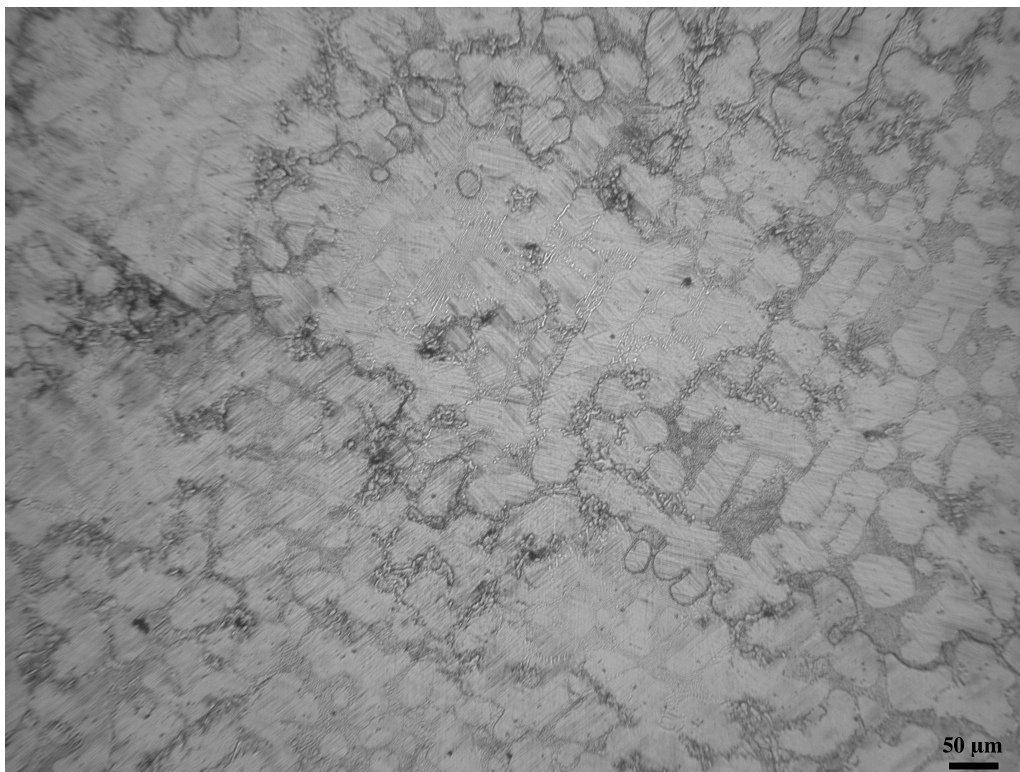


Figure 95. Etched microstructure of specimen 10 (as-received); original magnification: 200X.

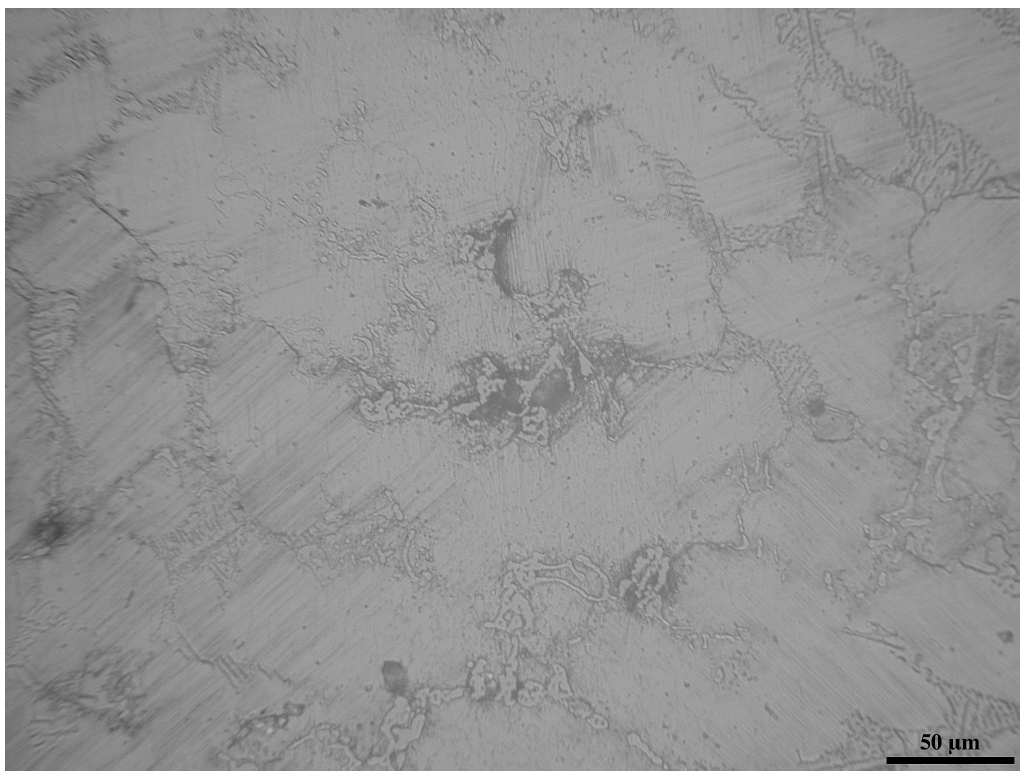


Figure 96. Etched microstructure of specimen 10 (as-received); original magnification: 500X.

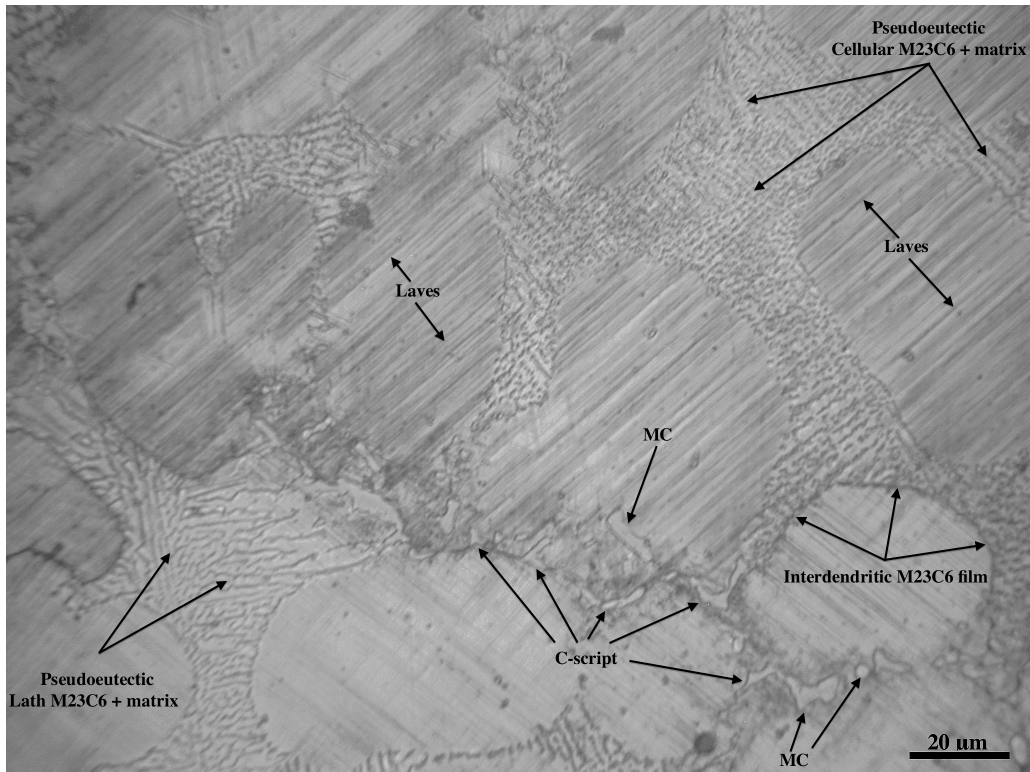


Figure 97. Etched microstructure of specimen 10 (as-received); original magnification: 1000X.
Microconstituents identified for metallographic reference purposes.

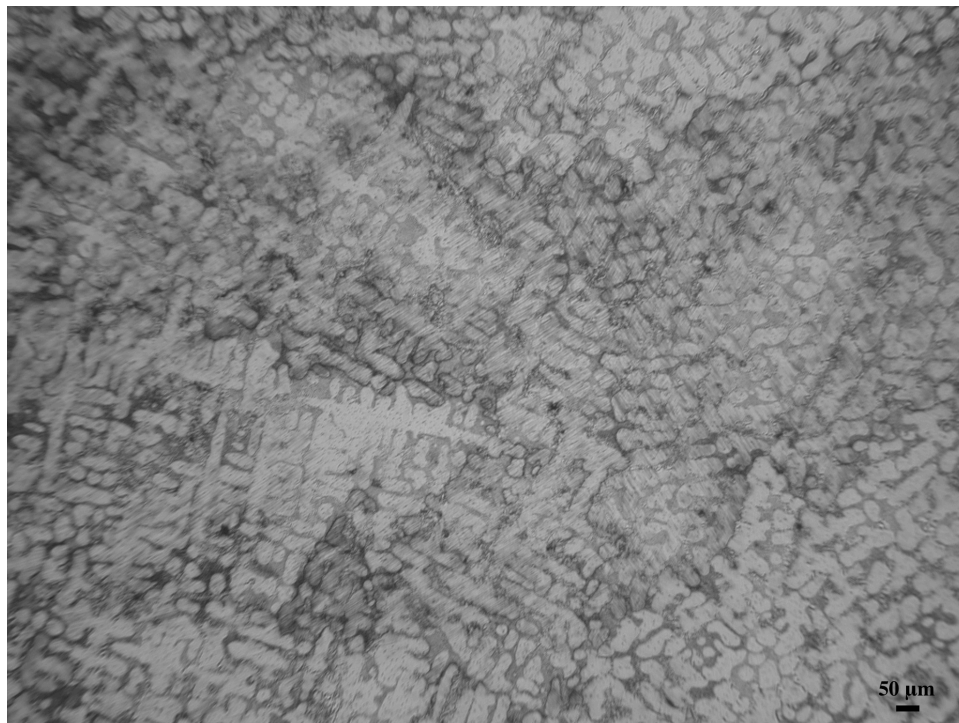


Figure 98. Etched microstructure of specimen 11 (as-received); original magnification: 100X.

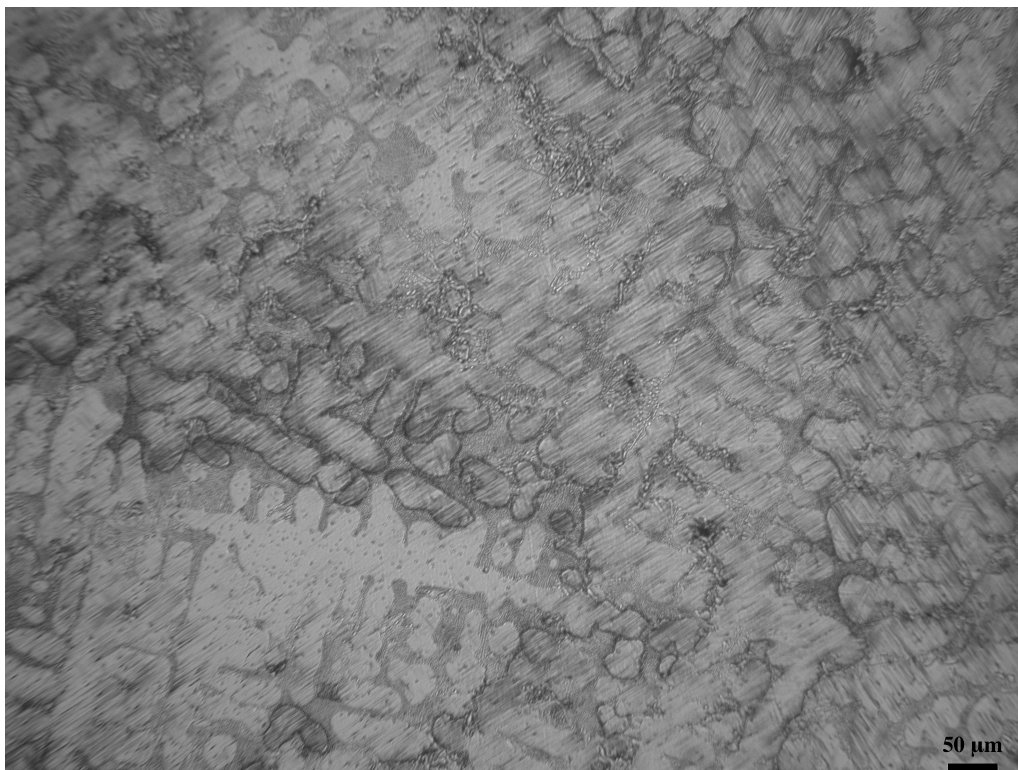


Figure 99. Etched microstructure of specimen 11 (as-received); original magnification: 200X.

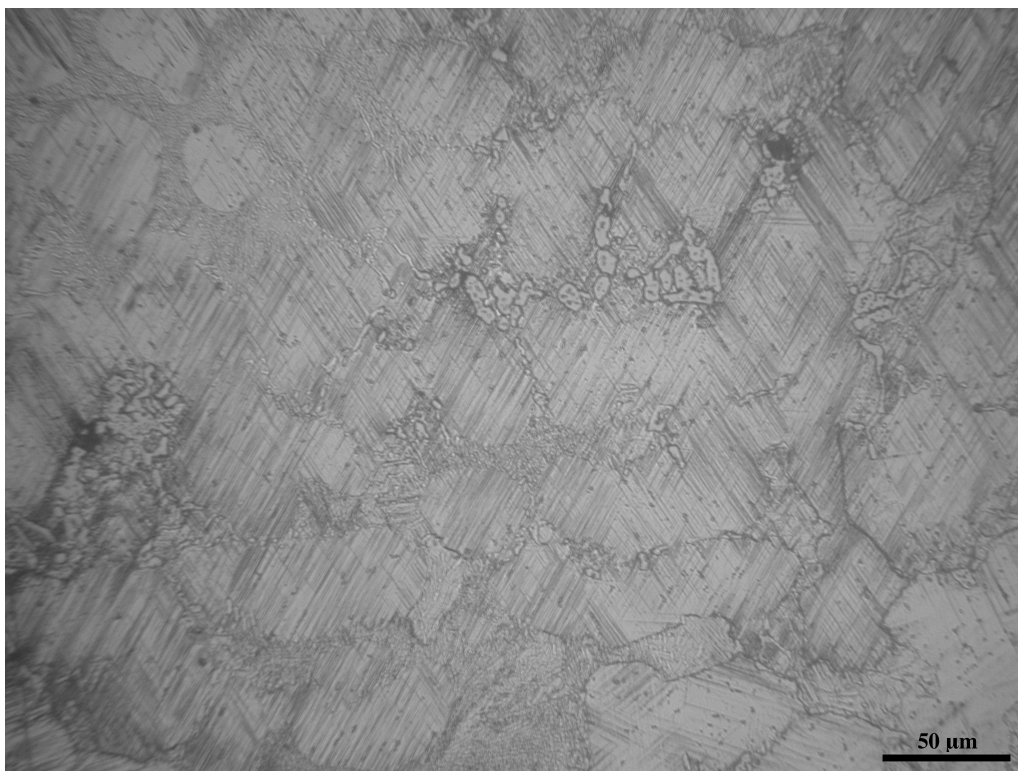


Figure 100. Etched microstructure of specimen 11 (as-received); original magnification: 500X.

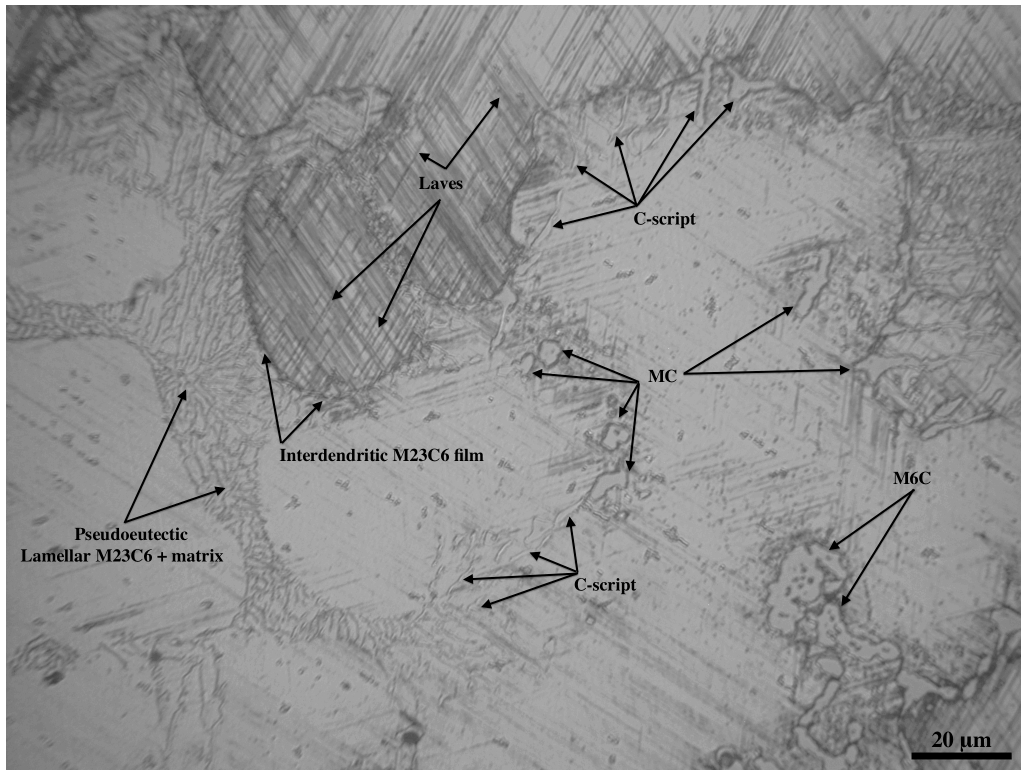


Figure 101. Etched microstructure of specimen 11 (as-received); original magnification: 1000X.
Microconstituents identified for metallographic reference purposes.

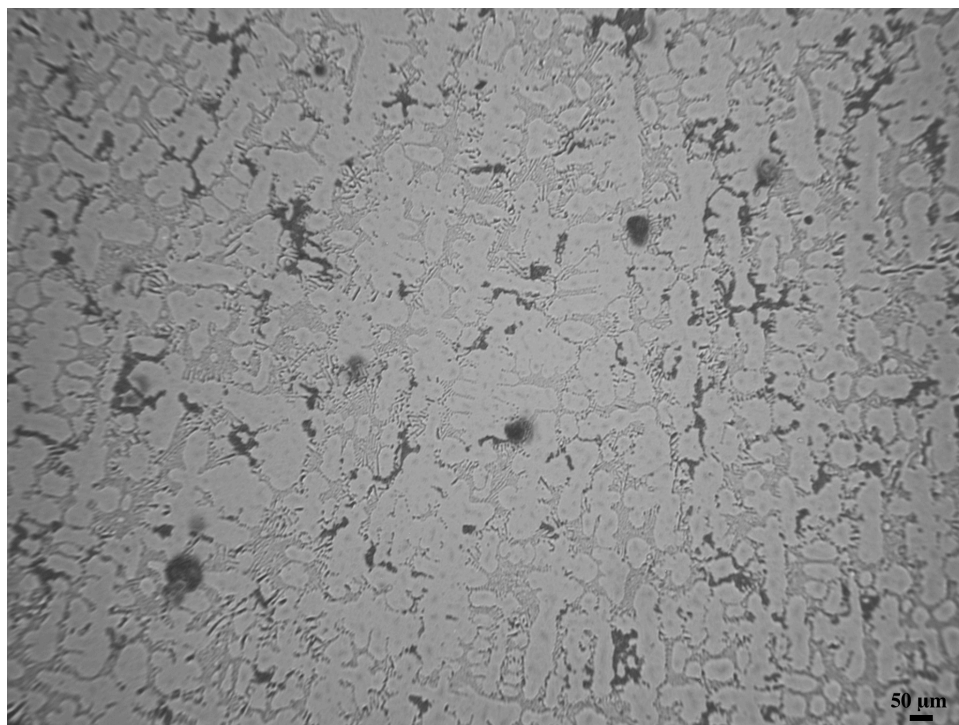


Figure 102. Etched microstructure of specimen 12 (as-received); original magnification: 100X.

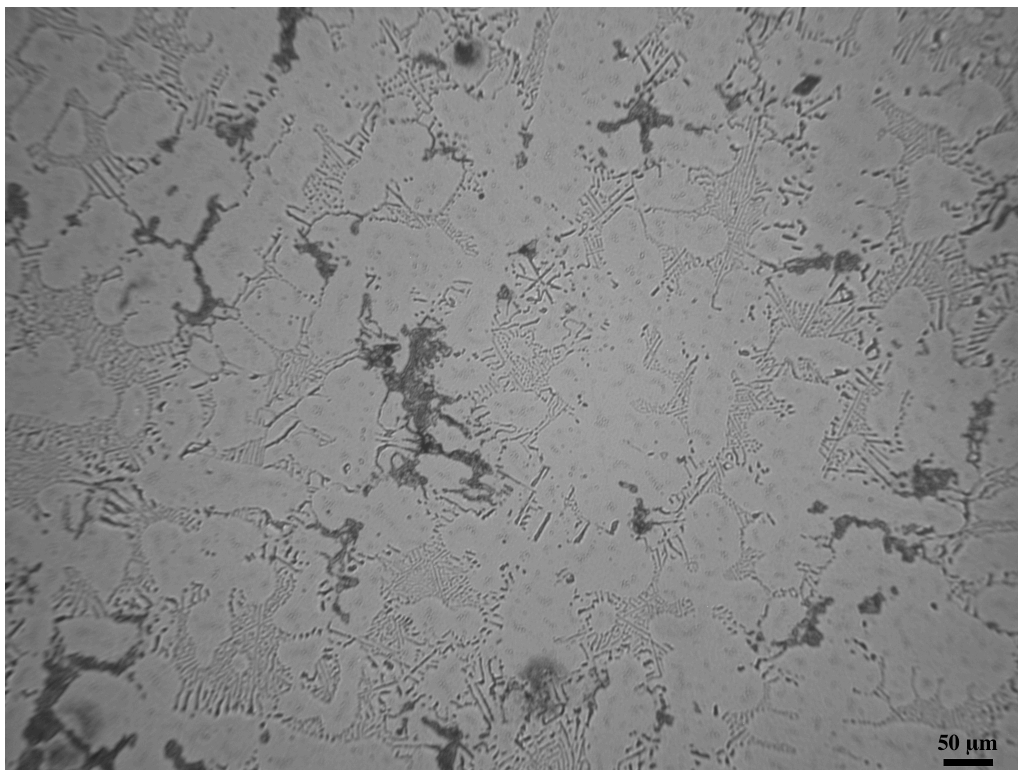


Figure 103. Etched microstructure of specimen 12 (as-received); original magnification: 200X.

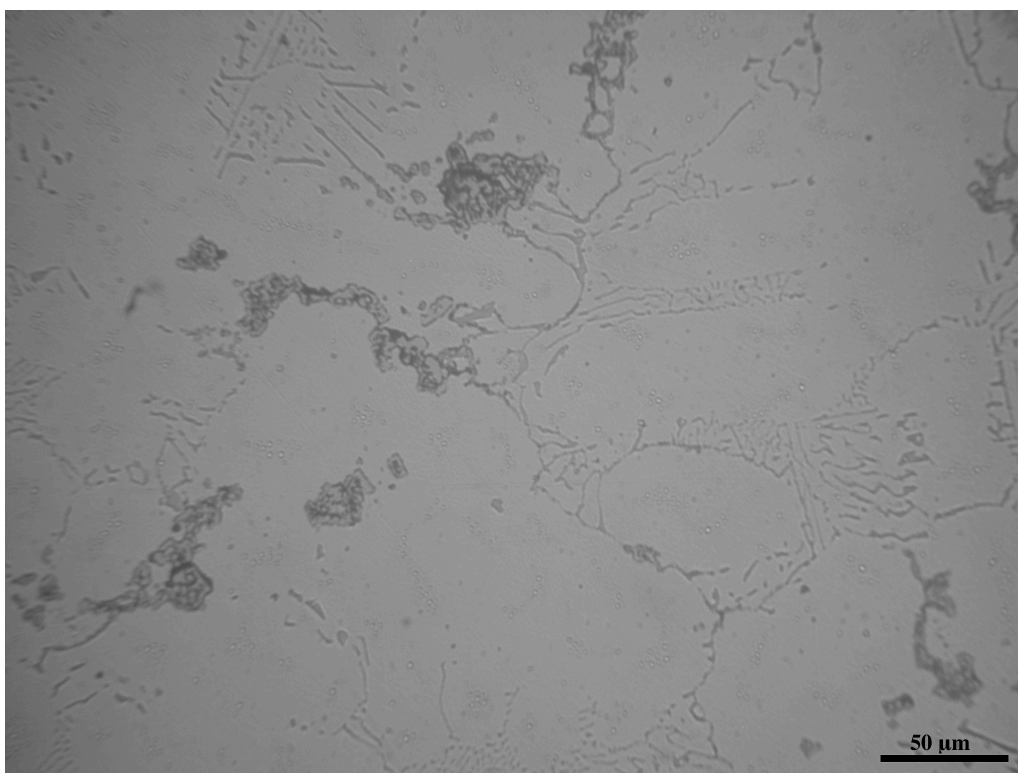


Figure 104. Etched microstructure of specimen 12 (as-received); original magnification: 500X.

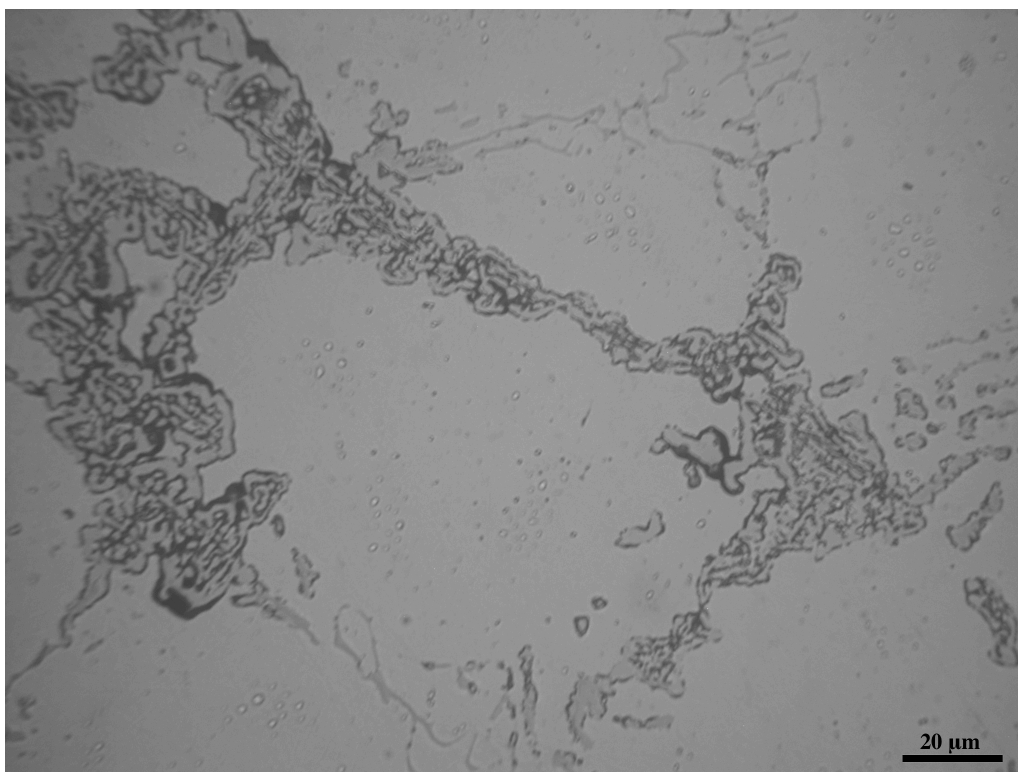


Figure 105. Etched microstructure of specimen 12 (as-received); original magnification: 1000X.

Appendix B

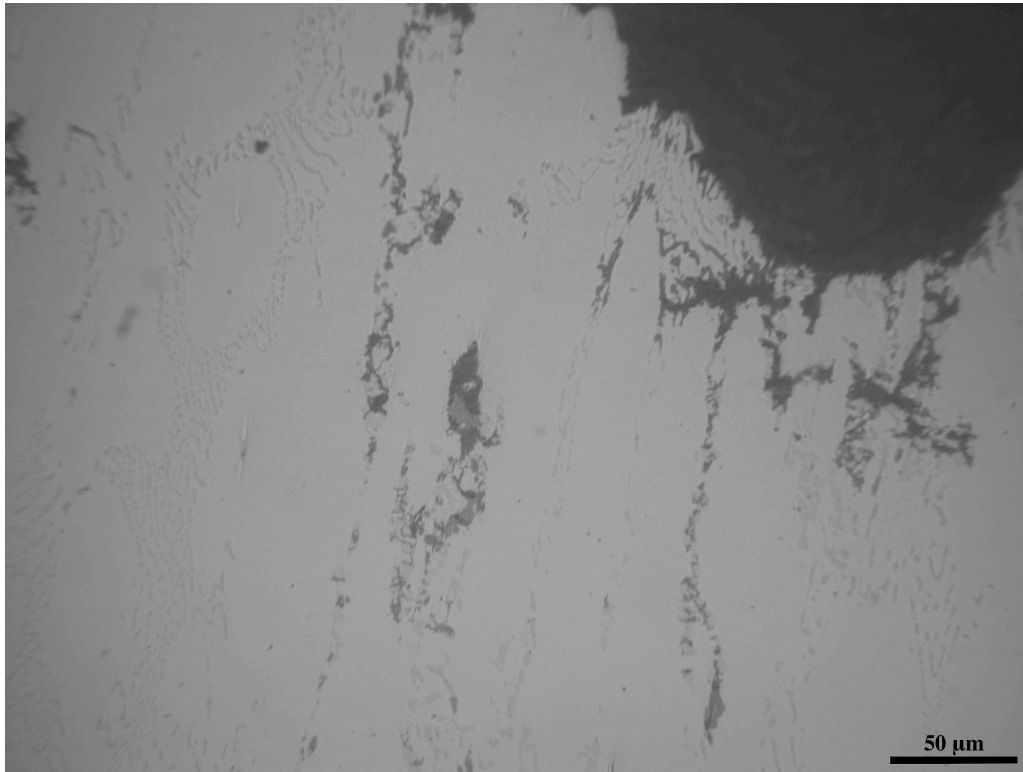


Figure 107. Un-etched microstructure of specimen S1 (rupture surface); magnification: 500X.

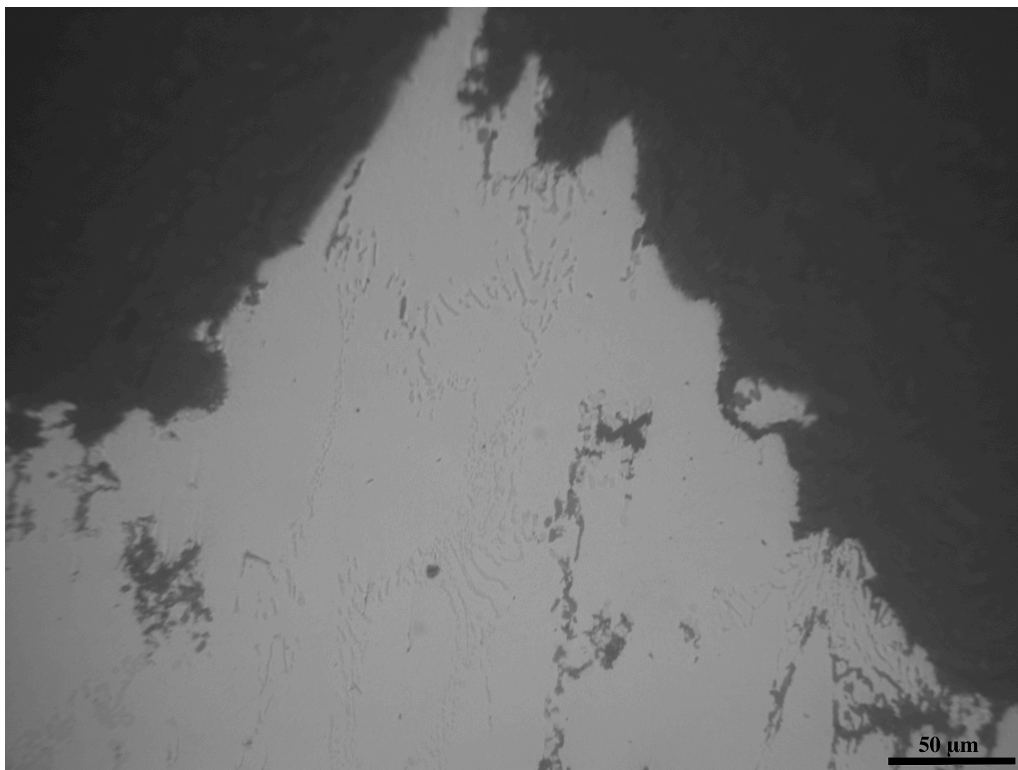


Figure 108. Un-etched microstructure of specimen S1 (rupture surface); magnification: 500X.

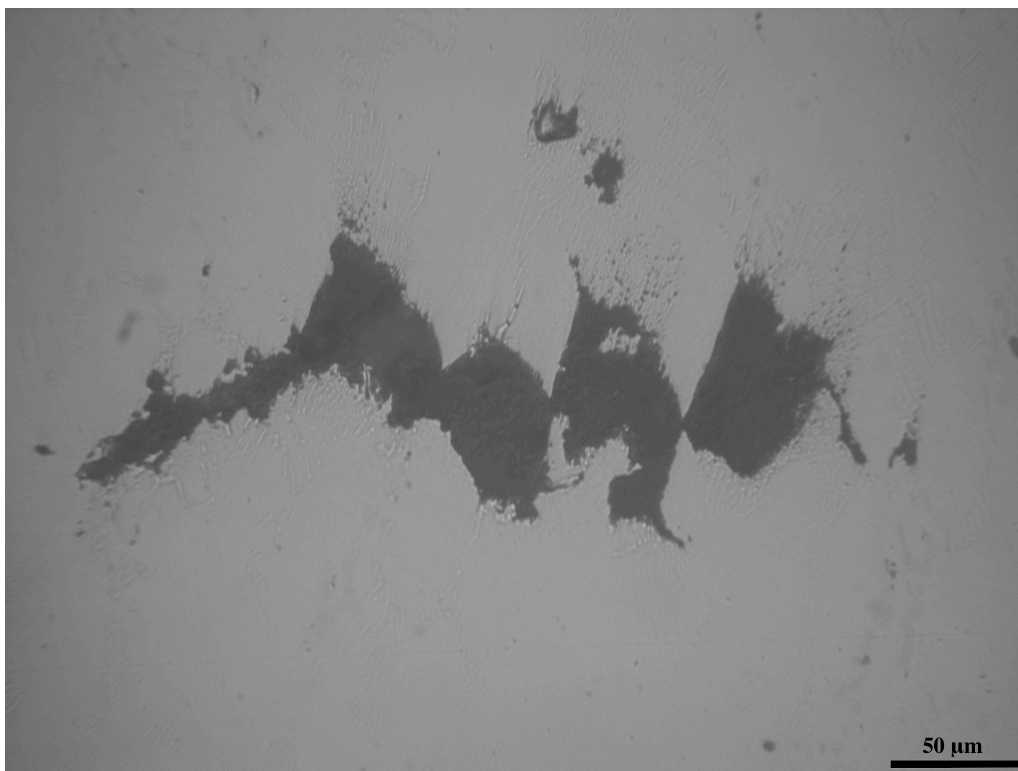


Figure 109. Un-etched microstructure of specimen S1 (at core); magnification: 500X.

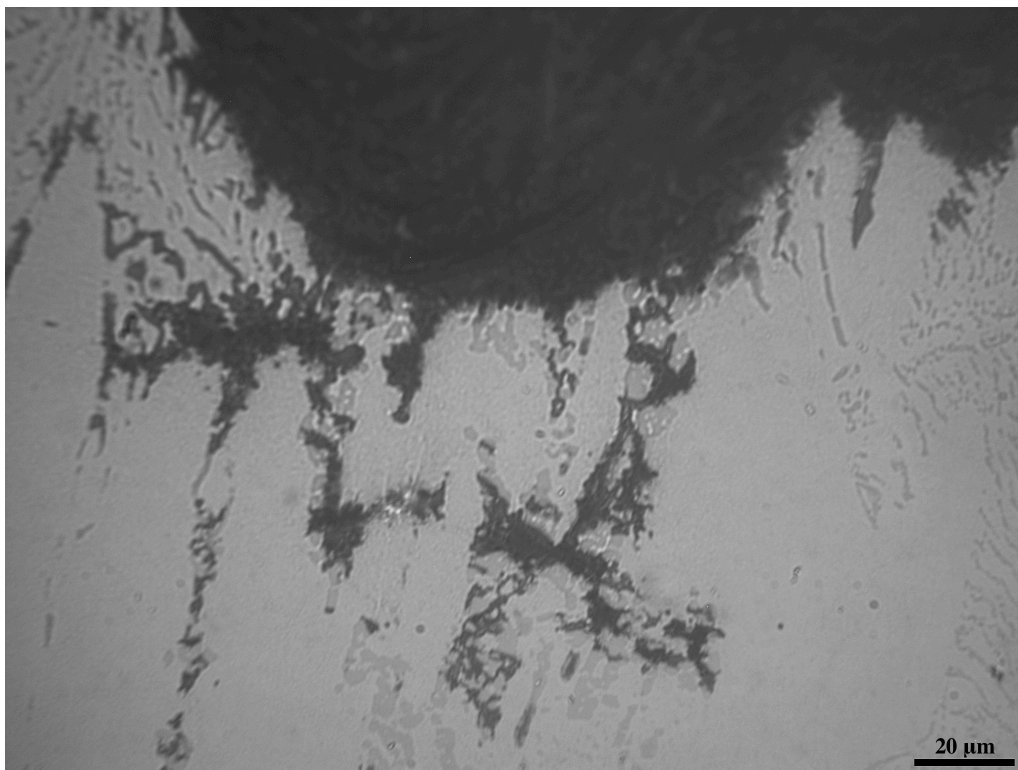


Figure 110. Un-etched microstructure of specimen S1 (rupture surface); magnification: 1000X.

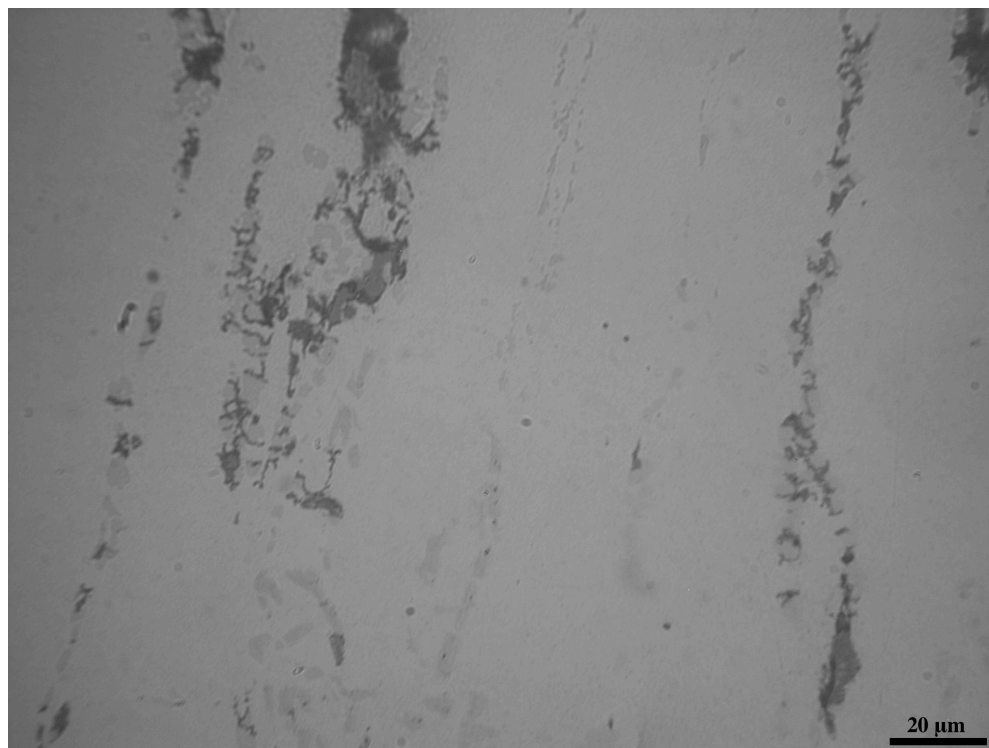


Figure 111. Un-etched microstructure of specimen S1 (rupture surface); magnification: 1000X.



Figure 112. Un-etched microstructure of specimen S1 (at core); magnification: 1000X.

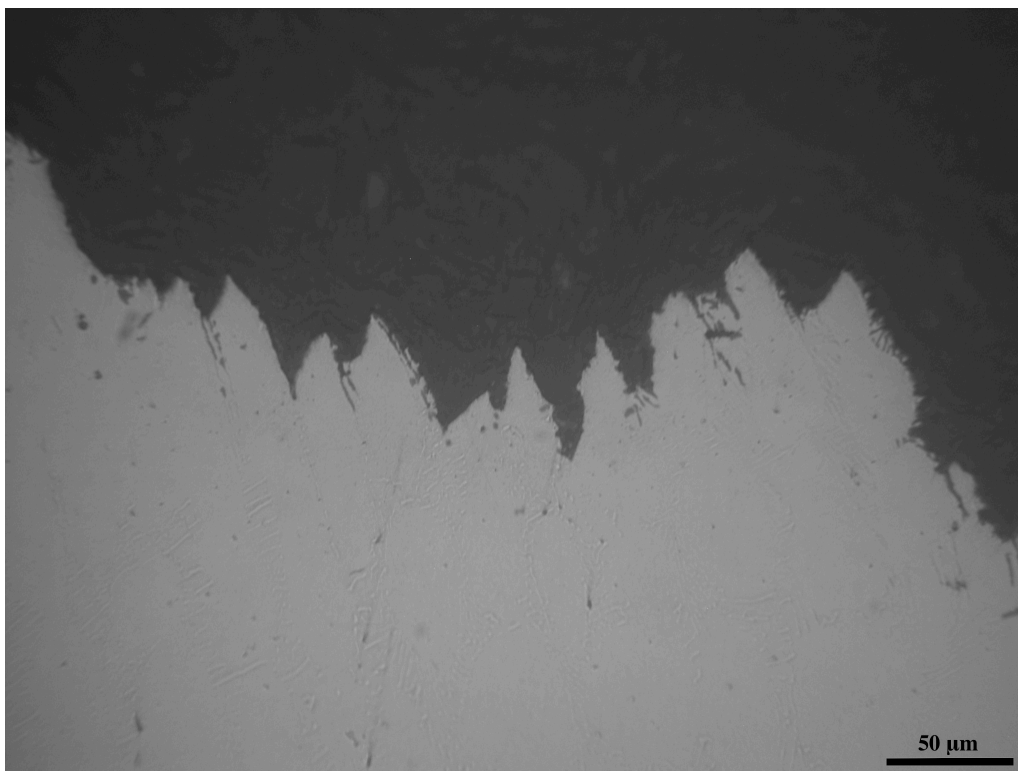


Figure 113. Un-etched microstructure of specimen S2 (rupture surface); magnification: 500X.

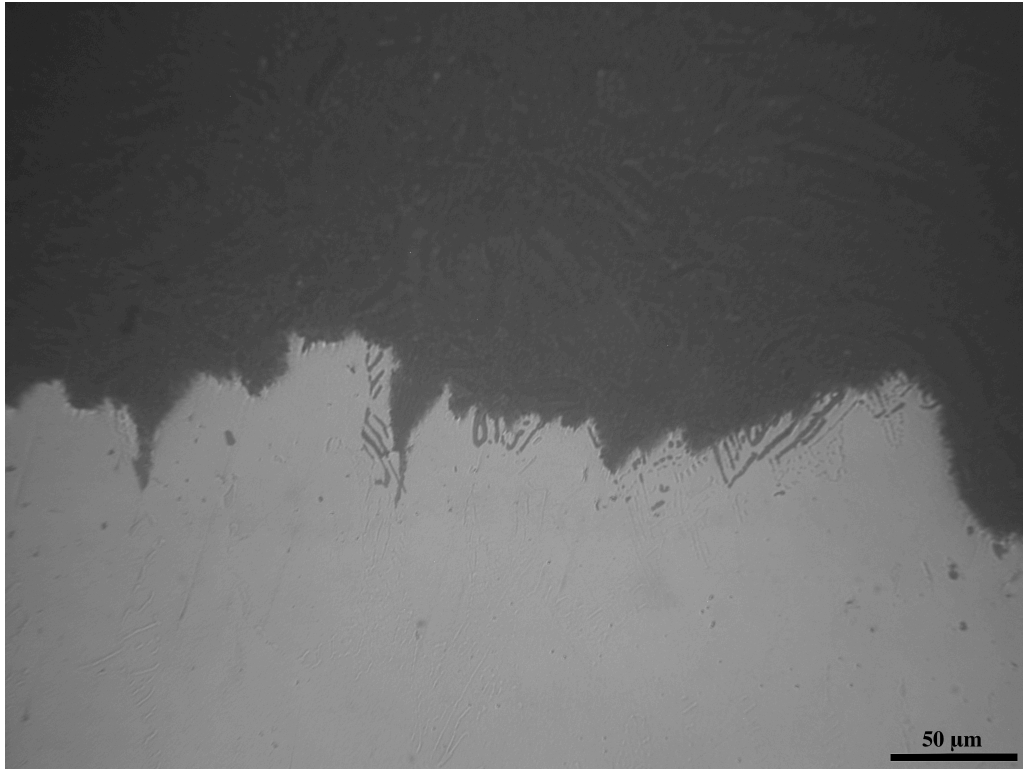


Figure 114. Un-etched microstructure of specimen S2 (rupture surface); magnification: 500X.

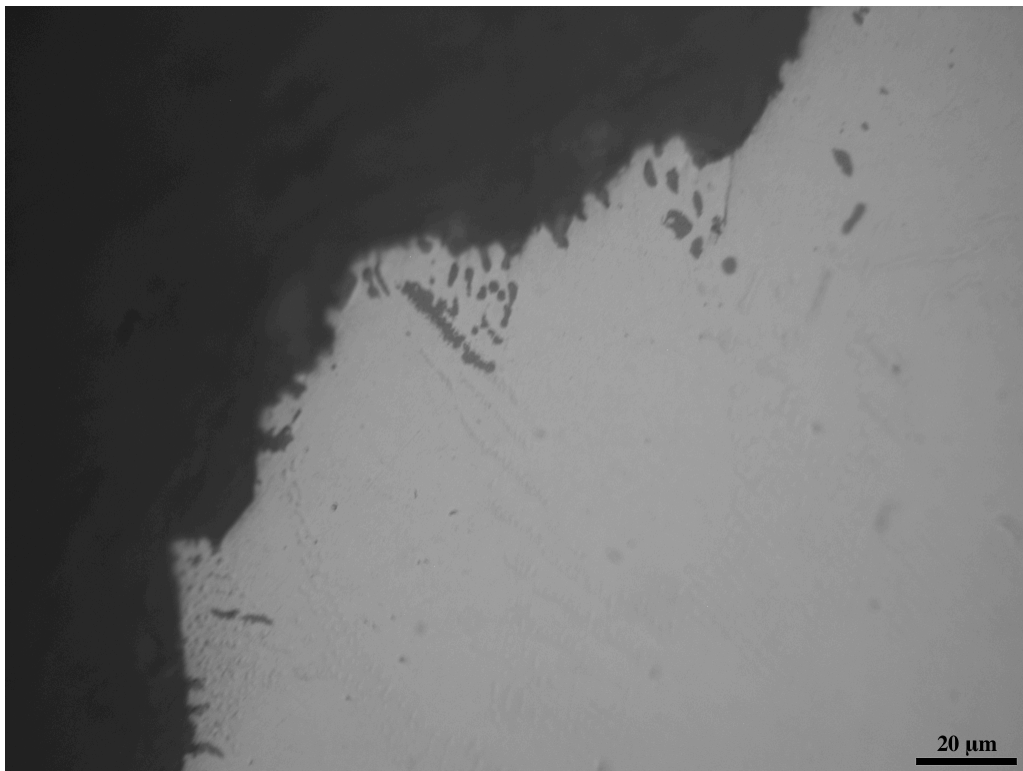


Figure 115. Un-etched microstructure of specimen S2 (rupture surface); magnification: 1000X.

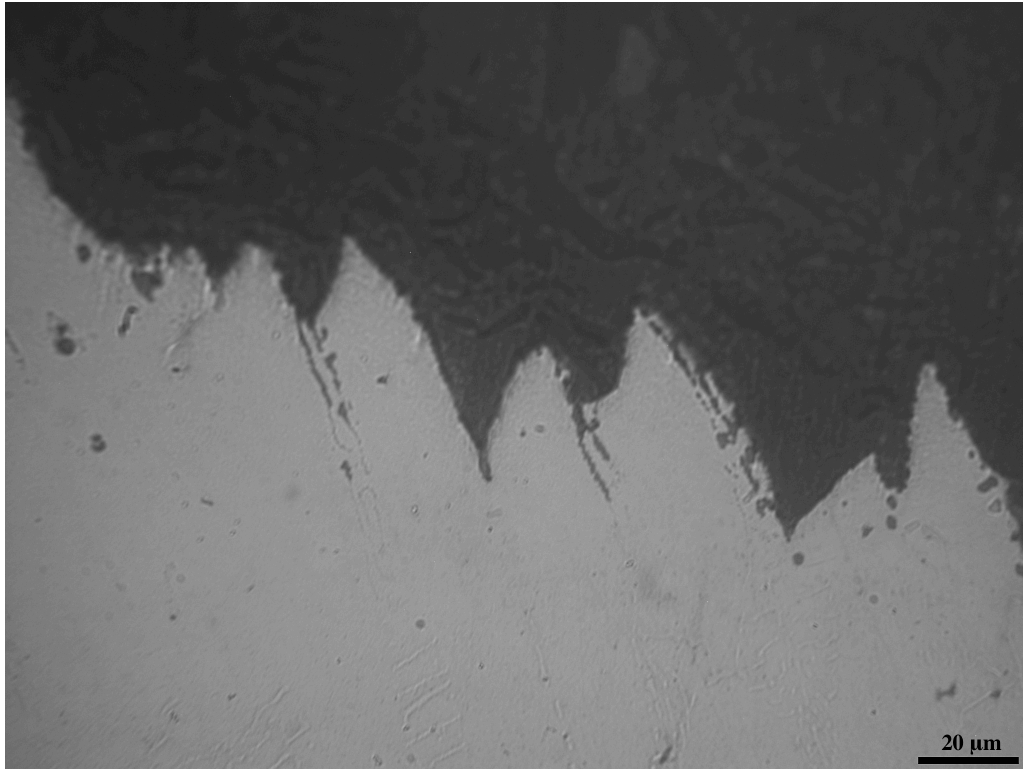


Figure 116. Un-etched microstructure of specimen S2 (rupture surface); magnification: 1000X.

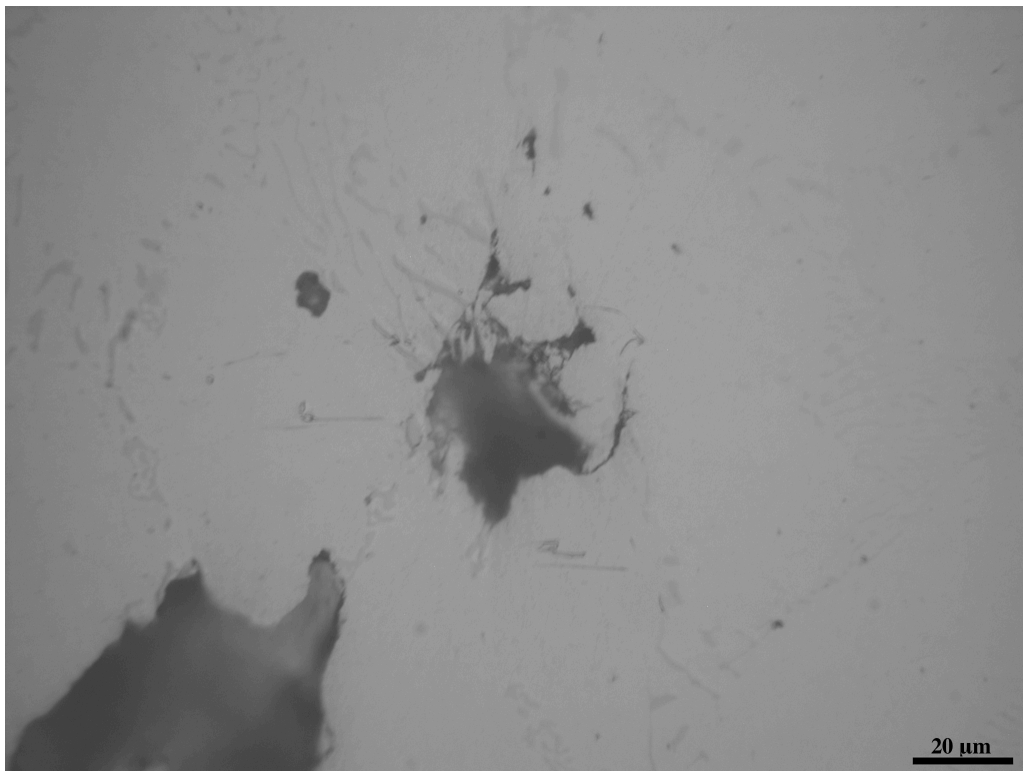


Figure 117. Un-etched microstructure of specimen S2 (at core); magnification: 1000X.

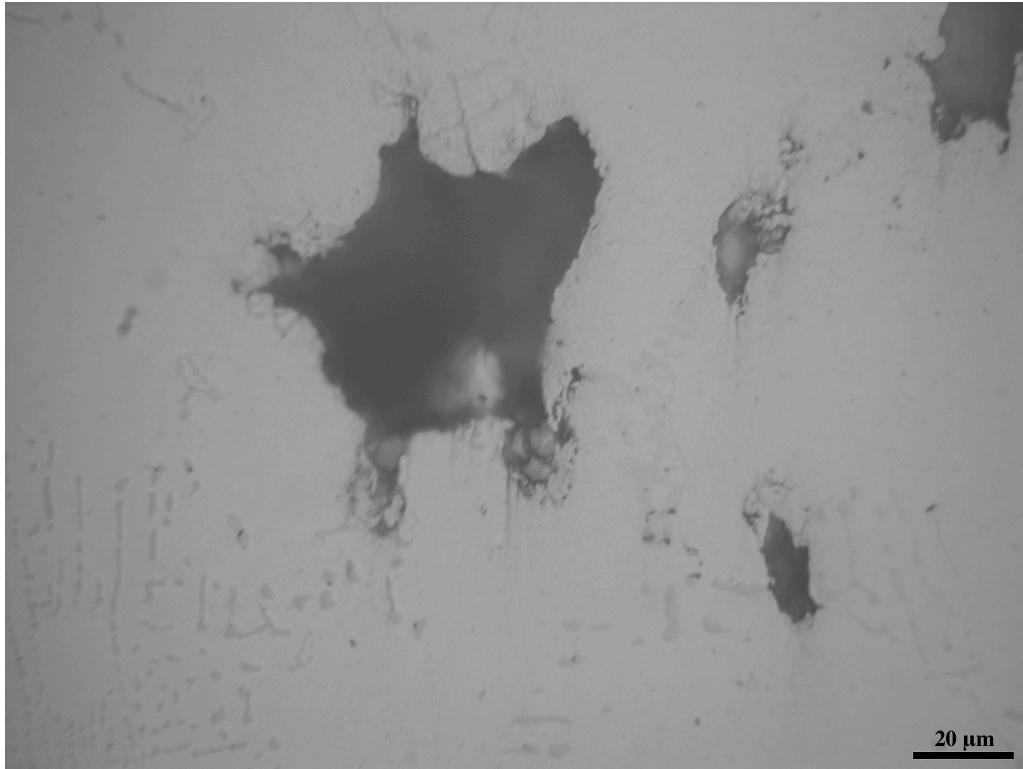


Figure 118. Un-etched microstructure of specimen S2 (at core); magnification: 1000X.

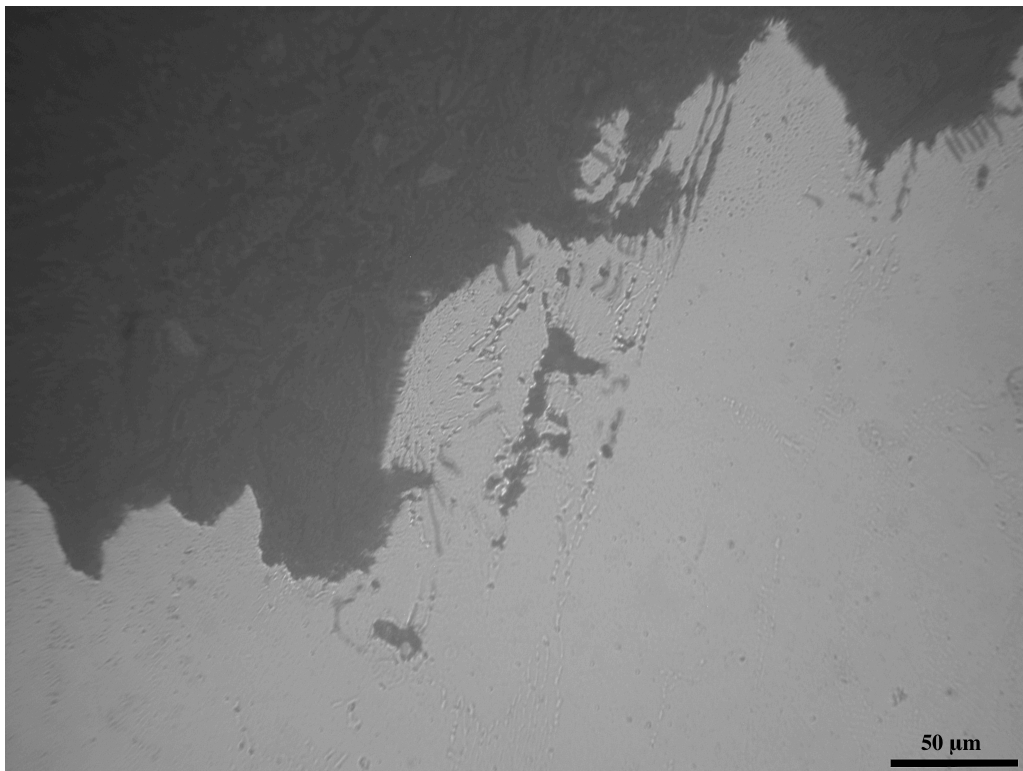


Figure 119. Un-etched microstructure of specimen S4 (rupture surface); magnification: 500X.



Figure 120. Un-etched microstructure of specimen S4 (at core); magnification: 500X.

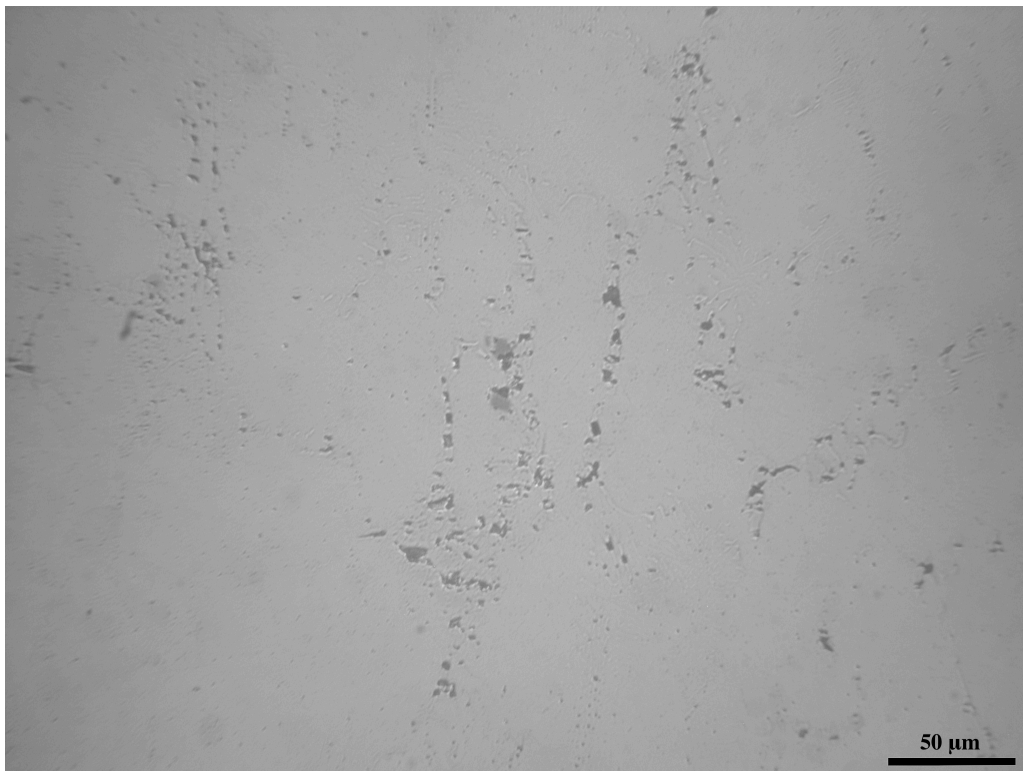


Figure 121. Un-etched microstructure of specimen S4 (at core); magnification: 500X.

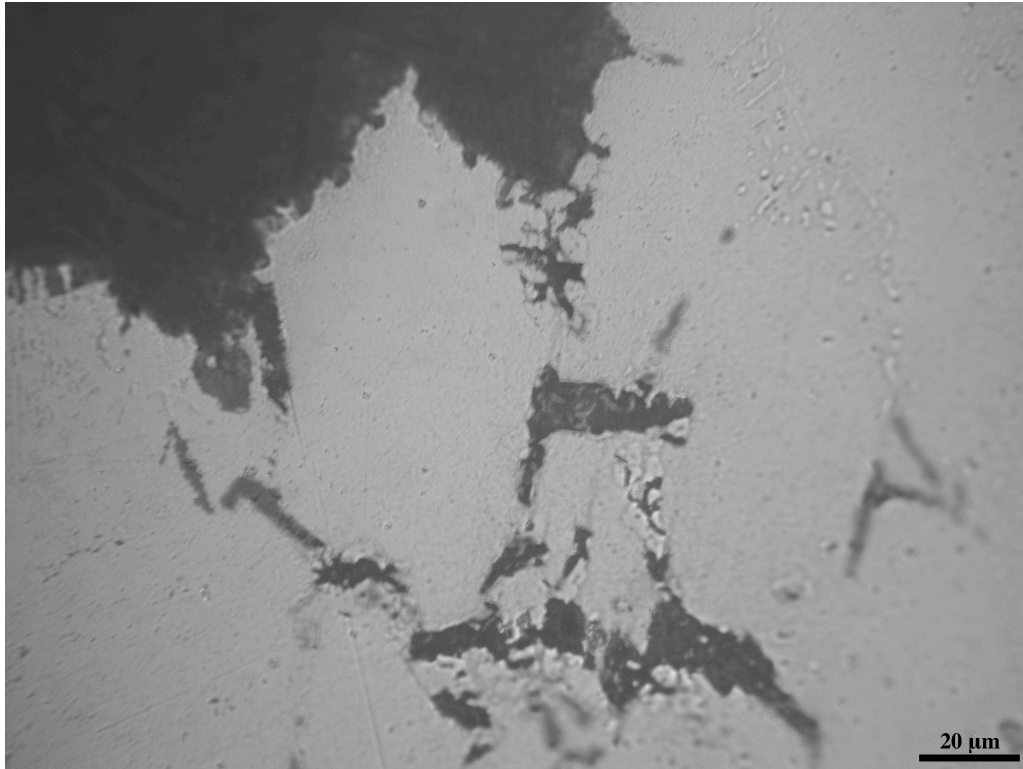


Figure 122. Un-etched microstructure of specimen S4 (rupture surface); magnification: 1000X.

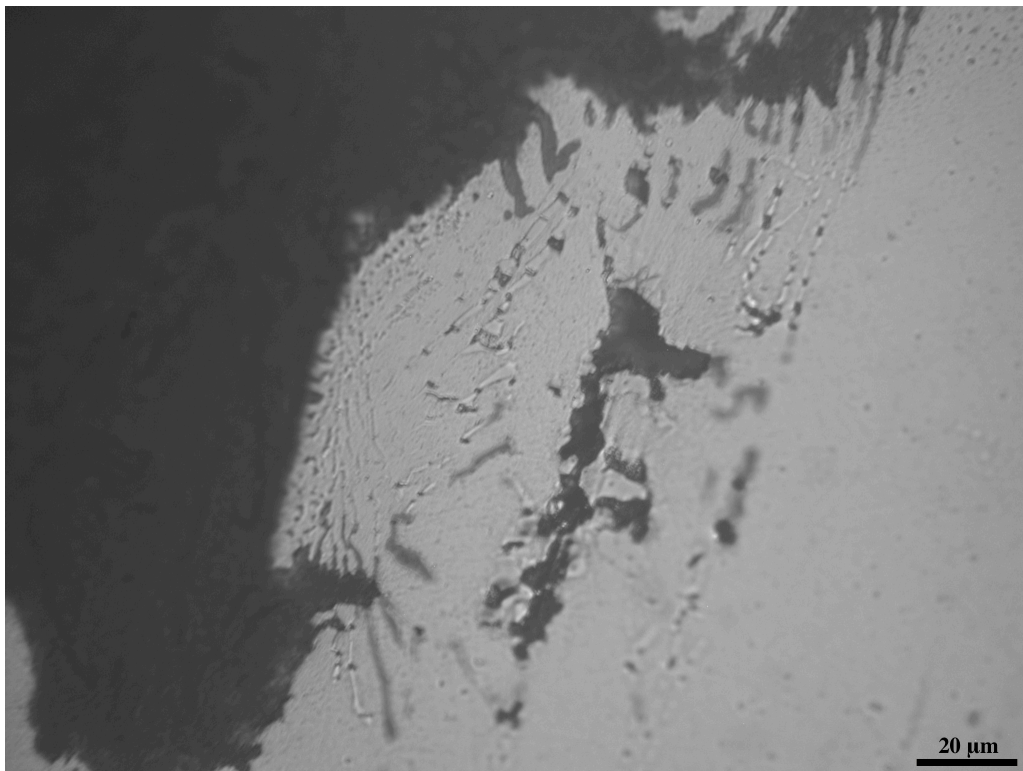


Figure 123. Un-etched microstructure of specimen S4 (rupture surface); magnification: 1000X.



Figure 124. Un-etched microstructure of specimen S4 (at core); magnification: 1000X.

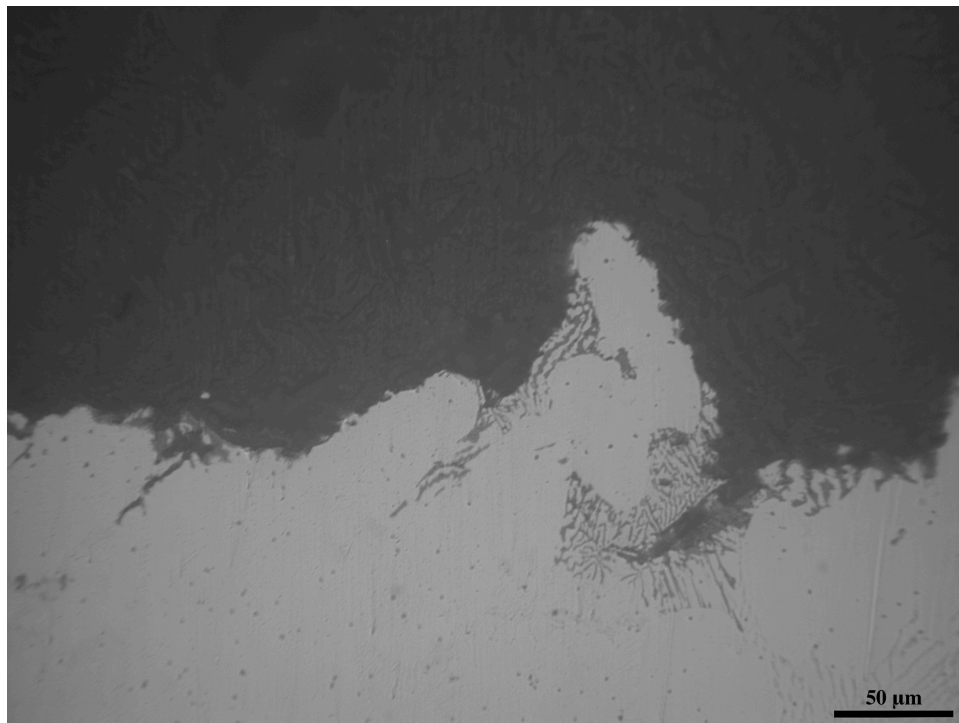


Figure 125. Un-etched microstructure of specimen S5, set 128 (rupture surface); magnification: 500X.

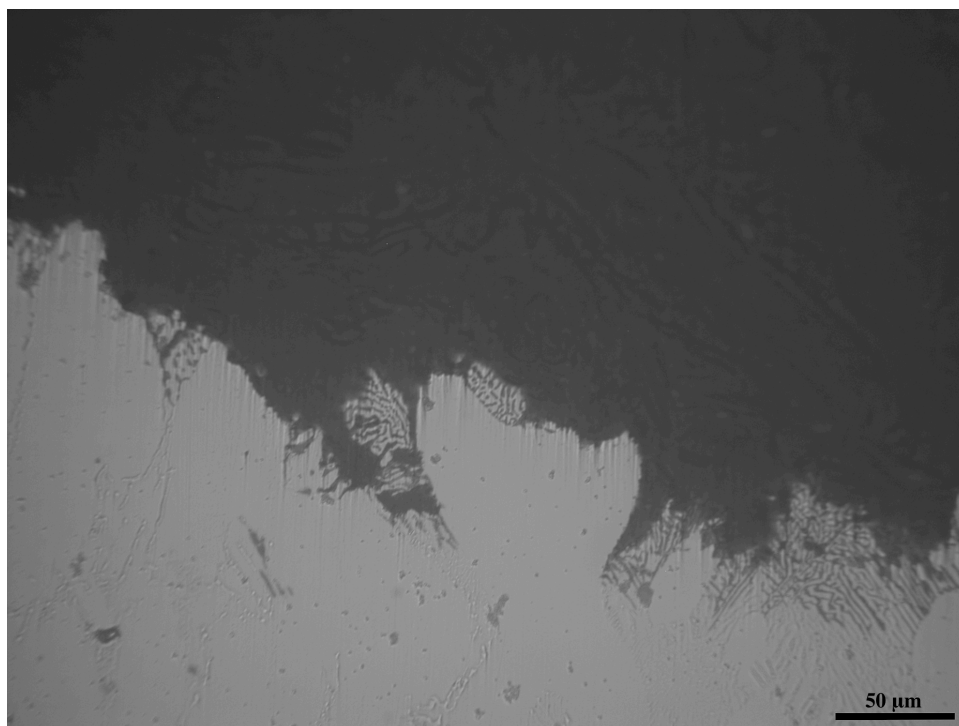


Figure 126. Un-etched microstructure of specimen S5, set 128 (rupture surface); magnification: 500X.

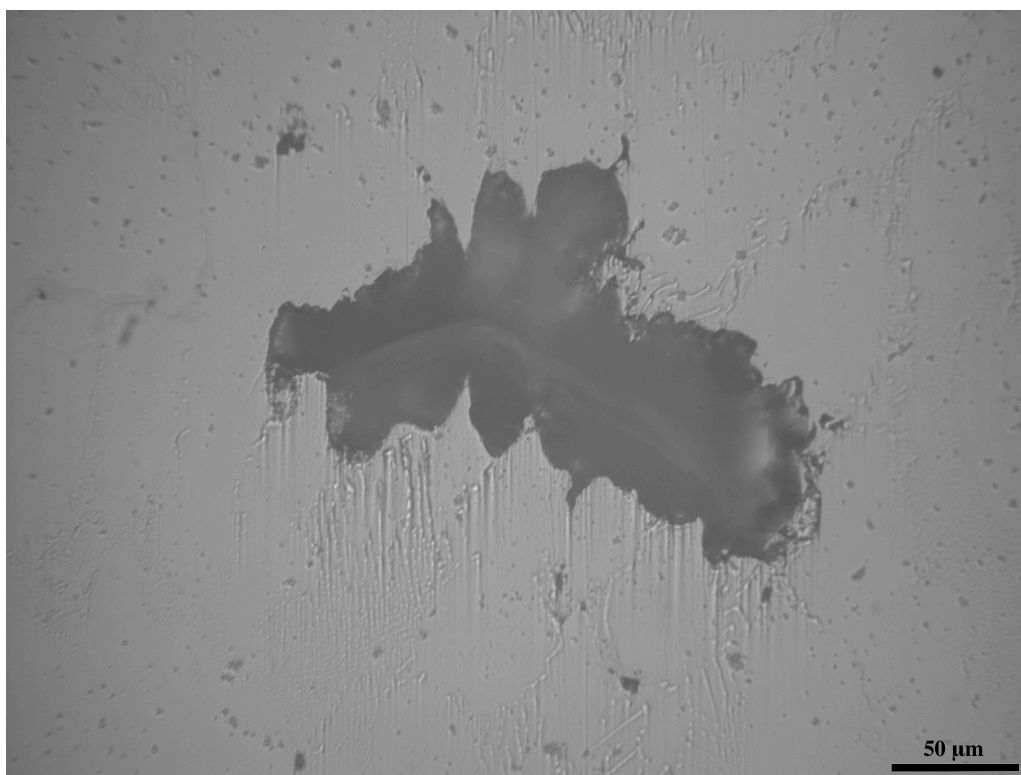


Figure 127. Un-etched microstructure of specimen S5, set 128 (core); magnification: 500X.

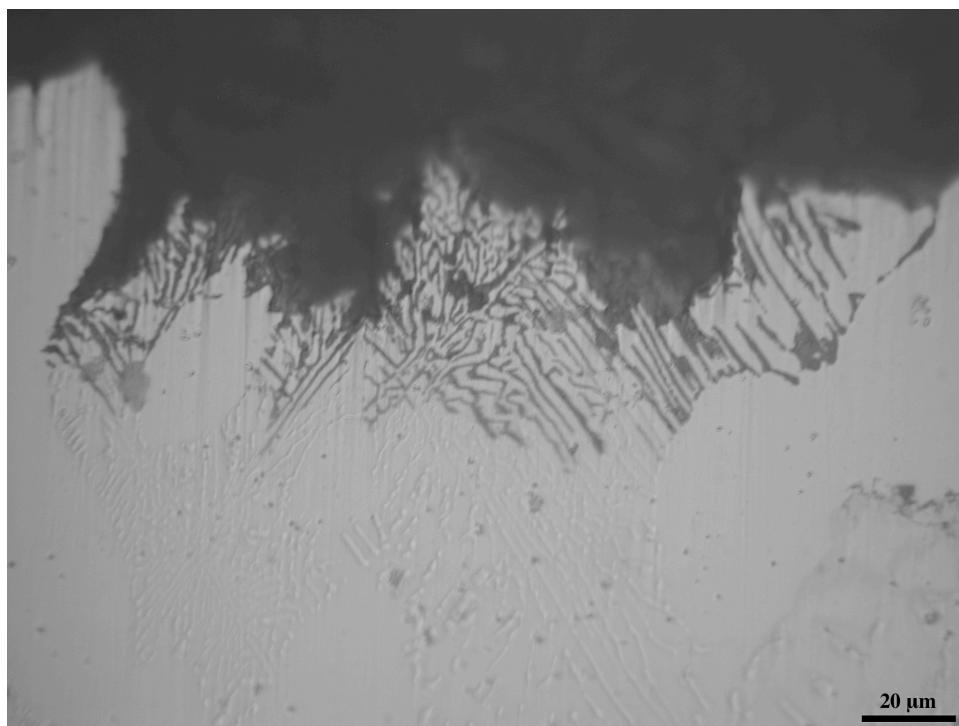


Figure 128. Un-etched microstructure of specimen S5, set 128 (rupture surface); magnification: 1000X.

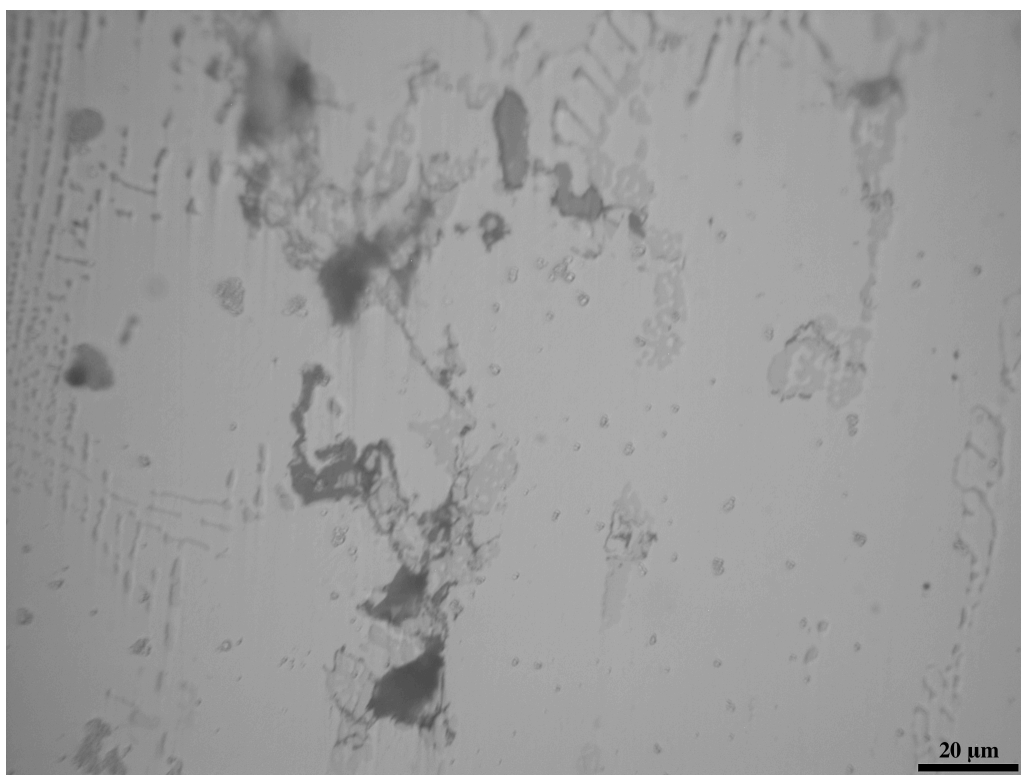


Figure 129. Un-etched microstructure of specimen S5, set 128 (at core); magnification: 1000X.

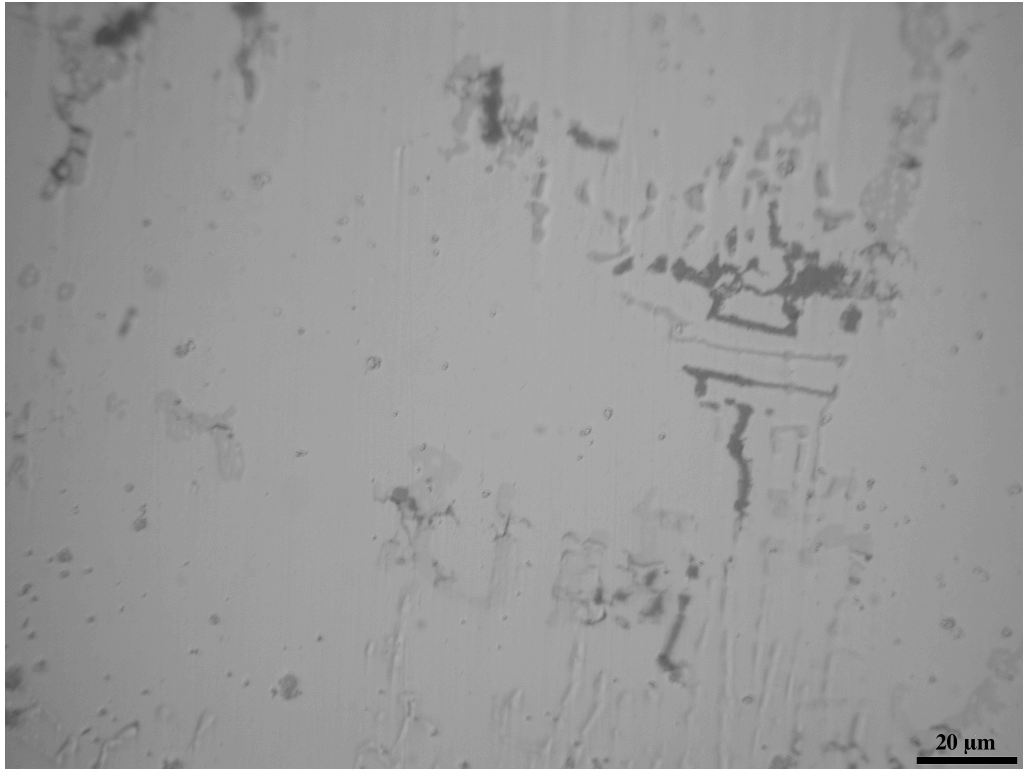


Figure 130. Un-etched microstructure of specimen S5, set 128 (at core); magnification: 1000X.

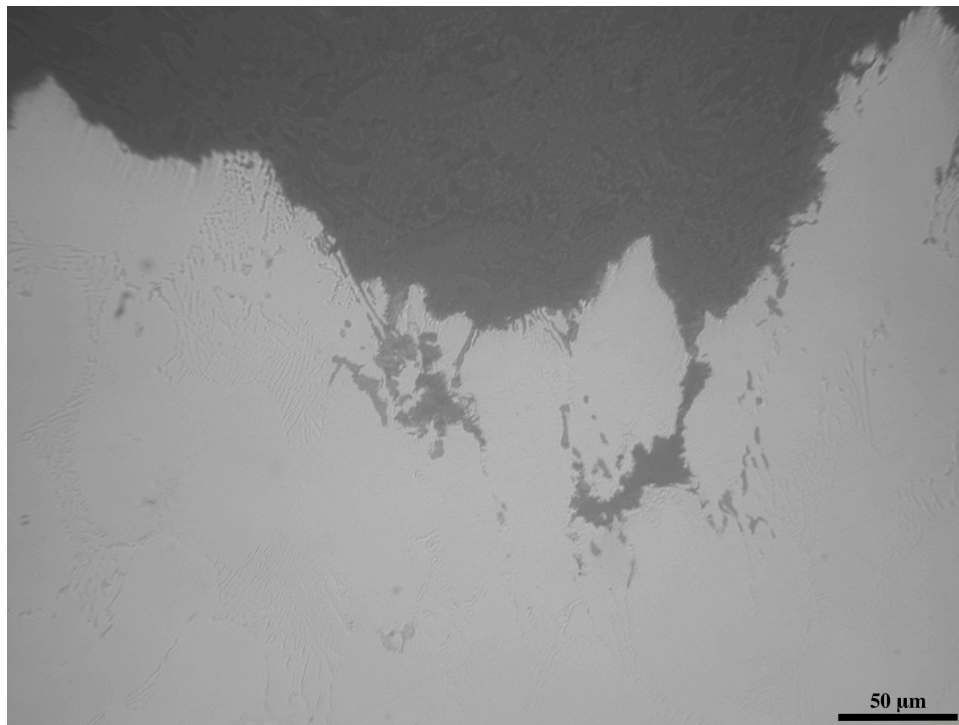


Figure 131. Un-etched microstructure of specimen S5, set 821 (rupture surface); magnification: 500X.

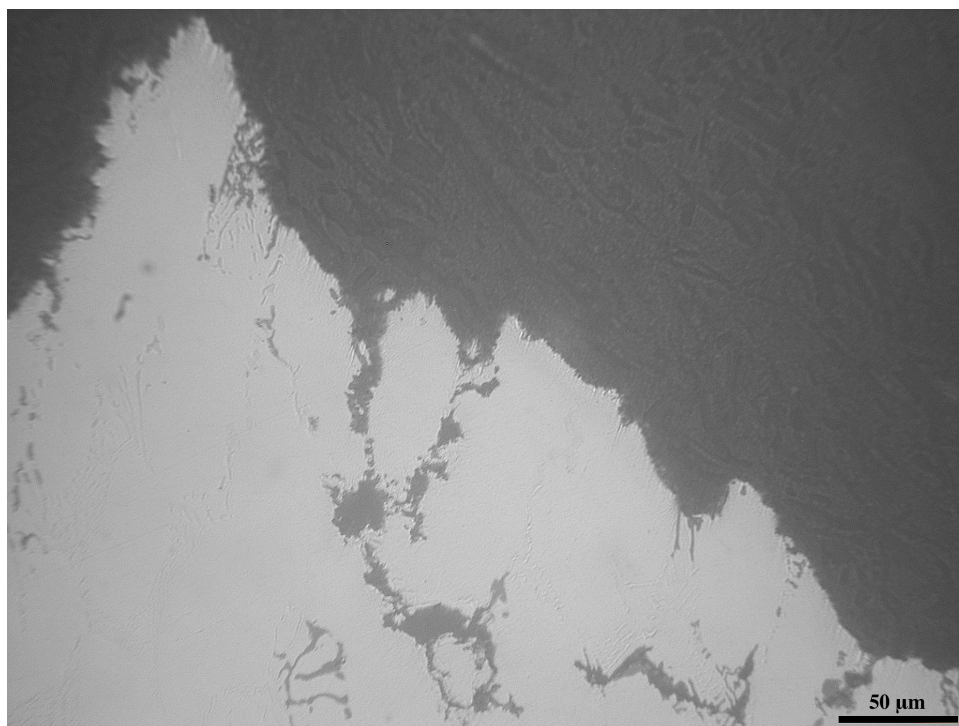


Figure 132. Un-etched microstructure of specimen S5, set 821 (rupture surface); magnification: 500X.

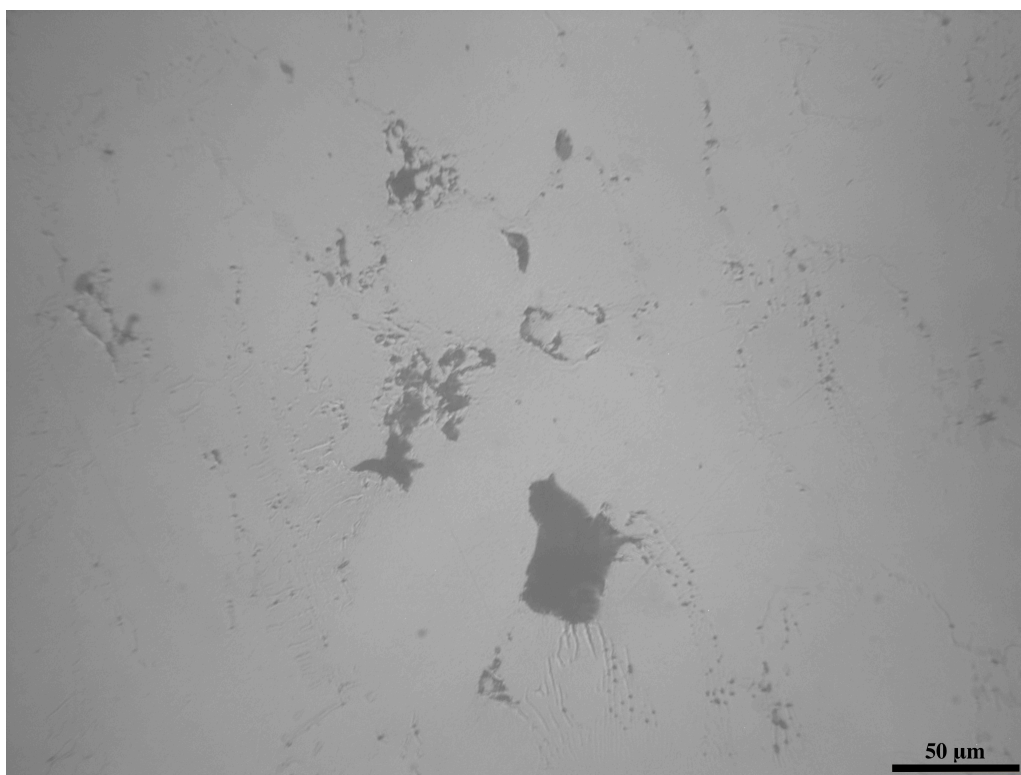


Figure 133. Un-etched microstructure of specimen S5, set 821 (at core); magnification: 500X.

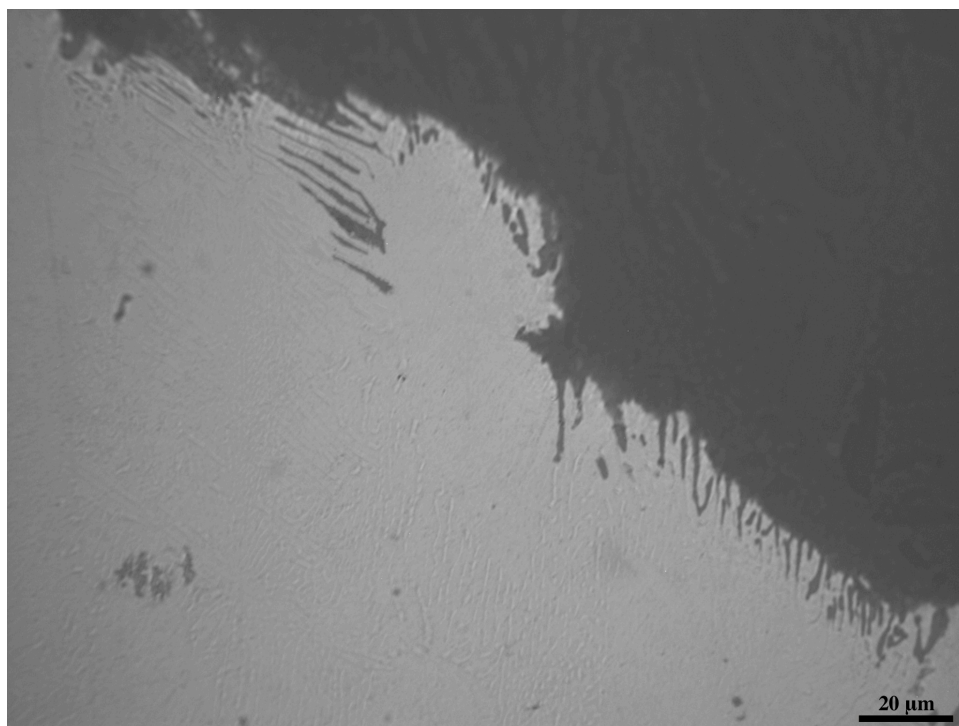


Figure 134 Un-etched microstructure of specimen S5, set 821 (rupture surface); magnification: 1000X.

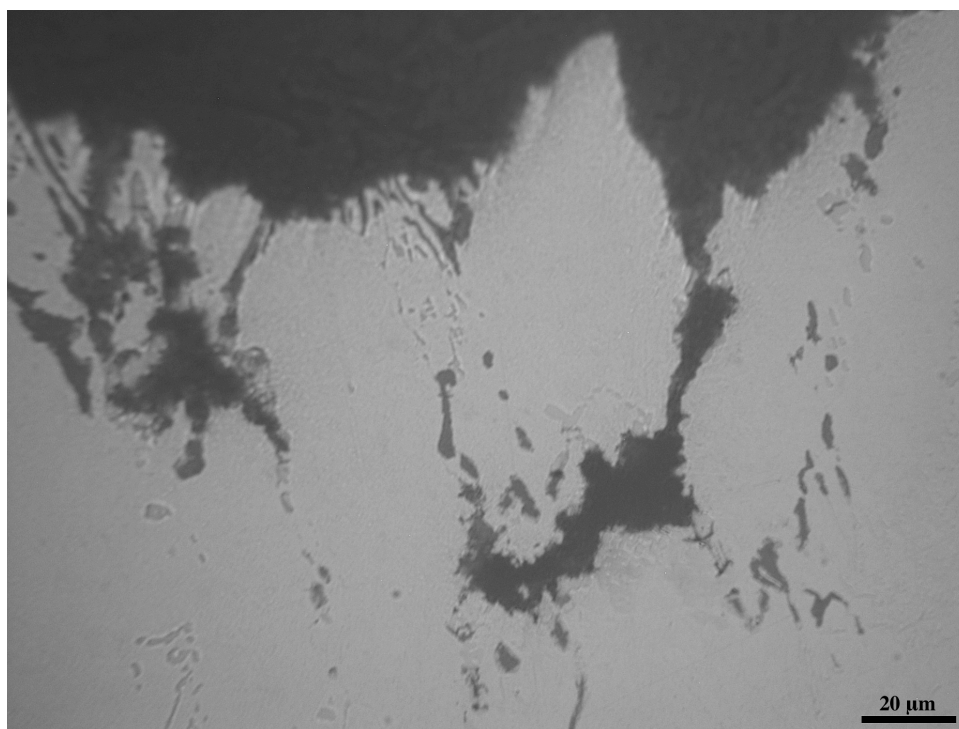


Figure 135. Un-etched microstructure of specimen S5, set 821 (rupture surface); magnification: 1000X.

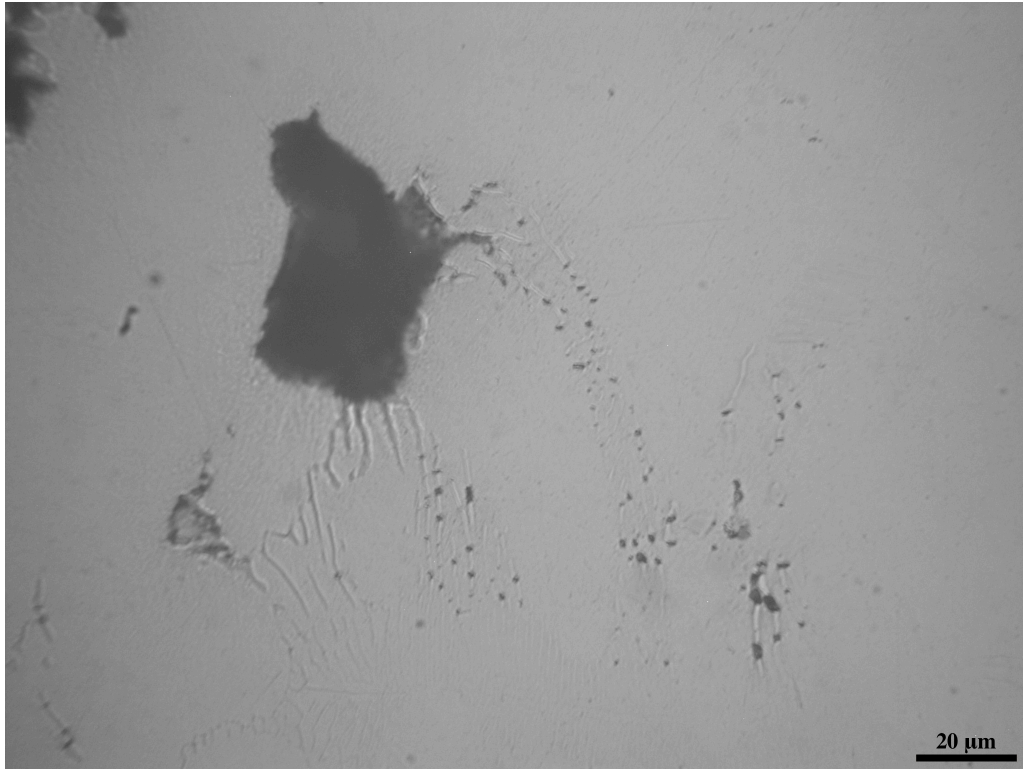


Figure 136. Un-etched microstructure of specimen S5, set 821 (at core); magnification: 1000X.

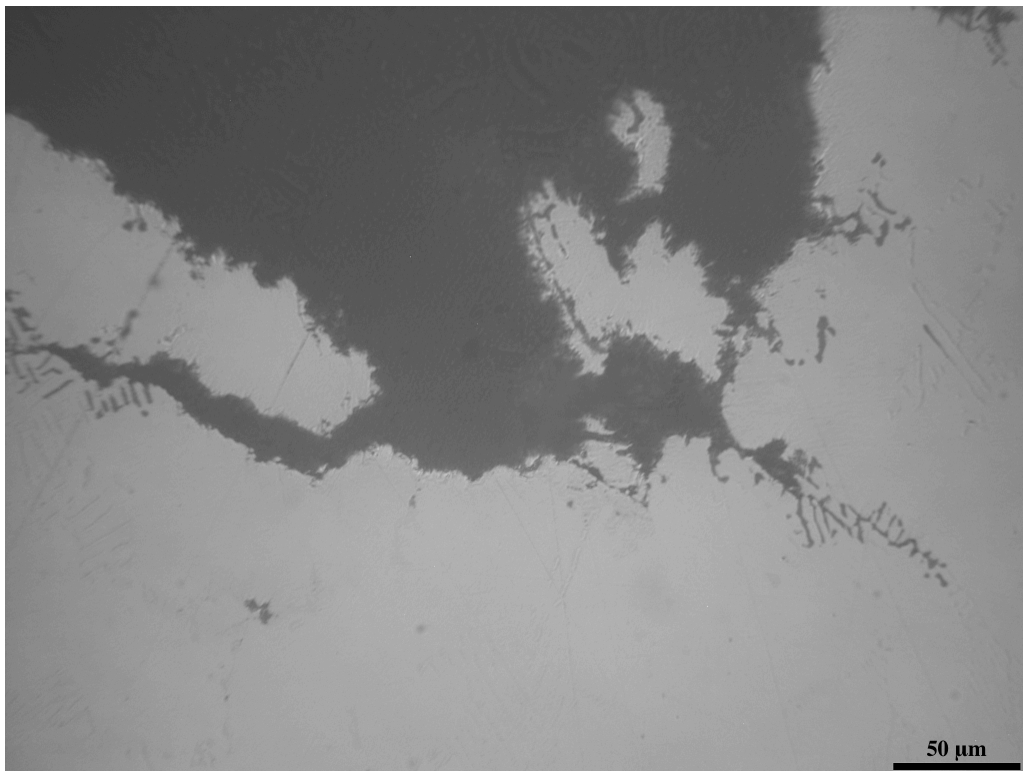


Figure 137. Un-etched microstructure of specimen S7 (rupture surface); magnification: 500X.

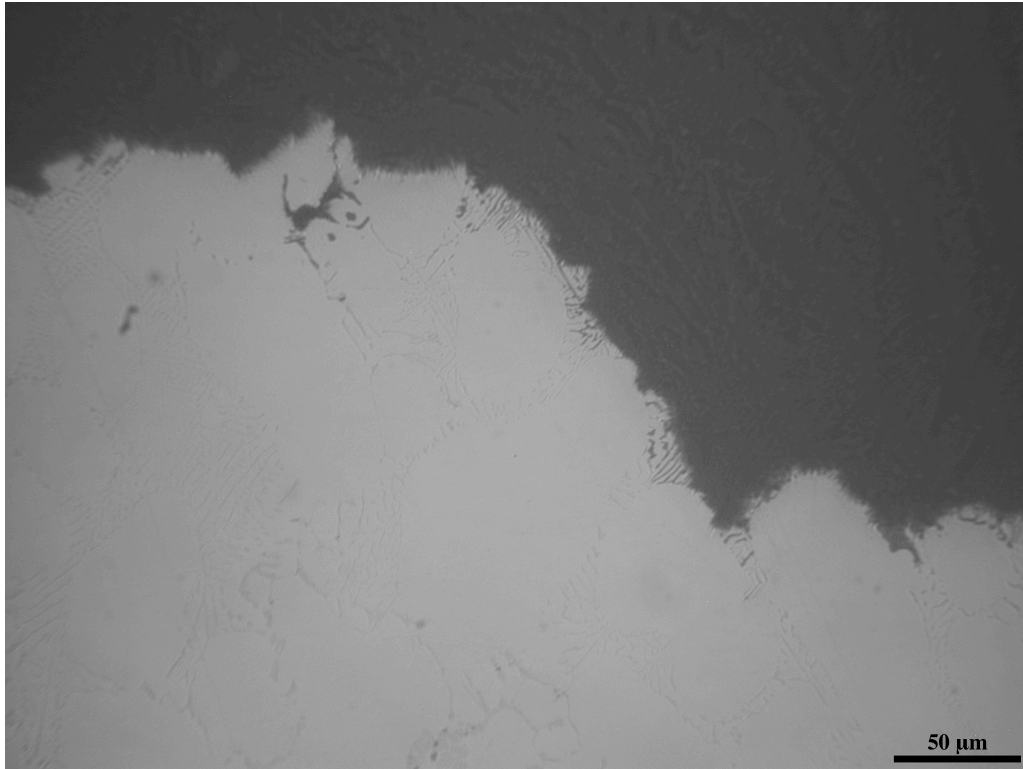


Figure 138. Un-etched microstructure of specimen S7 (rupture surface); magnification: 500X.

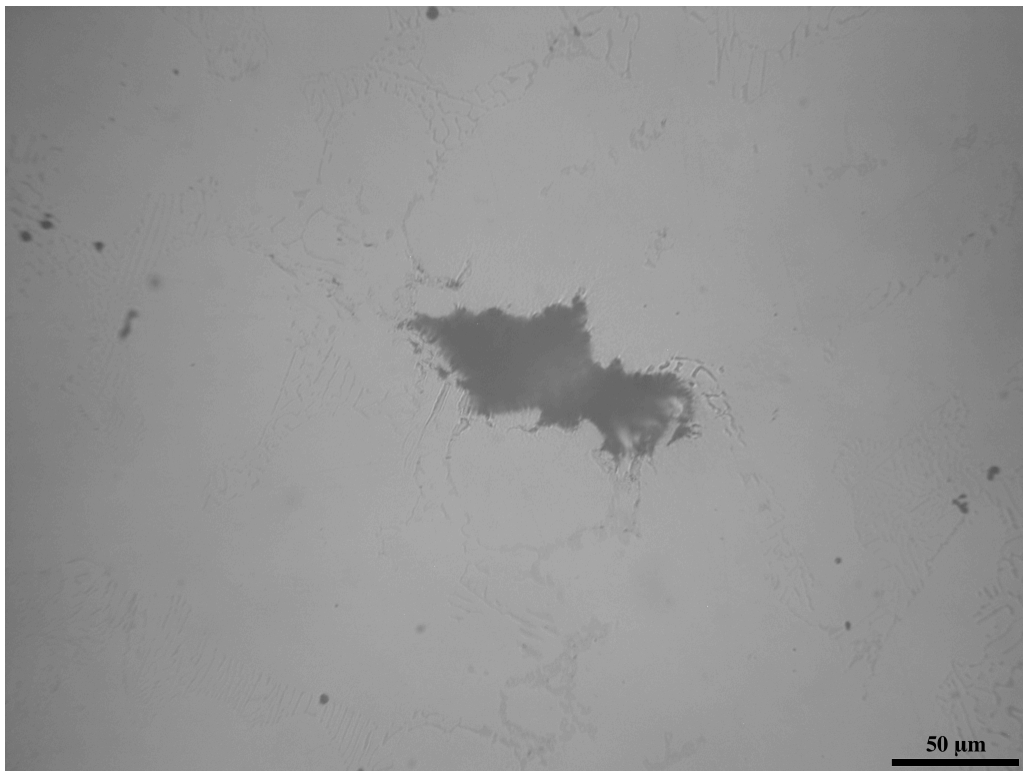


Figure 139. Un-etched microstructure of specimen S7 (at core); magnification: 500X.

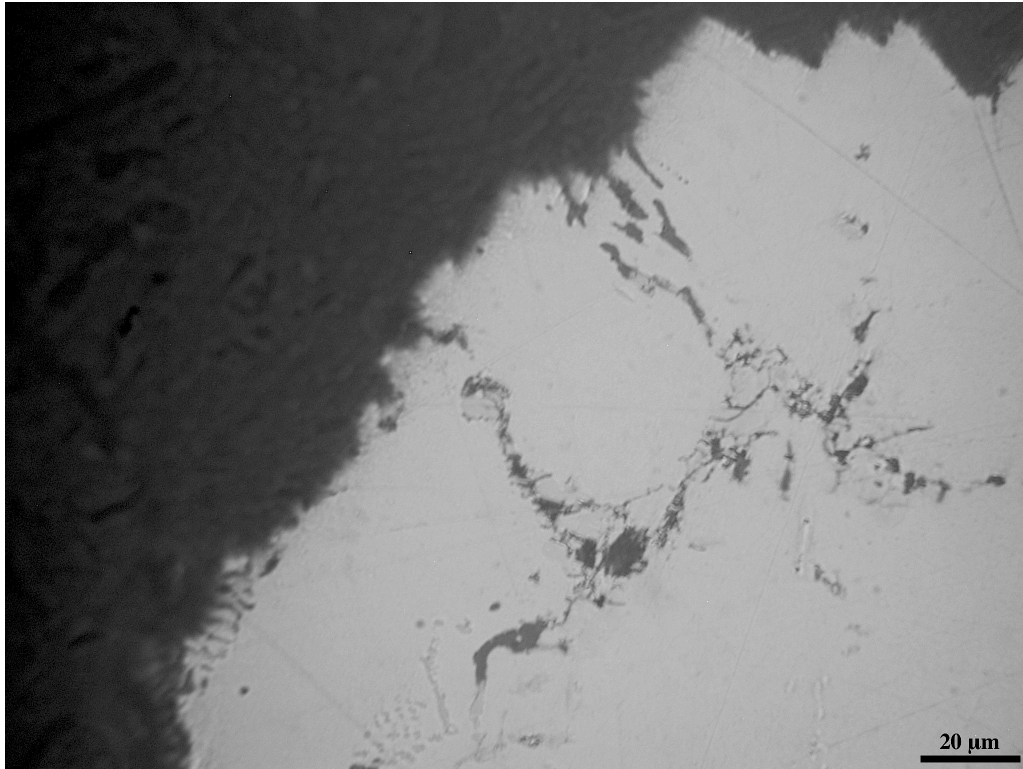


Figure 140. Un-etched microstructure of specimen S7 (rupture surface); magnification: 1000X.

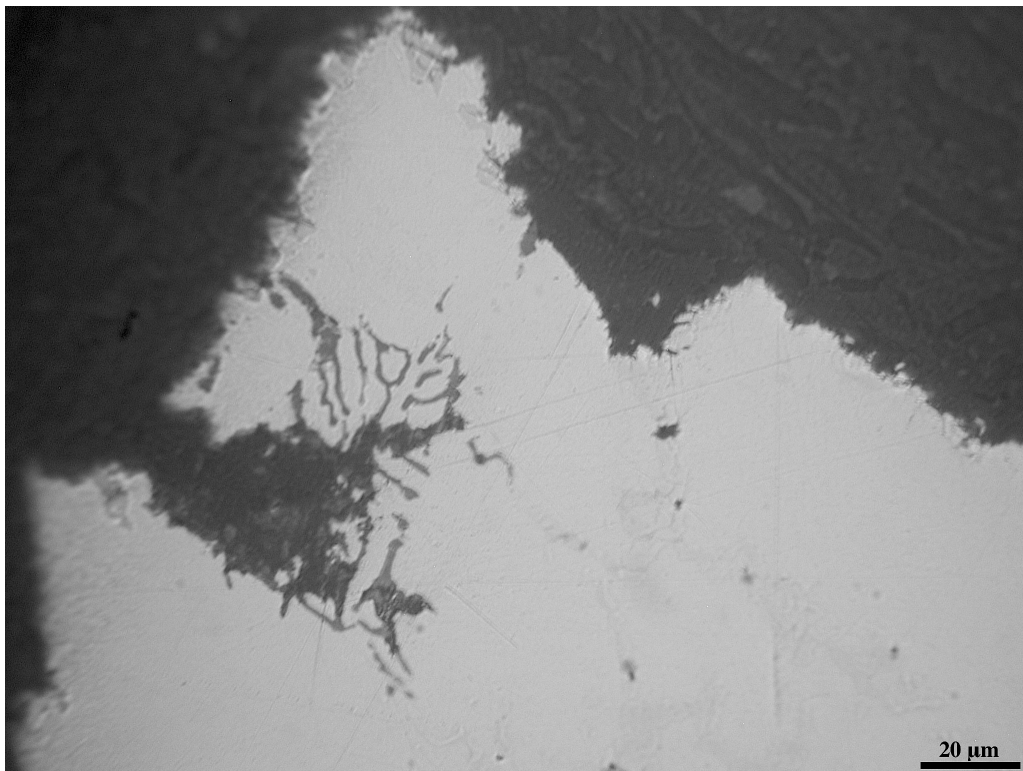


Figure 141. Un-etched microstructure of specimen S7 (rupture surface); magnification: 1000X.



Figure 142. Un-etched microstructure of specimen S7 (at core); magnification: 1000X.

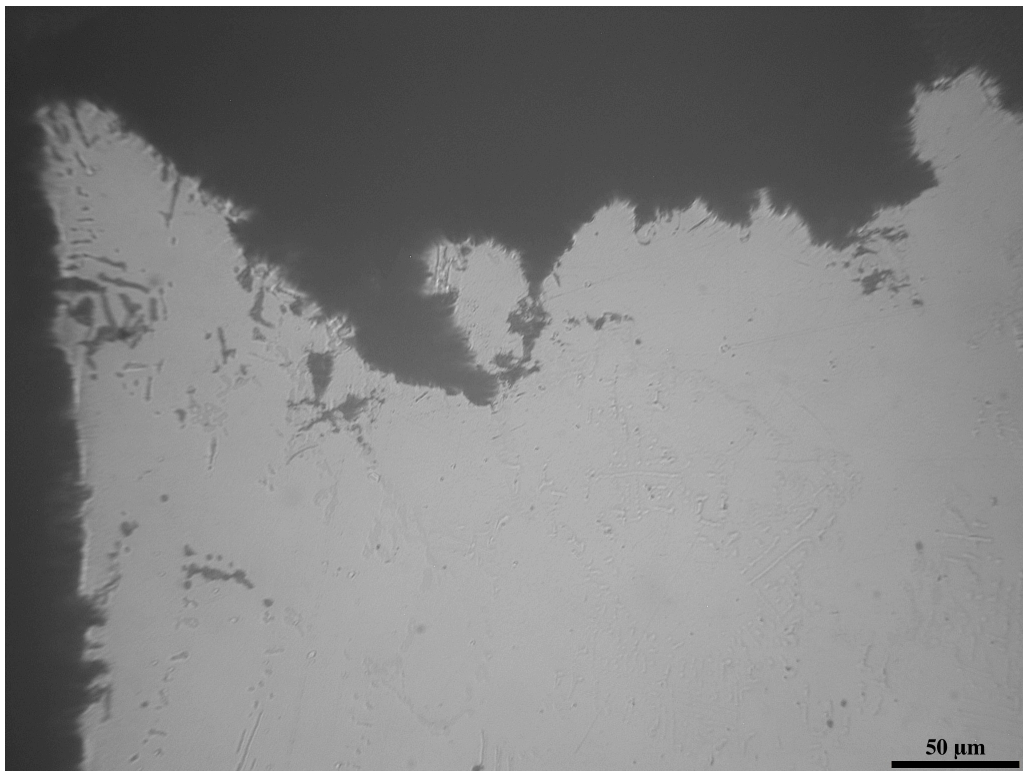


Figure 143. Un-etched microstructure of specimen S9 (rupture surface); magnification: 500X.

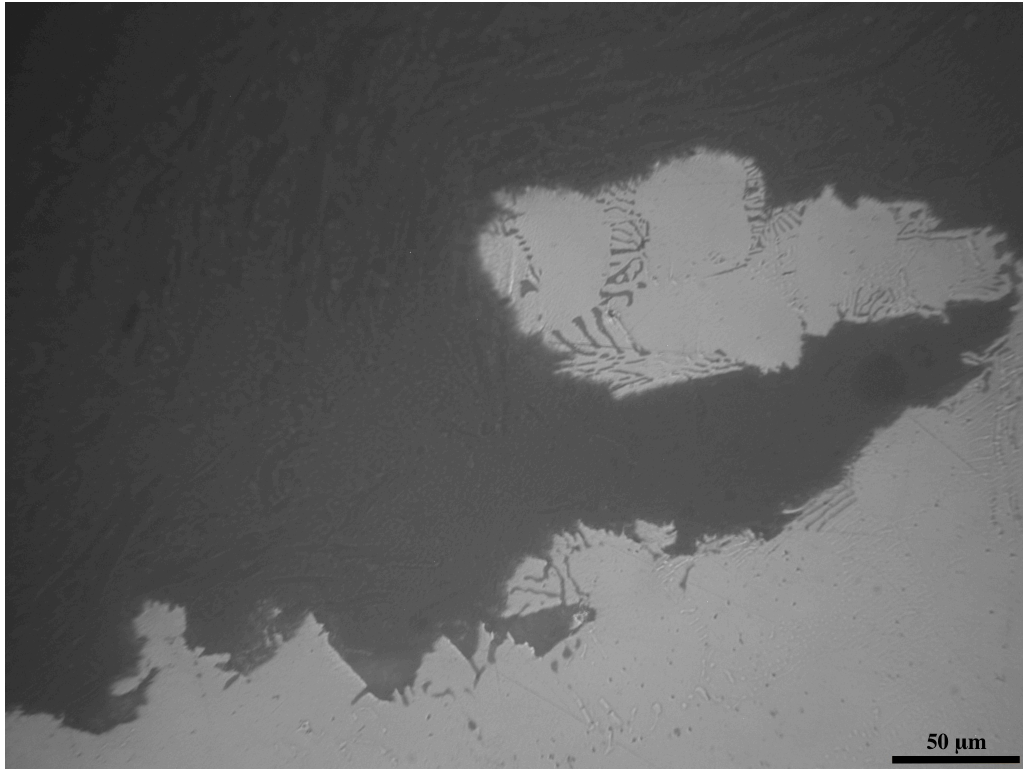


Figure 144. Un-etched microstructure of specimen S9 (rupture surface); magnification: 500X.

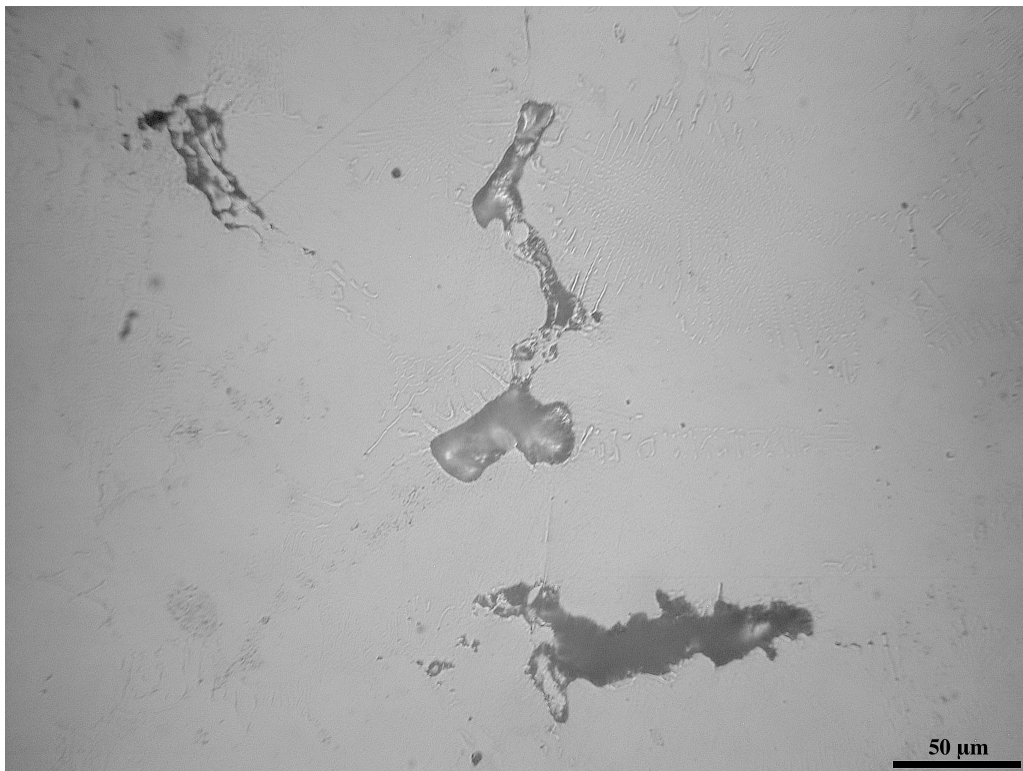


Figure 145. Un-etched microstructure of specimen S9 (at core); magnification: 500X.

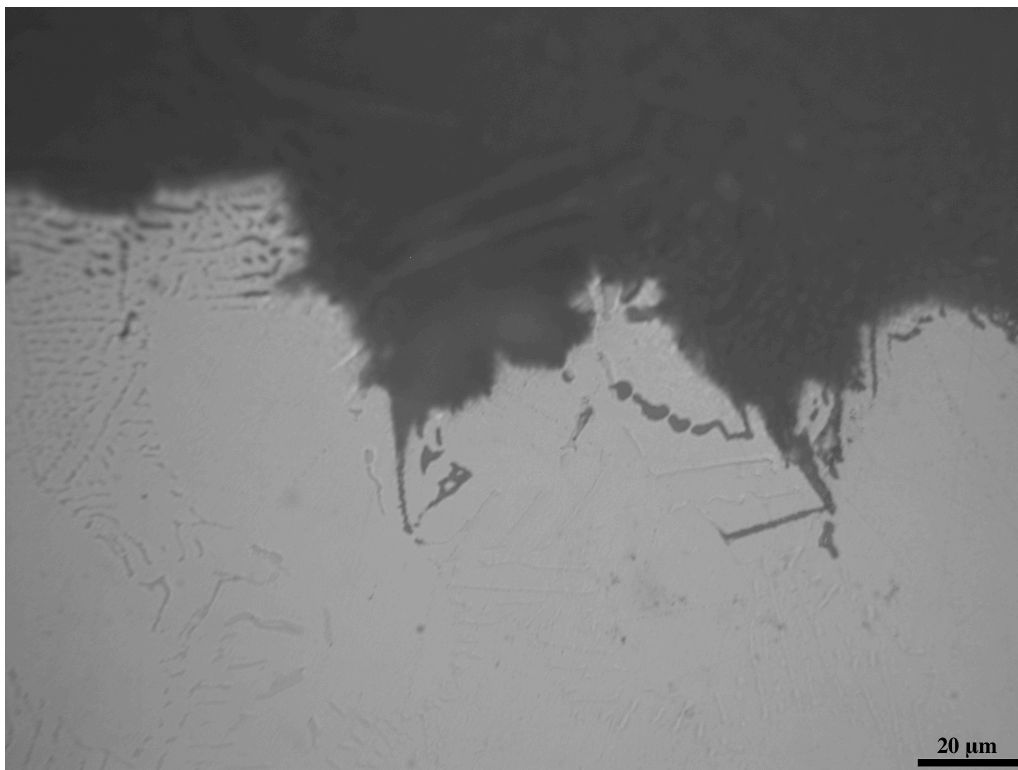


Figure 146. Un-etched microstructure of specimen S9 (rupture surface); magnification: 1000X.

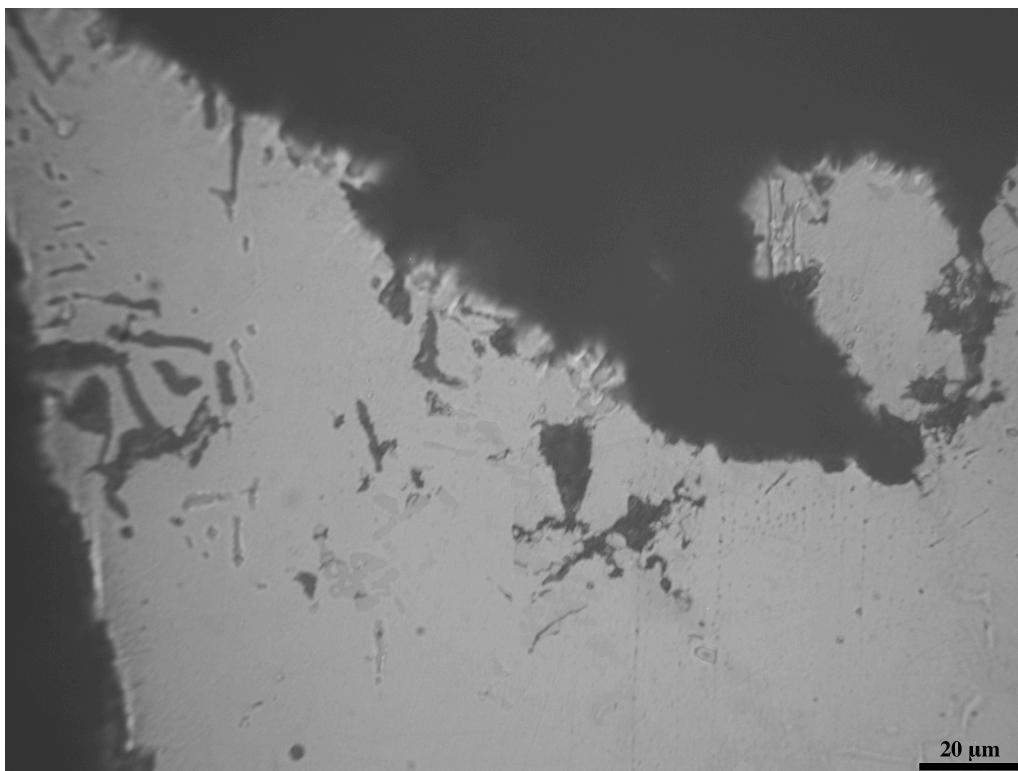


Figure 147. Un-etched microstructure of specimen S9 (rupture surface); magnification: 1000X.

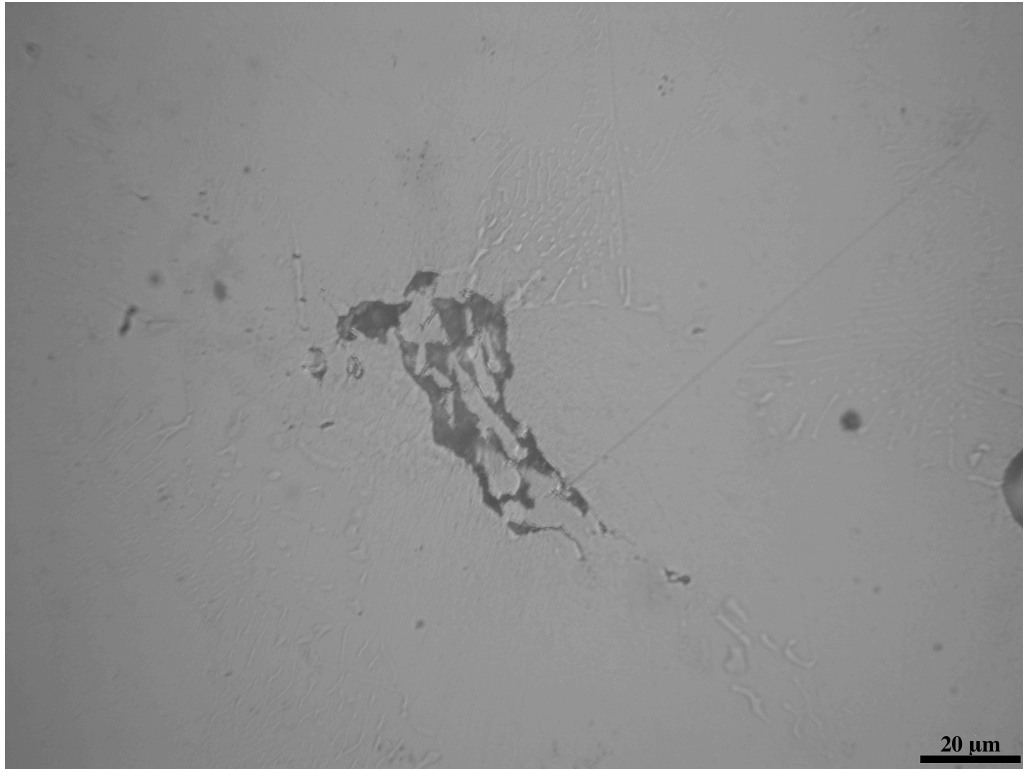


Figure 148. Un-etched microstructure of specimen S9 (at core); magnification: 1000X.

Appendix C

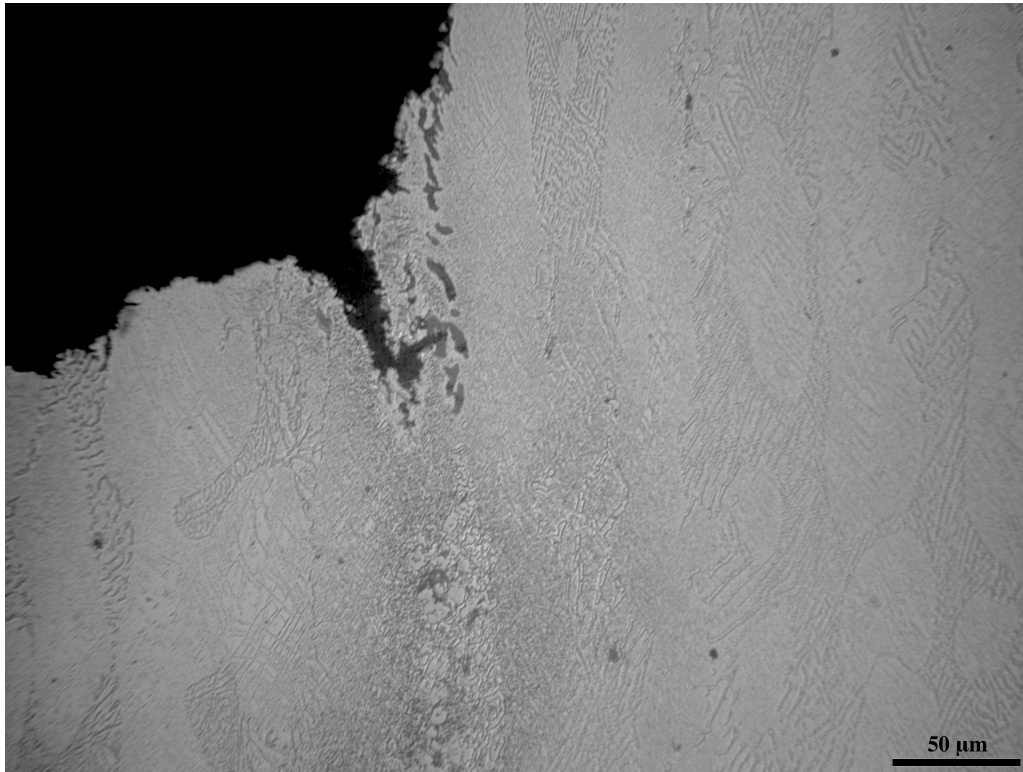


Figure 149. Etched microstructure of specimen S1 (rupture surface); magnification: 500X.

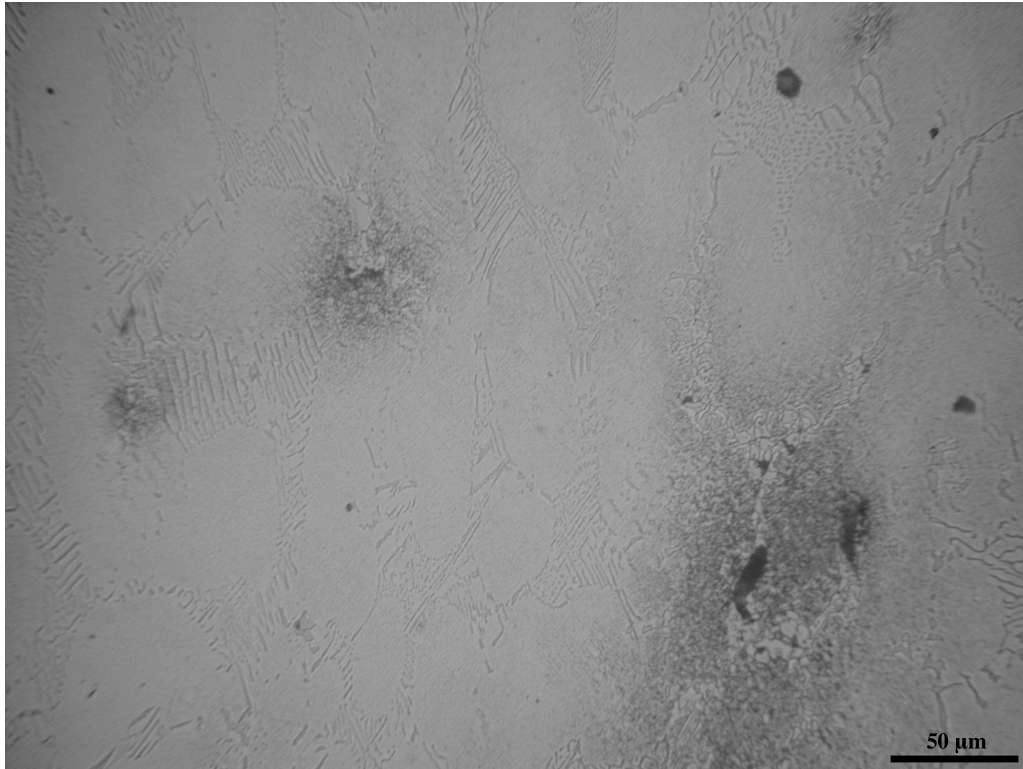


Figure 150. Etched microstructure of specimen S1 (at core); magnification: 500X.

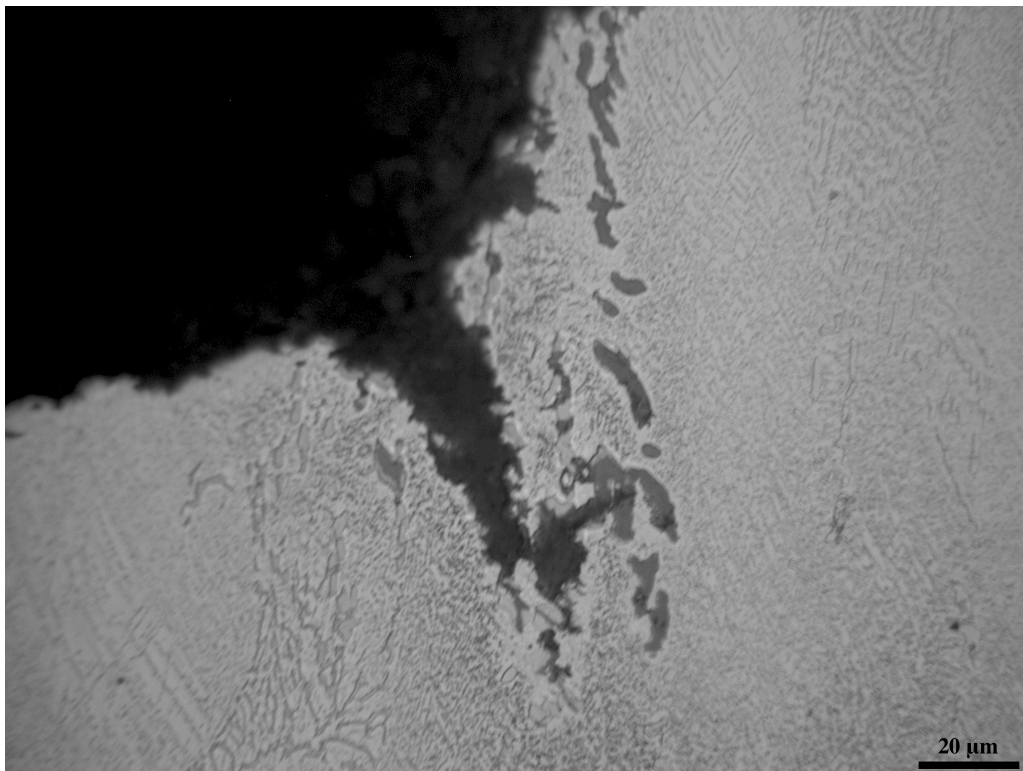


Figure 151. Etched microstructure of specimen S1 (rupture surface); magnification: 1000X.

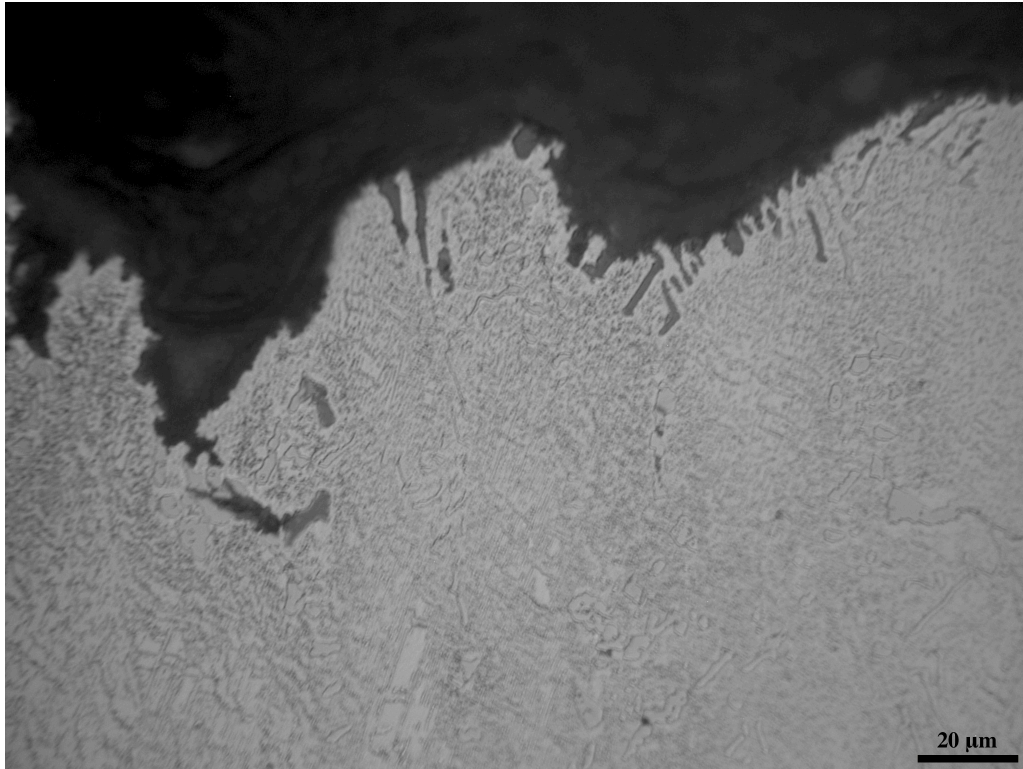


Figure 152. Etched microstructure of specimen S1 (rupture surface); magnification: 1000X.

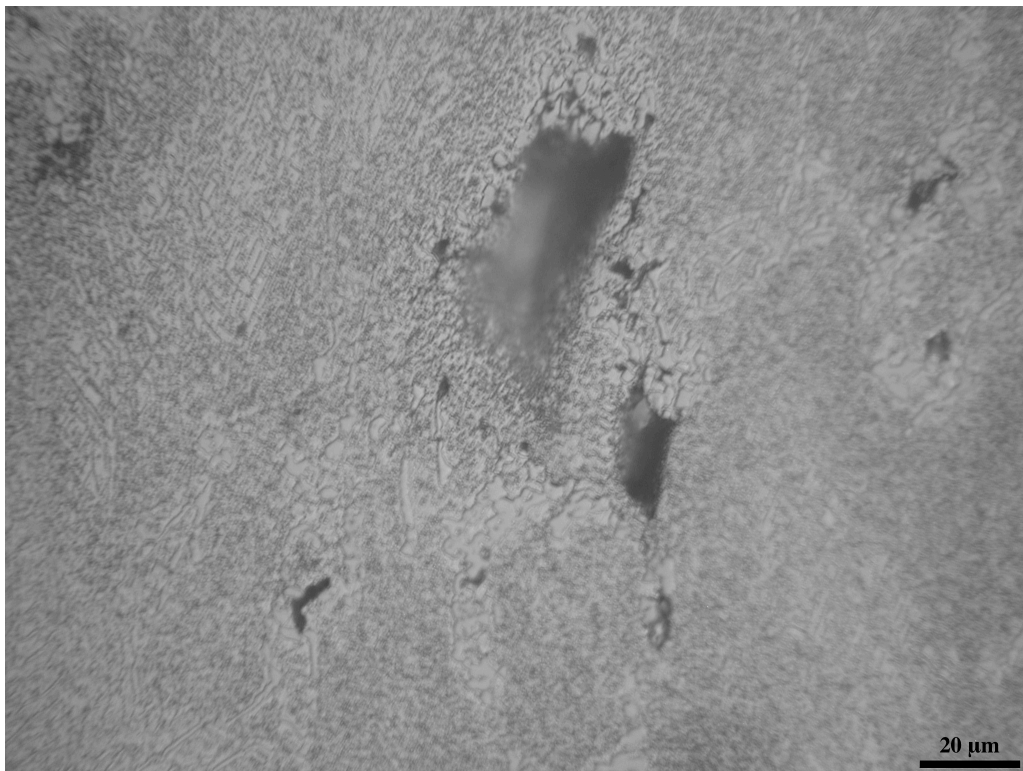


Figure 153. Etched microstructure of specimen S1 (at core); magnification: 1000X.

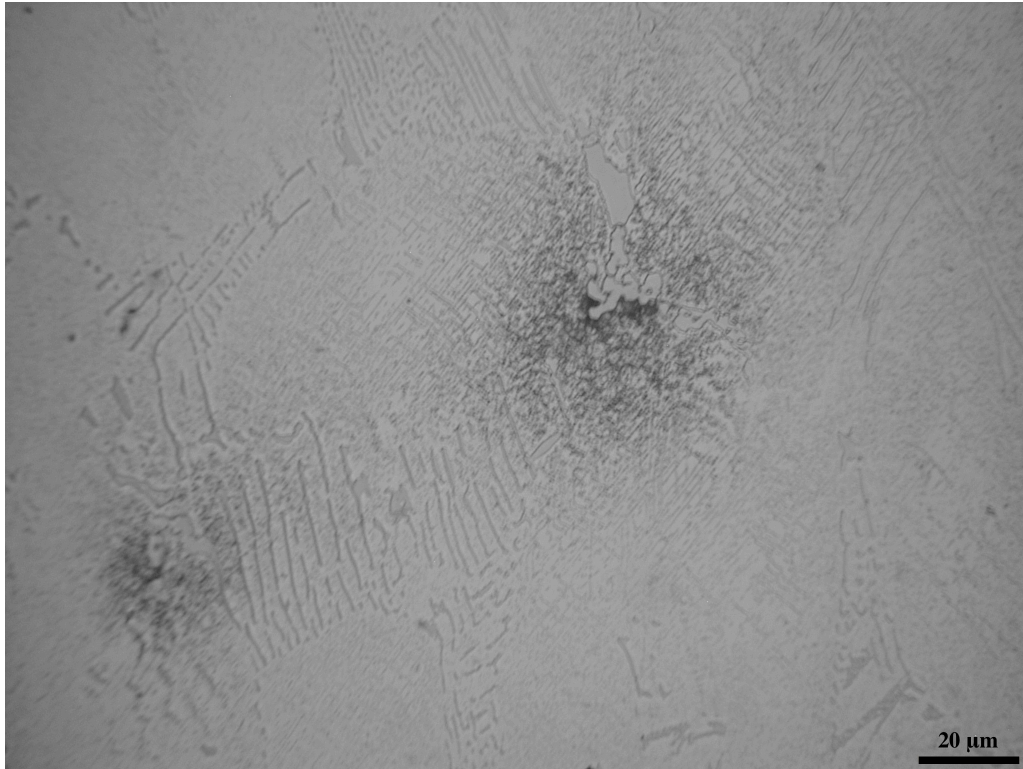


Figure 154. Etched microstructure of specimen S1 (at core); magnification: 1000X.

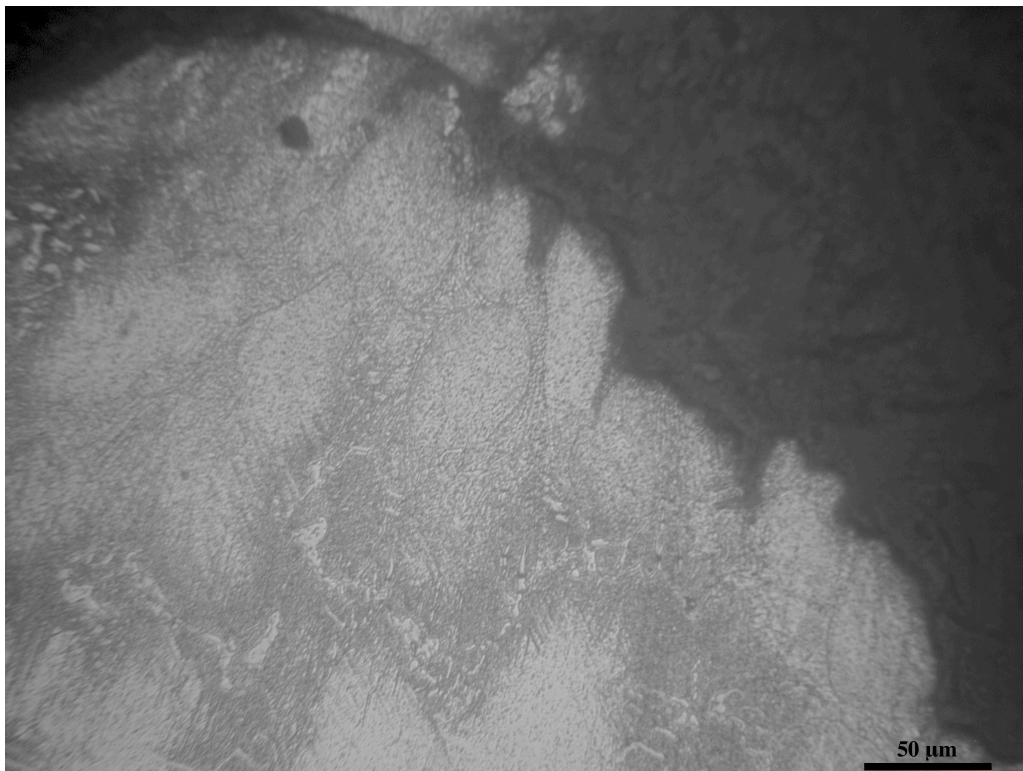


Figure 155. Etched microstructure of specimen S2 (rupture surface); magnification: 500X.

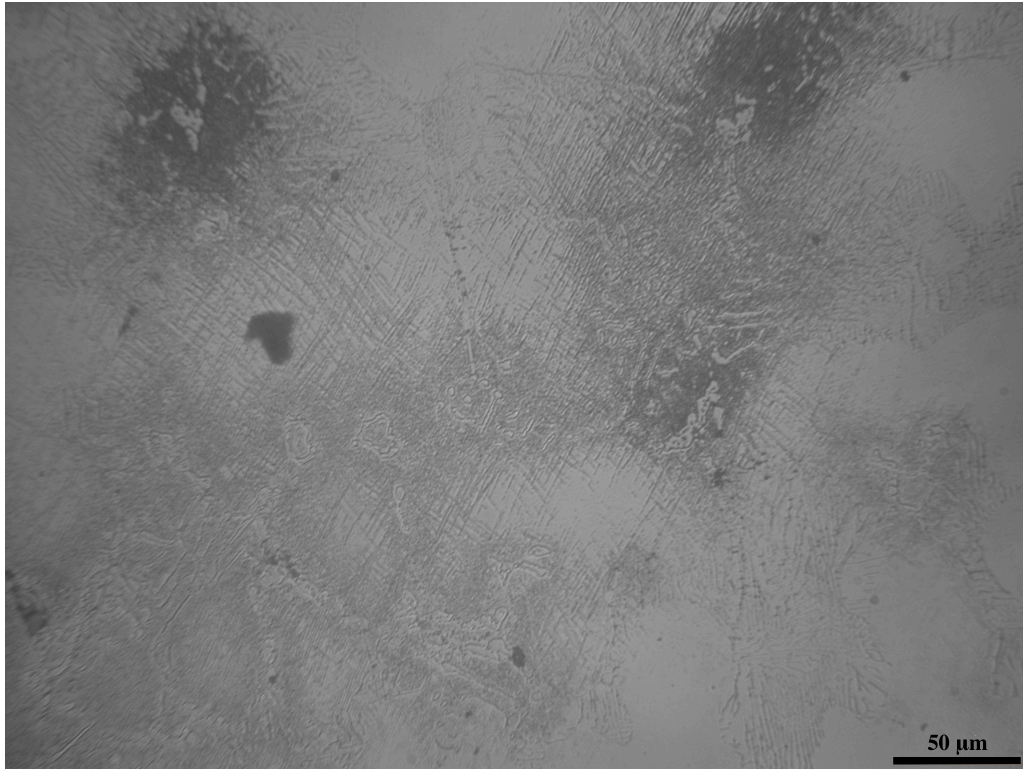


Figure 156. Etched microstructure of specimen S2 (at core); magnification: 500X.

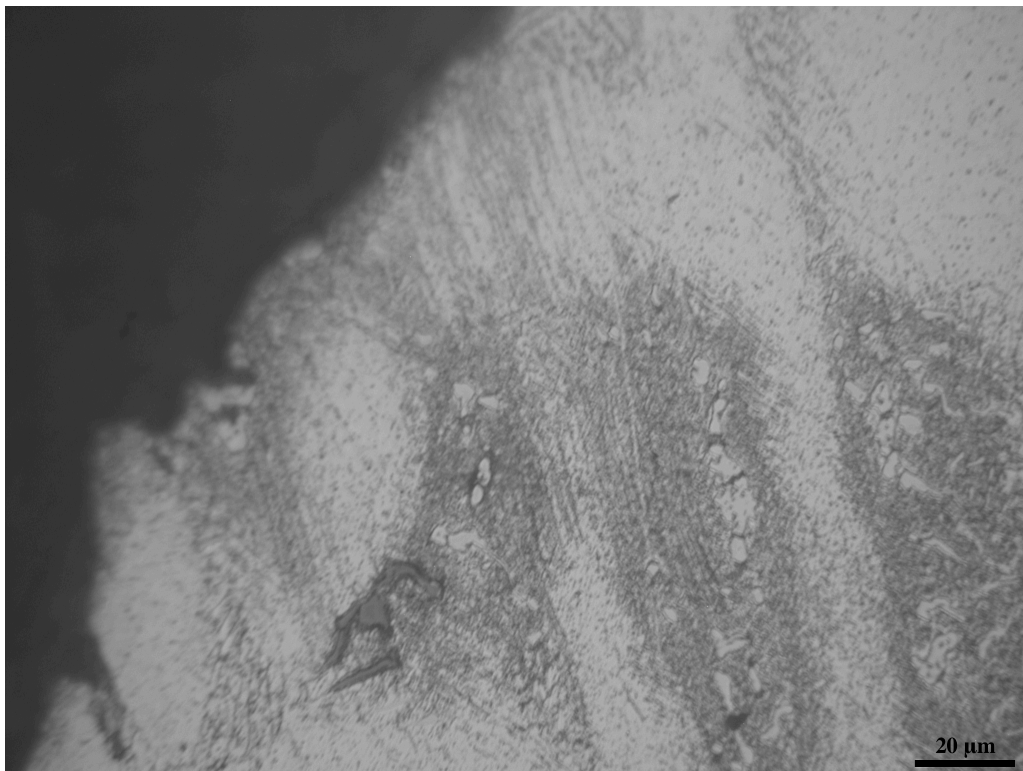


Figure 157. Etched microstructure of specimen S2 (rupture surface); magnification: 1000X.

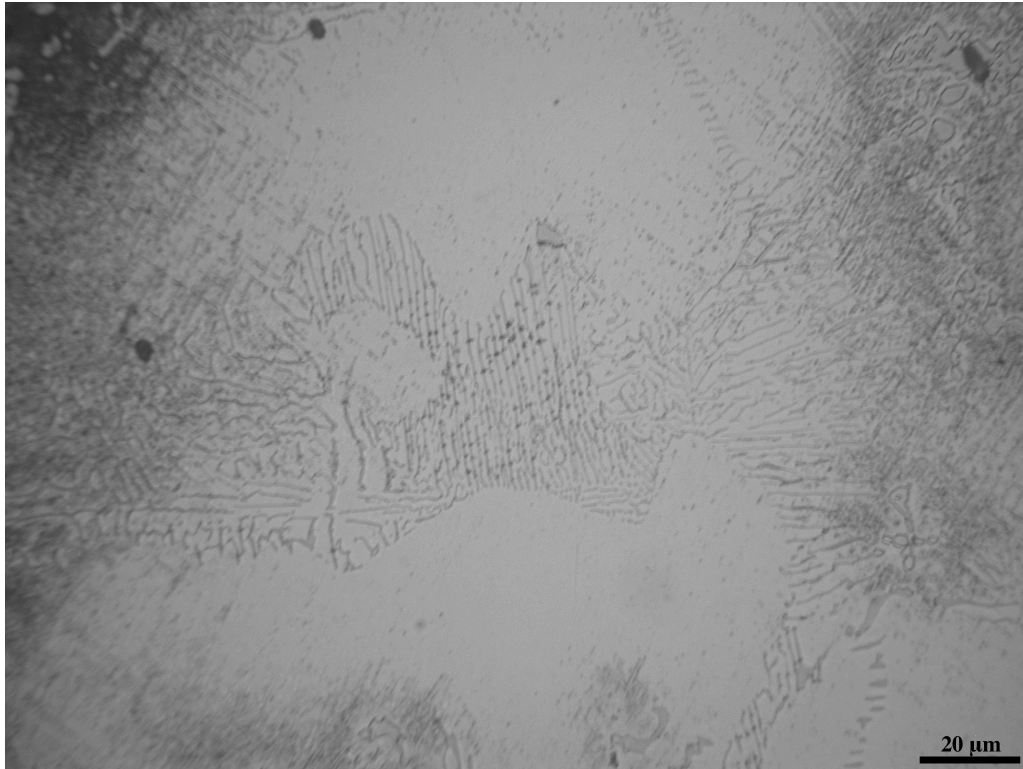


Figure 158. Etched microstructure of specimen S2 (at core); magnification: 1000X.

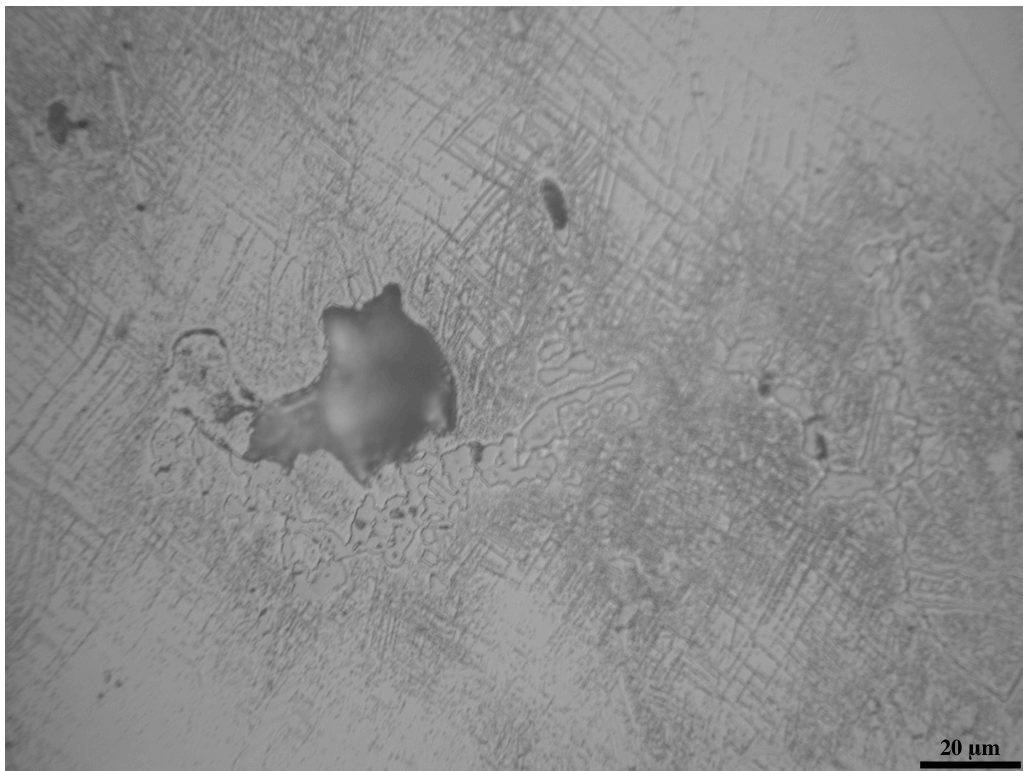


Figure 159. Etched microstructure of specimen S2 (at core); magnification: 1000X.

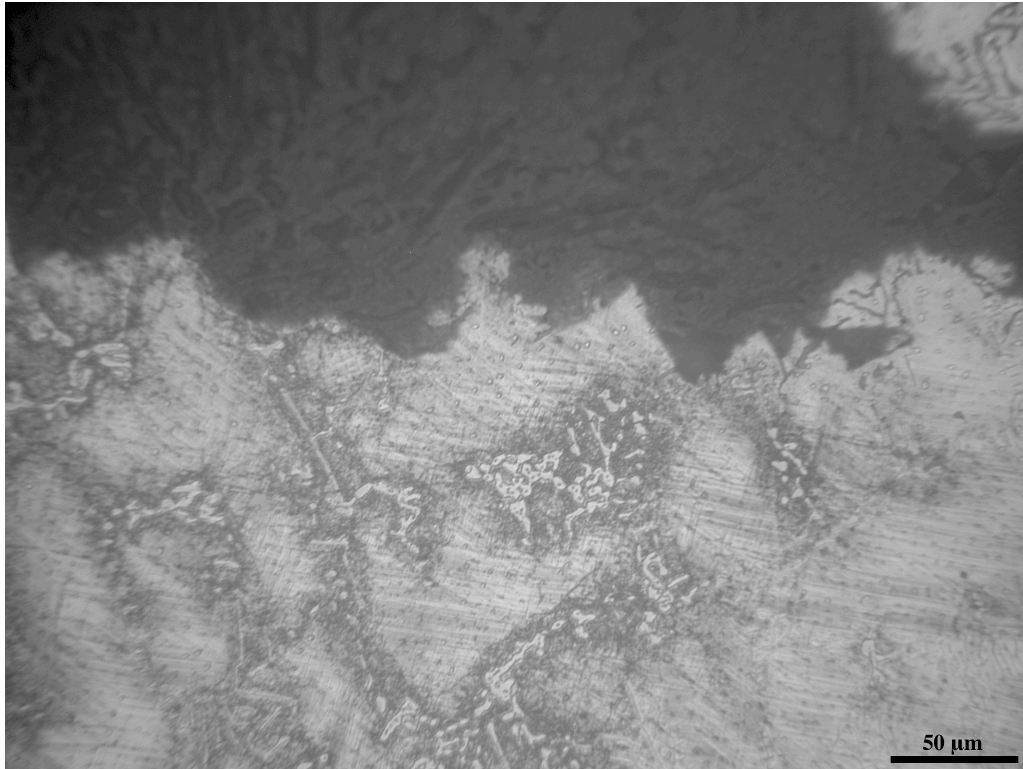


Figure 160. Etched microstructure of specimen S4 (rupture surface); magnification: 500X.

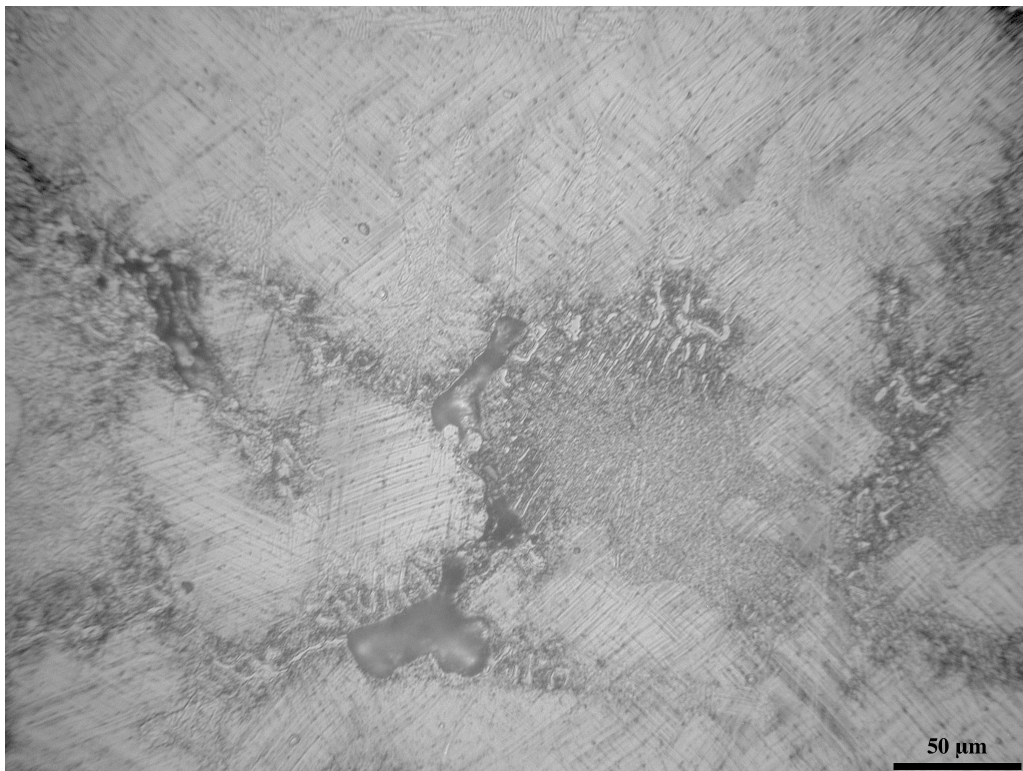


Figure 161. Etched microstructure of specimen S4 (at core); magnification: 500X.



Figure 162. Etched microstructure of specimen S4 (rupture surface); magnification: 1000X.

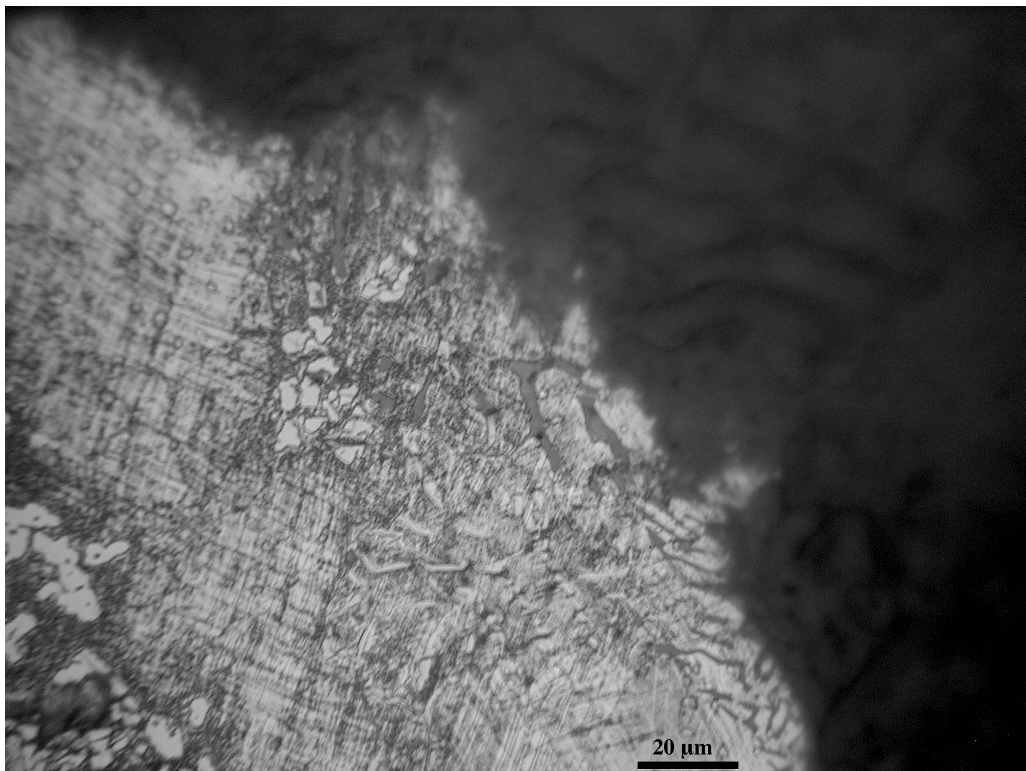


Figure 163. Etched microstructure of specimen S4 (rupture surface); magnification: 1000X.

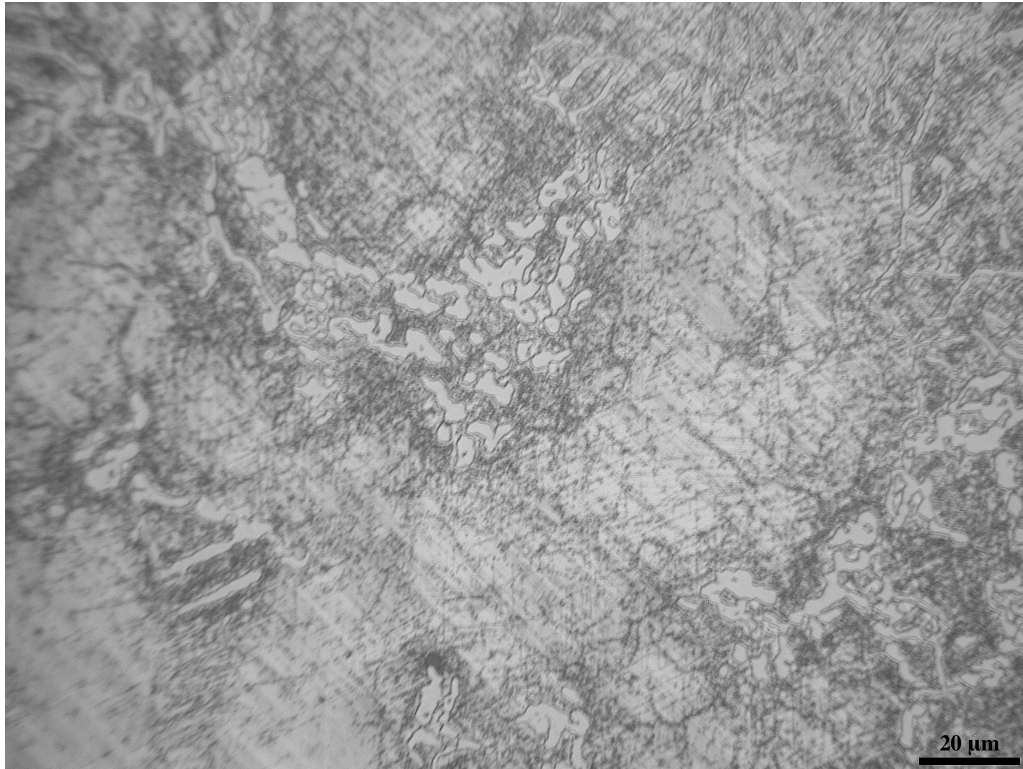


Figure 164. Etched microstructure of specimen S4 (at core); magnification: 1000X.

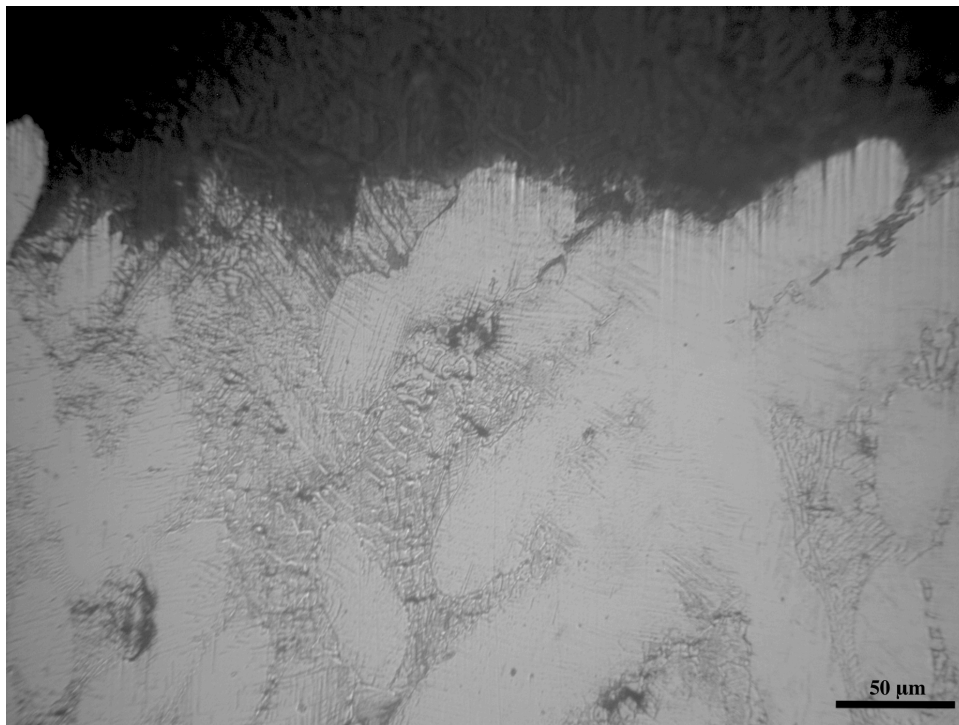


Figure 165. Etched microstructure of specimen S5, set 128 (rupture surface); magnification: 500X.

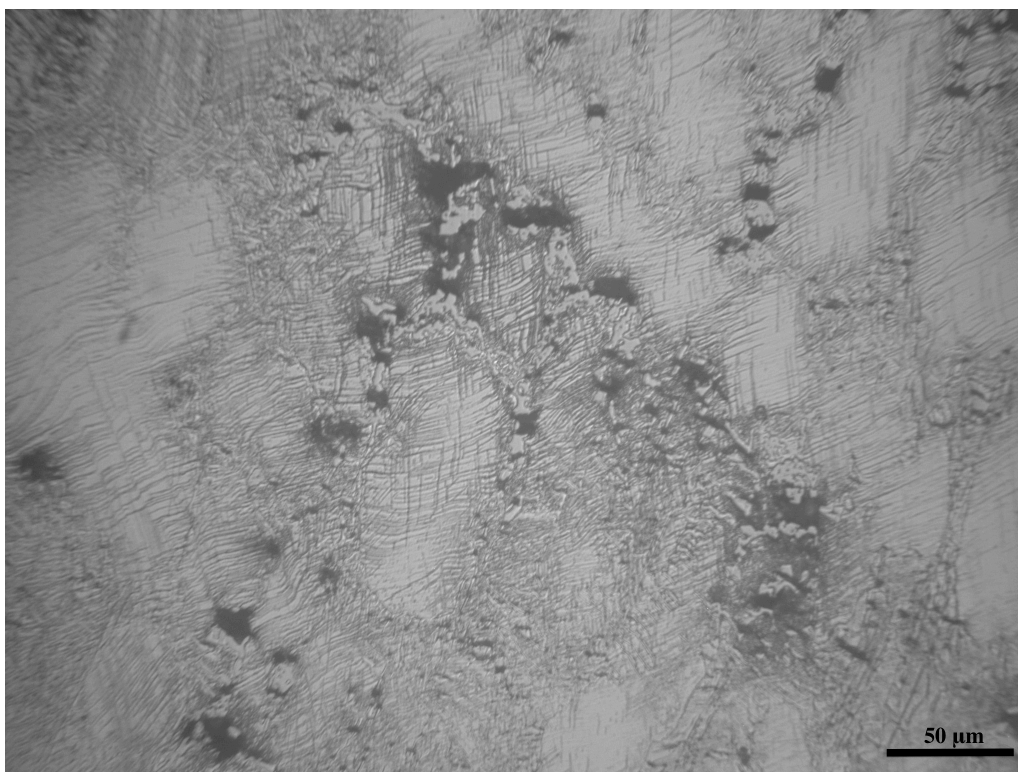


Figure 166. Etched microstructure of specimen S5, set 128 (at core); magnification: 500X.

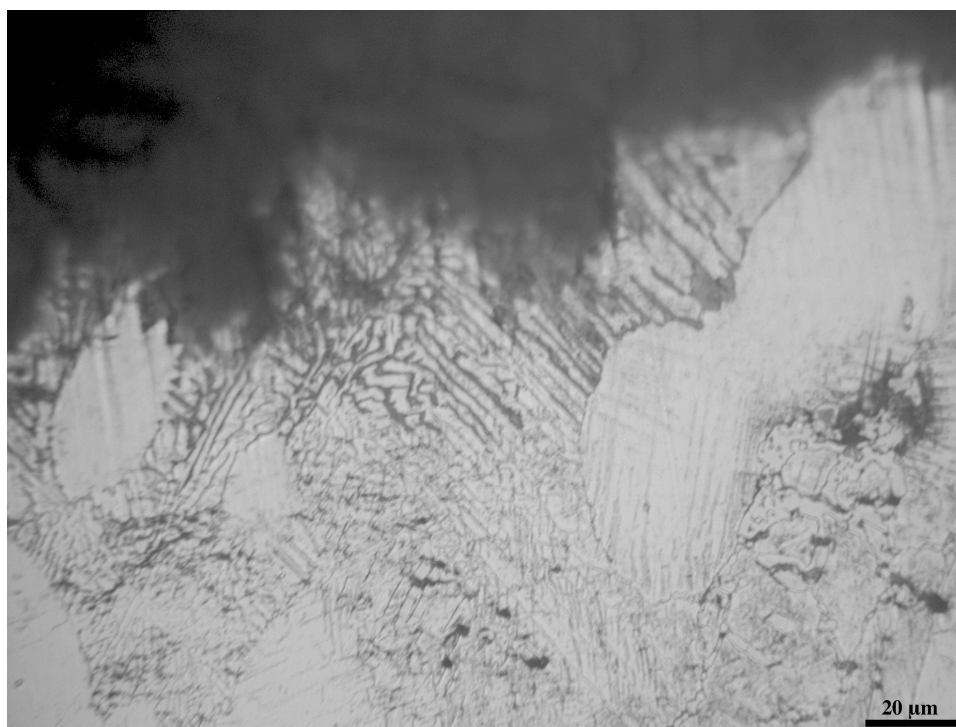


Figure 167. Etched microstructure of specimen S5, set 128 (rupture surface); magnification: 1000X.

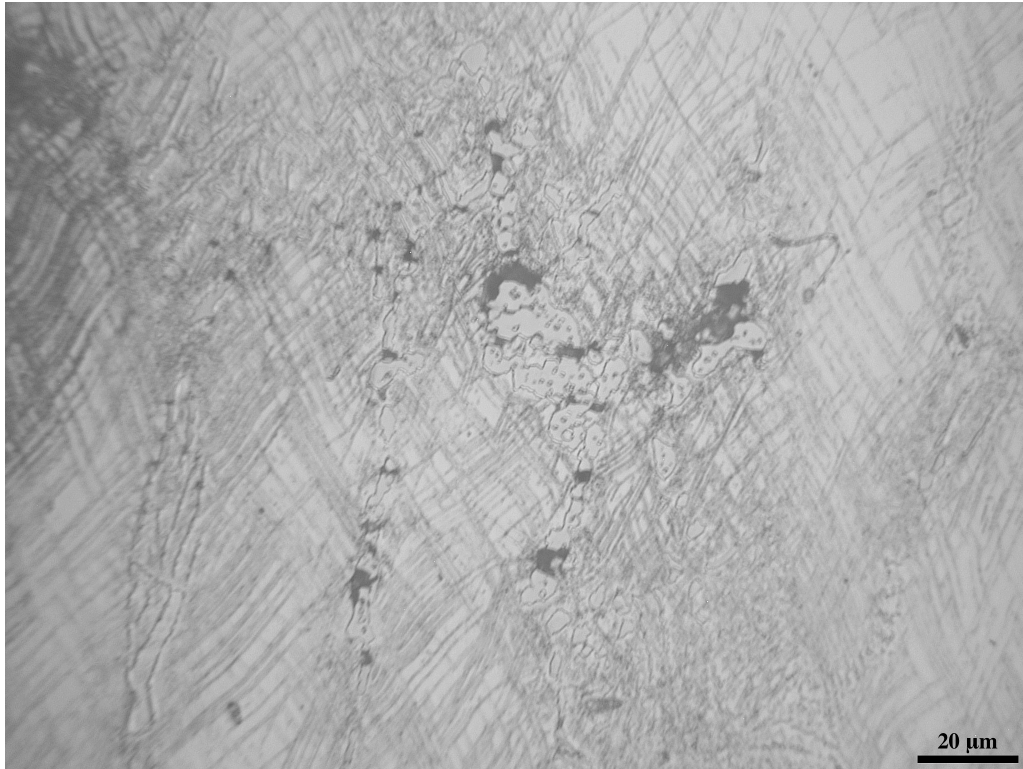


Figure 168. Etched microstructure of specimen S5, set 128 (at core); magnification: 1000X.

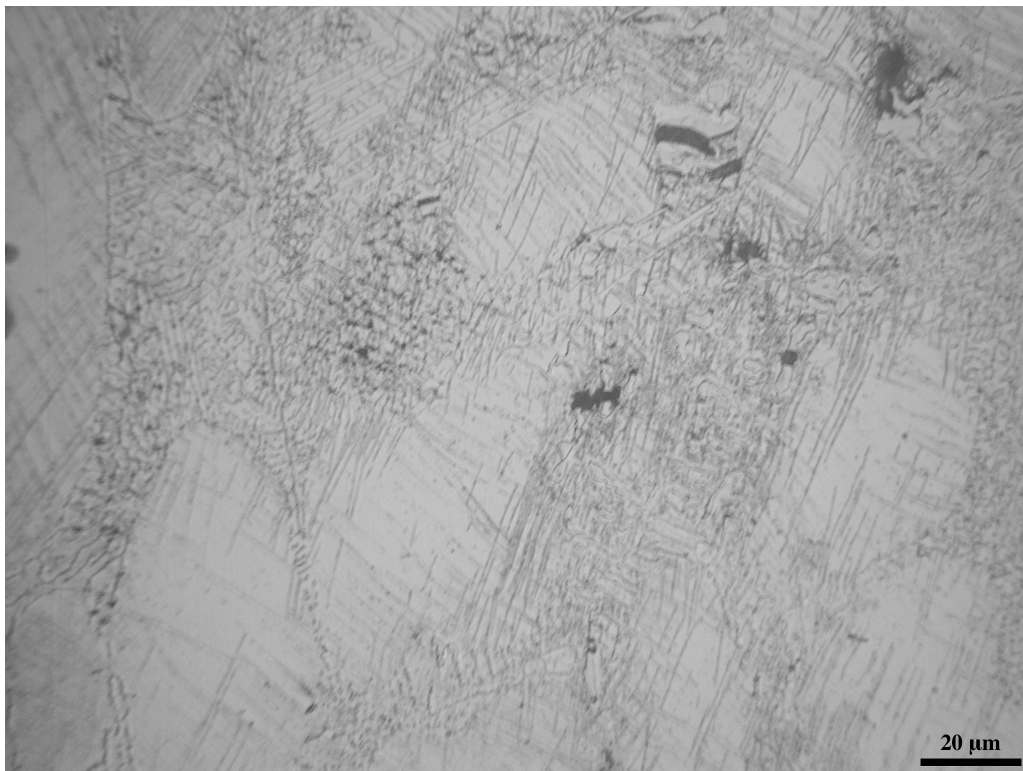


Figure 169. Etched microstructure of specimen S5, set 128 (at core); magnification: 1000X.

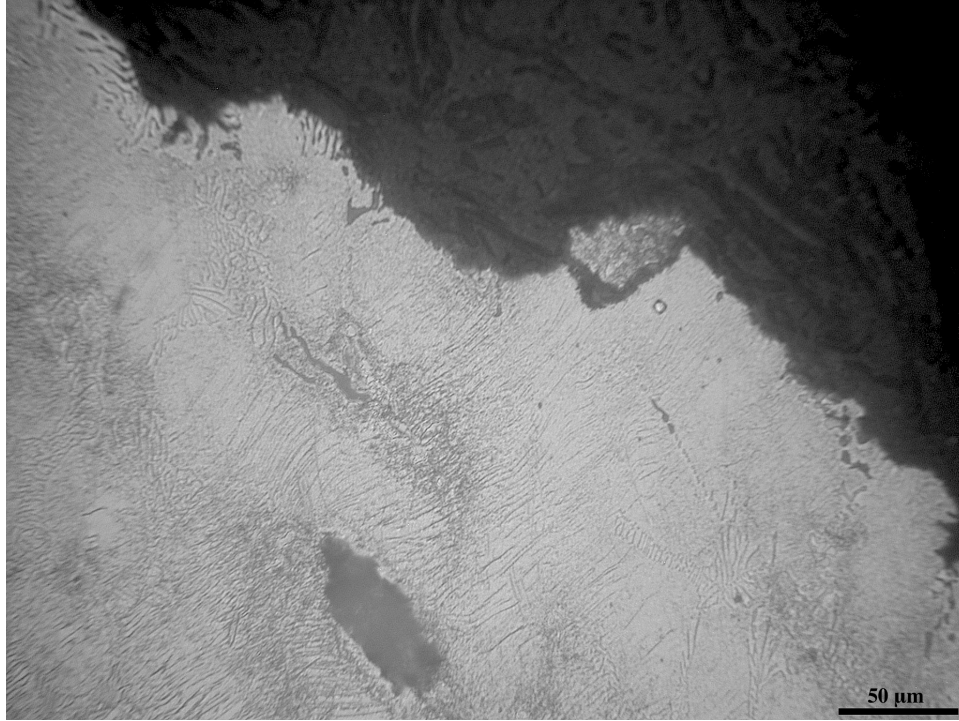


Figure 170. Etched microstructure of specimen S5, set 821 (rupture surface); magnification: 500X.

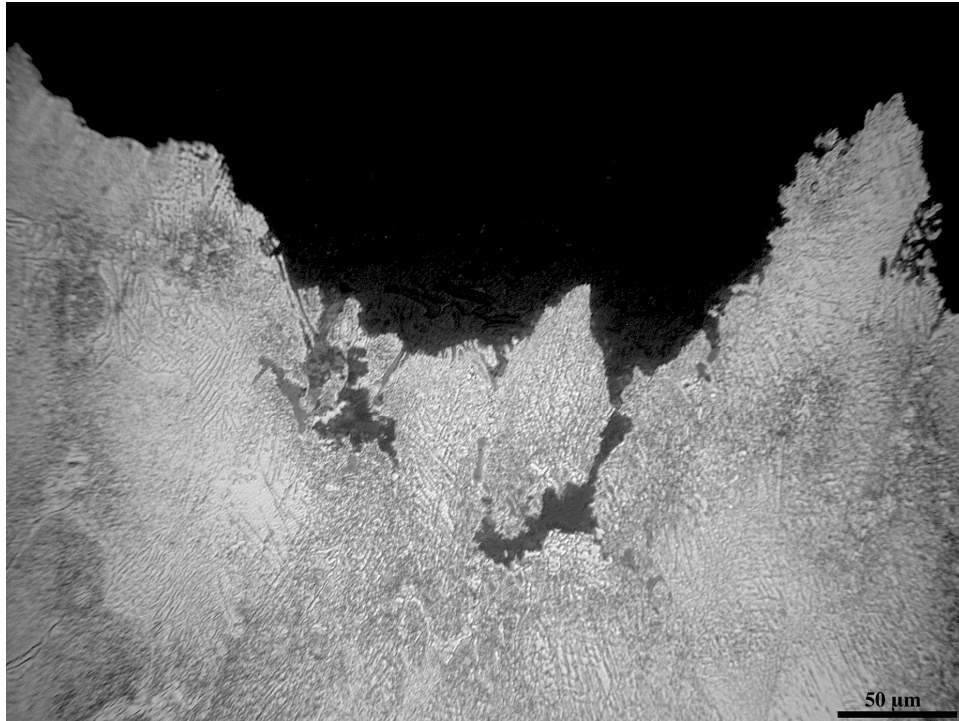


Figure 171. Etched microstructure of specimen S5, set 821 (rupture surface); magnification: 500X.



Figure 172. Etched microstructure of specimen S5, set 821 (at core); magnification: 500X.

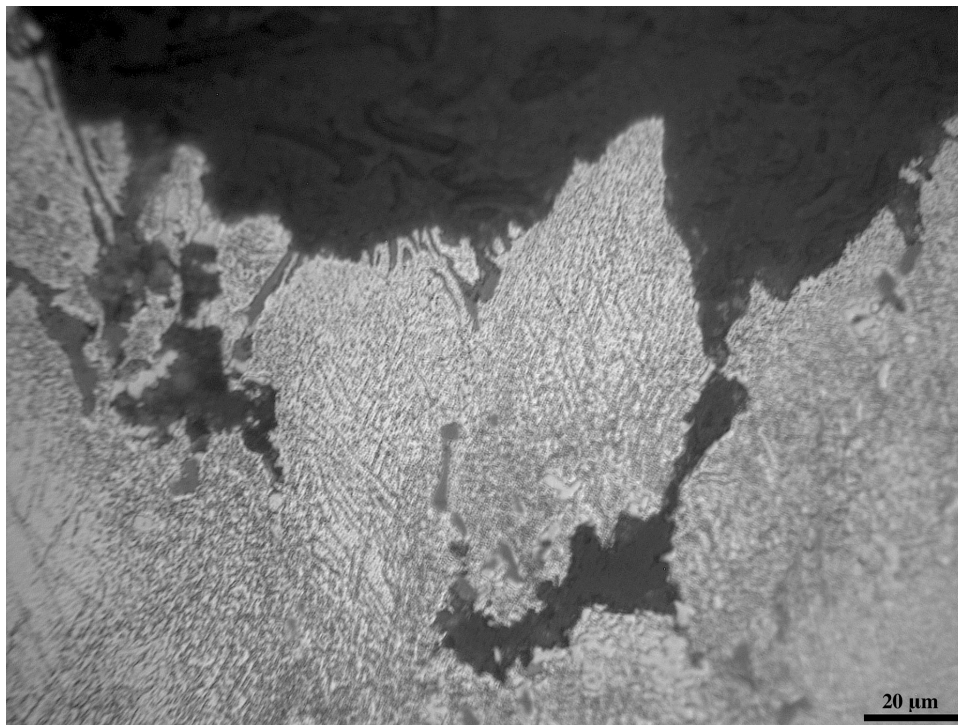


Figure 173. Etched microstructure of specimen S5, set 821 (rupture surface); magnification: 1000X.

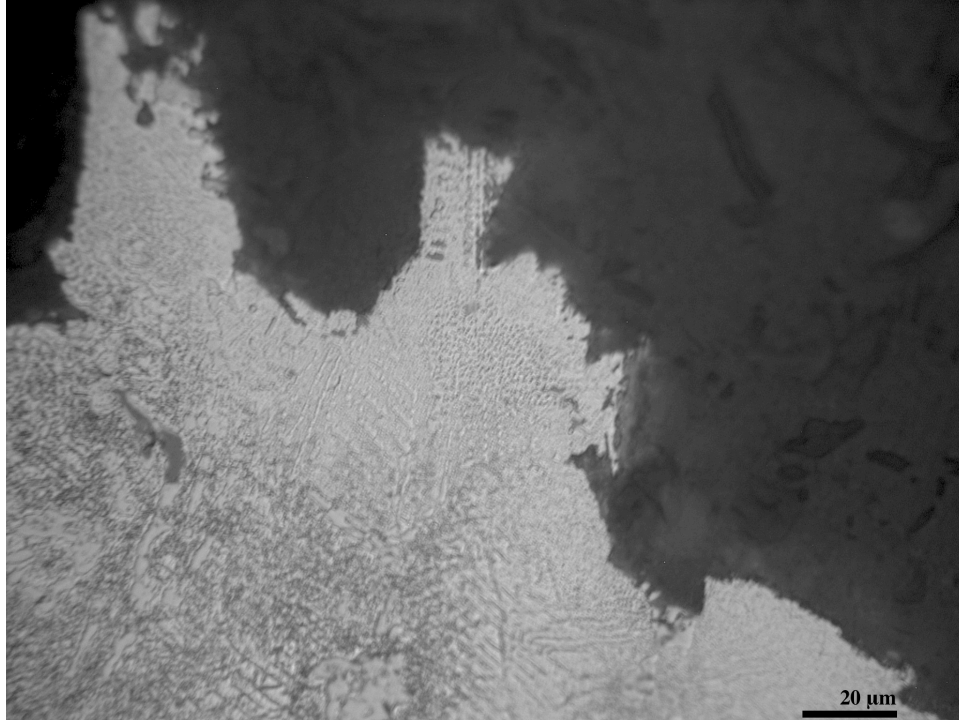


Figure 174. Etched microstructure of specimen S5, set 821 (rupture surface); magnification: 1000X.



Figure 175. Etched microstructure of specimen S5, set 821 (rupture surface); magnification: 1000X.

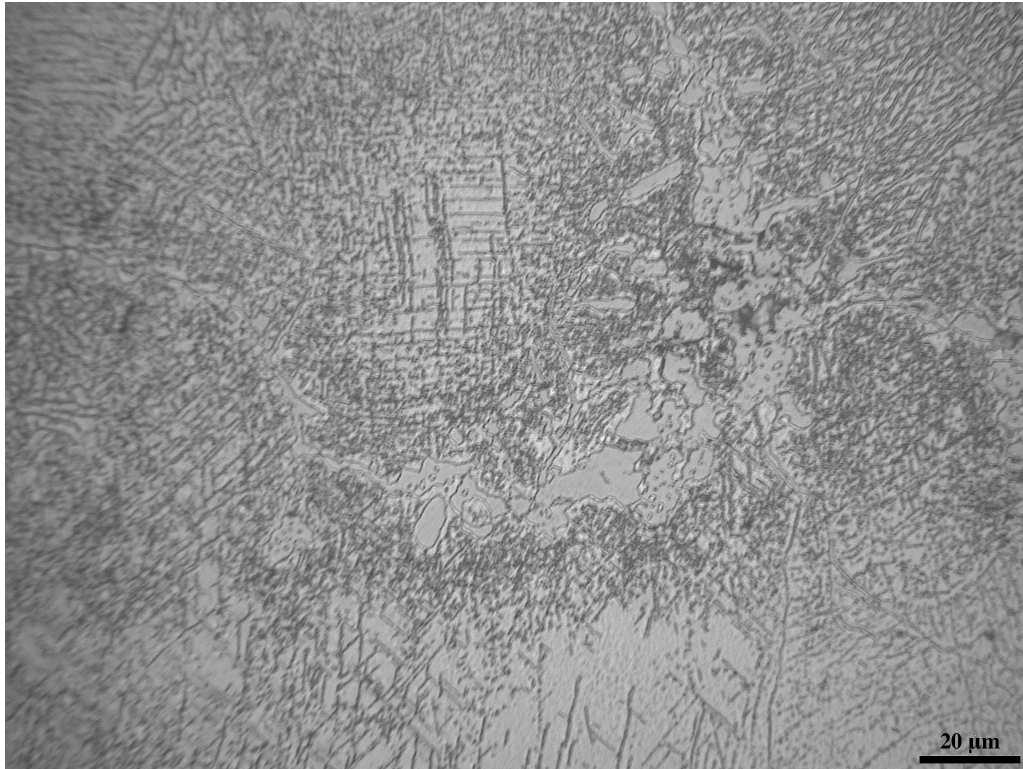


Figure 176. Etched microstructure of specimen S5, set 821 (at core); magnification: 1000X.

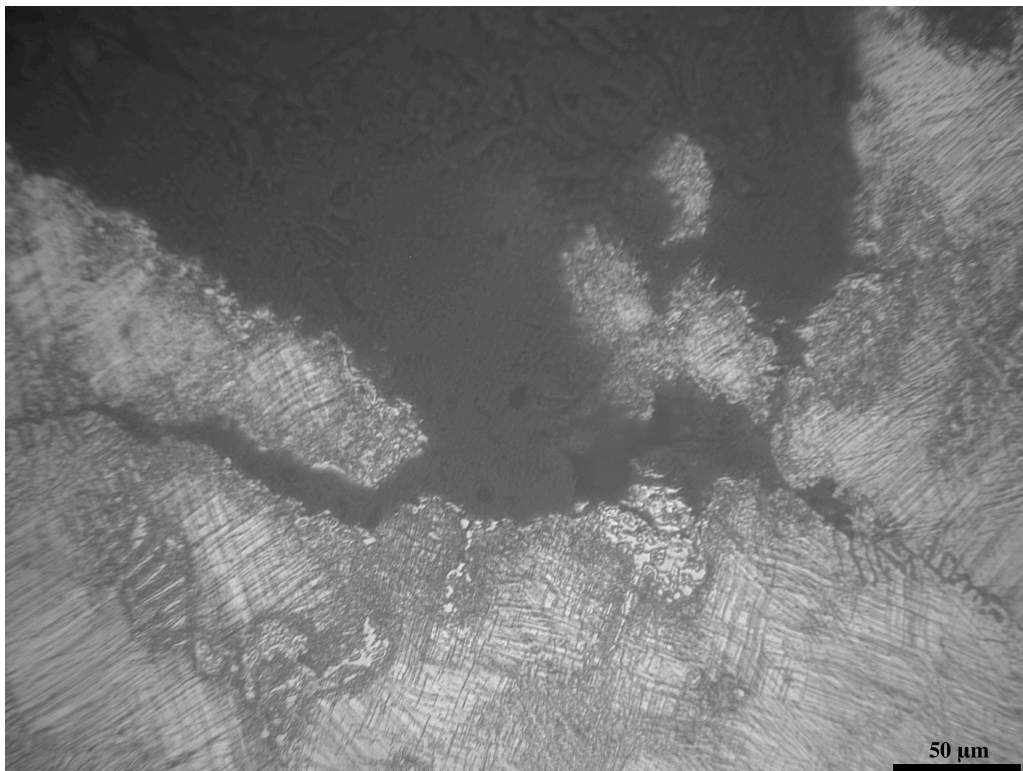


Figure 177. Etched microstructure of specimen S7 (rupture surface); magnification: 500X.



Figure 178. Etched microstructure of specimen S7 (at core); magnification: 500X.

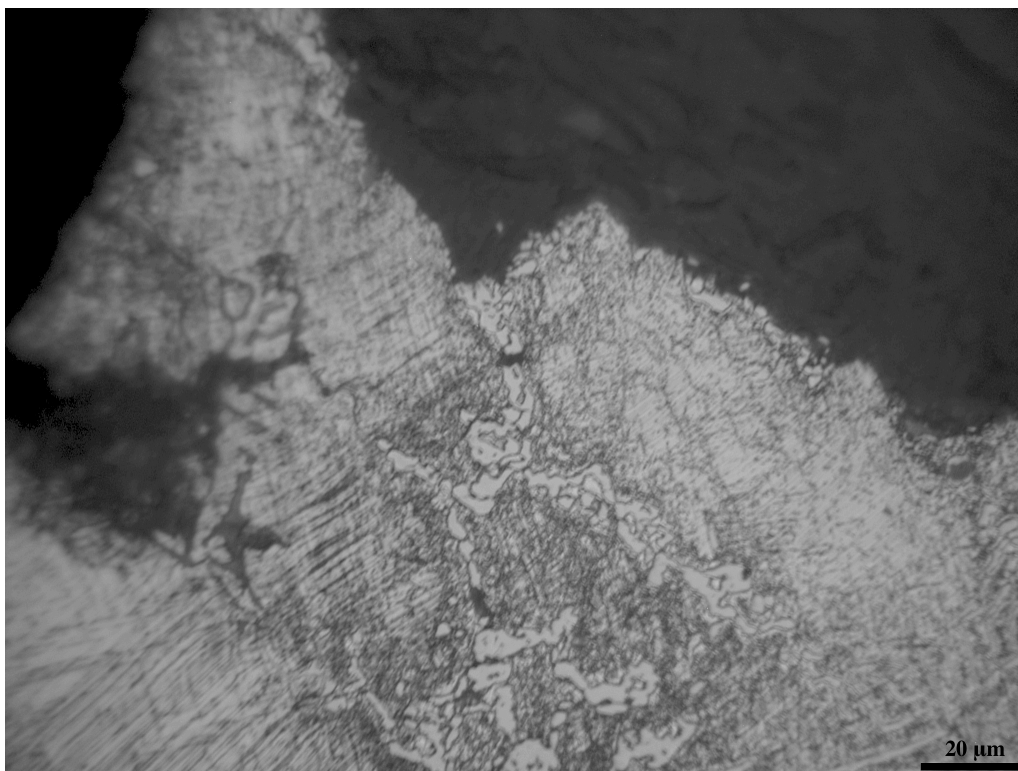


Figure 179. Etched microstructure of specimen S7 (rupture surface); magnification: 1000X.

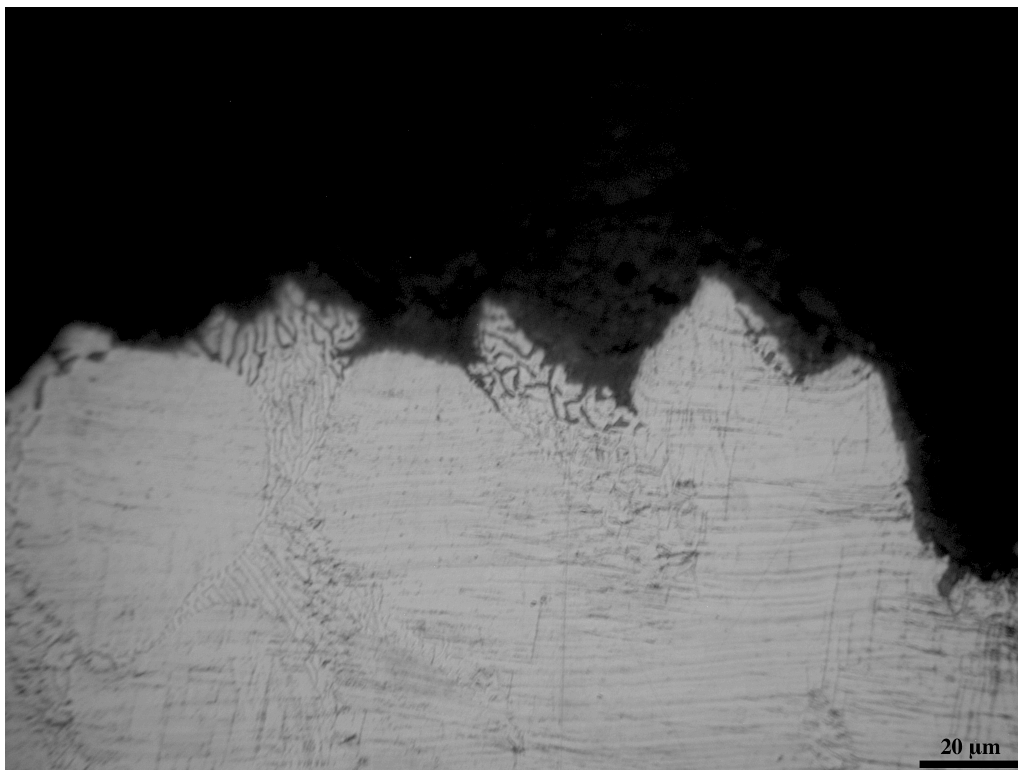


Figure 180. Etched microstructure of specimen S7 (rupture surface); magnification: 1000X.



Figure 181. Etched microstructure of specimen S7 (at core); magnification: 1000X.

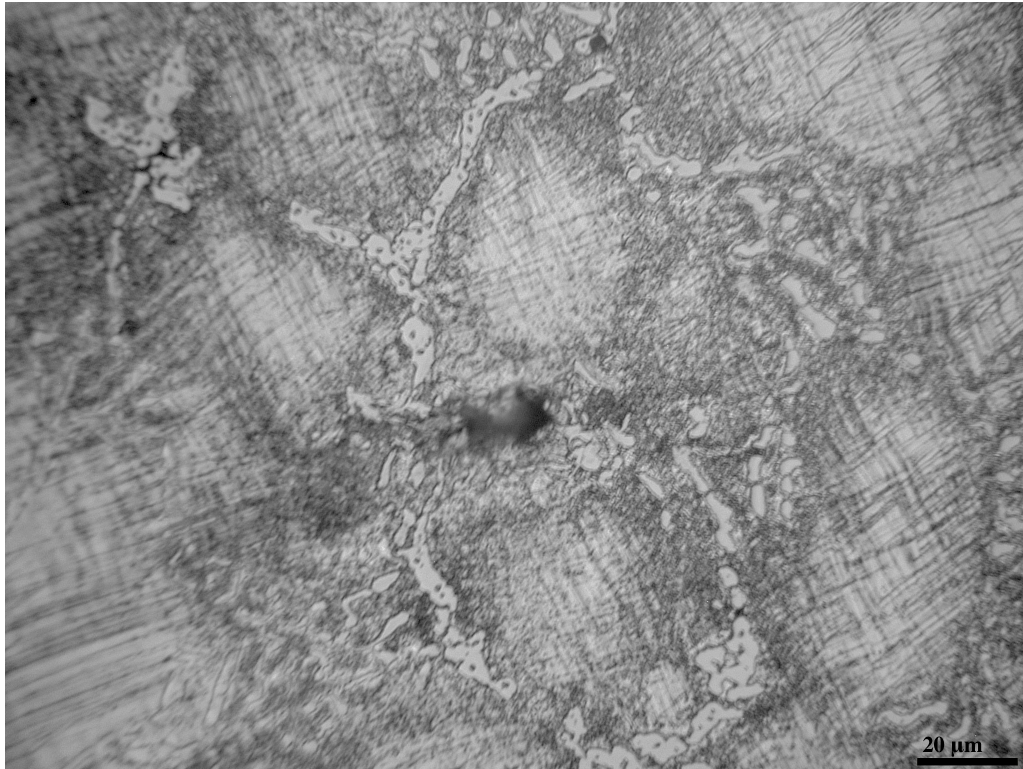


Figure 182. Etched microstructure of specimen S7 (at core); magnification: 1000X.

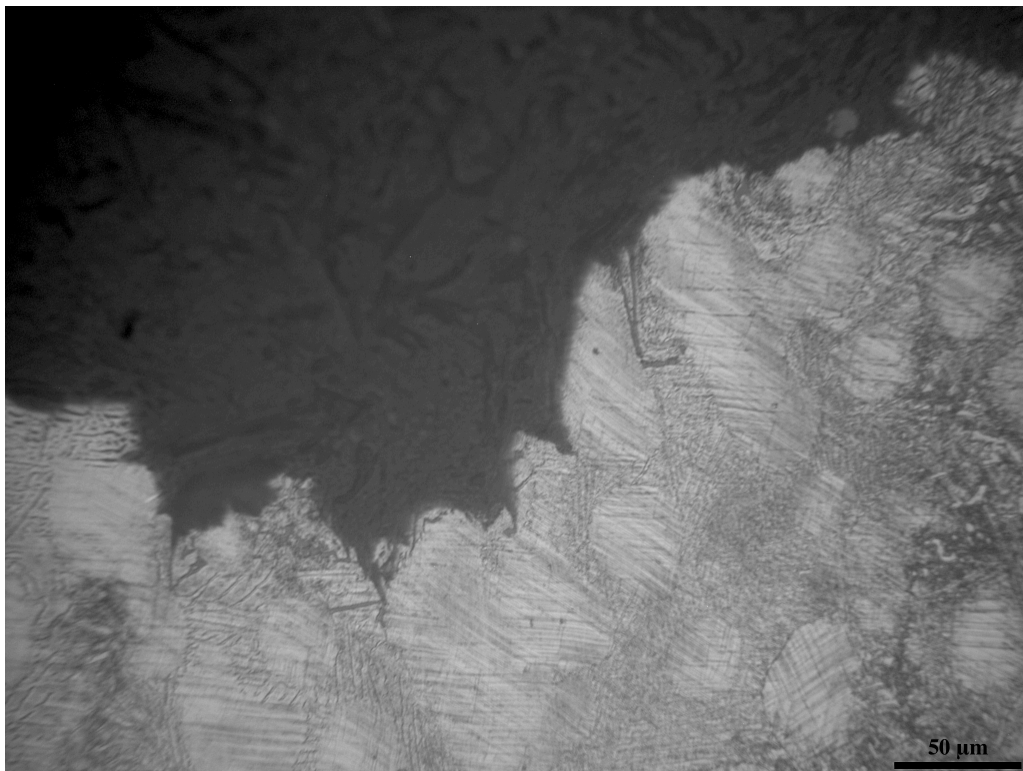


Figure 183. Etched microstructure of specimen S9 (rupture surface); magnification: 500X.



Figure 184. Etched microstructure of specimen S9 (at core); magnification: 500X.

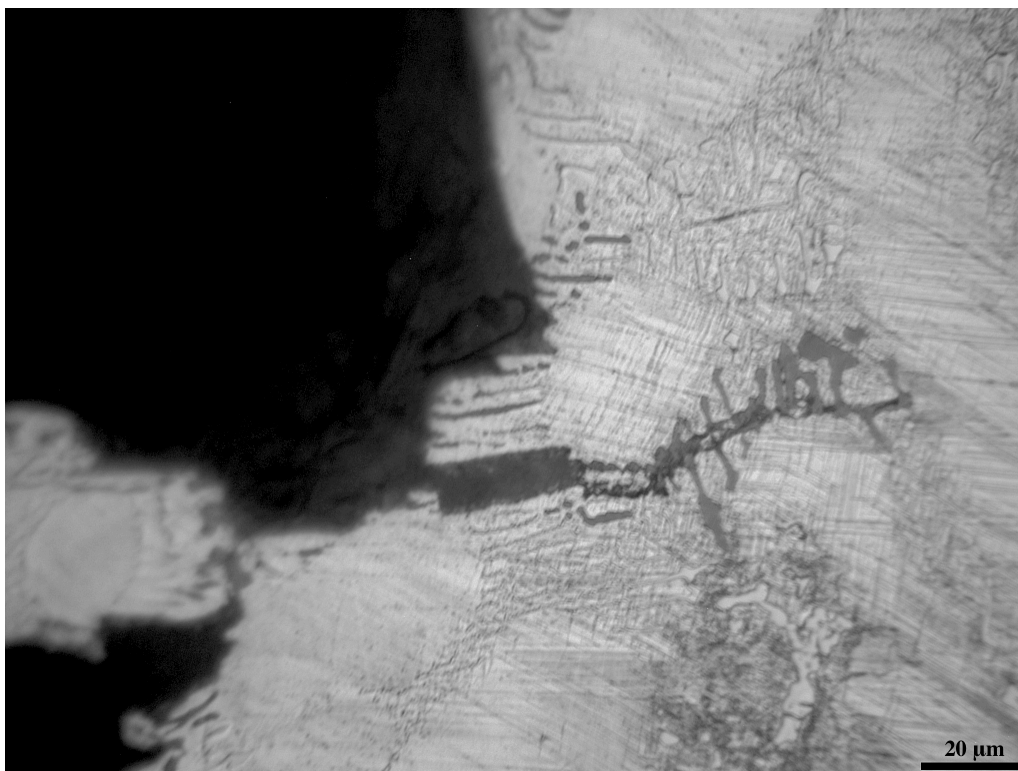


Figure 185. Etched microstructure of specimen S9 (rupture surface); magnification: 1000X.

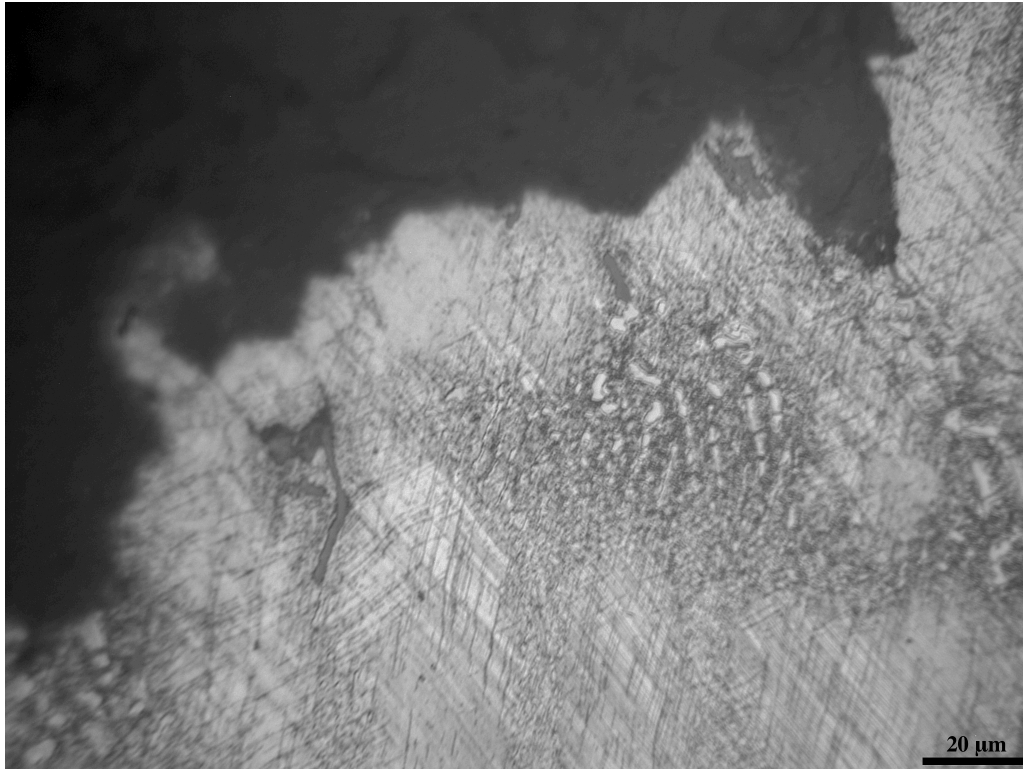


Figure 186. Etched microstructure of specimen S9 (rupture surface); magnification: 1000X.

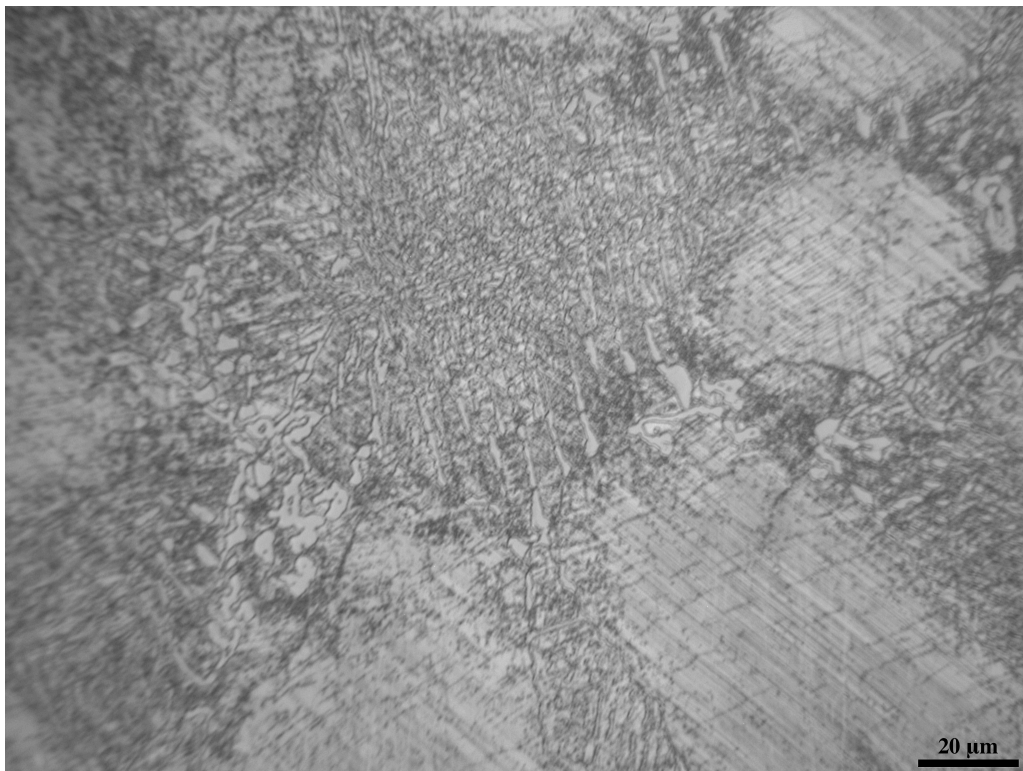


Figure 187. Etched microstructure of specimen S9 (at core); magnification: 1000X.

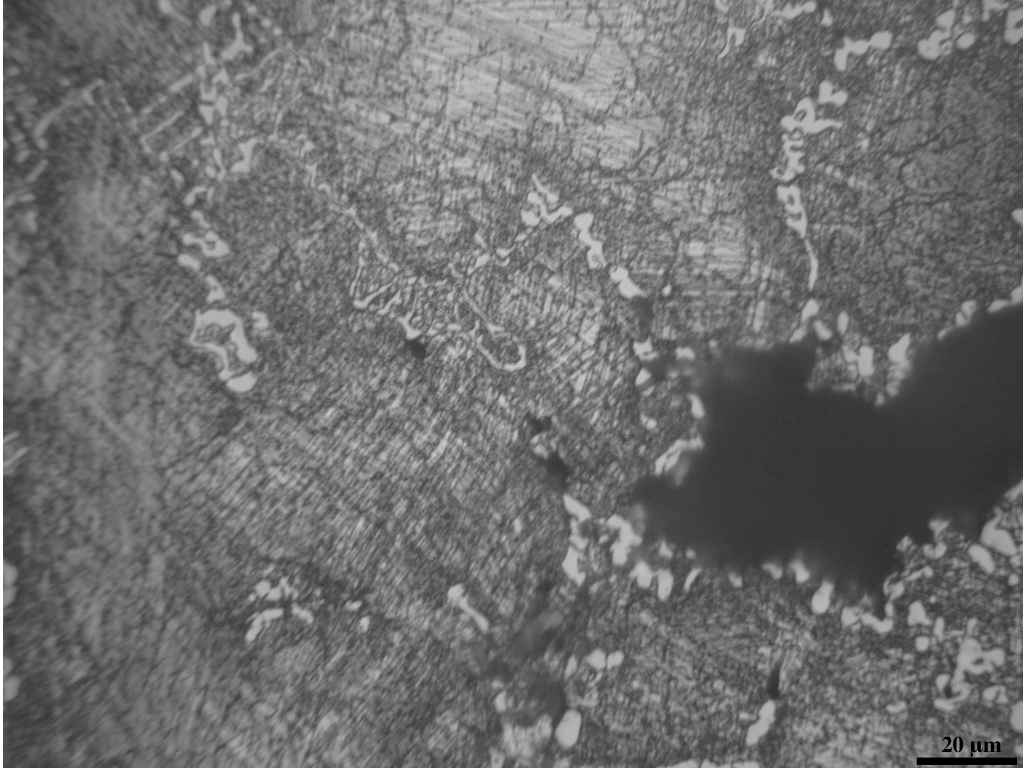


Figure 188. Etched microstructure of specimen S9 (at core); magnification: 1000X.

Appendix D

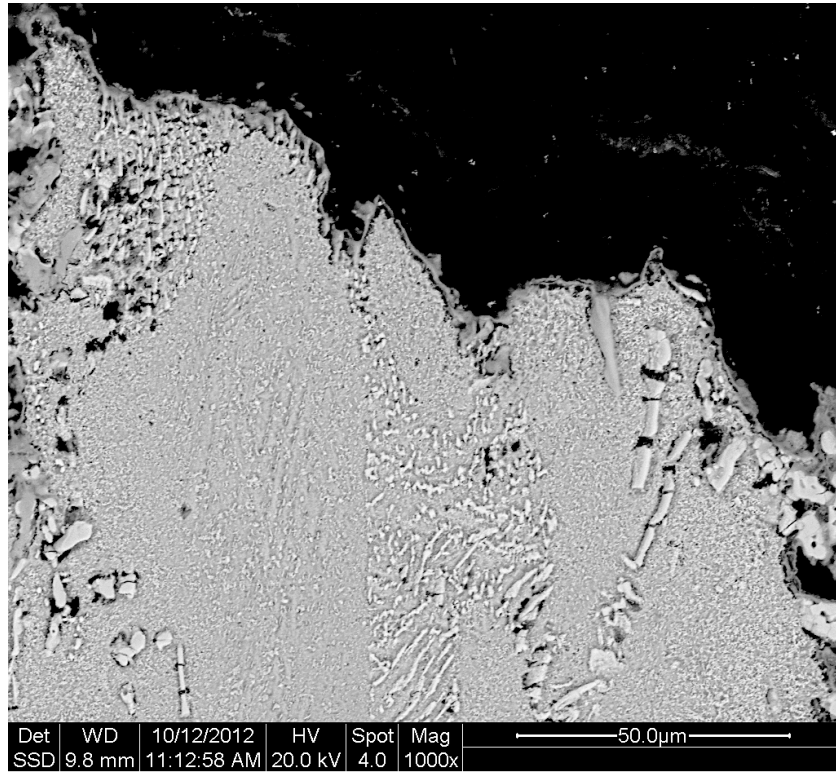


Figure 189. Etched microstructure of specimen S1 (rupture surface); magnification: 1000X.

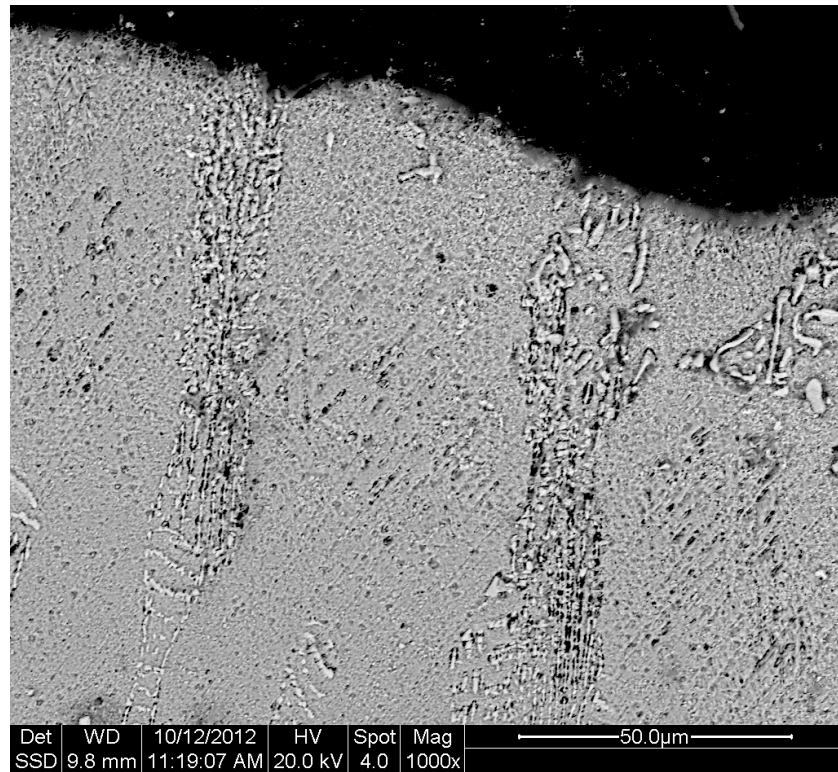


Figure 190. Etched microstructure of specimen S1 (rupture surface); magnification: 1000X.

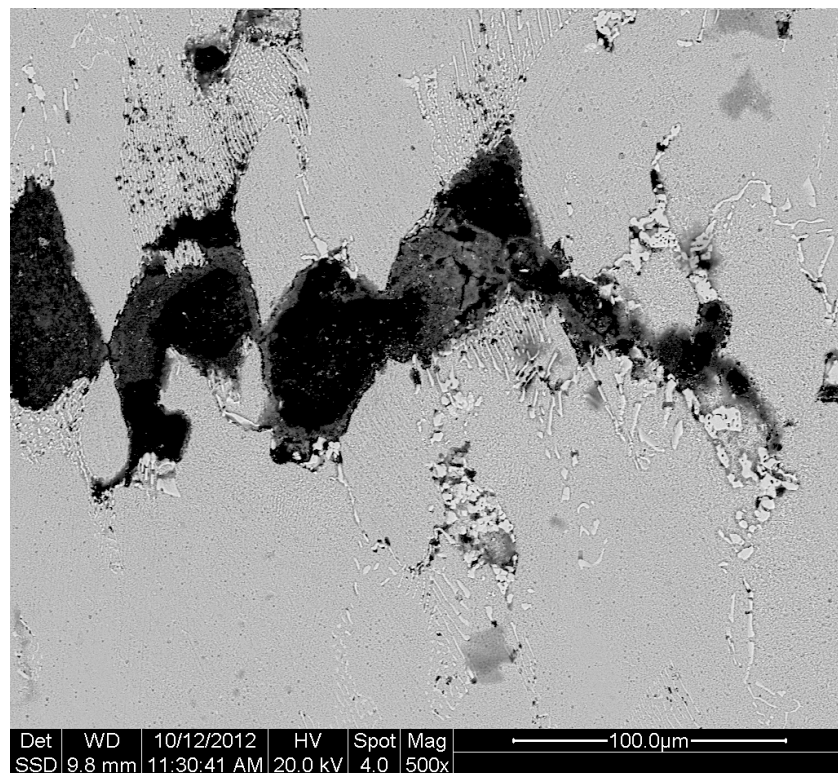


Figure 191. Etched microstructure of specimen S1 (at core); magnification: 500X.

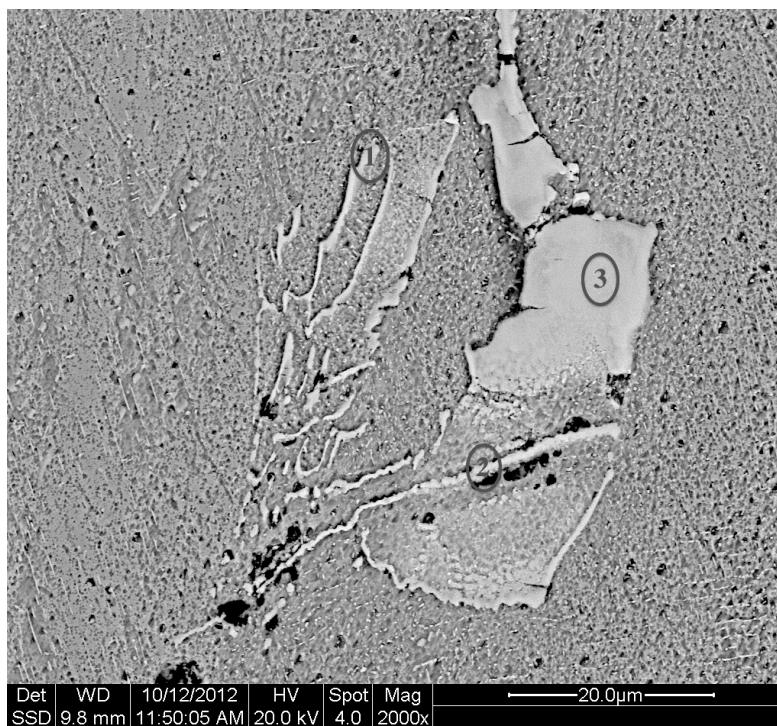


Figure 192. Etched microstructure of specimen S1 (at core); magnification: 2000X. Numbered ovals indicate where EDS analyses were conducted.

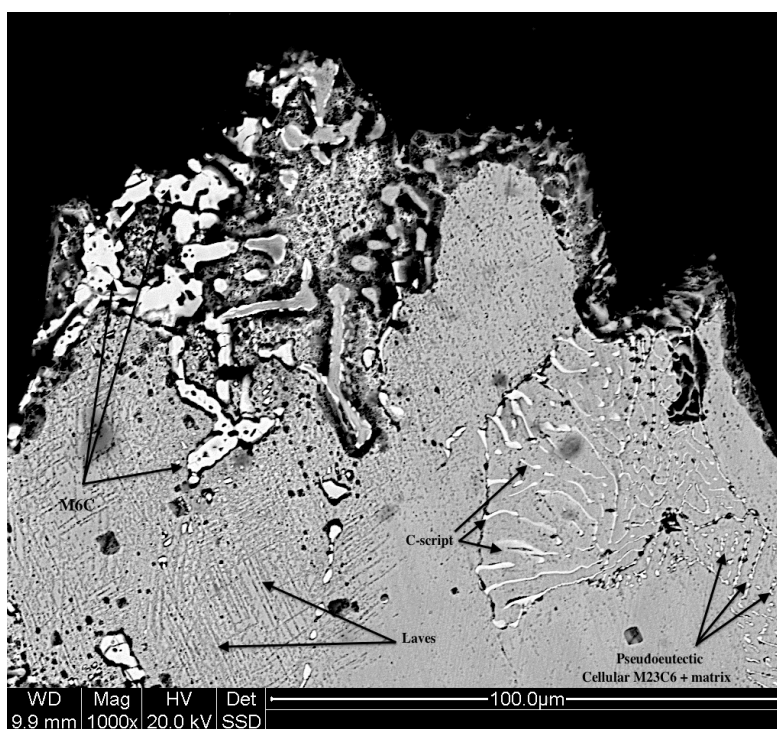


Figure 193. Etched microstructure of specimen S2 (rupture surface); magnification: 1000X. Microconstituents identified for metallographic reference purposes.

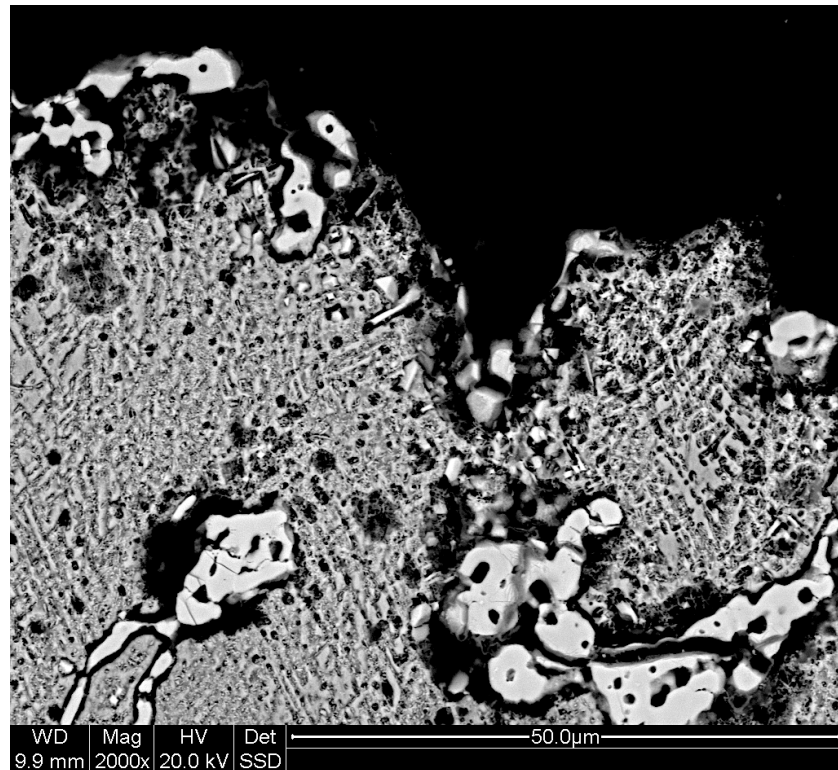


Figure 194. Etched microstructure of specimen S2 (rupture surface); magnification: 2000X.

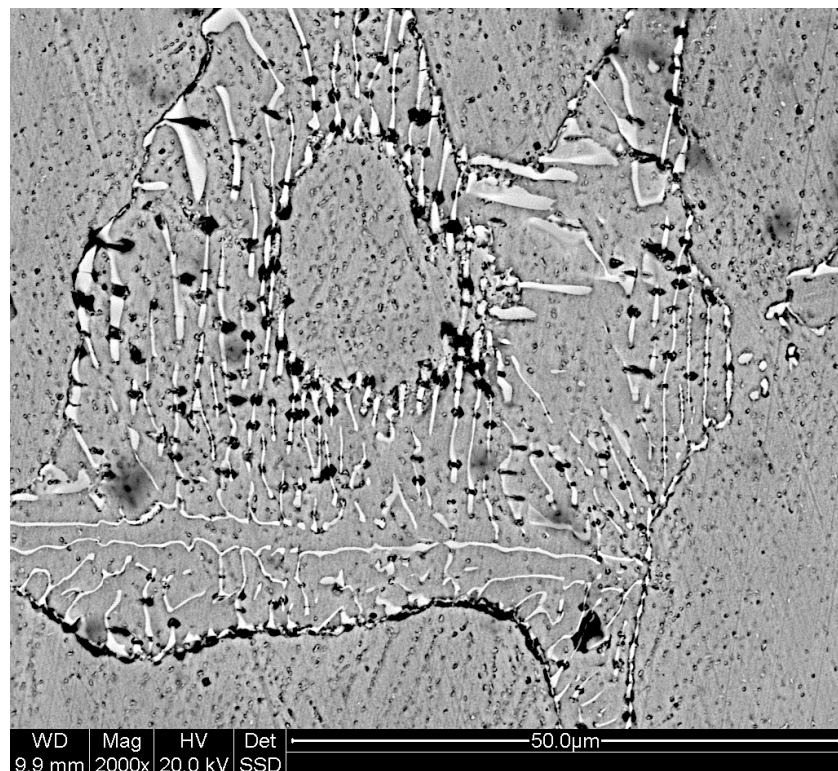


Figure 195. Etched microstructure of specimen S2 (at core); magnification: 2000X.

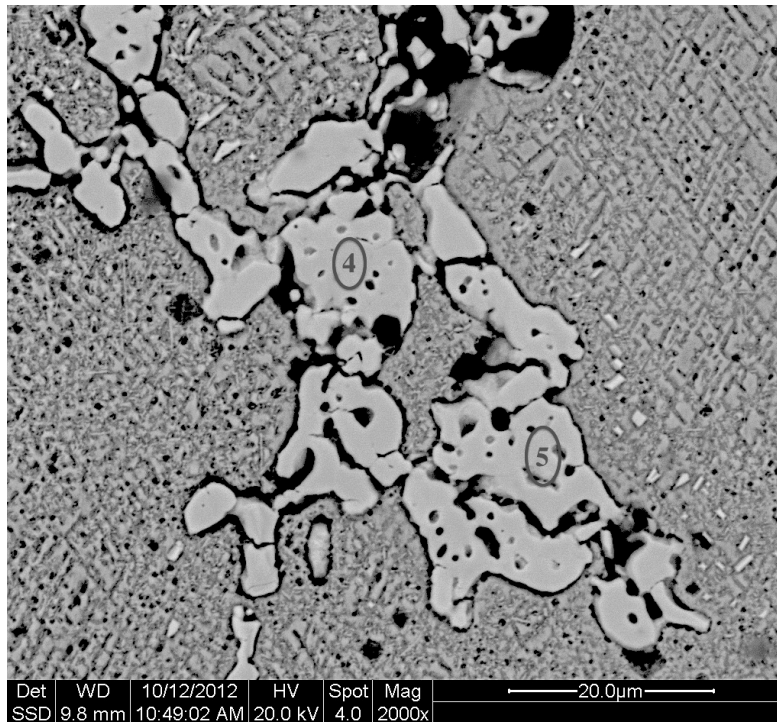


Figure 196. Etched microstructure of specimen S2 (at core); magnification: 2000X. Numbered ovals indicate where EDS analyses were conducted.

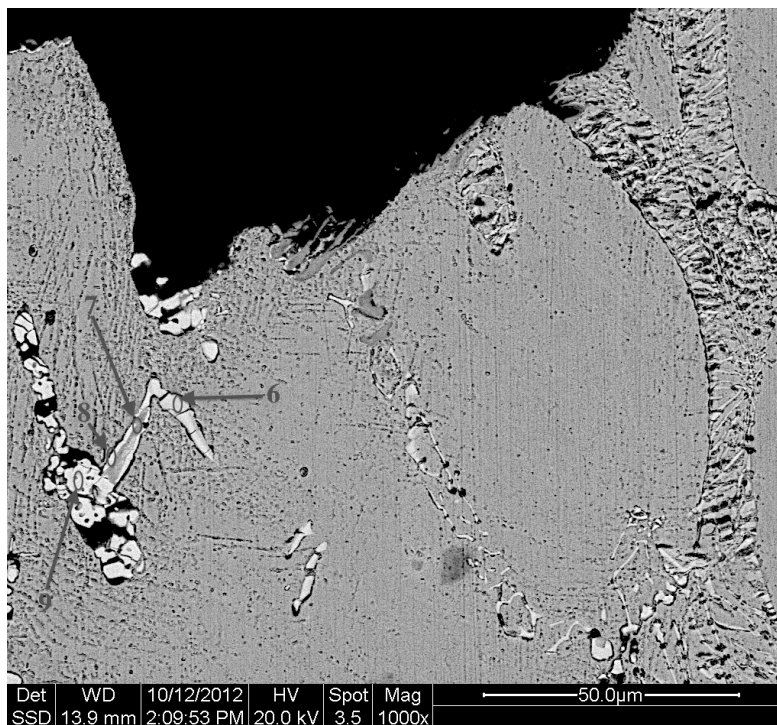


Figure 197. Etched microstructure of specimen S4 (rupture surface); magnification: 1000X. Numbered ovals indicate where EDS analyses were conducted.

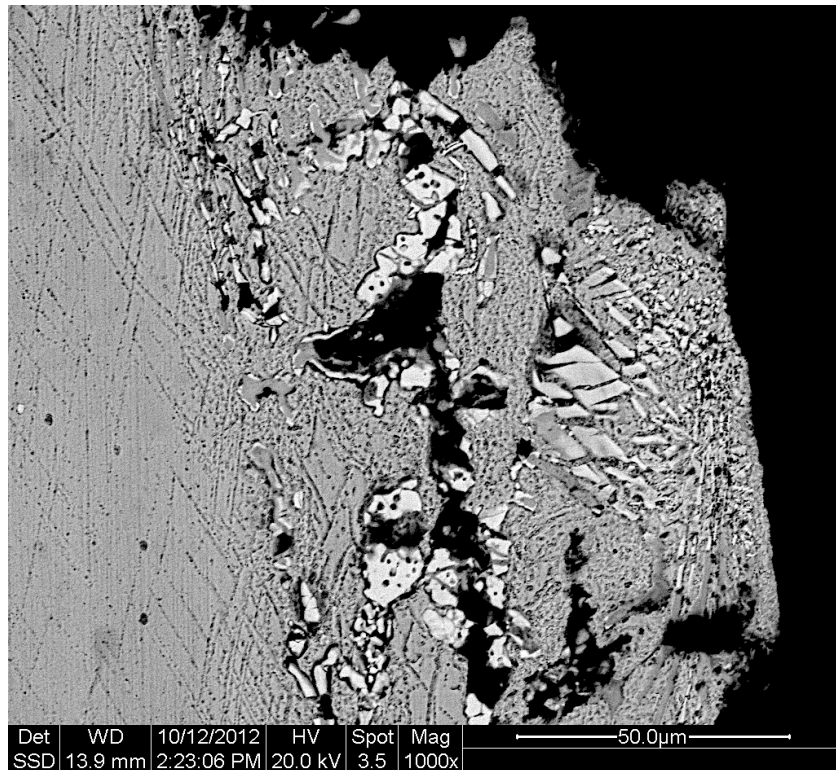


Figure 198. Etched microstructure of specimen S4 (rupture surface); magnification: 1000X.

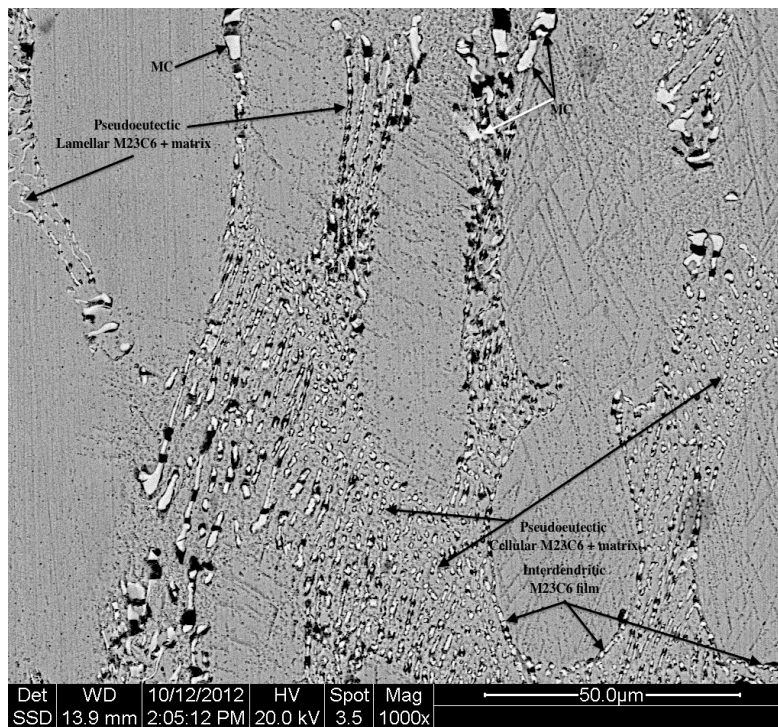


Figure 199. Etched microstructure of specimen S4 (at core); magnification: 1000X.
Microconstituents identified for metallographic reference purposes.

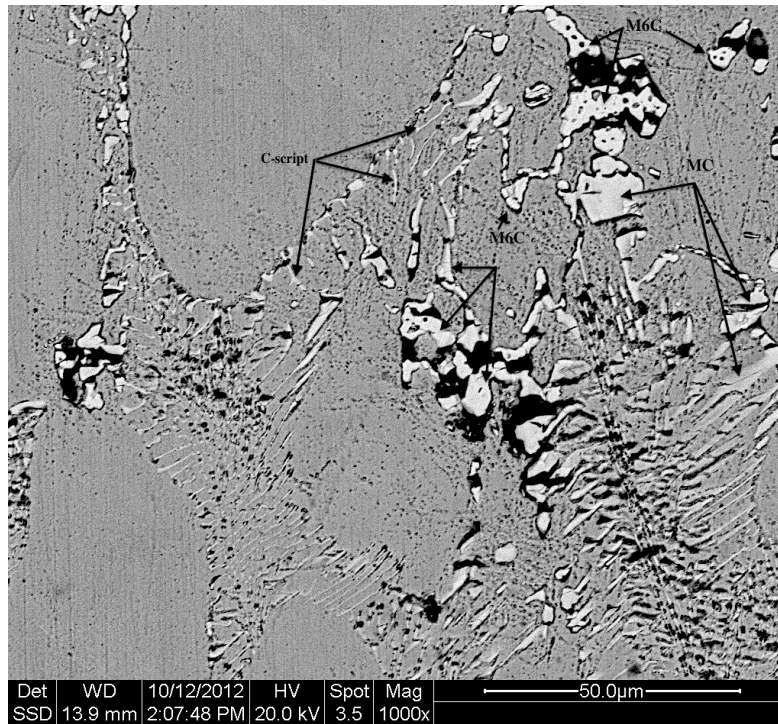


Figure 200. Etched microstructure of specimen S4 (at core); magnification: 1000X.
Microconstituents identified for metallographic reference purposes.

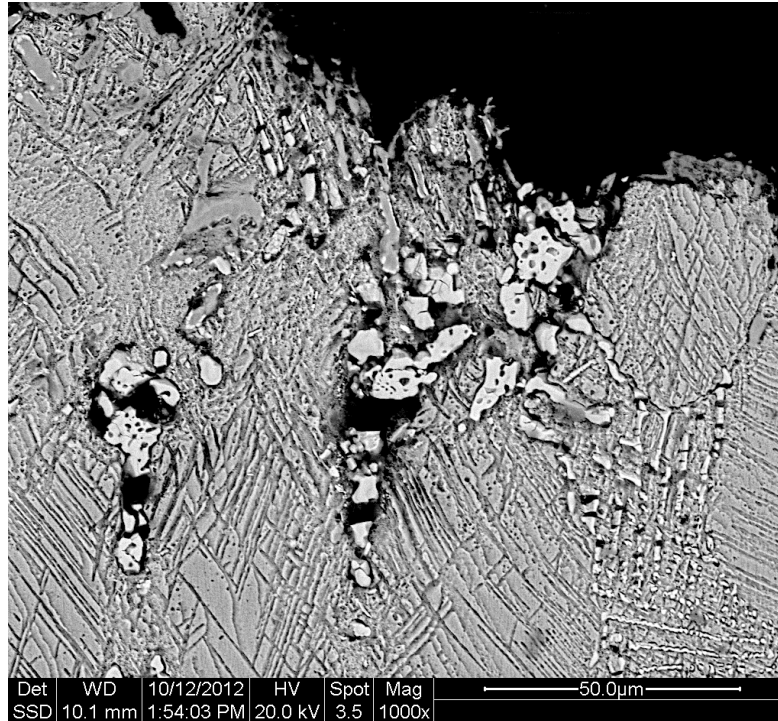


Figure 201. Etched microstructure of specimen S5, set 128 (rupture surface); magnification: 1000X.

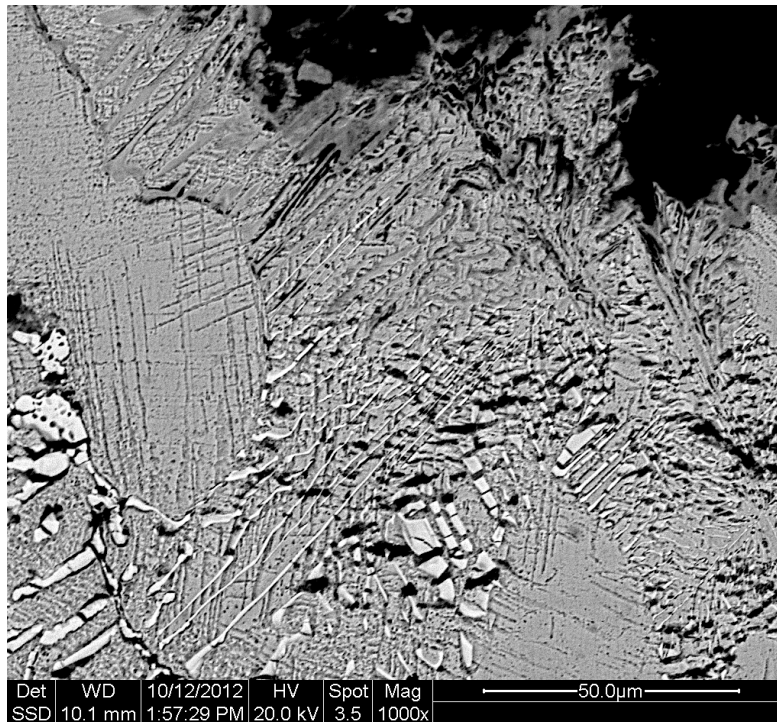


Figure 202. Etched microstructure of specimen S5, set 128 (rupture surface); magnification: 1000X.

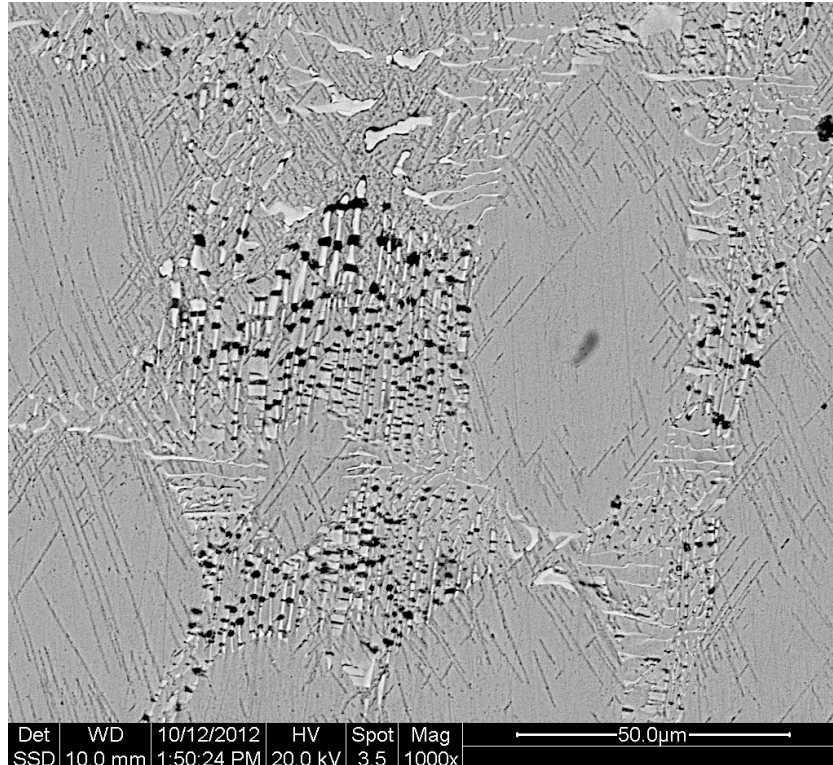


Figure 203. Etched microstructure of specimen S5, set 128 (at core); magnification: 1000X.

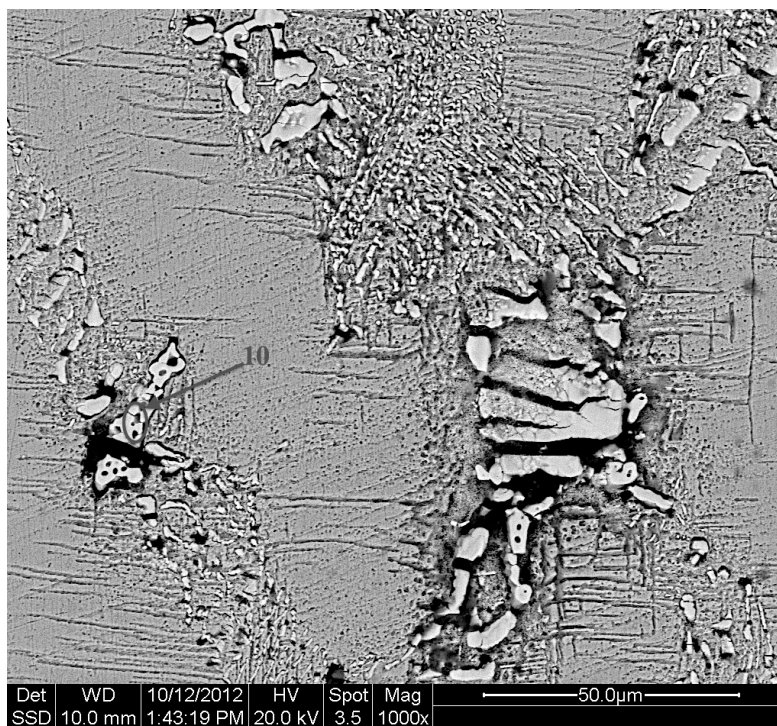


Figure 204. Etched microstructure of specimen S5, set 128 (at core); magnification: 1000X. A numbered oval indicates where an EDS analysis was conducted.

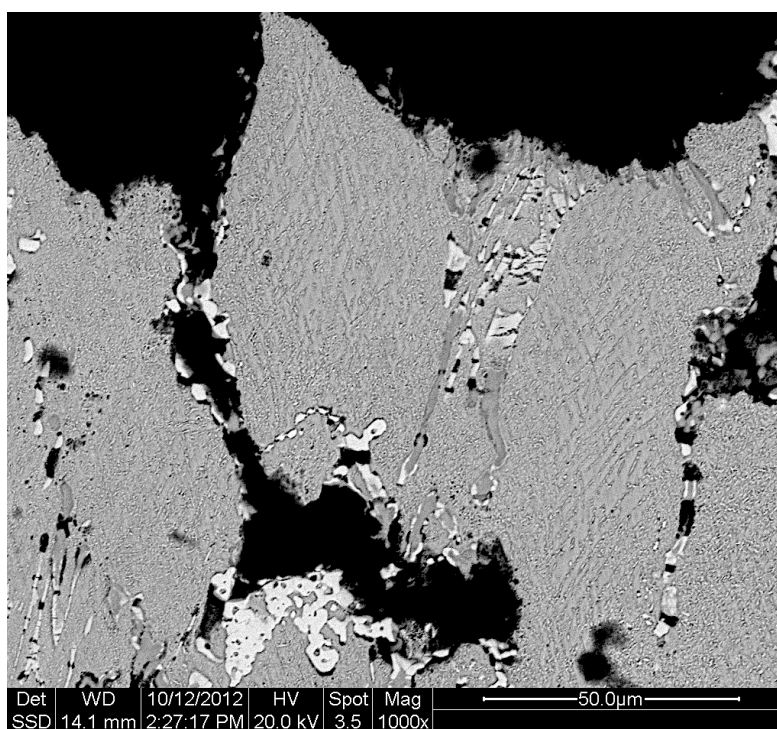


Figure 205. Etched microstructure of specimen S5, set 821 (rupture surface); magnification: 1000X.

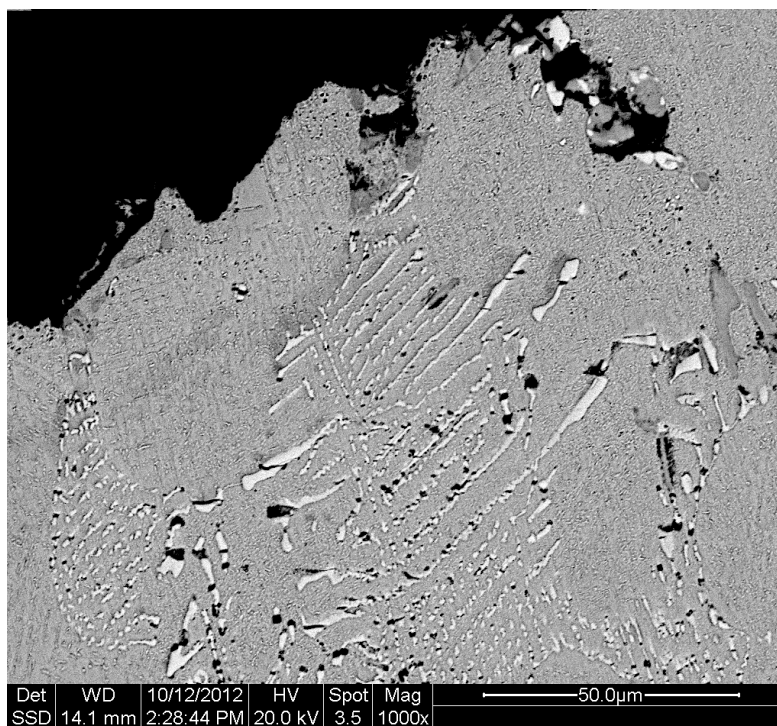


Figure 206. Etched microstructure of specimen S5, set 821 (rupture surface); magnification: 1000X.

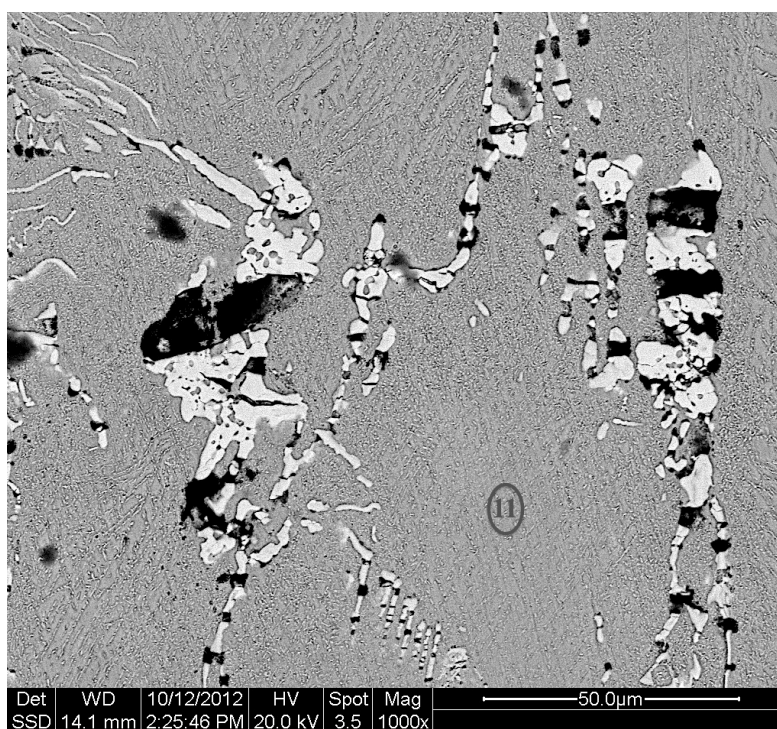


Figure 207. Etched microstructure of specimen S5, set 821 (at core); magnification: 1000X. A numbered oval indicates where an EDS analysis was conducted.

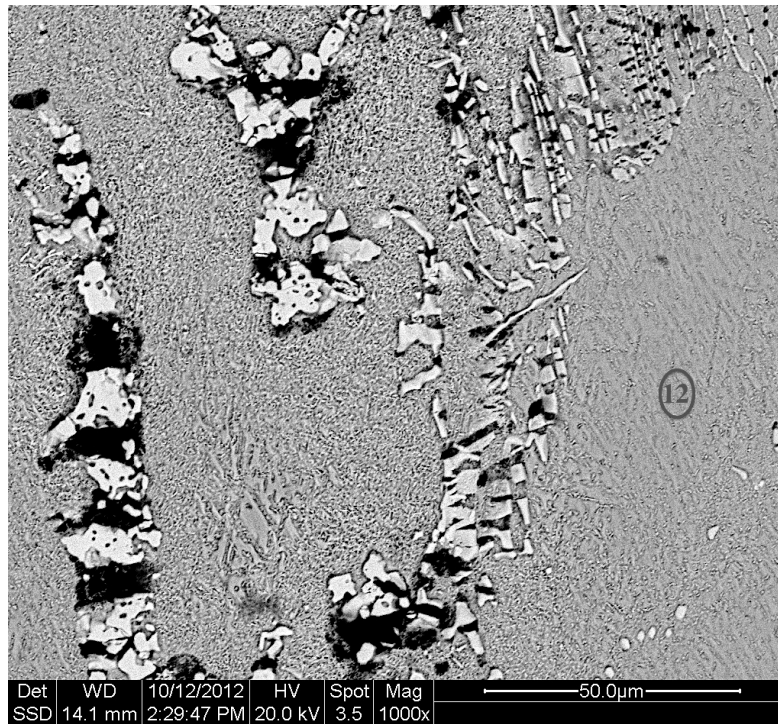


Figure 208. Etched microstructure of specimen S5, set 821 (at core); magnification: 1000X. A numbered oval indicates where an EDS analysis was conducted.

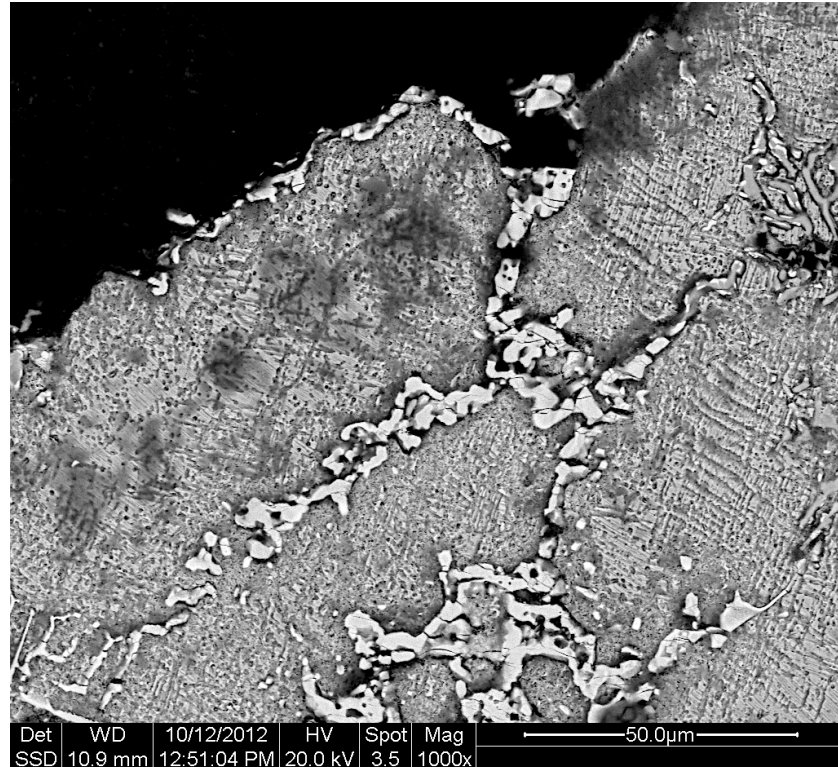


Figure 209. Etched microstructure of specimen S7 (rupture surface); magnification: 1000X.

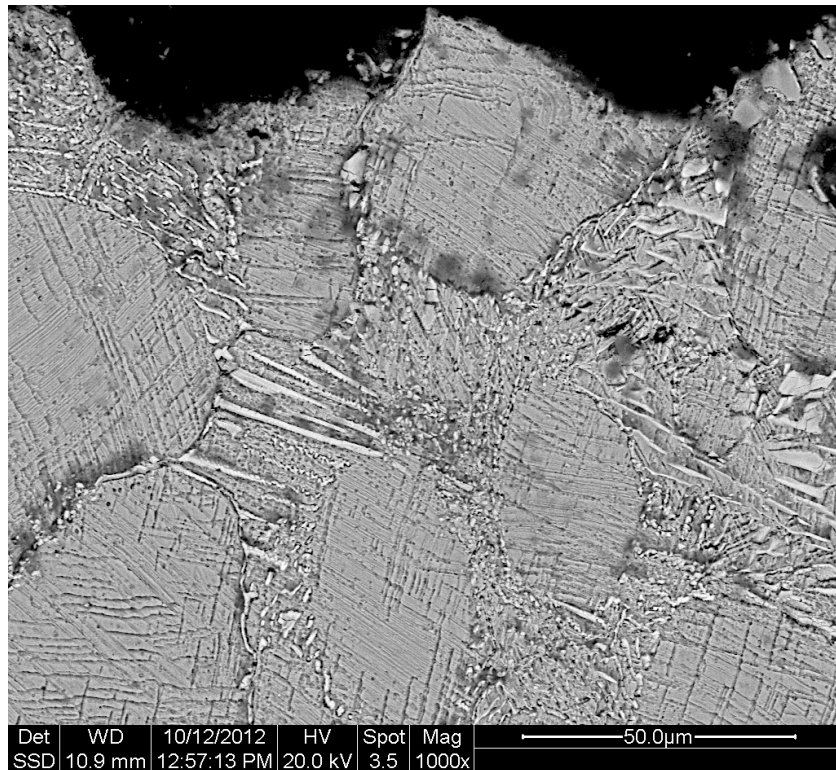


Figure 210. Etched microstructure of specimen S7 (rupture surface); magnification: 1000X.

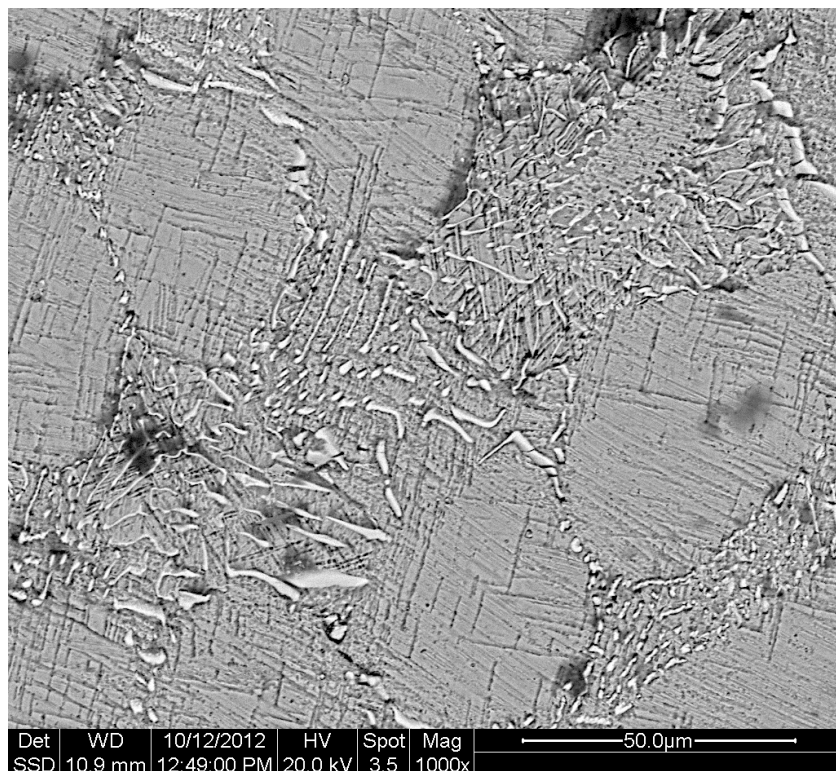


Figure 211. Etched microstructure of specimen S7 (at core); magnification: 1000X.

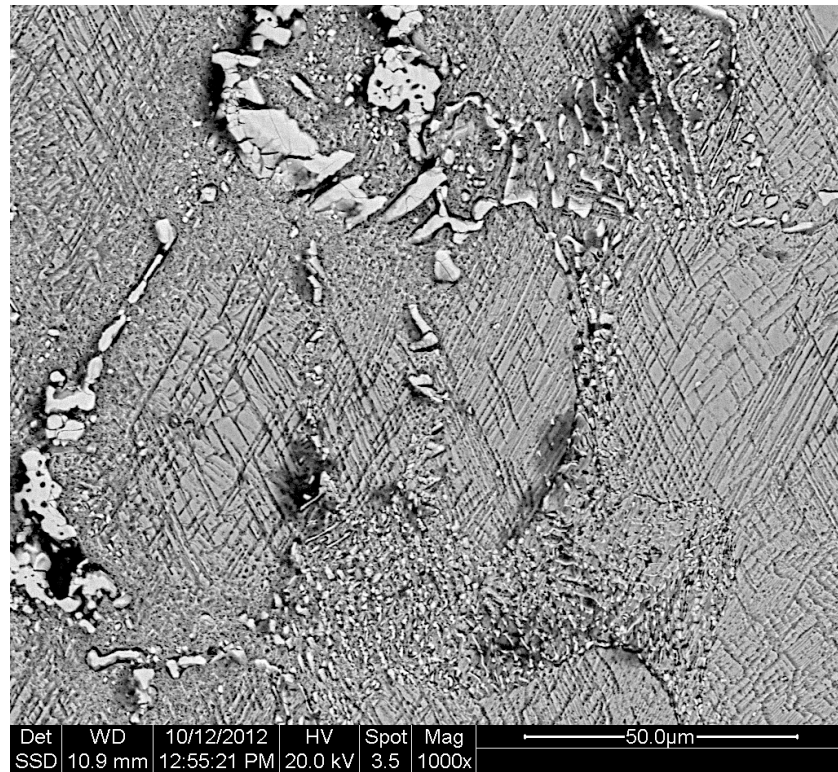


Figure 212. Etched microstructure of specimen S7 (at core); magnification: 1000X.

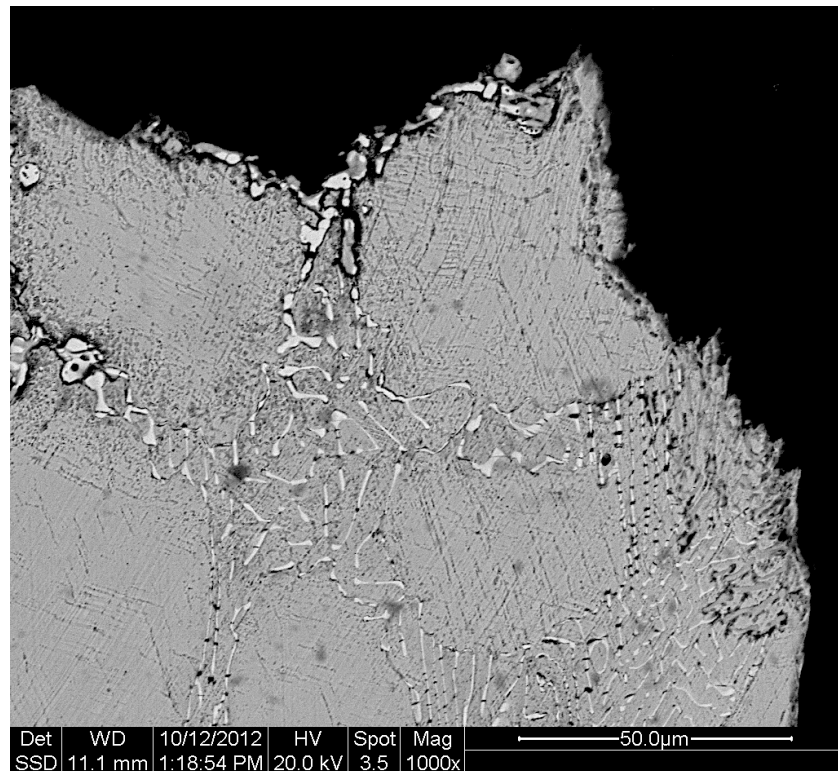


Figure 213. Etched microstructure of specimen S9 (rupture surface); magnification: 1000X.

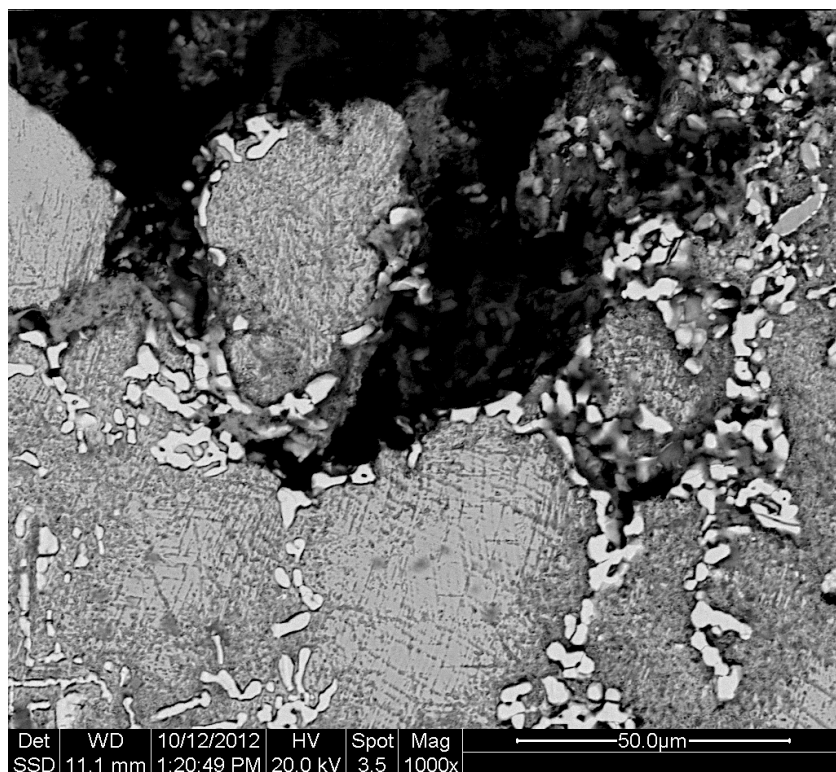


Figure 214. Etched microstructure of specimen S9 (rupture surface); magnification: 1000X.

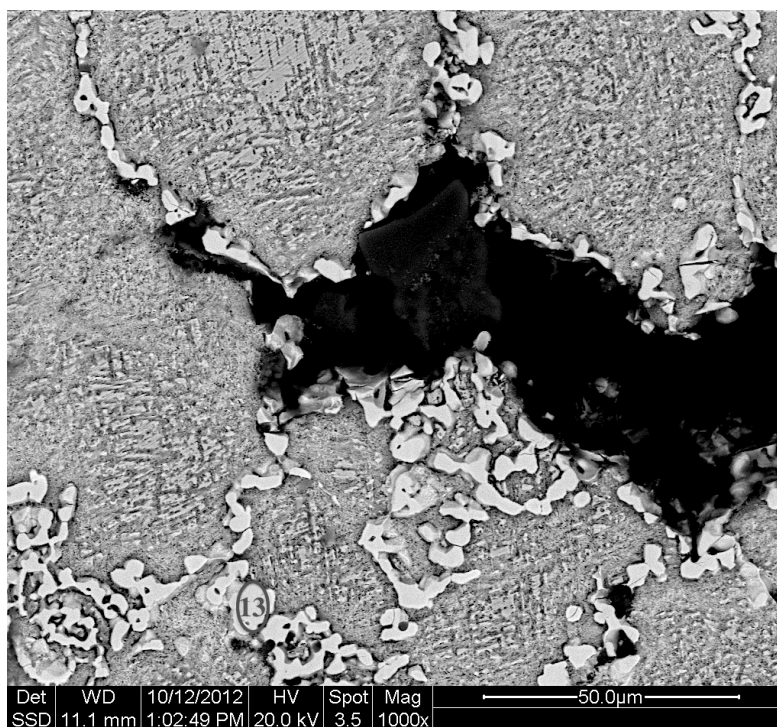


Figure 215. Etched microstructure of specimen S9 (at core); magnification: 1000X. A numbered oval indicates where an EDS analysis was conducted.

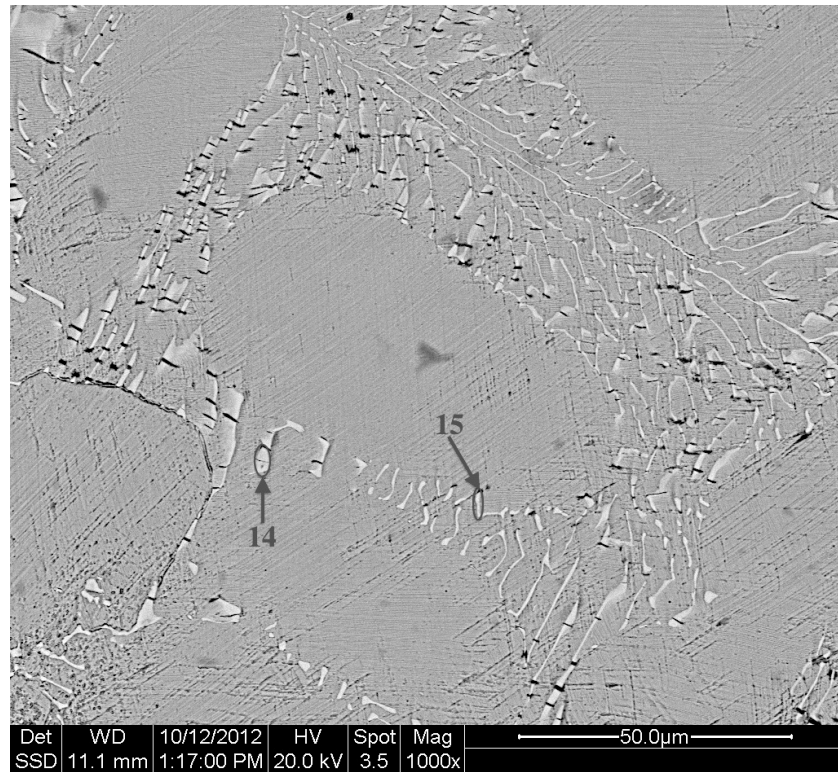


Figure 216. Etched microstructure of specimen S9 (at core); magnification: 1000X. Numbered ovals indicate where EDS analyses were conducted.

References

- [1] Cross, H. C., Badger, F. S., Badger, W. L., Bergen, L. S., Foley, F. B., Schoefer, E. A., & Welch, L. E. (1948). Heat-Resistant Castings. In T. Lyman (Ed.), *Metals Handbook* (pp. 576-581). Cleveland, OH: The American Society For Metals.
- [2] Beltran, A. M. (1987). Cobalt-Base Alloys. In C. T. Sims, N. S. Stoloff, & W. C. Hagel (Eds.), *Superalloys II* (pp. 135-163). New York, NY: John Wiley & Sons.
- [3] Sims, C. T. (1987). Superalloys: Genesis and Character. In C. T. Sims, N. S. Stoloff, & W. C. Hagel (Eds.), *Superalloys II* (pp. 1-26). New York, NY: John Wiley & Sons.
- [4] Weiss, V., Sessler, J. G., Syracuse University, U. S., & Mechanical Properties Data Center (Battelle Memorial Institute), U. S. (1963). *Aerospace Structural Metals Handbook (II)*. New York, NY: Syracuse University Press.
- [5] Mehl, R. F., Bankard, M. H., Federico, A. M., Fortin, P. E. (1972). Microstructure of Wrought Heat-Resistant Alloys. In: T. Lyman, H.E. Boyer, W. J. Carnes, P.M. Unterweiser et al. (Eds.), *Metals Handbook, Vol. 7: Atlas of Microstructures of Industrial Alloys* (8th ed., p. 260). Metals Park, OH: The American Society for Metals.
- [6] American Society for Testing Materials. (1954). *Report on the Elevated-Temperature Properties of Selected Super-Strength Alloys, Special Technical Publication No. 160*. Baltimore, MD: W. F. Simmons & H. C. Cross.
- [7] Reed-Hill, R. E., & Abbaschian, R. (1994). *Physical Metallurgy Principles* (3rd ed., p. 845). Boston, MA: PWS Publishing Company.

- [8] Ashby, M. F., Gandhi, C., & Taplin, D. M. R. (1983). Fracture-mechanism Maps and their Construction for F.C.C. Metals and Alloys. In M. F. Ashby & L. M. Brown (Eds.), *Perspectives in Creep Fracture* (pp. 1-32). New York, NY: Pergamon Press.
- [9] Goods, S. H., & Brown, L. M. (1983). The Nucleation of Cavities by Plastic Deformation. In M. F. Ashby & L. M. Brown (Eds.), *Perspectives in Creep Fracture* (pp. 71-86). New York, NY: Pergamon Press.
- [10] Murr, L. E. (1998). *Interfacial Phenomena in Metals and Alloys*. New Delhi, India: CBLS.
- [11] Benac, D. J., & Swaminathan, V. P. (2002). Elevated-Temperature Life Assessment for Turbine Components, Piping, and Tubing. In W. T. Becker & R. J. Shipley (Eds.), *ASM Handbook, Volume 11: Failure Analysis and Prevention* (pp. 289-312). Materials Park, OH: ASM International.
- [12] Porter, D. A., Easterling, K. E., & Sherif, M. Y. (2009). *Phase Transformations in Metals and Alloys* (3rd ed). Boca Raton, FL: Taylor and Francis Group.
- [13] ASTM Standard E139, 2011, "Standard Test Methods for Conducting Creep, Creep-Rupture, and Stress-Rupture Tests of Metallic Materials," ASTM International, West Conshohocken, PA, 2011, DOI: 10.1520/E0139-11, www.astm.org
- [14] Boyer, H. E. (1988). *Atlas of Creep and Stress-Rupture Curves*. Metals Park, OH: ASM International.
- [15] Patterson, B. (2002). *Service Life Residual Creep and Rupture Properties Evaluation of the Superalloy Udimet 500*. (Master's degree thesis).
- [16] Viswanathan, R. (1989). *Damage Mechanisms and Life Assessment of High Temperature Components*. Metals Park, OH: ASM International.

[17] ASTM Standard E8/E8M, 2011, “Standard Test Methods for Tension Testing of Metallic Materials,” ASTM International, West Conshohocken, PA, 2011, DOI: 10.1520/E0008_E0008M-11, www.astm.org

[18] Lvova, E. (2007). A Comparison of Aging Kinetics of New and Rejuvenated Conventionally Cast GTD-111 Gas Turbine Blades. *Journal of Materials Engineering and Performance*, 16 (2). Retrieved from: <http://www.springerlink.com/content/kkmp06j814688865/>

Curriculum Vita

Jonathan C. Contreras was born in El Paso, Texas. The first and only son of Juan Carlos and Carmen Lorena Contreras, he graduated from Eastwood High School in El Paso, Texas, in the summer of 2006. He entered the University of Texas at El Paso (UTEP) with a Presidential Excellence Scholarship in the fall of 2006. In the course of pursuing his Bachelor of Science (B. Sc.) degree in Metallurgical and Materials Engineering (MME), he worked as an undergraduate teaching and research assistant for the MME department at UTEP and underwent an internship at a Freeport-McMoRan Copper and Gold mine in Bagdad, Arizona; during this time, he led and was involved in several student organizations within the MME department. In the fall of 2009, he graduated Magna Cum Laude with a B. Sc. in MME and entered the UTEP Graduate School in the spring of 2010, in pursuit of a Master of Science (MS) degree in MME. During his graduate studies, he worked as a graduate teaching and research assistant for the MME department at UTEP, as well as a failure analysis apprentice for Herrera, Stafford, and Associates; he was the lead author of the journal publication “Failure Analysis Case Study on a Fractured Tailwheel Fork” that was published in 2011 in the *Journal of Failure Analysis and Prevention*. His research experiences and interests include failure analysis and material performance, as well characterization and remnant life/damage assessments of superalloy components used in elevated-temperature service environments.

Permanent address: 4025 W. 103rd Avenue
Westminster, CO, 80031

This thesis was typed by Jonathan C. Contreras.